

Zn₃P₂ as an earth-abundant photovoltaic material: from growth to device

Présentée le 20 janvier 2023

Faculté des sciences et techniques de l'ingénieur
Laboratoire des matériaux semiconducteurs
Programme doctoral en science et génie des matériaux

pour l'obtention du grade de Docteur ès Sciences

par

Rajrupa PAUL

Acceptée sur proposition du jury

Prof. M. Ceriotti, président du jury
Prof. A. Fontcuberta i Morral, directrice de thèse
Prof. E. Garnett, rapporteur
Prof. H. Weman, rapporteur
Prof. K. Sivula, rapporteur

Remember to celebrate milestones
as you prepare for the road ahead.
— Nelson Mandela

To my family...

Acknowledgements

It seems only yesterday that I had my first day in EPFL, I guess it is appropriate to say time flies when you are enjoying what you do. While I will always cherish and fondly look back on this phase of my life, this journey by no means was easy and would not have been possible without the support of many. I would like to extend my gratitude to each and every one who has made this journey possible.

First and foremost, I would like to thank my thesis supervisor **Prof. Anna Fontcuberta i Morral** for believing in me and giving me the opportunity to be a part of her team. Throughout this journey, she has provided me with her constant support and guidance. She has never discouraged an idea and always sought to inspire her students. She has been a great mentor, offering advice and encouragement with a perfect blend of wit and humour. She is very compassionate and always supports her students through thick and thin, especially during the lockdown, when research came to a halt and it was easy to feel demoralized, she made sure of the well-being of her students and their mental health. Her research philosophy and work ethics are commendable and a source of motivation for many. I wholeheartedly thank her for inspiring me to be the scientist I'm today.

I would like to express my sincere gratitude to members of the jury **Prof. Michele Ceriotti**, **Prof. Helge Weman**, **Prof. Erik Garnett**, and **Prof. Kevin Sivula** for agreeing to be on my thesis defence committee and for taking the time to review the thesis manuscript. I look forward to our discussion.

I would like to acknowledge all my collaborators who have helped me progress in my research. I have had the privilege to collaborate with scientific groups both in and outside EPFL. First, I would like to thank **Prof. Qihua Xiong** and **Andrés Granados del Águila** from Nanyang Technological University for their support on the photoluminescence study. **Prof. Ignacio Íñiguez de la Torre** and **Héctor Sánchez Martín** from the University of Salamanca for hosting me this summer in their laboratory and providing their support on electrical measurements. **Prof. Jessica Boland** and **Xinyun Liu** from the University of Manchester for carrying out the terahertz spectroscopy measurements and providing valuable insight into the study. **Dr. Franz-Josef Haug** and **Julien Hurni** from PV-Lab EPFL for accommodating my request on various measurements. Finally, I would like to thank **Prof. Albert Polman** and **Stefan Tabernig**

from AMOLF for carrying out simulations and measurements related to the photovoltaic study. I would like to thank all my semester and thesis students, especially **Shreyas Joglekar**, **Nicolas Humblot**, **Vanessa Conti**, and **Joel Reñé Sopera**, for your significant contribution to this thesis.

It has been an absolute delight to be a part of LMSC and I would like to express my appreciation for all the LMSC group members. The old II-V team, **Simon Escobar Steinvall**, **Mahdi Zamani**, and **Elias Stutz**, I highly value your support and collaboration on everything zinc phosphide related and more. Thank you **Jean-Baptiste Léran** for teaching every small detail of the MBE and never being tired of my questions, thanks for your relentless support. **Nicolas Tappy**, your passion for coffee and physics astounds me. You have been a great office mate all these years providing insight and knowledge in every topic (from pasta making to optics). And I sincerely thank you for giving us our lab mascot. **Andrea Guinto**, thanks for being the worst, jokes aside it has been a pleasure sharing the office space with a “ninja”. **Mirjana Dimitrievska**, your passion and drive for science is motivating, and only you can envision a fun journal art cover. Thanks for all your support in the last phase of my thesis. **Valerio Piazza**, it is inspiring how well you manage all the different topics you work on. I highly appreciate your guidance and support in the last few years; it has been invaluable. **Didem Dede**, your vivacious smile and attitude can uplift anyone’s spirit, and your passion for your work is admirable. I will always cherish our late-night discussion about life. **Nicholas Paul Morgan**, I have never heard you say no to anyone asking for your help in the cleanroom or otherwise, thanks for sharing your technical know-how and insight on various topics. **Santhanu Paniker Ramanandan**, your motivation for work is inspiring (and a little scary). I appreciate your encouragement and listening to my rants. **Claire Blaga**, thanks for all the enjoyable moments. Also, thanks a lot for your help with CL and Raman measurements. **Anja Tiede** I have known you for a short time but I can definitely say I will miss our conversations, and thanks a ton for the measurement at AMOLF.

I would like to thank the newbies in the group, **Michele Zendrini**, **Thomas Hagger**, **Gabriel Iseli**, and **Stefano Marinoni**, for making all the lunch conversations fun.

I would also like to thank some of the ex-members of LMSC, **Dmitry Mikulik**, **Luca Francaviglia**, **Martin Friedl**, **Wonjon Kim**, **Lea Ghisalberti**, **Lucas Güniat**, and **Akshay Balgarkashi**, for all the good times we spent in and outside lab.

I highly appreciate the technical support provided by the team at CMI and CIME, in particular, **Zdenek Benez** for all the training and informative conversations, **Adrien Toros** for helping with all the difficult bonding, and **Lucie Navratilova** for answering my endless query on FIB.

Thanks to **Monika Salas Tesar** for running all the administrative work effortlessly and for all the good health tips.

I will forever treasure some of the lasting friendships, thanks to **Anna Kukolova** and **Sho Watanabe** for making this journey fun and exciting. Thanks for including me in all your plans even though you knew the answer. **Marica Giordano** and **Anna Kukolova**, you made

Acknowledgements

the conference in Singapore an enjoyable trip. **Ping Che** thank you for all the invites to the delicious dumpling dinners. **Rajam Elancheliyan**, thanks for being such a great friend for the last 12 years.

Finally, I would like to express my heartfelt gratitude to my family for supporting me through this journey, without them none of this would have been possible. I thank my **mom**, **dad**, and **sister** for always being by my side and believing in me. I especially thank my **mom** for encouraging me to chase my dreams. I would like to thank my life partner, **Andrés**, for being a part of this roller-coaster ride, thanks for your unconditional support, patience, and understanding. You inspire the best in me.

Lausanne, 20 September 2022

Rajrupa Paul.

Abstract

The development of cost-effective and earth-abundant semiconducting materials is imperative for the sustainable deployment of photovoltaic technology. Zinc phosphide (Zn_3P_2) is a promising candidate for terawatt-scale electricity generation. It has a near-optimal bandgap of 1.5 eV, a high visible-light absorption coefficient (10^4 - 10^5 cm^{-1}) near the band edge, a long minority-carrier diffusion length (5-10 μm), and both zinc and phosphorous are earth-abundant elements. However, the highest recorded efficiency stands at 6% for multicrystalline Zn_3P_2 wafer solar cells. In the last 40 years, there has not been any significant improvement in the efficiencies of Zn_3P_2 -based solar cells. Material challenges include a lack of compatible substrate for growth and control over the doping of the material. One of the key issues associated with Zn_3P_2 -based solar cells is the limited understanding of the correlation between the functional properties and the crystalline structure and defect density of the material. In this thesis, we explore an alternative approach for the growth of Zn_3P_2 that circumvents the need for a lattice-matched substrate. In addition, we investigate the electrical properties of Zn_3P_2 thin films and highlight the role of composition and growth conditions on the material property. Finally, we demonstrate a minimally processed solar cell device with an efficiency value of 4.4% and propose a working principle.

In the first part of this thesis, we demonstrate the growth of Zn_3P_2 on graphene using molecular beam epitaxy. The growth proceeds via van der Waals epitaxy and shows a preferentially crystallographic orientation. We delve into the growth process by identifying the key growth parameters and determining the limiting factors. The material structure and optical functionality were also studied using Raman and photoluminescence spectroscopy. The second part of this thesis presents the progress on the understanding of the electrical properties of Zn_3P_2 thin films. We used several different characterization techniques to demonstrate the role of composition and microstructure on the electrical transport mechanism and carrier concentration. We showcase a hole mobility of $125 \text{ cm}^2/\text{Vs}$ for high-quality single crystalline Zn_3P_2 thin films and the ability to modify the carrier density by the composition (Zn-to-P ratio). In the final part of the thesis, we showcase a Zn_3P_2 thin film-based solar cell with relatively high open-circuit voltage (0.528 V) and short-circuit current ($13.7 \text{ mA}/\text{cm}^2$). We investigate the dominant recombination mechanism in the material using the ideality factor obtained from dark and light measurements. We highlight the possible loss mechanisms of the solar cell and provide a perspective on this new generation of Zn_3P_2 -based solar cells.

Keywords: Zinc phosphide, earth-abundant, solar cells, II-V semiconductor, van der Waals epitaxy, Raman spectroscopy, photoluminescence, electrical transport, conductivity, electric transport mechanism, device fabrication, defects, focused ion beam microfabrication

Riassunto

Lo studio di materiali semiconduttori che siano poco costosi e disponibili in grandi quantità è necessario per sviluppare in modo sostenibile la tecnologia fotovoltaica. Il fosfuro di zinco (Zn_3P_2) è un candidato promettente nell'ottica dell'insieme di tecnologie per la generazione di terawatt di elettricità: ha un band gap quasi ottimale di 1.5 eV, un alto coefficiente di assorbimento nel visibile (10^4 - 10^5 cm^{-1}), una importante lunghezza di diffusione dei portatori minoritari (5-10 μm) e sia lo zinco che il fosforo sono materiali presenti in abbondanza sulla Terra. Nonostante ciò, al momento la massima efficienza mai ottenuta per una cella solare policristallina in Zn_3P_2 è del 6% e negli ultimi 40 anni non c'è stato un miglioramento significativo di celle solari basate sul fosfuro di zinco. Le difficoltà legate a questo materiale includono la mancanza di substrati compatibili per la crescita e lo scarso controllo sul livello di drogaggio. In particolare, uno dei problemi principali legati alle celle solari in fosfuro di zinco è l'ancora limitata comprensione del rapporto tra le proprietà funzionali, la struttura cristallina e la densità di difetti del materiale. In questa tesi si esplorerà un modo alternativo per la crescita di Zn_3P_2 , in grado di evitare la necessità di avere un substrato con un reticolo di dimensioni adatte. Inoltre, si investigheranno le proprietà elettriche di film sottili di Zn_3P_2 , sottolineando il ruolo della composizione e delle condizioni di crescita. Infine, si illustrerà la fabbricazione di una cella solare con un'efficienza del 4.4% e se ne proporrà un principio di funzionamento.

Nella prima parte della tesi verrà spiegata la crescita di Zn_3P_2 su grafene mediante l'uso di epitassia da fasci molecolari. La crescita è realizzata con epitassia di van der Waals e mostra un'orientazione cristallografica preferenziale. Il processo di crescita è stato studiato identificandone i parametri principali e i fattori limitanti, mentre la struttura del materiale e le sue funzionalità ottiche sono state caratterizzate con spettroscopia di Raman e di fotoluminescenza. La seconda parte della tesi è legata alla comprensione delle proprietà elettriche di film sottili di Zn_3P_2 . Sono state impiegate diverse tecniche di caratterizzazione per analizzare l'impatto della composizione e della microstruttura sul trasporto elettrico e la concentrazione dei portatori. In particolare, è stato dimostrato che la mobilità delle lacune può raggiungere il valore di $125 \text{ cm}^2/\text{Vs}$ per film sottili monocristallini di Zn_3P_2 di alta qualità e che la composizione (il rapporto tra Zn e P nei campioni) è in grado di modificare la densità di portatori.

Nella parte finale della tesi si illustreranno i dettagli di una cella solare in Zn_3P_2 basata su film sottili e con tensione di circuito aperto (0.528 V) e densità di corrente di corto circuito (13.7 mA cm^{-2}) relativamente alte. I meccanismi di ricombinazione dominanti nel materiale sono stati investigati analizzando il fattore di idealità ottenuto da misure al buio e sotto illuminazione. Infine, i possibili meccanismi di perdita del dispositivo sono stati analizzati, donando una prospettiva sul futuro della nuova generazione di celle solari basate sul fosfuro di zinco.

Parole chiave: Fosfuro di zinco, materiali abbondanti, celle solari, semiconduttori II-V, epitassia di van der Waals, spettroscopia di Raman, fotoluminescenza, trasporto elettrico, conduttività, capacità, meccanismi di trasporto elettrico, fabbricazione del dispositivo, microfabbricazione con fascio ionico localizzato, difetti.

Contents

Acknowledgements	i
Abstract	v
List of figures	xiii
List of tables	xix
1 Introduction & Motivation	1
2 Properties and Growth of Zn_3P_2	7
2.1 Properties of Zn_3P_2	7
2.1.1 Physical Properties	7
2.1.2 Optoelectronic Properties	8
2.1.3 Electrical Properties	11
2.2 Zn_3P_2 Growth Overview	15
2.3 Epitaxial Growth	16
2.3.1 van der Waals Epitaxy	17
3 Experimental Methods	25
3.1 Molecular Beam Epitaxy	25
3.2 Optical Spectroscopy	28
3.2.1 Raman Spectroscopy	28
3.2.2 Photoluminescence Spectroscopy	30
3.3 Device Fabrication	31
3.3.1 Electron Beam Lithography	31
3.3.2 Focused Ion Beam	34
3.4 Electrical Characterization	36
3.4.1 Transmission Line Measurement	36
3.4.2 Hall Effect Measurement	37
3.4.3 Conductive Atomic Force Microscopy	40
4 van der Waals epitaxy of earth-abundant Zn_3P_2 on graphene for photovoltaics	43
4.1 Accompanying information	43
4.2 Abstract	43

4.3	Introduction	44
4.4	Experimental Details	45
4.4.1	Growth of Zn_3P_2	45
4.4.2	Characterization	45
4.5	Results and Discussion	46
4.6	Conclusions	55
4.7	Acknowledgments	56
5	Zn/P ratio and microstructure defines carrier density and electrical transport mechanism in earth-abundant $\text{Zn}_{3-x}\text{P}_{2+y}$ thin films	57
5.1	Accompanying information	57
5.2	Abstract	57
5.3	Introduction	58
5.4	Experimental Details	59
5.4.1	Materials and devices	59
5.4.2	Characterization	60
5.5	Results and Discussion	62
5.5.1	Structural properties of Zn_3P_2 thin films	62
5.5.2	Electrical Measurements	62
5.6	Conclusion	71
5.7	Acknowledgements	72
6	Carrier generation and collection in $\text{Zn}_3\text{P}_2/\text{InP}$ heterojunction solar cells	73
6.1	Accompanying information	73
6.2	Abstract	73
6.3	Introduction	74
6.4	Experimental Details	75
6.4.1	Materials and device fabrication	75
6.4.2	Characterization	75
6.5	Results and Discussion	77
6.6	Conclusion	85
6.7	Acknowledgments	86
7	Conclusion and Outlook	87
A	Supplementary information for “van der Waals epitaxy of earth-abundant Zn_3P_2 on graphene for photovoltaics”	91
A.1	Raman spectra	91
A.2	XRD measurements	91
A.3	Effect of Total Flux	92
A.4	EBSD	93
A.5	Photoluminescence	95

Contents

B	Supplementary information for “Zn/P ratio and microstructure defines carrier density and electrical transport mechanism in earth-abundant $\text{Zn}_{3-x}\text{P}_{2+y}$ thin films ”	97
C	Supplementary information for “Carrier generation and collection in $\text{Zn}_3\text{P}_2/\text{InP}$ heterojunction solar cells”	101
	C.1 Optical simulations	103
	C.2 Electronic simulations	103
	Bibliography	105
	Curriculum Vitae	134

List of Figures

1.1	The band gap of a semiconductor showing the presence of (a) acceptor defect-induced energy level, (b) broadening to an impurity band due to increased defect density, (c) band tail formation leading to a reduction in the band gap.	3
1.2	Theoretical Shockley-Queisser detailed-balance limit as a function of the band gap, the materials highlighted in green represent earth-abundant elements, the materials depicted in purple contain rare-earth elements, and the materials denoted in black contain toxic elements.	4
2.1	(a) The Zn–P phase diagram calculated using the parameters optimized in the current work [84] for the exponential (dotted-line) and LET model (solid line) of liquid interaction parameter, reprinted from [84], Copyright 2019, with permission from Elsevier. (b) Crystal structure representation of Zn_3P_2 tetragonal unit cell along different crystal planes, adapted from [76].	8
2.2	(a) Steady-state PL measurements of etched Zn_3P_2 wafers at different temperatures, the inset depicts the energies, as a function of temperature. (b) Room temperature intensities of the various PL peaks from etched Zn_3P_2 wafers as a function of laser pump intensity, the inset depicts the normalized PL spectra over similar range of laser pump intensities. Reprinted from [125], with the permission of AIP Publishing	9
2.3	PL spectra obtained from monocrystalline thin film acquired with a 488 nm laser at (a) 12 K, where the PL peaks from the InP substrate are depicted with grayed out areas, the inset shows magnified view of the peaks near 1.52 eV, and (b) 230 K. Adapted from [261].	11
2.4	Cross-sectional (a) STEM-DF image of the interface between Mg/p- Zn_3P_2 , and (b) STEM-EDS mapping across the Mg/p- Zn_3P_2 interface. Reprinted with permission from [115]. Copyright 2018 American Chemical Society.	12
2.5	(a) Symmetric HRXRD scans of the Zn_3P_2 on GaAs substrate for increasing Zn_3P_2 layer thickness. (b) Hole mobility of Zn_3P_2 as a function of layer thickness, the filled circles represent the data from strained films and the open circles depicts the data from partially relaxed films. Reprinted from [25], Copyright 2013, with permission from Elsevier.	13
2.6	Barrier heights of different metal contacts on Zn_3P_2 as a function of the metal work function. Reprinted from [299], with the permission of AIP Publishing. . .	14

2.7	SEM images of (a) amorphous (top) and polycrystalline (bottom) Zn_3P_2 thin films grown on InP substrate, the scale bars correspond to 1 μm , adapted from [311]. (b) Zn_3P_2 nanostructures at different stages of growth on InP substrate, the scale bars are 500 nm, adapted from [66].	15
2.8	(a) SEM images of triangular-shaped WS_2 crystals grown onto hBN flake, reprinted with permission from [196], Copyright 2014 American Chemical Society. (b) SEM image of vertically aligned ZnO nanowire array grown on muscovite mica substrate, inset shows cross-sectional SEM image of the vertical nanowires, reprinted with permission from [275], Copyright 2012 American Chemical Society. (c) Schematic illustrations of vdWE (left) and QvdWE (right), reprinted from [13], with permission from Royal Society of Chemistry.	19
2.9	(a) SEM image of InP crystal grown on graphene/ SiO_2 /Si, scale bar in the image corresponds to 1 μm , reprinted from [184], with the permission of John Wiley & Sons. (b) SEM image of CdTe nanowires grown on muscovite mica substrate, inset shows the magnified SEM image, reprinted from [13], with permission from Royal Society of Chemistry.	21
2.10	(a) Top-view SEM image of the overgrown AlGaIn pyramid arrays grown on graphene, the inset shows the magnified view of the same sample, the scale bar in the inset is 2 μm , reprinted from [186], with the permission of AIP Publishing. (b) Top-view SEM image of GaN crystals grown on graphene, reprinted from [105], with the permission of IOP Publishing, Ltd.	22
3.1	MBE system (a) schematic representation of the MBE chamber, and (b) photograph of the Veeco GENxplor MBE system used in this thesis.	26
3.2	Raman spectra obtained from Zn_3P_2 grown on graphene at (a) 300 K, and (b) 15 K, the different modes are highlighted for the lower temperature measurement.	29
3.3	Major radiative recombination processes (a) band-to-band recombination, (b) recombination between a free and a localized carrier, (c) recombination between the levels of a single impurity, (d) recombination between an acceptor and a donor, and (e) recombination between free or bound excitons.	30
3.4	Optical image of a Hall bar structure processed on the micro-crack.	32
3.5	Schematic representation of the fabrication steps used for processing the electrical device structures.	33
3.6	SEM image of a fabricated Hall bar structure.	34
3.7	Schematic representation of FIB (a) milling, and (b) deposition, process.	35
3.8	Schematic representation of (a) the top-view of a TLM structure, highlighting the dimensions, (b) a common measurement outcome, where the resistance is plotted as a function of the distance. The cross-sectional view showing the representative electric field lines (c) low ρ_c , and (d) high ρ_c	37

3.9	Schematic representation of (a) a Hall bar, highlighting the dimensions, the current injection, the Hall voltage, and the longitudinal voltage, and (b) a common measurement outcome, where the resistance is plotted as a function of the applied magnetic field.	39
3.10	Schematic representation of the temperature dependence of (a) carrier concentration, (b) mobility and the contribution from different scattering mechanisms, and (c) conductivity, in a semiconductor adapted from [90].	39
4.1	(a-f) Representative scanning electron micrographs of growths of Zn_3P_2 on graphene as a function of temperature and V/II ratio; (g) room temperature Raman spectra of samples shown in a-c, indicating that for V/II = 1.55 crystalline Zn_3P_2 is formed, while for lower V/II ratios crystalline zinc is found in addition, and for higher V/II ratios the material is amorphous.	47
4.2	(a-c) SEM images of (a) commercial graphene, (b) Zn_3P_2 triangular flakes grown on graphene after growing for 20 min, and (c) Zn_3P_2 triangular flakes grown on graphene after growing for 90 min; (d) schematic representation of the growth evolution of Zn_3P_2 on graphene; (e-f) AFM images of Zn_3P_2 grown on graphene for (e) 80 min and (f) 150 min; (g) highlights two different morphologies of Zn_3P_2 grown on graphene; (h-i) cross-sectional SEM images of Zn_3P_2 grown on graphene for (h) 240 min and (i) 300 min; (j) plot showing the time evolution of the surface coverage (red triangular symbol) and vertical dimensions (blue circular symbol) of Zn_3P_2 flakes on graphene; the solid lines in the graph is a guide to the eye.	49
4.3	(a) XRD pattern of a Zn_3P_2 film showing the tetragonal structure and a preferential orientation. Only 101 family of planes are observed in the pattern; (b-c) Bright-field TEM images of the triangular Zn_3P_2 flake grown on graphene; (d) HRTEM image of the triangular Zn_3P_2 flake, showing a d-spacing of 0.568 nm; (e) electron diffraction pattern obtained from the Zn_3P_2 flake along the [210] zone axis.	52
4.4	(a-b) PL spectra at room temperature excited with 633 nm illumination with different powers (a) of sample A, which is Zn_3P_2 grown on graphene for 100 min; inset shows the SEM image of sample A, (b) of sample B, which is Zn_3P_2 grown on graphene for 250 min; inset shows the SEM image of sample B; (c-d) PL spectra at temperatures from 300 to 200 K excited with 633 nm illumination at 621 μW of (c) sample A, and (d) sample B; (e-f) PL spectra done by decreasing the temperature below 200 K excited with 532 nm illumination (e) at 946 μW on sample A, and (f) at 92 μW on sample B; (g-h) PL spectra at cryogenic temperature using different powers (g) on sample A at 10 K excited with 633 nm illumination, and (h) on sample B at 5.8 K excited with 532 nm illumination.	53

5.1	Fabrication process of the electrical device on Zn_3P_2 thin films: (a) schematic representation of the device fabrication steps, (step 1) alignment marker definition, (step 2) hall bar definition after the second EBL and RIE process, (step 3) contact deposition using sputtering after the third EBL process, (step 4) isolation of the device using FIB milling. (b) SEM image of the final device.	61
5.2	Cross-sectional SEM micrographs of the (a) monocrystalline Zn_3P_2 thin film (b) polycrystalline Zn_3P_2 thin film. Out-of-plane diffraction from (c) InP (100) substrate (d) monocrystalline Zn_3P_2 thin film showing only the 00h family of planes (e) polycrystalline Zn_3P_2 thin film showing a textured growth. SIMS measurements from (f) monocrystalline Zn_3P_2 thin film (M1) with Zn/P ratio ~ 1.47 (g) polycrystalline Zn_3P_2 thin film (P2) with Zn/P ratio ~ 1.64	63
5.3	(a) Optical image of the TLM structure used for the measurements. TLM plots showing resistance as a function of the length, obtained from (a) monocrystalline Zn_3P_2 thin film (M1) (b) polycrystalline Zn_3P_2 thin film (P2), on i-InP (100) substrates (c) monocrystalline Zn_3P_2 thin film on n-InP (100) substrate (M3). . .	65
5.4	Temperature-dependent resistance plot showcasing the semiconducting behaviour of (a) monocrystalline Zn_3P_2 thin film (M1), and the corresponding fitting for thermally activated conduction (inset) (b) polycrystalline Zn_3P_2 thin film (P2), and the corresponding fitting for thermally activated conduction between 300-200 K and NNR between 200-100 K (inset). (c) Temperature-dependent I-V characteristics obtained from monocrystalline Zn_3P_2 thin film with a Zn/P ratio ~ 1.58 (M4) plotted on a semi-logarithmic scale (d) the corresponding temperature-dependent I-V characteristics plotted on a log-log scale, three distinct transport regions are visible : ($I \propto V$) ohmic region, ($I \propto V^m$, $m > 2$) TFL region, and ($I \propto V^2$) SCLC region, the dashed lines represent the tangents with slopes 2 and 8 used for determining V_{TFL} at 300 K and slopes 2 and 15 for determining V_{TFL} at 150 K	68
5.5	(a) Schematic representation of the planar configuration used for the C-V measurements, L_t is the distance between the Schottky and the ohmic contacts. The C-V plot obtained by varying L_t from (b) monocrystalline Zn_3P_2 thin film (M1) (c) polycrystalline Zn_3P_2 thin film (P2). (d) Plot showing the measured carrier concentration as a function of the Zn/P ratio (the error bars represent standard deviation due to L_t variation for each sample), the corresponding semi-logarithmic plot (inset) highlights the sample with the highest carrier concentration ($1.22 \times 10^{19} \text{ cm}^{-3}$) and lowest Zn/P (1.16) ratio. The stoichiometric Zn/P ratio is at 1.5, represented by the dashed line. The details of the plotted sample are listed in Table 5.1	70
5.6	(a) I-V characteristic of the monocrystalline and polycrystalline Zn_3P_2 thin film grown on i-InP (100) substrate measured in a top-down configuration (inset). (b) Semi-logarithmic I-V curve obtained from monocrystalline Zn_3P_2 thin film grown on (p-, n-, i-) InP substrates and polycrystalline Zn_3P_2 thin film grown on i-InP.	71

6.1	(a) Schematic representation of the process employed for the fabrication of Zn_3P_2 solar cell, ITO is deposited on the surface of the as-grown Zn_3P_2 thin film with sputtering, followed by the deposition of Au as the back contact, and Ag is sputtered using a mask to form the top contact. (b) Schematic representation of the final device containing the Au back contact, InP substrate, Zn_3P_2 thin film, sputtered ITO layer, and the Ag top contact. (c) Photograph of a fully fabricated cell.	76
6.2	(a) SEM image of the as-grown Zn_3P_2 thin film on InP substrate. (b) RBS measurements from Zn_3P_2 thin film depicts a Zn/P ratio ≈ 1.32 . (c) The decay of photoinduced charge carrier density plotted as a function of pump-probe delay time measured by OPTP spectroscopy at different pump fluence.	78
6.3	(a) Representative J-V curves obtained in dark (denoted by black line) and under 1-sun illumination (denoted by red line), the inset shows the actual device measure that had an active area of 0.467 cm^2 . (b) Dark J-V curve plotted in semi-logarithmic scale depicting the three distinct regions, region I corresponds to the voltage range $< 0.25 \text{ V}$, region II corresponds to the voltage range between 0.25 V and 0.53 V , region III corresponds to the voltage range $> 0.53 \text{ V}$	80
6.4	(a) Light intensity dependence of J-V characteristics of the device, the measurements were performed at different illumination intensities ranging from 0 sun (dark) to 1.125 suns (which corresponds to 1125 W/m^2). The different solar cell parameters are extracted from the light intensity dependent J-V curve and plotted as a function of the light intensity (b) short-circuit current density J_{sc} , (c) fill factor FF, (d) power conversion efficiency η , (e) open-circuit voltage V_{oc} , the red dashed line denotes the part of the plot used for extracting the ideality factor from the semi-logarithmic plot of light intensity against the V_{oc}	82
6.5	Simulated band alignment between the Zn_3P_2 layer and ITO at the front side, and the Zn_3P_2 layer and InP at the back side, the blue solid line represents the conduction band (CB), the red solid line represents the valence band (VB), the blue dashed line depicts the quasi-fermi level for electrons (QF_e), and the red line depicts the quasi-fermi level for holes (QF_h), the simulation is done under different bias voltages (a) 0 V, (b) 0.4 V, (c) 0.8 V, and (d) 1 V. (e) The EQE obtained from the measured device (denoted with purple line) and the reference Si (denoted with red line). (f) Simulated absorption obtained from Zn_3P_2 (denoted by the solid orange line), InP (denoted by the green solid line), and ITO (denoted by grey line) for the wavelength range of 300 nm to 1000 nm. (g) Simulated I-V diagram obtained from Zn_3P_2 generation (denoted by the solid orange line), from InP generation (denoted by the green solid line), and from the combined (Zn_3P_2 and InP) generation (denoted by the solid purple line).	84
A.1	Raman spectra of Zn_3P_2 grown on graphene at 150°C with varying V/II ratio	92

A.2	(a) XRD of Zn_3P_2 samples grown on graphene at 150 °C at a $V/II = 0.83$ for 240 minutes, inset represents the corresponding SEM image for the sample: (b) XRD of Zn_3P_2 samples grown on graphene at 150 °C at a $V/II = 0.83$ for 150 minutes .	93
A.3	(a-c) SEM images of Zn_3P_2 grown on graphene for 30 minutes at 150 °C and at a $V/II = 1.55$ with (a) P_2 BEP of 8.75×10^{-8} Torr, (b) P_2 BEP of 4.30×10^{-7} Torr, (c) P_2 BEP of 9.18×10^{-7} Torr.	93
A.4	(a) EBSD map of Zn_3P_2 grown on graphene under optimal growth conditions showing the preferential orientation, (b) corresponding EBSD pole figure, (c) Schematic representation of the tetragonal unit cell of Zn_3P_2 in pseudo-cubic form.	95
A.5	(a) Plot of room temperature PL intensities for peaks at 1.52 eV and 1.42 eV as a function of laser power done on sample A with 633 nm illumination, (b) PL spectra of sample A at 200 K as a function of laser power excited with 633 illumination; (c) Plot of PL intensities for peak at 1.26 eV as a function of laser power done on sample B at 5.8 K excited with 532 nm illumination.	96
B.1	Optical microscope image of the monocrystalline Zn_3P_2 thin film demonstrating micro-cracks formed due to large thermal coefficient mismatch between the Zn_3P_2 thin film ($14 \times 10^{-6} \text{K}^{-1}$) [163] and the substrate ($4.35 \times 10^{-6} \text{K}^{-1}$) [85] (a) bare thin film (b) thin film after the second EBL step, the surface is coated with PMMA except for the exposed area, which contains the hall bar. The hall bar is positioned away from the existing micro-cracks on the sample.	97
B.2	I-V characteristic obtained as a function of distance between two contacts from (a) monocrystalline Zn_3P_2 thin film (M1) (b) polycrystalline Zn_3P_2 thin film (P2), on i-InP (100) substrate	98
B.3	I-V characteristic obtained as a function of distance between two contacts from (a) monocrystalline Zn_3P_2 thin film on n-InP (100) substrate (M3), a switch from linear I-V curve to non-linear I-V curve is observed at $\sim 100 \mu\text{m}$	98
B.4	Hall effect measurement done at 300 K using an injection current 0.1 μA (a) longitudinal resistance (R_{XX}) (b) transverse resistance (R_{XY}), plotted as a function of magnetic field.	99
B.5	COMSOL simulation of the band alignment between (a) p-InP and p- Zn_3P_2 (b) n-InP and p- Zn_3P_2 , a nominal carrier concentration of 10^{15}cm^{-3} is assumed for Zn_3P_2 and 10^{18}cm^{-3} for InP	99
C.1	The decay of pump intensity in the Zn_3P_2 thin film.	101
C.2	The dark ideality factor is plotted as a function of the voltage, where the ideality factor-voltage characteristic is calculated by numerical differentiation according to Equation. C.2, and the ideality factor is obtained from the plateau.	102

List of Tables

1.1	Device properties and the corresponding growth techniques of some of the Schottky and heterojunction solar cells that is based on Zn_3P_2 photovoltaic absorber.	5
5.1	Measured sample names with corresponding substrate type, crystallinity, Zn/P ratio, resistivity, and carrier concentration.	64
C.1	List of parameters used for the semiconductors in the drift-diffusion simulations.	104

1 Introduction & Motivation

Energy sources are vital for socio-economic development, any form of economic growth surges energy consumption. In 2020, the yearly global power consumption was close to 23200 TWh according to the International Energy Agency (IEA), which was primarily provided by fossil fuels. However, the current IPCC report warns against the impact of global warming of 1.5 °C above pre-industrial levels and highlights the need for immediate intervention in all sectors to reduce emissions [47, 56]. Renewable sources of energy can provide an efficient pathway to meet the growing energy demand while simultaneously mitigating the issues of global warming [117, 146, 244]. Ambitious renewable support policies and the declining cost of technology are raising the share of renewable energy in the global power mix [204]. Presently, around 28% of global power demand is met by renewable energy sources, of which only 3% comes from solar energy. To meet an appreciable portion of the future global energy demand, the installed capacity of the terrestrial photovoltaics must increase to at least 5 TW. Crystalline silicon solar cells dominate the present photovoltaic market, given the abundance of the material and the technical know-how of silicon-based technology [190, 303, 149, 314, 218, 232]. However, as silicon is an indirect band gap material, the solar cell must be sufficiently thick to allow efficient optical absorption [101, 9, 132]. Additionally, the processing of silicon is very cost-intensive; the typical manufacturing process involves high-temperature (1500-2000 °C) heating in an electrode arc furnace [77, 126]. Almost all the current commercial photovoltaic technologies suffer from material or resource constraints, which directly hinder their role in TW scale applications. To promote the large-scale deployment of solar cells, the process must be economical and sustainable. An alternative approach is the use of earth-abundant thin-film photovoltaic materials. Wadia *et al.* estimated the electricity contribution and cost impact of material extraction to solar modules, by evaluating the maximum TWh and the minimum cost per watt of 23 different photovoltaic compounds [281]. They demonstrated that photovoltaic materials with significantly lower extraction costs (such as FeS₂ and Zn₃P₂) when performing at 10% power conversion efficiencies can deliver the same lifetime energy output as devices performing above 20% with consideration of 3/4 material reduction. In the last decade, emerging earth-abundant thin-film photovoltaic technologies have been heavily researched due to their promise of low-cost and large-scale applications [248, 150,

153, 230, 283]. Among these materials, copper-based quaternary kesterite compounds such as $\text{Cu}_2\text{ZnSnS}_4$ (CZTS), $\text{Cu}_2\text{ZnSnSe}_4$ (CTZSe), and their alloys have gained popularity as a prospective environmentally friendly alternative for CIGS and CdTe technologies [309, 157, 59, 23, 242]. The structure of CZTS can be derived from the CuInS_2 chalcopyrite structure, just by replacing half of the indium atoms with zinc and the other half with tin [157]. They have a direct band gap of around 1.1 to 1.5 eV with a high absorption coefficient (over 10^4 cm^{-1}), and a crystalline tetragonal unit cell structure [213, 215]. The efficiency of kesterite-based solar devices has increased significantly from 0.66% in 1997 [112] to 12.6% in 2014 [288] and 13.8% in 2016 for small-area solar cells [284]. Even though there has been considerable progress in the performance of kesterite solar cells, the efficiencies fall far below the predicted value of 28% for this technology from the Shockley-Queisser limit [284]. One of the major limitations is the presence of defects, which lead to the formation of band tails and contribute to the recombination process [248, 223, 278, 87]. Given the complex phase diagram of CZTS, various secondary phases and intrinsic defects are produced [157, 215]. Additionally, the correlation between the chemical composition and transport properties of the carriers is highly complicated and not well understood [157]. Moreover, a large deficit in the open-circuit voltage (V_{OC}) has been observed in kesterite-based solar cells relative to their band gap [284]. The low efficiencies associated with kesterite-based solar cells have been attributed to the deficit in the V_{OC} [89, 88]. There are several hypotheses regarding the low V_{OC} values, such as non-Ohmic back electrical contacts, a poor-quality interface between the CZTS and the CdS buffer layer, and large amounts of defects and disorder in the bulk absorber [284, 89, 26]. The V_{OC} value in a solar cell is defined by the band gap of the absorber material, however, defects are known to modify the electronic bandstructure [257]. Localized states near the top of the valence band or at the bottom of the conduction band can be formed due to lattice disorder. When the concentrations of such defects are adequately high, they interact to form an impurity band, and as the density of defects increases the tail states become more and more dominant and penetrate further into the band gap [297, 276, 298, 110]. Figure 1.1 shows the schematic representation of the effect of defect states on the electronic band structure, it can be seen that localized defect states are associated with band tailing and narrowing of the band gap. Despite the promising properties of kesterite-based solar cells, several key challenges need to be addressed before their commercial application [41, 241]. Iron sulfide (FeS_2) or pyrite has gained substantial attention as a material for thin film photovoltaic application, due to its abundance, low toxicity, and extremely low cost [69, 212, 183, 83]. The extraction cost of this material is so low that a pyrite-based solar cell with only 4% efficiency could be as economical as a monocrystalline silicon-based solar cell with 20% efficiency [281]. Iron sulfide has a direct band gap energy of 0.95 eV and a high absorption coefficient ($\sim 5 \times 10^5 \text{ cm}^{-1}$), which is suitable for photovoltaic applications [212, 5, 224, 294]. However, there are a number of limitations associated with FeS_2 , mainly due to the poor thermal instability of the material [142, 226]. Additionally, the dark current values are significantly high due to phase impurities and the high density of surface states that acts as acceptors. Like pyrites, copper sulfide (Cu_2S) is also a low-cost and non-toxic solar cell material, however, it has an indirect band gap energy of 1.21 eV [93, 200, 155]. Even though the highest reported efficiencies for Cu_2S -based solar cells

is 9.15% [27], research on these devices have mostly been abandoned due to the migration of Cu^+ into other layers and the presence of mixed phases (ranging from Cu_2S that has metallic conduction to quasi-metallic behaviour). At first glance, most of the earth-abundant thin-film photovoltaic materials look promising with optimal band gap energies and high absorption coefficients. Nonetheless, there are some key limitations for this type of emerging material, such as loss of V_{OC} due to band tailing effect, presence of high recombination centres, the presence of deleterious secondary phases, and phase stability. The success and the practical implementation of emerging earth-abundant thin-film photovoltaic materials largely depend on the economic aspect and research efforts to further improve these materials.

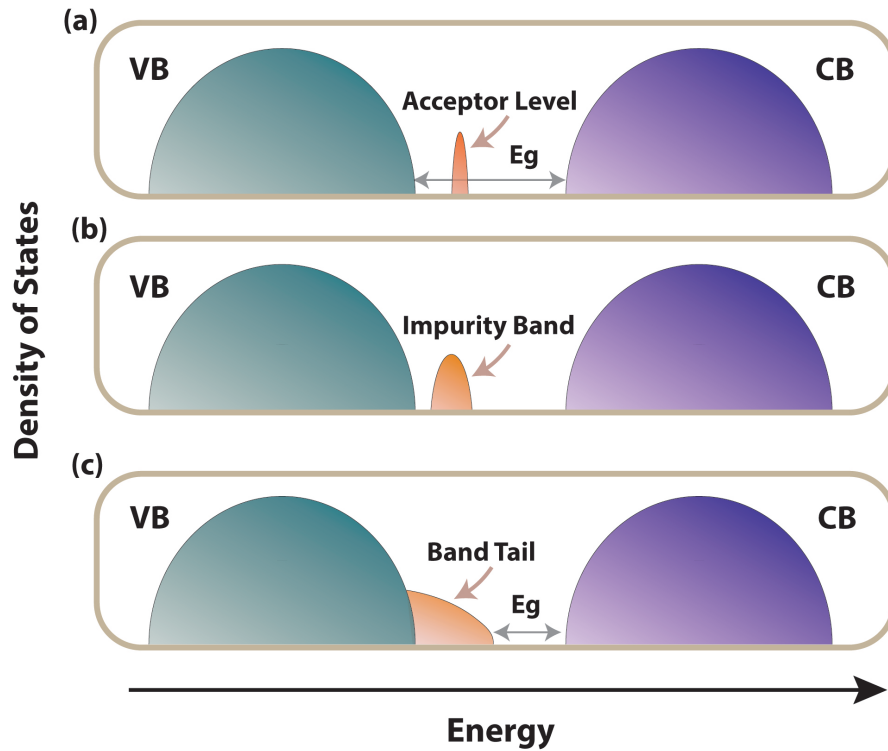


Figure 1.1: The band gap of a semiconductor showing the presence of (a) acceptor defect-induced energy level, (b) broadening to an impurity band due to increased defect density, (c) band tail formation leading to a reduction in the band gap.

Zinc phosphide (Zn_3P_2) is a strong contender for earth-abundant thin-film solar cells [28, 210, 176, 125], the material properties are promising for photovoltaic application along with low material extraction cost. Zn_3P_2 has a direct bandgap of 1.5 eV placing it close to the maxima of the Shockley-Queisser limit [68] (as shown in Figure 1.2). It also has a high absorption coefficient $>10^4 \text{ cm}^{-1}$ [68, 72] in the optical range and a long minority carrier diffusion length of 5-10 μm [206]. The low processing temperatures and high phase stability make Zn_3P_2 ideal from a fabrication and cost standpoint. Additionally, both phosphorous and zinc are mined at an industrial scale, thus making the transition to large-scale application simplified [281].

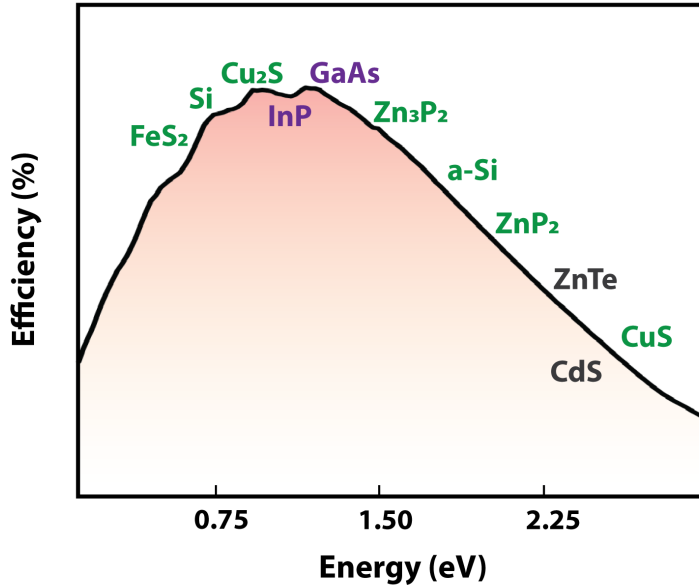


Figure 1.2: Theoretical Shockley-Queisser detailed-balance limit as a function of the band gap, the materials highlighted in green represent earth-abundant elements, the materials depicted in purple contain rare-earth elements, and the materials denoted in black contain toxic elements.

Since the 1970s, Zn_3P_2 has been sporadically researched as a photovoltaic material. The first successful Zn_3P_2 -based solar cell was fabricated using magnesium as Schottky contact. A record-setting efficiency of $\sim 6\%$ was demonstrated for Zn_3P_2 polycrystalline (the estimated grain size was in the range of 0.001 to 0.1 cm^2) wafers [20]. A more recent attempt to fabricate a similar bulk Zn_3P_2 device has given an efficiency value of 4.50% [121]. Whereas an efficiency of 4.3% was recorded for Mg Schottky contact Zn_3P_2 thin film solar cells [19]. Given the limitations of metal-semiconductor Schottky devices and the lack of reliable n-type doping of Zn_3P_2 , Zn_3P_2 -based heterojunction devices have been alternatively explored. A suitable heterojunction material should have a bandgap of at least 2.7 eV to function as an emitter to limit absorption losses in the UV range [109, 191, 24]. Low bandgap emitter material can lead to absorption losses, which can significantly reduce photocurrent. Additionally, the electron affinity should be similar to that of Zn_3P_2 (3.6 eV) [24]. Emitter material with similar low electron affinity will circumvent the issue of a conduction band cliff at the heterojunction interface [25]. The doping concentration for the emitter should be high to achieve the maximum barrier height for the heterojunction device. Whereas the mobility of the carrier should be high even at higher doping concentrations. Finally, the interface quality should be good as this determines the interfacial recombination [122, 124]. Among the different emitter materials used for the development of Zn_3P_2 -based heterojunction solar cells, ITO has shown the most promising efficiency. An efficiency value of 2.1% has been demonstrated

for heterojunction solar cells fabricated with large grain polycrystalline wafers of Zn_3P_2 and ITO [265]. Additionally, ZnSe has been proposed as the ideal emitter material for Zn_3P_2 absorber solar cells. $\text{Zn}_3\text{P}_2/\text{ZnSe}$ -based heterojunction solar cells have demonstrated the highest open-circuit voltage (V_{OC}) value of 810 mV [22]. However, the overall efficiency of 0.81% has been achieved so far for this type of solar cell. Table 1.1 summarizes the device properties of Zn_3P_2 -based solar cells taken from the literature. There are some key material challenges that need to be addressed for the practical implementation of Zn_3P_2 -based solar cells. The large lattice parameter of the Zn_3P_2 unit cell makes epitaxial growth inconvenient due to the lack of suitable substrates. Alternatively, Escobar *et al.* have shown the growth of nanostructures that are known to accommodate larger lattice mismatch [254, 255]. This opens the avenue for the growth of high-quality Zn_3P_2 on commercially available substrates. The n-type doping in Zn_3P_2 has rarely been achieved, this limits the fabrication and utilization of homojunction solar cells. The contribution of defect states in Zn_3P_2 on band tailing and its effect on the electrical properties has not been studied in detail. Only recently, Stutz *et al.* highlighted the presence of band tails in Zn_3P_2 and its impact on the bandgap [261]. Moreover, surface preparation plays an integral role in the recombination process and the presence of surface states has shown to severely impact device performance. Nonetheless, Zn_3P_2 possesses immense potential as an absorber material that is yet to be fully investigated. This present work explores a new approach for the growth of Zn_3P_2 that overcomes the limitation of lattice-matched substrates. Additionally, we study the material properties and fabricate Zn_3P_2 -based solar cells.

Table 1.1: Device properties and the corresponding growth techniques of some of the Schottky and heterojunction solar cells that is based on Zn_3P_2 photovoltaic absorber.

Junction Material	Efficiency (%)	V_{oc} (mV)	J_{sc} (mAcm^{-2})	Fill Factor	Growth ^a
ZnSe	0.81	810	1.55	0.5	CSS [22]
CdS	1.6	300	11.1	0.35	Evaporation [139]
ZnS	0.01	780	0.05	0.35	MBE [24]
Mg	5.96	492	14.93	0.71	PVT [21]
ITO	2.1	280	18.4	0.4	PVT [265]
ZnO	1.97	260	11	0.59	PVT [191]

^a Growth method abbreviations: Close space sublimation (CSS), Molecular beam epitaxy (MBE), and physical vapour transport (PVT).

This thesis is divided into seven chapters:

Chapter I: Introduction & Motivation

In the first chapter, the topic is introduced and the motivation behind the current work is clearly stated. The topic is placed in a wider scientific context and evaluated in terms of competing technologies.

Chapter II: Properties and Growth of Zn_3P_2

In the second chapter, the properties of Zn_3P_2 are reviewed and the common growth techniques are discussed. We start with a detailed review of the work on the optical, electrical, and structural properties of Zn_3P_2 . Different growth techniques are highlighted with their potential advantages and pitfalls. A new growth approach is discussed in depth.

Chapter III: Experimental Methods

In the third chapter, the experimental methods that are relevant to this thesis are presented. We start by discussing the growth technique used in this thesis and its potential advantages over other commonly used methods. The fabrication method used for the device preparation is illustrated. Finally, the optical and electrical characterization used most frequently in this thesis has been described in depth.

Chapter IV: van der Waals epitaxy of earth-abundant Zn_3P_2 on graphene for photovoltaics

In the fourth chapter, the main results of this thesis are presented. Our results include an alternative approach to the growth of Zn_3P_2 using van der Waals epitaxy. The growth mechanism is elucidated, and the structural and optical properties of the material have been characterized. Finally, we fabricated a simple Zn_3P_2 -based solar cell, which demonstrates the possibility of pushing the efficiency of Zn_3P_2 -based solar cells.

Chapter V: Zn/P ratio and microstructure defines carrier density and electrical transport mechanism in earth-abundant $\text{Zn}_{3-x}\text{P}_{2+y}$ thin films

We also investigated the electrical properties of Zn_3P_2 thin films grown on InP substrate using MBE. Our study highlights the limitations related to the material and demonstrates a path to tune the functionality.

Chapter VI: Carrier generation and collection in $\text{Zn}_3\text{P}_2/\text{InP}$ heterojunction solar cells

Finally, we fabricated a simple Zn_3P_2 -based solar cell, which demonstrates the possibility of pushing the efficiency of Zn_3P_2 -based solar cells.

Chapter VII: Conclusion & Outlook

In the final chapter, we conclude the topic and present an outlook for future research.

2 Properties and Growth of Zn_3P_2

In this chapter, first I will give a detailed overview of the properties of Zn_3P_2 , and the existing material challenges. Next, I will discuss the growth techniques most commonly used for the growth of Zn_3P_2 and then introduce the growth technique used in this thesis. This chapter is by far not exhaustive, it rather focuses on the topics which are relevant for this thesis and motivates some of the studies performed.

2.1 Properties of Zn_3P_2

2.1.1 Physical Properties

A good understanding of the phase diagram of a material system is key to designing growth experiments for high-quality crystal growth and for investigating the feasibility of material integration. Figure 2.1(a) shows the phase diagram for the Zn-P system. It is apparent from the phase diagram that there are two stoichiometric compounds in this binary system [84], which are zinc phosphide (Zn_3P_2) and zinc diphosphide (ZnP_2). Both the compounds exist in a low-temperature (α) and high-temperature (β) phase. An amorphous phase has also been reported [25], but this phase is not thermodynamically stable and it is mostly obtained due to kinetically limited growth processes. For Zn_3P_2 the α to β transformation occurs at 850 °C and the melting temperature for β - Zn_3P_2 is 1140 °C. The α - Zn_3P_2 has a tetragonal structure (as shown in Figure 2.1(b)), while the β - Zn_3P_2 has a cubic structure. Even though all crystalline phases of Zn_3P_2 demonstrate semiconducting properties, the α - Zn_3P_2 is most interesting as its electronic properties are compatible with photovoltaics [21, 72]. Here onwards we will only discuss the α - Zn_3P_2 , and we refer to it as Zn_3P_2 .

The tetragonal unit cell of Zn_3P_2 contains 40 atoms (or 8 formula units) [312, 76], which is relatively larger than many other III-V and II-VI compounds. The unit cell has dimensions $a = b = 8.097 \text{ \AA}$ and $c = 11.45 \text{ \AA}$ and it belongs to the $\text{P4}_2/\text{nmc}$ space group [176]. The zinc (cations) and phosphorous (anions) are stacked in alternative planes along the c-axis of the unit cell. The structure of Zn_3P_2 is commonly described as a defective antifluorite structure, where

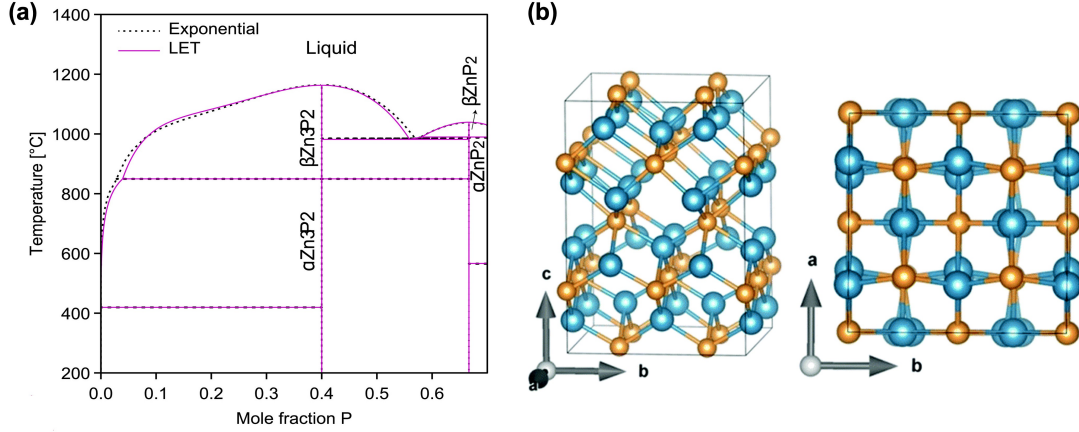


Figure 2.1: (a) The Zn–P phase diagram calculated using the parameters optimized in the current work [84] for the exponential (dotted-line) and LET model (solid line) of liquid interaction parameter, reprinted from [84], Copyright 2019, with permission from Elsevier. (b) Crystal structure representation of Zn_3P_2 tetragonal unit cell along different crystal planes, adapted from [76].

the phosphorous atoms form a cubic close packing and three-quarters of the tetrahedral voids are occupied by the zinc atoms and the remaining voids are unoccupied [312, 176]. It can also be viewed as an assemblage of four cubic sub-cells similar to fluoride structure, where one-quarter of the cations are missing. The cation vacancies occur in pairs along all four body diagonals of the cubic sub-cells with equal frequency [201]. The ordering of these vacancies makes the Zn_3P_2 unit cell volume four times larger than that of the fluoride-like sub-cells, which leads to an overall decrease in symmetry. The zinc atoms are coordinated with phosphorous atoms that are located at the four corners of the distorted tetrahedron. Whereas, the phosphorous atoms are located at the centres of the weakly distorted cubes, where six out of eight vertices of each cube are occupied by zinc atoms. A conventional tetrahedrally bonded semiconductor has an average of 2 valence electrons per bond. Whereas for Zn_3P_2 it is 4/3 valence electrons per bond, this results in a distribution of equilibrium bond lengths. In Zn_3P_2 , not all the atoms are tetrahedrally coordinated, the majority of the bond lengths lie below 2.5 Å, which is in agreement with the sum of covalent radii in tetrahedral coordination (2.4 Å), whereas the remaining of the bond lengths are closer to the ionic radii (2.86 Å). Additionally, the fractional ionicity of Zn_3P_2 is reported between 0.17-0.19 [256]. Therefore, the chemical nature of bonds in Zn_3P_2 is a complex ionic-metallic-covalent bond.

2.1.2 Optoelectronic Properties

The optoelectronic properties of Zn_3P_2 make it favourable for solar cell applications, such as long minority carrier diffusion lengths (7-10 μm) [300, 125], strong absorption in the visible spectrum ($>10^4$ - 10^5 cm^{-1}) [310, 269], and an almost ideal direct bandgap ($\sim 1.5 \text{ eV}$) [125, 261].

The high absorption coefficient of Zn_3P_2 near the band edge (with 90% of light absorption occurring in the first 10 μm of the material) is significantly larger than that of high-quality GaAs [269]. It has an absorption onset of around 1.4-1.5 eV, which is near the optimal value of 1.35 eV for a single junction device under terrestrial insolation. The absorption properties of a semiconductor are determined by its electronic band structure. However, there has been a long-standing debate regarding the fundamental bandgap of Zn_3P_2 , some studies suggest it is a direct bandgap semiconductor [260] whereas other studies suggest it is an indirect bandgap semiconductor [125]. In general experimental studies agree upon a direct interband transition at 1.5 eV. This transition occurring in the range 1.3-1.4 eV has been attributed by some groups to an indirect band transition [125] and by others to defect-related transition [261]. Theoretical studies on the band structure of Zn_3P_2 have also given different results, but these results largely depend on the type of functional used for the simulation. More recent theoretical studies done on the Zn_3P_2 band structure show the conduction band minimum (CBM) and the valence band maximum (VBM) lie at the gamma point, which indicates a direct bandgap [305].

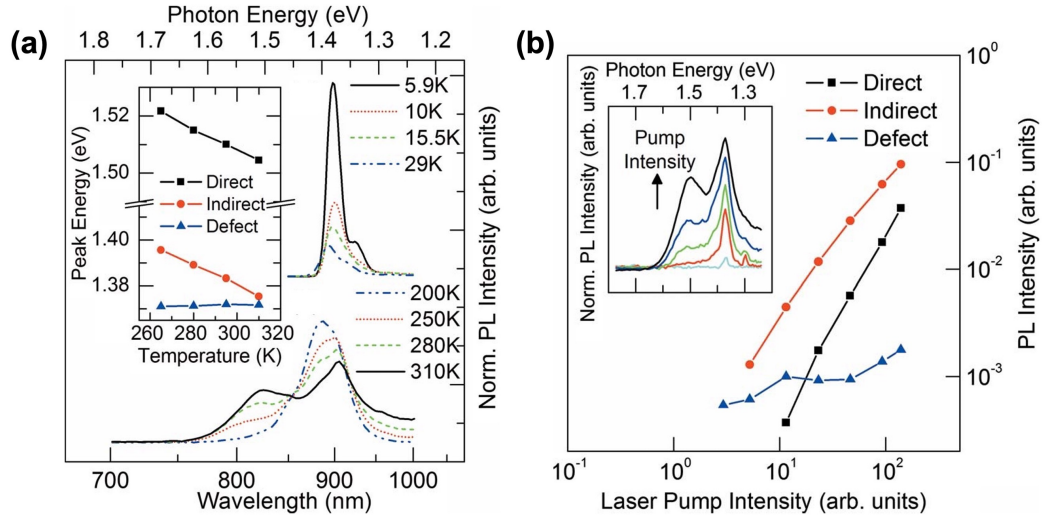


Figure 2.2: (a) Steady-state PL measurements of etched Zn_3P_2 wafers at different temperatures, the inset depicts the energies, as a function of temperature. (b) Room temperature intensities of the various PL peaks from etched Zn_3P_2 wafers as a function of laser pump intensity, the inset depicts the normalized PL spectra over similar range of laser pump intensities. Reprinted from [125], with the permission of AIP Publishing

Near-room-temperature steady-state photoluminescence measurements of Zn_3P_2 reported by Kimball *et al.* show two peaks centred at 1.38 eV and 1.50 eV [125], as shown in Figure 2.2(a). They ascribed these two peaks to interband transition based on the results of the power-dependent photoluminescence measurements. They observed no change in the peak positions of the two peaks with the increase in the pump power, while the intensity of the peaks increases with the pump power (as shown in Figure 2.2(b)) indicating a high density of states which is consistent with photoluminescence signals derived from interband transitions.

Whereas, similar steady-state photoluminescence measurements done by Stutz *et al.* show the presence of a band tail [261]. The photoluminescence measurements were performed on off-stoichiometric Zn_3P_2 thin film (Rutherford backscattering showed a uniform composition of 55% zinc and 45% phosphorous, which makes the thin film slightly phosphorous rich). Even though the Zn_3P_2 thin film is off-stoichiometric the corresponding Raman measurements showed a typical fingerprint of the D4h α - Zn_3P_2 lattice. The lattice of Zn_3P_2 is known to accommodate relatively large compositional variations without altering its crystalline structure. The photoluminescence measurement showed two distinct sets of peaks, one at low-energy range (1.26–1.31 eV) and the other at high-energy range (1.52–1.54 eV). Figure 2.3(a) shows that at lower temperatures, the low-energy peaks have very high photoluminescence intensities, while the high-energy peaks are much weaker in intensity. Even though contradictory in comparison to other materials, it has been widely reported for Zn_3P_2 that defect transitions dominate the optical response at lower temperatures [261, 160], whereas interband transitions are more pronounced at room temperatures. Peak broadening is observed with the increase in temperature and the low-energy peaks are shifted to higher energies (1.32–1.4 eV), while the high-energy peaks do not show any significant shift in peak position with increasing temperature, as shown in Figure 2.3(b). Additionally, the low-energy peaks shift to higher energies and become asymmetric with increasing laser powers. This type of peak behaviour dependence on temperature and laser power is attributed to band tail recombination mechanisms. Stutz *et al.* explain the lack of agreement on the presence of the indirect fundamental band edge could be due to the existence of a defect band or band tail [261]. High amounts of randomly distributed charged defects can cause spatial potential fluctuations which in turn lead to the formation of tails in the electron or hole densities of states, at energies above the valance band maximum or below the conduction band minimum [261, 236]. Thus, the observation of the band tail is highly dependent on the defect concentrations in the measured sample. Different experimental methods have been used to investigate the defect-related transitions in Zn_3P_2 , and even though there is a wide range of reported energy levels for these defects [160, 251], there is an overall consensus regarding the type of defect, all the reported defect types are acceptor-like. Therefore, the discrepancies observed in the optical measurements for bandgap determination mostly arise due to the presence and the densities of these defects, which in turn are largely dependent on the growth techniques, conditions, and eventually post-growth treatments.

Demers *et al.* determined the role and formation energies of intrinsic point defects in the Zn_3P_2 using density-functional theory (DFT) simulations [61]. The formation energies of both the acceptor defects (zinc vacancies and phosphorous interstitials) in Zn_3P_2 are low, which leads to the intrinsic p-type nature of Zn_3P_2 . Zinc interstitials are known donor defects in Zn_3P_2 , and to date, there has been one experimental evidence of n-type Zn_3P_2 grown under zinc-rich conditions using molecular beam epitaxy (MBE) [262]. However, the n-type carrier concentrations obtained were very low ($\sim 10^{10} \text{ cm}^{-3}$). The difficulty in n-type doping of Zn_3P_2 arises from the high formation energy of Zn interstitial defect [305, 61]. In addition, it has been seen that when Zn_3P_2 is doped with electron donors a large number of acceptor defects

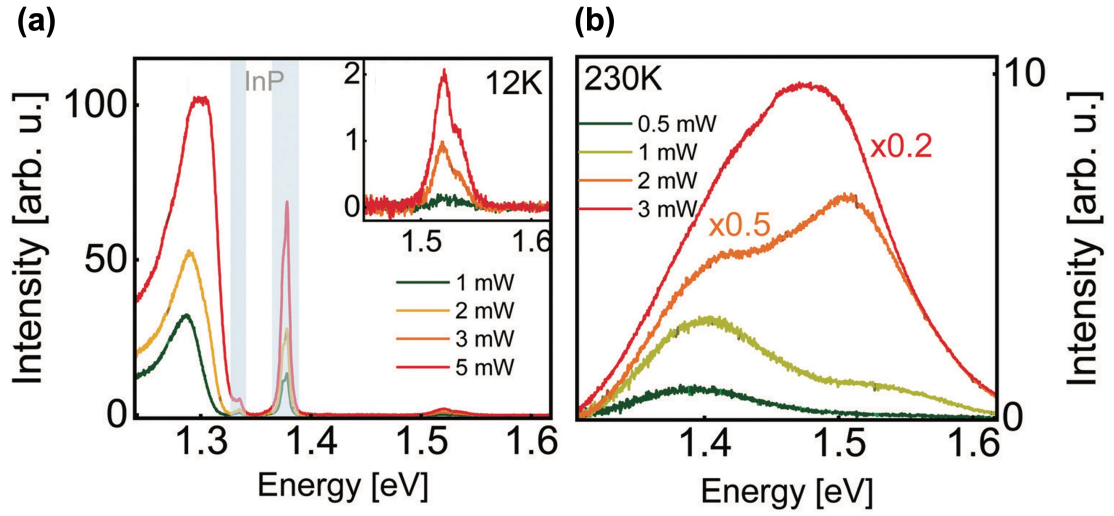


Figure 2.3: PL spectra obtained from monocrystalline thin film acquired with a 488 nm laser at (a) 12 K, where the PL peaks from the InP substrate are depicted with grayed out areas, the inset shows magnified view of the peaks near 1.52 eV, and (b) 230 K. Adapted from [261].

are created that act as 'electron-sinks' and capture mobile electrons thus neutralizing the doping and lowering the Fermi-level back towards the p-type regime [305, 114]. The doping characteristics of Zn_3P_2 were calculated using DFT hybrid functional method by Yin *et al.* Their study reveals doping with group III-A elements (such as Al, Ga, In) and group VI elements (such as S, Se) could result in n-type Zn_3P_2 when grown under zinc-rich conditions [305]. Whereas, doping with the group I elements (such as Na, and Cu) may produce better p-type Zn_3P_2 than non-doped Zn_3P_2 . They also demonstrated that the P-P bond formed by the incorporation of phosphorous interstitials changes the charge state of the defect from a triple-hole acceptor to a single-hole acceptor [305]. The partial density of states reveals the VBM mainly has a phosphorous p-character and the CBM mainly exhibits a mixed p and s-character from both phosphorous and zinc states. The theoretical studies provide insight into the band structure and point defect characteristics in Zn_3P_2 . Additionally, they provide a better understanding of the experimental results of doping Zn_3P_2 and provide a guideline for doping Zn_3P_2 .

2.1.3 Electrical Properties

The success of a solar cell design is largely dependent on the charge carrier transport properties of the materials used. Of particular importance are the minority carrier diffusion length and the conductivity of the absorber material, which ensures efficient collection of the photo-generated carriers. For thin-film solar cells, it is desirable to have an absorber material with a carrier diffusion length in the order of its thickness. Some studies have shown that p-type Zn_3P_2 has a long minority-carrier diffusion length and consequently a long minority-carrier lifetime [125]. However, to date, the highest reported efficiency for Zn_3P_2 based solar cells stands at ~6% [36]. Since the 1979 publication of Catalano *et al.* on Zn_3P_2 Schottky barrier solar

cell, there have been several attempts to break the record efficiency by proposing alternative junction schemes. The main disadvantages of the Schottky barrier solar cell are the low attainable barrier height and increased surface recombination [65]. Zn_3P_2 solar cell devices made with magnesium are reported to have a high concentration of interface trap states, which limits the open-circuit voltage due to Fermi-level pinning. Furthermore, subsequent studies on $\text{Mg}/\text{Zn}_3\text{P}_2$ solar cells have revealed the formation of an intermediate layer between Zn_3P_2 and Mg due to interdiffusion. Catalano *et al.* showed the formation of a buried p-n homojunction on heating (at 100 °C) evaporated Mg contacts using spectral response and electron-beam-induced current (EBIC) measurements [34]. They attributed the homojunction formation to n-type doping of Zn_3P_2 by Mg and they demonstrated the formation of Mg_3P_2 as an intermediate layer between the Mg contact and the n-type Zn_3P_2 using Auger electron spectroscopy, secondary ion mass spectroscopy, and X-ray photoelectron spectroscopy [18]. Similar studies done by Kimball *et al.* showed that the intermediate layer formed was an alloy of Mg-P-Zn and no n-type conductivity of Zn_3P_2 was observed in Hall effect measurements [123]. However, a more recent study on the interface between Mg and Zn_3P_2 was done by Katsube *et al.*, they demonstrated the presence of a ternary compound as the intermediate layer [115]. A schematic representation of the interface structure of $\text{Mg}/\text{Zn}_3\text{P}_2$ solar cells is shown in Figure 2.4(a). The interdiffusion of material leads to the formation of $\text{Mg}(\text{Mg}_x\text{Zn}_{1-x})_2\text{P}_2$ layer. Figure 2.4(b) shows the cross-sectional STEM-EDS map of the interface, the STEM-EDS map depicts the presence of voids and intermixing. While the ternary compound grows epitaxially on Zn_3P_2 and has a low lattice mismatch, the interface between Mg and $\text{Mg}(\text{Mg}_x\text{Zn}_{1-x})_2\text{P}_2$ is unstable and forms an atmosphere sensitive Mg -rich phosphide phase which degrades the device by forming voids around the interface.

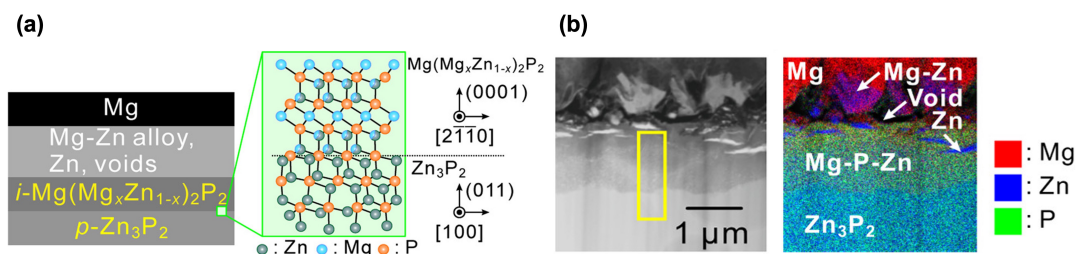


Figure 2.4: Cross-sectional (a) STEM-DF image of the interface between $\text{Mg}/\text{p-Zn}_3\text{P}_2$, and (b) STEM-EDS mapping across the $\text{Mg}/\text{p-Zn}_3\text{P}_2$ interface. Reprinted with permission from [115]. Copyright 2018 American Chemical Society.

Given the limitations of Schottky based Zn_3P_2 solar cells and the difficulties in doping Zn_3P_2 n-type for homojunction solar cells [114], various studies have been dedicated to understanding the Zn_3P_2 based heterojunction solar cells. Some common emitter materials used for Zn_3P_2 heterojunction solar cells are ZnO , ITO , CdS , ZnSe , and ZnS [191, 205, 24, 109, 22]. Among the different emitter materials, ZnSe has garnered the most attention due to its band alignment with Zn_3P_2 . The $\text{ZnSe}/\text{Zn}_3\text{P}_2$ interface has a negligible conduction-band offset and a significantly large valence-band offset, which makes the junction an efficient hole-blocking

layer. Even though the highest reported efficiency for $\text{ZnSe}/\text{Zn}_3\text{P}_2$ solar cell is just about 0.81% the open-circuit voltages are considerably higher than other Zn_3P_2 based solar cells [22], thus highlighting the importance of band alignment between the emitter and absorber material. Heterojunction solar cells of $\text{ITO}/\text{Zn}_3\text{P}_2$ have shown the best efficiency (1.1%) among all the reported heterojunction structures [265]. There are some added advantages of using ITO as a heterojunction such as, it is degenerately n-type which could improve the fill factor of the solar cell by reducing the series resistance, it serves as a transparent contact, and it has a refractive index of 2.1, which implies it can be used as an anti-reflective coating for the device [265]. In comparison to Schottky junction solar cells, the heterojunction architecture has fewer fundamental limitations and has a wider scope for improvement by exploring different combinations of emitter materials.

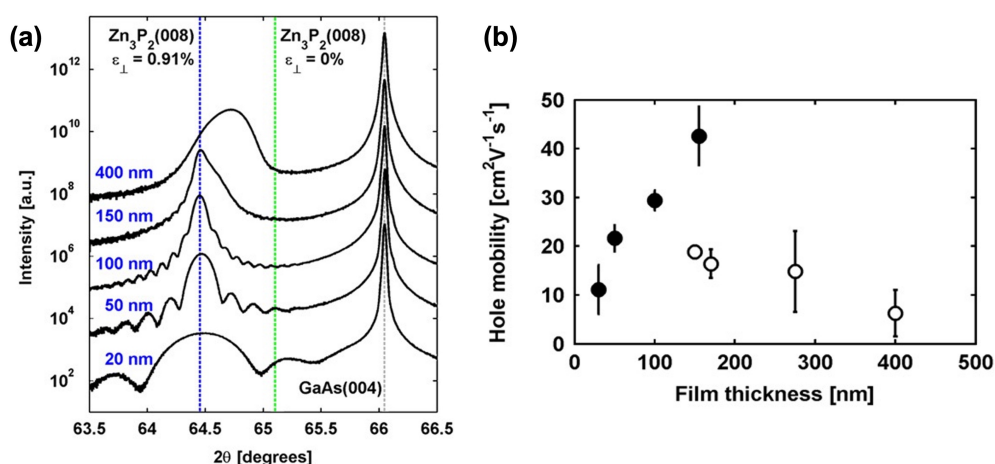


Figure 2.5: (a) Symmetric HRXRD scans of the Zn_3P_2 on GaAs substrate for increasing Zn_3P_2 layer thickness. (b) Hole mobility of Zn_3P_2 as a function of layer thickness, the filled circles represent the data from strained films and the open circles depicts the data from partially relaxed films. Reprinted from [25], Copyright 2013, with permission from Elsevier.

Some other aspects to consider when addressing the issues related to Zn_3P_2 -based solar cells are the challenges associated with making reliable electrical contacts and the electronic transport properties of the material. The electronic transport properties have been explored for single-crystalline and polycrystalline Zn_3P_2 grown using different techniques. Mostly p-type conductivity of intrinsic Zn_3P_2 and hole mobility values ranging from 10-40 $\text{cm}^2\text{V}^{-1}\text{s}^{-1}$ have been reported [25, 122]. Wang *et al.* demonstrated that for single crystal Zn_3P_2 samples the Hall mobility varied with temperature as approximately $T^{1.5}$ in the range 130 and 200 K and as approximately $T^{-1.1}$ in the range 200 and 380 K, which indicates that charged impurity scattering dominates at lower temperatures and acoustic lattice scattering dominates at higher temperatures [287]. Bosco *et al.* have illustrated the effect of strain on mobility, strained films of Zn_3P_2 grown epitaxially on GaAs show higher mobility than partially relaxed films [25]. Figure 2.5(a) shows the HRXRD measurements of Zn_3P_2 with varying thickness grown on GaAs substrate, for thin films up to 150 nm a shift in the $\text{Zn}_3\text{P}_2(008)$ peak position with respect to

the bulk 2θ was observed. The shift indicates an out-of-plane strain of $\sim 0.91\%$. Figure 2.5(b) shows the mobility values as a function of the Zn_3P_2 film thickness, the strained films have comparatively higher mobilities than partially relaxed films. Additionally, interfacial defects present in partially or fully relaxed films can cause charge scattering thereby reducing mobility. Additionally, they reported a decrease in carrier concentration in partially relaxed films. Misfit and threading dislocations that are formed upon relaxation not only cause charged-carrier scattering but are also known to act as acceptor-compensation sites in semiconducting materials. Consequently, a high density of dislocations formed in partially relaxed Zn_3P_2 film is expected to compensate the phosphorous interstitials in Zn_3P_2 that are responsible for the intrinsic p-type behaviour. The resistivity values of Zn_3P_2 are highly dependent on growth conditions, values ranging from $1\text{--}10^4 \Omega\text{cm}$ have been reported for as-grown Zn_3P_2 [35, 265]. Diffusion doping of Zn_3P_2 with Ag has been shown to only moderately increase the hole density and the conductivity of the material [121]. While Zn_3P_2 is intrinsically p-type due to phosphorous interstitials and zinc vacancies, it is also desirable to dope the material extrinsically to have better control over the process, for this purpose Ag and Cd is commonly used as p-type dopants.

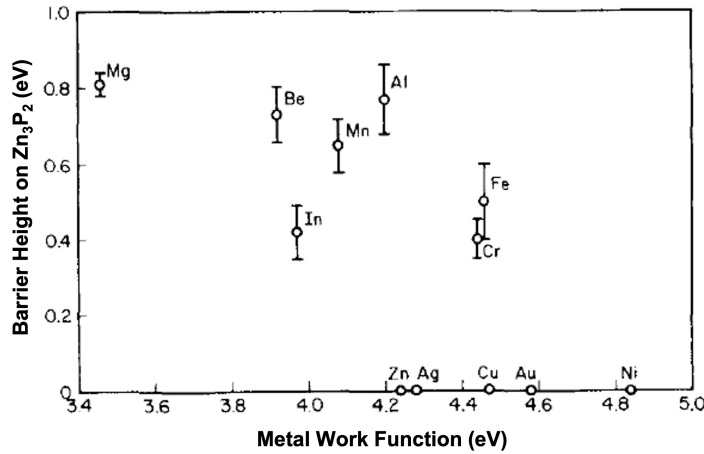


Figure 2.6: Barrier heights of different metal contacts on Zn_3P_2 as a function of the metal work function. Reprinted from [299], with the permission of AIP Publishing.

As mentioned in the previous section, n-type doping of Zn_3P_2 is challenging due to the self-compensation effect [114]. Another important area to consider when making devices are the electrical contacts, the metal-semiconductor contact is either defined as an ohmic contact or a Schottky contact depending on the barrier height formed. The type of device determines the desirability of ohmic or Schottky or both contacts, such as ohmic contacts are necessary as the final connection of a semiconductor device to an on-chip metallic layer whereas for a Schottky junction solar cell a barrier height at the junction is preferred. Wyeth *et al.* studied contact barrier heights for twelve metals on Zn_3P_2 [299]. Figure 2.6 shows the measured barrier heights for metal contacts on Zn_3P_2 as a function of the metal work function. They elucidated that the

determining factor for ohmic contacts is not the metal work function but it is the chemical heat of reaction of the contact metal phosphide, which hints at the formation of an interfacial compound. Metals like Cu, Au, Ag, Zn, and Ni were shown to form ohmic contact while Mg, Mn, In, Fe, Cr, Be, and Al forms Schottky contact.

2.2 Zn_3P_2 Growth Overview

Most growth technique used for Zn_3P_2 takes advantage of the fact that Zn_3P_2 sublimes congruently. This allows a straightforward deposition of Zn_3P_2 film on a target substrate by sublimation in vacuum, examples of such growth techniques are thermal evaporation, close space sublimation and hot-wall deposition. Even though these techniques are successful in producing single-crystalline Zn_3P_2 with good optoelectronic quality, they lack the controllability of the process and in particular the fine details of the stoichiometry. MBE is characterized by low growth rates ($\sim 1 \text{ \AA s}^{-1}$) and the ultra-high vacuum ensures low impurity incorporation which fosters high-quality epitaxial films. The first use of MBE for Zn_3P_2 growth was reported by Suda *et al.*, where Zn_3P_2 was grown on semi-insulating GaAs [262]. Two separate high-purity elemental sources were used to grow Zn_3P_2 film at 200 °C. By controlling the zinc and phosphorous fluxes they were able to obtain epitaxial n-type Zn_3P_2 on GaAs (001) substrates. Bosco *et al.* utilized a compound source for the growth of Zn_3P_2 film on GaAs substrate (001) using MBE [25]. The substrate selection is based on lattice matching, as the phosphorous sub-lattice of Zn_3P_2 is similar to that of arsenic in GaAs with room temperature lattice mismatch lower than 1.3%. The Zn_3P_2 compound source alone resulted in amorphous growth, an additional Zn flux was necessary to produce crystalline Zn_3P_2 [25]. This is mainly due to the high vapour pressure of Zn which results in lower sticking coefficients. For optimal growth, the reported substrate temperatures were in the range of 200–235 °C. At lower temperatures, amorphous growth was reported whereas for growth temperatures above 250 °C a drastic decline in growth rate was observed due to the lower sticking coefficient of Zn at higher temperatures [25].

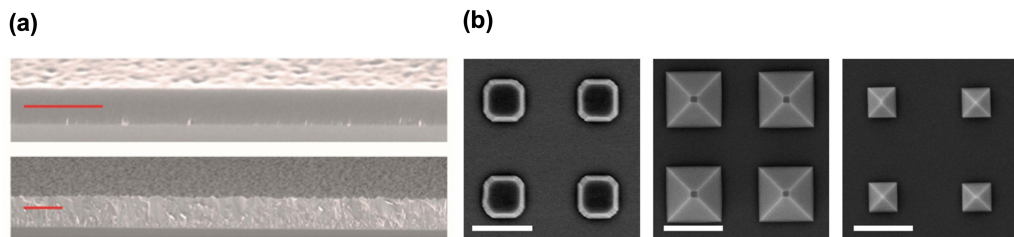


Figure 2.7: SEM images of (a) amorphous (top) and polycrystalline (bottom) Zn_3P_2 thin films grown on InP substrate, the scale bars correspond to 1 μm , adapted from [311]. (b) Zn_3P_2 nanostructures at different stages of growth on InP substrate, the scale bars are 500 nm, adapted from [66].

In recent studies, Zamani and Escobar *et al.* have demonstrated high-quality Zn_3P_2 thin film and nanostructure growth on InP (001) substrate using elemental source MBE [311, 70, 255].

Figures 2.7(a,b) show the SEM images of the Zn_3P_2 thin films and nanostructures grown on InP. The substrate choice is motivated by a low lattice-mismatch (2.4%) between the phosphorous sub-lattice of Zn_3P_2 and phosphorous in InP (001). For the thin film growth, the substrate preparation plays an important role, degassing the substrate at 580 °C (to remove native oxide) for a minimum of 30 minutes is critical for monocrystalline Zn_3P_2 growth. Additionally, the nanostructures of Zn_3P_2 were grown using selective area epitaxy (SAE) by patterning a 30 nm thick SiO_2 mask on InP substrate, this is a unique technique that takes the advantage of lateral overgrowth for high-quality thin film formation. A local variation in the stoichiometry of the grown Zn_3P_2 as a function of pattern dimensions for a given growth condition was observed [255]. Thus, SAE could provide tunability of doping just by changing the patterns locally. The use of MBE drastically lowers the growth temperatures in comparison to chemical vapour deposition methods, the lower temperatures significantly reduce the number of grown-in defects caused due to strain arising from thermal expansion mismatch. Furthermore, the precise control of fluxes allows better tunability of composition and doping of the grown material.

2.3 Epitaxial Growth

Epitaxy is defined as the oriented growth of crystalline material on a single-crystalline substrate. Epitaxial growth is widely used in the development of modern technology, especially in the fields of solid-state electronics, optoelectronics, and photonics [274]. There are two types of epitaxial growth, homoepitaxy (refers to the case where the epilayer and the substrate are the same material, such as epitaxial Si deposited on Si wafer) and heteroepitaxy (refers to the case where the epilayer and the substrate are different materials, such as AlAs deposited on GaAs). Homoepitaxial growth typically results in a high-quality single-crystalline epilayer, due to the closely matched lattice parameters and strain-free interfacial bonding. The main shortcomings of homoepitaxy are the high cost and the availability of high-quality single-crystalline wafers. In conventional heteroepitaxy, the quality of the grown epilayer is largely dependent on the crystal structure, the lattice parameter, and the coefficient of thermal expansion of the substrate. The lattice mismatch between the substrate and the epilayer determines the amount of strain. For a lattice mismatch of less than 9%, the growth usually occurs pseudomorphically [274, 16] (i.e., for a sufficiently thin film the epilayer would be elastically strained to follow the interatomic spacing of the substrate). With increasing epilayer thickness, the elastic strain energy increases, which is eventually relaxed by the formation of defects. These defects are in form of dislocation that relieves a portion of the misfit, as the film grows thicker more and more misfit-dislocations are formed until at a certain thickness the elastic strain is completely eliminated. For a large enough lattice mismatch the spacing between misfit dislocations decreases giving rise to poor quality epilayer. In epitaxial semiconducting films defects such as misfit-dislocations, grain boundaries, twins, and stacking faults introduce local inhomogeneities, which give rise to a short lifetime and non-radiative recombination of charge carriers. These defects can severely degrade electronic/photonics device performance

[167]. Several strategies have been adopted to reduce the defect density in heteroepitaxy, such as low-temperature buffer layer, lattice-engineered buffer layer, domain-matched epitaxy, metamorphic buffer layer, compliant substrate, epitaxial lateral overgrowth, strained layer superlattice, and thermal treatments [71, 252, 199]. Even though advanced heteroepitaxy techniques can help in mitigating the problems associated with lattice mismatch. Challenges remain when working with systems with large lattice mismatch, large thermal expansion coefficient mismatch, and different polarities. Additionally, the thermal and chemical stability of the substrate is also important when using high-temperature growth techniques.

2.3.1 van der Waals Epitaxy

In 1984, Koma *et al.* introduced the concept of van der Waals epitaxy (vdWE), they successfully demonstrated the growth of Se thin-film on a cleaved Te substrate and NbSe_2 film on 2H-MoS_2 [130]. The growth of Se thin-film on Te substrate occurred strain-free even for monolayer coverage despite a lattice mismatch of 20% [130]. Te has a crystal structure that consists of spiral chains bound by weak van der Waals force. When cleaved along the chains no dangling bonds are expected on the cleaved surface. The growth of the epilayer in vdWE proceeds via van der Waals forces due to the absence of dangling bonds. vdWE can result in good quality heterostructures with a very abrupt interface, even between materials with large lattice mismatch [302, 285, 50, 131]. The key aspect of vdWE is a dangling bond free surface, this can be achieved by using 3D/2D layered materials (where, the atoms in the layer are covalently bonded and the layers are held together by van der Waals force, such as mica, graphene, hexagonal boron nitride) [180, 154, 221], or by using a 3D material with a passivated surface (such as H-passivated silicon) [99]. Heteroepitaxial films with lattice mismatch greater than 60% can be grown by vdWE [131], this is due to the nature of the bond formed at the interface. The van der Waals bond is not a chemical bond like covalent or ionic bonds, instead, it originates due to dipole interactions between atoms. In comparison to chemical bonds, it is very weak and can accommodate large lattice mismatches [13, 130, 152]. Hence, the epilayer grows unstrained on the van der Waals substrate with its bulk lattice parameters. The epilayer grown with vdWE substrate shows an orientational crystalline relation with the substrate. Unlike conventional heteroepitaxy which is coherent, epilayer grown by vdWE demonstrates incommensurate/incoherent in-plane lattices at the interface [13, 8].

Even though vdWE was introduced in 1984, it was not until the discovery of graphene in 2004 that this growth technique gained major traction. Due to the interesting properties of graphene [197, 14, 188, 145], there has been a lot of research and rapid advancement in this field. This has led to the standardization of the growth technique and the possibility of large-scale fabrication techniques [12]. The unique properties of graphene are due to its crystal structure. The carbon atoms in graphene are arranged hexagonally on a 2D plane, popularly known as the honeycomb lattice. The hexagonal planar structure occurs due to sp^2 -hybridization between the s and the p (p_x and p_y) orbitals [304]. The p_z orbital is perpendicularly oriented to the planar structure and forms pi-bonds with the neighbouring carbon atoms, this bond

provides weak interaction between graphene layers. The sigma bonds formed between the sp^2 hybridized orbitals are responsible for the robustness of the material. Whereas, the pi-bonds result in pi-band, which is half-filled and responsible for the conductivity of the material [304, 3]. In ambient conditions, the charge carriers in graphene can propagate with minimal scattering as they behave like massless Dirac fermions [195]. Such unique characteristics give rise to semimetallic behaviour, anomalous quantum Hall effect, and absence of localization in graphene. Additionally, graphene is known for its excellent electrical and thermal conductivity, high mechanical robustness and superb optical transparency [197, 195, 14, 188, 145]. There are many ways to fabricate graphene, among which the simplest method is the scotch tape. It is a mechanical exfoliation method where graphite flakes are thinned down to a monolayer [37]. Even though it is a straightforward method which can produce defect-free monolayer graphene, it is not suitable for large-scale production as the flakes are relatively small (up to 100 μm). Chemical vapour deposition (CVD) is used widely for large-scale high-quality preparation of graphene. For the CVD growth of graphene, a transition metal (like Cu or Ni) is used as a catalyst and as a substrate [42]. The process temperature is around 1000 $^\circ\text{C}$ which is required for the decomposition of the hydrocarbon source (e.g. methane) into carbon atoms by the catalyst. The formation mechanism of graphene is controlled by the solubility property of the metal [147, 6]. The solubility of carbon is low in Cu this terminates the growth after the Cu surface is covered with graphene as the absence of a catalyst hinders methane decomposition [116]. Whereas, Ni has high solubility of carbon and can dissolve higher amounts of carbon atoms precipitating on the surface during cooling to form additional layers of graphene [156]. Usually, CVD-grown graphene is polycrystalline with grain sizes ranging from a few microns to hundreds of microns, nonetheless, some newer studies have shown the possibility to increase the domain size up to a centimetre-scale. After the CVD growth of graphene on a metal substrate, the graphene is coated with a protective polymer and the metal substrate is etched away and the graphene is transferred to a substrate of choice (ex: Si wafer with SiO_2 on top). The process of etching, transferring, and drying give rise to cracks and folds on the graphene which is not ideal for vdWE (we will discuss this in detail in the later section). An alternative way to achieve wafer-scale single-crystalline graphene is by thermal decomposition of SiC, however, the process is far more expensive. The main interest in graphene as a van der Waals substrate is due to its 2D structure, thermal stability, scalability, cost-effectiveness, and relative abundance. Moreover, the unique properties of graphene open the possibility for the fabrication of flexible functional devices.

Quasi van der Waals Epitaxy

As described earlier the growth of 2D material on a 2D substrate is defined as vdWE, the interaction at the interface is purely due to van der Waals forces (e.g. WS_2 on h-BN [196], as shown in Figure 2.8(a)). Whereas, quasi van der Waals epitaxy (QvdWE) is described as the growth of 3D crystalline material on a 2D substrate (or vice versa) (e.g. ZnO nanowire array [275] on mica, as shown in Figure 2.8(b)). Figure 2.8(c) shows the schematic representation of the different types of epitaxy [13]. In QvdW heteroepitaxy there is a combination of van der

Waals and covalent (or ionic/metallic) interaction at the interface. The interaction between the 3D epilayer and 2D substrate is about two orders of magnitude weaker than the chemical bonds formed at the interface of a 3D epilayer and 3D substrate. However, this interaction is stronger than vdW forces between 2D materials. The weak bonds between the epilayer and the 2D substrate can accommodate the thermal mismatch arising during high-temperature growths.

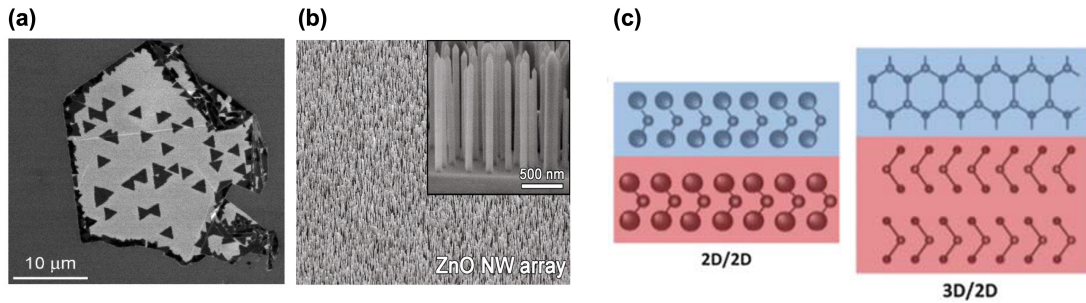


Figure 2.8: (a) SEM images of triangular-shaped WS_2 crystals grown onto hBN flake, reprinted with permission from [196], Copyright 2014 American Chemical Society. (b) SEM image of vertically aligned ZnO nanowire array grown on muscovite mica substrate, inset shows cross-sectional SEM image of the vertical nanowires, reprinted with permission from [275], Copyright 2012 American Chemical Society. (c) Schematic illustrations of vdWE (left) and QvdWE (right), reprinted from [13], with permission from Royal Society of Chemistry.

Additionally, the low growth-axis bond energies in QvdWE can aid in mitigating strain resulting from the inplane lattice mismatch between the substrate and the epilayer [95, 152, 228]. Thus, QvdWE provides the same advantages over conventional heteroepitaxy as vdWE, namely, higher tolerance for lattice and thermal expansion coefficient mismatch and facilitates the fabrication of flexible devices. A wide selection of materials has been grown on 2D material using QvdWE such as ZnO [275], GaAs [2], GaN [95], CdS [267], ZnSe [295], and so on. Depending on the material and the growth conditions the growth could either be planar [184] (such as flakes and thin films, as shown in Figure 2.9(a)) or non-planar [13] (such as nanowires and tripods, as shown in Figure 2.9(b)). Due to the absence of dangling bonds on the surface of 2D materials, the nucleation is suppressed significantly and only occurs when the surface state changes, such as in the steps, ridges, and grain boundaries. The adsorption and migration of adatoms on 2D material play an important role in the growth. Nakada *et al.* demonstrated the theoretical study of adatom adsorption and migration on graphene using the first-principles band calculation method based on DFT [189]. The adsorption energy is defined as the energy required to remove an adatom from graphene. The hexagonal structure of graphene has differential adatom adsorption sites, such as the centre of the hexagon (known as the hollow site, denoted by H), the midpoint of a carbon-carbon bond (known as the bridge site, denoted by B) and the site above a carbon atom (known as the top site, denoted by T). Different atoms have different preferential adsorption in these sites [189, 98], such as transition metal

elements are most stable at the H-site, whereas H, F, Cl, Br, and I atoms are most stable at T-site. The highest adsorption energy was shown for C, N, and O. Migration energy or migration energy barrier is defined as the energy needed by an adatom to move from site to site on graphene. A low migration energy barrier or small migration energy ensures the adatoms can move easily across graphene even at room temperature. However, the formation probability of stable nuclei becomes significantly small when the migration energy barrier is too low. At a given temperature the interplay between the adsorption energy and migration energy determines the growth characteristics. For the growth of GaN on graphene, it was shown that nitrogen acts as a nucleation site due to the large adsorption and migration energies [1, 43, 189]. Another important parameter that influences the growth characteristics is the bulk cohesive energy [2]. When the adsorption energy is larger than the bulk cohesive energy the probability of adatoms sticking to graphene increases, this promotes the likelihood of 2D growth. Whereas, if the adsorption energy is lower than the bulk cohesive energy the growth would follow a 3D mode as the incoming adatoms would preferentially stick on top of the existing nuclei than on graphene. In some cases growth defects are intentionally introduced to aid the adsorption of the atoms. Commonly oxygen and nitrogen plasma treatments are used to manufacture these defects. The creation of controlled point defects is desirable to promote surface activity in graphene, however, large amounts of defects could deteriorate the growth quality. Raman spectroscopy is used to monitor the changes in the graphene upon plasma treatment. Raman spectra of pristine graphene show two distinct peaks, the G band around 1580 cm^{-1} and the 2D band around 2700 cm^{-1} , which corresponds to the in-plane optical vibrational mode activated by intervalley double resonance [169]. On oxygen plasma treatment new features related to the defect activated bands are observed (the D band around 1340 cm^{-1} and the D' band around 1620 cm^{-1}) in the Raman spectra. Thus, structural changes in the graphene lattice can be easily monitored by the defect activated peaks and the change in the $I(\text{D})/I(\text{G})$ ratio (I is the peak intensity). Chung *et al.* investigated the growth of GaN on oxygen plasma-treated graphene, even though the oxygen plasma step increases the surface activity of graphene, it did not improve the epilayer quality [51]. Therefore, an intermediate layer of high-density ZnO nanowalls was grown on the oxygen plasma-treated graphene substrate, which in turn improved the growth quality of the GaN layer. Another way to increase nucleation and promote 2D growth is by employing an element with high adsorption energy and low migration energy barrier, Li *et al.* showed by incorporating Al after an oxygen plasma step the nucleation rates were enhanced on graphene [151]. The addition of Al promotes the formation of a dense nucleation layer which in turn increases the adsorption for Ga and N and helps in the re-crystallization process. The size of the nucleated island increases on thermal annealing and subsequently coalesces with adjacent islands to form a uniform film. For non-planar growth (such as nanowires) it is important to have a high growth rate in the out-of-plane direction in comparison to the in-plane direction. The anisotropic growth of the nanowire could be due to VLS, VS, dislocation-driven or self-catalysed.

ZnO nanowires have been grown using QvdWE, Kim *et al.* demonstrated the growth of vertically aligned ZnO nanowires using catalyst-free MOVPE [120]. They observed distinct growth

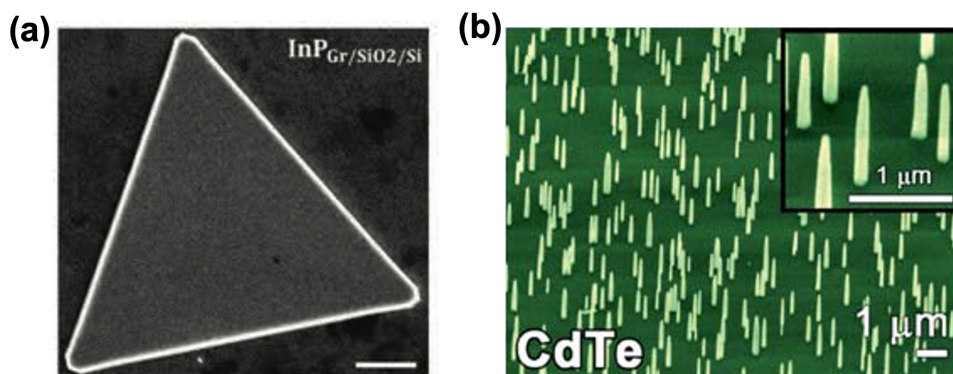


Figure 2.9: (a) SEM image of InP crystal grown on graphene/ SiO_2 /Si, scale bar in the image corresponds to $1\text{ }\mu\text{m}$, reprinted from [184], with the permission of John Wiley & Sons. (b) SEM image of CdTe nanowires grown on muscovite mica substrate, inset shows the magnified SEM image, reprinted from [13], with permission from Royal Society of Chemistry.

behaviour depending on the location, on graphene the ZnO nanowires grew vertically but in adjacent areas, with no graphene coverage (on SiO_2 /Si surface) the nanowires of ZnO grew tilted with no preferential orientation. Additionally, nanowalls of ZnO were observed in the step edges due to increased nucleation and growth rate. The temperature had a strong influence on the morphology and the density of the nanowires, with an increase in temperature the nanowires grew longer due to an increase in surface diffusion and the density was reduced due to reduced nucleation sites. Similar observations were also noted for InAs nanowires grown using catalyst-free MOVPE [97], the roughness in graphene substrate caused by graphene ledges and kinks facilitates heterogeneous nucleation and growth of the nanowires, however, if the roughness or the disorder increases too much the vertical growth deteriorates. The yield of vertically aligned nanowires decreased significantly with increasing surface roughness even though the overall nucleation density increased. They hypothesized in the absence of graphene steps and ledges point defects and vacancies in graphene could act as nucleation sites and are conducive to vertically aligned InAs nanowire arrays. GaAs has been grown on a graphitic substrate using the self-catalyzed VLS method with MBE. Munshi *et al.* reported the importance of the contact angle of the catalyst droplet for the growth of vertical nanowires [185]. For higher growth temperatures the nanowires grew vertically with a uniform hexagonal cross-section however the yield was very low and high densities of Ga droplets were formed. The contact angle of the Ga droplets was high indicating the nonwetting character of the Ga on graphene which in turn doesn't favour nanowire formation. The vertical yield of the nanowires significantly increases with the decrease in growth temperatures, this was attributed to the increased wetting of Ga and subsequently smaller contact angle formation. However, at lower temperatures, the parasitic growth also increases. To avoid the parasitic growth and to enhance the vertical nanowire growth they adopted a two-temperature growth method in which a low-temperature nanowire nucleation step was followed by a high-temperature nanowire

growth step. Several parameters influence the growth on graphene such as temperature, type of adatoms, and defects. For a given material system the growth temperatures are significantly lower on graphene than on conventional substrates due to the low adsorption of most adatoms on graphene surface for a given temperature. Thus, temperature plays a significant role in controlling the growth on graphene. Additionally, the incorporation of an element with high adsorption energy can aid the nucleation process and encourage growth. It is evident from the planar and non-planar growth on graphene that the presence of local defects is important for nucleation and growth, however depending on the type and density of these defects it might be deleterious for the growth as the growth mechanism is significantly different due to difference in adatom adsorption and migration behaviour, furthermore, this can lead to inhomogeneous growth on graphene.

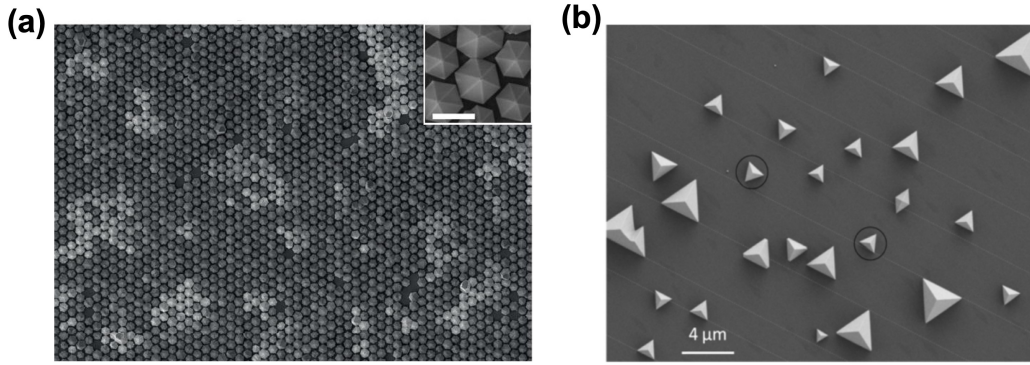


Figure 2.10: (a) Top-view SEM image of the overgrown AlGaIn pyramid arrays grown on graphene, the inset shows the magnified view of the same sample, the scale bar in the inset is $2\ \mu\text{m}$, reprinted from [186], with the permission of AIP Publishing. (b) Top-view SEM image of GaN crystals grown on graphene, reprinted from [105], with the permission of IOP Publishing, Ltd.

Some other approaches in QvdWE are selective area epitaxy and remote epitaxy. Position controlled fabrication is of importance in nanostructure-based devices, Munshi *et al.* demonstrated selective area growth of AlGaIn nanopillar arrays on graphene using a patterned mask for optoelectronic applications [186], as shown in Figure 2.10(a). This lays the foundation of nanostructure array-based devices on graphene with high yield and functionality. Ebeam lithography followed by etching was used to pattern the oxide mask on graphene which was then used as a template for AlGaIn growth using MOVPE. The growth mechanism of SAE on van der Waals substrate is fundamentally similar to QvdWE, except for the added benefit of spatial control. In contrast, the working principle of remote epitaxy [118] is markedly different as the substrate beneath the van der Waals substrate influences the growth significantly, which in the case of QvdWE acts as mere support. Figure 2.10(b) shows an SEM image of GaN grown on graphene/SiC substrate via remote epitaxy [105]. Remote atomic interaction through 2D materials is governed by the polarity of the atomic bonds, both in the substrate below the 2D

material and the 2D material itself. The potential field from the ionically bonded substrate (i.e. polar materials, e.g. GaN, GaAs, and so on) can penetrate through the few layers of graphene (depending on the strength of ionicity), whereas the potential field from the covalently bonded substrate (i.e. non-polar materials, e.g. Si and Ge) is effectively screened by the graphene monolayer. Kong *et al.* demonstrated the growth of high-quality orientationally aligned monocrystalline GaN epilayer grown on monolayer graphene coated GaN(0001) substrate [133]. In contrast, the growth of Si on monolayer graphene coated Si(001) substrate gave rise to polycrystalline growth. The potential fluctuation from the GaN substrate is transmitted through the monolayer graphene and the electrostatic interaction with the GaN substrate is preserved at the epitaxial surface. The incoming adatoms on the surface of graphene coated GaN(0001) substrate stabilize at the energetically favourable potential minima and in turn, follow the epitaxial registry of the substrate. The polarity of the 2D material can also affect the atomic arrangement in the epilayer, it was shown that polar 2D material (eg: h-BN) can partially screen the field from the substrate due to increased inhomogeneity of the potential distribution and thus giving rise to the coexistence of two distinct crystalline orientations in the same epilayer. On increasing the number of monolayers of the 2D material the growth completely transforms from remote epitaxy to QvdWE. High-quality single-crystalline thin film can be obtained using Remote epitaxy on 2D material coated substrates, the grown thin film can be easily transferred to any other substrate. This provides unique opportunities for the heterointegration of arbitrary single-crystalline thin films in functional applications. Additionally, the same 2D material coated substrate can be used for subsequent growths, thus making this process cost-effective. However, one main shortcoming of this process is the lack of compatibility with non-polar materials. Moreover, a new study suggests the possibility of “thru-hole” epitaxy [100].

3 Experimental Methods

This chapter presents an overview of the growth, fabrication, and characterization techniques primarily used in this thesis. First, the growth method is described in detail. Then, the optical characterization methods relevant to this work are stated. Next, I present the device fabrication techniques used for making electrical devices and finally, I state the main electrical characterizations used to understand the electrical properties of the material.

3.1 Molecular Beam Epitaxy

MBE is an epitaxial growth technique that operates under an ultrahigh vacuum (UHV) condition. The UHV condition minimizes the incorporation of contaminants in the epilayer, making this technique ideal for novel material investigation and device fabrication. MBE was initially developed in the late 1960s for the deposition of thin-film III-V semiconductors. Some of the pioneering work on understanding MBE growth highlighted the importance of the growth conditions for achieving high-quality epitaxial films [46, 60, 106, 103, 45]. Davey and Pankey demonstrated the growth of epitaxial GaAs films using MBE, they emphasized the importance of the substrate cleaning process and its impact on the epitaxial film quality [46]. Cho and Arthur illustrated the importance of growth temperature [46, 45]. They showed that excess As desorbs from the surface at temperatures above 300 °C, and the stoichiometric growth of epitaxial GaAs layer is favoured [46]. Since the early usage of MBE for the growth of III-V compound semiconductors particularly GaAs, it has evolved as a popular technique for growing numerous high-purity materials.

There are several variants of MBE based on the source type, such as solid source MBE (SSMBE) and gas source MBE (GSMBE) [274, 96, 73, 38]. An SSMBE is based on the utilization of solid sources, which are heated by thermal radiation or by electron beam impact. Whereas, a GSMBE utilizes hybrids, such as arsine (AsH_3) or phosphine (PH_3). The gas source is introduced into the UHV growth chamber and subsequently thermally cracked on contact with hot surfaces to form dimer beams. Additional, metal-organic compound sources (such as trisdimethyl-aminoarsenic (TDMAs) and triethylgallium (TEGa) used for the growth of GaAs)

could be used and it is called metal-organic MBE (MOMBE). Hereafter, I will only discuss the conventional solid source MBE system. MBE has a complex operating system, where the main module is maintained under a UHV condition. A typical setup consists of a growth and preparation chamber that are separated by a gate valve and individually pumped. Figure 3.1(a) shows the schematic representation of an MBE growth chamber. Some of the main components of a growth chamber are the source cells, the substrate heater, the beam flux monitor, shutters, the diagnostic system, and the pumping system. The MBE system used in this thesis is a Veeco GENxplor, as shown in Figure 3.1(b), and the details of the components will be discussed in light of the system used.

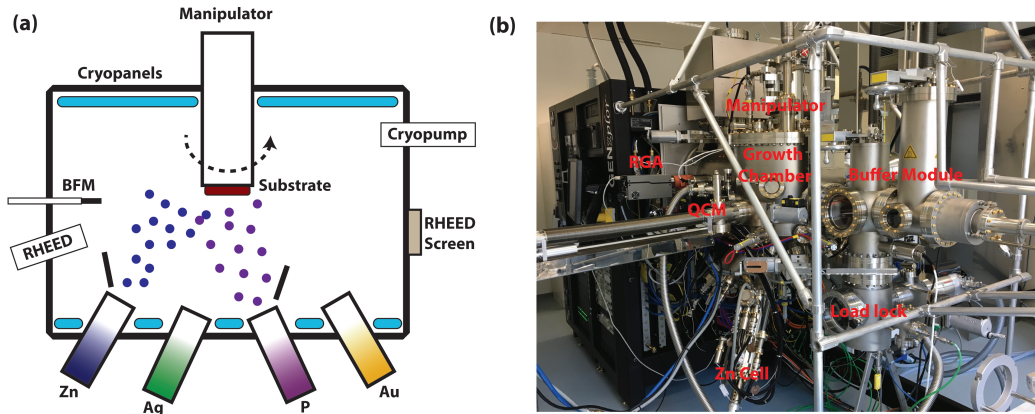


Figure 3.1: MBE system (a) schematic representation of the MBE chamber, and (b) photograph of the Veeco GENxplor MBE system used in this thesis.

The growth rates in MBE are usually very low, often in the order of 1 ML s^{-1} [274, 96]. To ensure high-purity growth the impurity levels should be lower than one part per million, which necessitates a low background pressure. Since not all residual impurities react and adhere to the surface of the grown material the impurity level of one part per million can be maintained with a background pressure of $\sim 10^{-11}$ Torr. To maintain the UHV conditions in our MBE system, the growth chamber is equipped with an ion pump, a titanium sublimation pump, cryopanel, and cryopumps. Additionally, the load-lock provides a fast and clean way to introduce samples into the UHV system, it has a turbomolecular pump and a scroll pump. The load-lock is vented to atmospheric pressure under an argon atmosphere for the introduction or removal of the substrates. Subsequently, the load-lock is degassed at 150°C for at least two hours to remove moisture and other impurities. The substrates are then moved from the load-lock to the preparation chamber. The preparation chamber has the provision for storing the substrates (up to 7 substrates at a time) and further degassing the substrates. Depending on the substrate material, it is degassed at temperatures ranging from $300\text{--}600^\circ\text{C}$. After the degassing step when the pressure of the preparation chamber reaches the optimal value the degassed substrate is transferred to the growth chamber. The substrate is placed on a substrate manipulator, which can azimuthally rotate continuously during growth to improve the uniformity across the substrate. In some cases, the rotation of

the substrate manipulator is turned off to study the composition or doping gradient along the diameter of the substrate. The substrate is heated from the backside and the temperature is measured using a thermocouple at the manipulator. The substrate temperature is also monitored during the growth using an infrared pyrometer installed at a heated viewport. The source cells are positioned at the bottom of the growth chambers and face the substrate at a 45° angle. Depending on the material, different types of source cells can be used, such as Knudsen cells, cracker cells, sublimation cells, and electron beam evaporation cells. Our MBE system is equipped with a valved effusion cell for zinc, a valved cracker cell for phosphorous (with GaP as the solid source), and effusion cells for gold, silver, and magnesium.

The ultra-pure (to minimize potential contamination) raw materials are placed in pyrolytic boron nitride (PBN) crucibles and loaded into the cell. In general, the molecular or atomic beams are generated by evaporating or sublimating the source material by radiatively heating the crucible with Ta heaters. Most of the cells used in our MBE are effusion cells, an effusion cell works as a thermal evaporator. There are different types of effusion cells depending on the application temperature such as the standard effusion cell, high-temperature effusion cell, and low-temperature effusion cell. The design of each effusion cell is based on specific evaporation requirements, such as a cold lip filament effusion cell, which has a short filament that does not reach the orifice of the crucible and is commonly used for Al evaporation. Additionally, an effusion cell must be designed to provide high purity, good time stability of the beam flux, and a high uniformity over the entire substrate area. Cracker cells are commonly used for group-V species that evaporate as tetramers (e.g. As, P, and Sb). The material is first thermally evaporated from the bulk of the cell, which subsequently passes through a hotter cracking zone tube where it decomposes the tetramers into dimers. A mechanical shutter with an actuation time of tenths of seconds is placed in front of each cell, which operates as an on/off control for the beam flux. The temperature of the cell determines the flux and it is precisely measured using a thermocouple. The thermocouple provides feedback to the temperature controller for power supply regulation. A beam flux monitor (BFM) is used to measure the beam equivalent pressure in the MBE. The filament of the BFM is inserted into the beam path close to the substrate to measure the beam equivalent pressure, this allows the calibration of the cells. Reflection high-energy electron diffraction (RHEED) is an in-situ characterization method commonly used in MBE for real-time feedback on the influence of growth conditions on the structure of the epitaxial layer. It provides information about the epilayer thickness, growth rate, surface roughness, and surface reconstruction [79, 277]. The substrate surface is probed using a high-energy electron at a grazing incidence, which is then diffracted by the surface layer. The diffraction spots formed on the fluorescent screen are known to oscillate during the growth, these oscillations correspond to the recurring roughening and smoothing of the substrate surface. The periodicity of oscillation coincides with the time needed to complete the one-monolayer growth, and hence it is used to estimate the growth rate.

In general, MBE has a number of advantages over other growth techniques. It provides growth conditions suitable for high-purity growth, which gives an insight into the properties of pristine materials. Additionally, it provides high degree of control over the parameters this is

essential for understanding the growth mechanism, especially for compound semiconductors. Nonetheless some of the major limitations of this technique is the low throughput (due to the low growth rate) and high cost of maintenance.

3.2 Optical Spectroscopy

Spectroscopy is the study of the interaction of electromagnetic radiation with matter. Optical spectroscopy measures the absorption, reflection, and emission of light by matter. Depending on the type of light-matter interaction and the wavelength of light there are several different spectroscopy techniques, such as Infrared, Raman, Ultraviolet-Visible, Photoluminescence, and so on. It is a non-destructive method used extensively for qualitative and/or quantitative understanding of material systems. Here I will only focus on Raman and Photoluminescence spectroscopy.

3.2.1 Raman Spectroscopy

Raman spectroscopy is based on the inelastic scattering of monochromatic light by a crystal lattice or molecule. When incident light interacts with a material, it can be scattered either elastically or inelastically. Most of the scattered light is at the same wavelength as the incident light, this elastic scattering is called Rayleigh scattering. Whereas, only about one photon in a million (0.0001%) is inelastically scattered [219]. The inelastic scattering process modifies the (ro-)vibrational state of the molecule [58]. This energy transfer in a crystal lattice creates/annihilates phonon (quasi-particle) in the lattice. According to the quantum mechanical description of Raman, the (ro-)vibrational energy states of molecules/phonons are discrete quanta [58, 104, 161]. The intermediate perturbed state inflicted by the incident light usually does not correspond to any electronic state of the system and is instead a virtual energy state. When the scattered photon has lower energy than the incident photon it is called Stokes Raman scattering. Whereas, when the scattered photon has higher energy than the incident photon it is called anti-Stokes Raman scattering. The anti-Stokes signal is much weaker than the Stokes signal in molecules as the population of energy states is governed by thermal statistics [104]. And, for phonons in crystals, the probability of the scattering target occupying a given vibrational quantum energy state obeys Bose-Einstein statistics [179].

Raman spectroscopy is a powerful technique for the characterization of 2D materials and phonon modes in crystals [75, 40, 44, 91, 166]. It is used for the determination of a wide array of material properties such as chemical structure, phase, strain, impurity, and thermal conductivity [104, 225, 129, 235, 62]. Raman spectroscopy was routinely used during this thesis to understand the quality of the as-grown Zn_3P_2 and the graphene substrate. Here, I give a generalized overview of the Raman spectra of Zn_3P_2 , more detailed studies are reported in Chapter 4. Depending on the crystal symmetry of the material certain transitions are allowed or forbidden, consequently, specific transitions can be Raman active or inactive. The rule describing the conditions where some modes are allowed or not is given by the selection rules

of the scattering process. According to group theory analysis, there are 39 Raman active modes for Zn_3P_2 with the following irreducible representation [175, 76, 260]:

$$\Gamma_{\text{Raman}} = 9A_{1g} + 10B_{1g} + 4B_{2g} + 16E_g \quad (3.1)$$

Here the A and the B modes correspond to the non-degenerate modes and the E mode corresponds to the doubly degenerate [76, 260, 201]. The 39 Raman modes of Zn_3P_2 are present below the frequency range of 400 cm^{-1} , which makes detection difficult due to the overlap of peaks. Stutz *et al.* showed a detailed analysis of the Zn_3P_2 Raman spectra and attributed the various peak centres to their contributing modes [260]. The peaks positioned below 210 cm^{-1} have more contribution from Zn-related vibrations, whereas peaks positioned above 225 cm^{-1} have more contribution from P-related vibrations. Additionally, a phonon gap is present in the range $210\text{-}225 \text{ cm}^{-1}$. Figure 3.2(a) and (b) show a typical Raman spectrum obtained from Zn_3P_2 at 300 K and 15 K, respectively. The different modes are highlighted for the low-temperature Raman spectra. The Raman spectra can also be correlated to the compositional variation in Zn_3P_2 , peak intensities of some of the modes vary with a change in the Zn/P ratio. Thus Raman spectroscopy plays an important role in the qualitative and quantitative characterization of Zn_3P_2 .

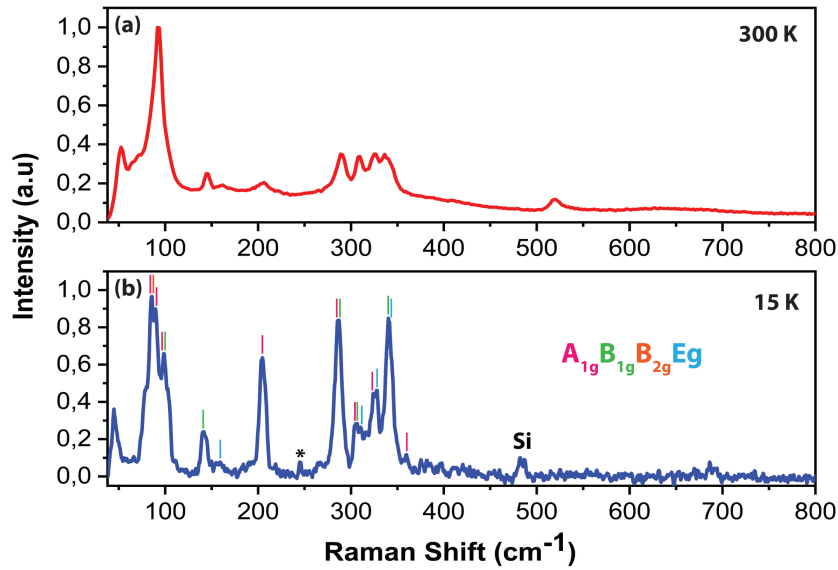


Figure 3.2: Raman spectra obtained from Zn_3P_2 grown on graphene at (a) 300 K, and (b) 15 K, the different modes are highlighted for the lower temperature measurement.

To measure the Raman spectra a Renishaw inVia confocal Raman setup. The system is configured with four different lasers (405 nm, 532 nm, 488 nm, and 785 nm) and it is combined with a charge-coupled detector through a high-resolution spectrometer comprising of gratings to disperse the Raman signal. The grating 3000 lines per millimetre (1/mm) provides a maximum

Raman spectral resolution of 0.8 cm^{-1} when coupled with the 532 nm laser. The majority of the measurements were done using a 532 nm laser either with a grating of 1800 l/mm or 3000 l/mm. The maximum incident power of the laser spot was limited to 1 mW and the spot of the laser was $\sim 1 \mu\text{m}$.

3.2.2 Photoluminescence Spectroscopy

In a thermodynamic non-equilibrium state a semiconductor can have surplus charges, which are created by carrier injection. This could be through carrier injection via contacts, an electron beam, or light absorption [90, 31]. Photoluminescence (PL) spectroscopy involves the excitation of a material with light and measuring its spontaneous emission signature. Photoluminescence provides information regarding the bandgap and the defects of a given material system. When a semiconducting material is illuminated with light energies higher than its bandgap, the carriers present in the material are excited to higher energy states. When these carriers return to their original state, they may do so via a radiative or non-radiative recombination process. When an electron and hole recombine radiatively, a photon is emitted and the energy of the emitted photon provides information about the optoelectronic properties of the material. The peak shape and position of the Photoluminescence spectra contain a number of information regarding the material. The peak width is closely related to the quality of the material, while a shift in the peak position may indicate band filling or a shift in energy levels (due to lattice expansion or contraction influenced by temperature or stress) [10, 64]. Additionally, power-dependent measurements can provide information about the underlying recombination mechanism [239].

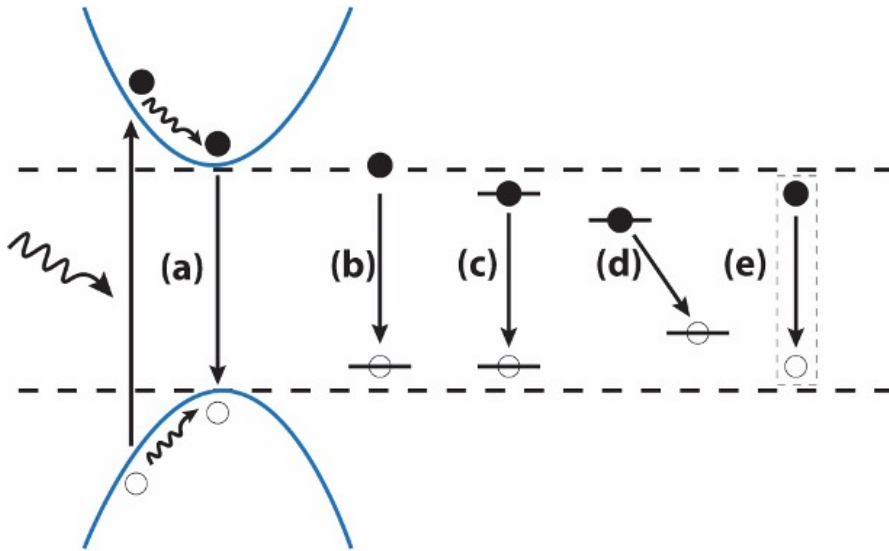


Figure 3.3: Major radiative recombination processes (a) band-to-band recombination, (b) recombination between a free and a localized carrier, (c) recombination between the levels of a single impurity, (d) recombination between an acceptor and a donor, and (e) recombination between free or bound excitons.

When carriers return to their original state, they can do so either immediately or after scattering, or they can recombine with another state away from their original state after diffusion. There are a number of recombination pathways as shown in Figure 3.3, some of which are radiative and the others are non-radiative. The most common radiative recombination processes are direct recombination (also known as band-to-band recombination), free-to-bound transition, donor-acceptor pair transition, and exciton transition. Non-radiative recombination is usually an undesired effect, where the entropy of the system is increased due to the generation of heat which in turn reduces the device performance. The non-radiative recombination mechanisms in a semiconductor are Auger recombination and recombination through defects. Extended defects that act as recombination centres are surfaces, grain boundaries, and dislocations. The break in crystal symmetry due to the presence of a surface induces midgap levels, which act as non-radiative recombination centres. Grain boundary is the interface between two grains. The decrease in the grain boundary area causes a decrease in the minority carrier lifetime, which can severely impact the performance of photovoltaic devices. When the average distance between grain boundaries is significantly larger than the minority carrier diffusion length the impact on the device performance is negligible. This makes the growth of monocrystalline or large-grain polycrystalline material enticing. Dislocations are also referred to as carrier sinks and the minority carrier lifetime is dependent on the dislocation density ($\tau^{-1} \propto n_d$, where τ is the carrier lifetime and n_d is the dislocation density) [90]. These non-radiative recombinations are not directly measured by Photoluminescence spectroscopy, however, they do reduce the overall luminescence of the material.

The setup used for the PL measurements is a LabRam HR Evolution HORIBA spectrometer. A monochromatic light source with wavelengths 532 or 633 nm was used. A diffraction grating of 300 l/mm was used for the measurements and a charge-couple device (CCD) detector collects the signal. The measurements were carried out in Prof. Qihua Xiong's lab at Nanyang Technological University in Singapore, for more information on the setting refer to Chapter 4.

3.3 Device Fabrication

To probe the electrical properties of Zn_3P_2 thin film grown on InP substrates several devices were fabricated to carry out the electrical measurements. All of the device fabrication steps were carried out in the cleanroom facility of the Centre of MicroNanoTechnology (CMI) and the characterization platform of the Interdisciplinary Centre for Electron Microscopy (CIME). In this thesis mainly electron beam lithography and focused ion beam were used for device fabrication, which is discussed in detail in Chapter 5. Additionally, we also fabricated photovoltaic devices, which are discussed in detail in Chapter 6.

3.3.1 Electron Beam Lithography

Electron beam lithography (EBL) is a lithography technique that utilizes focused electron beams for creating fine patterns for various applications. It is a high-resolution technique

capable of writing nanoscale features. EBL consist of three main steps: exposure of the resist, development of the resist, and pattern transfer. The electron beam scans across a surface coated with a resist sensitive to the electron beam to create the pattern. The resist could be a positive (the exposed area to the electron beam is removed on developing) or a negative (the unexposed area is removed on developing) resist and the choice of the resist largely depends on the desired resolution of the pattern. Moreover, the final resolution of the feature is an accumulative effect of each individual step in the process. The electron beam has a Gaussian distribution and the higher the energy of the beam lower the wavelength of the beam which ensures a small beam diameter. In general, an EBL system consists of an electron source, two or more lenses used for focusing the electron beam, a beam blanker for turning the beam on and off, a stigmator for compensating astigmatism, apertures for defining the beam, a deflection system for moving the beam, an electron detector for locating markers on the sample, and a Faraday cage used for the beam current measurement to ensure precise dose for resist exposure.

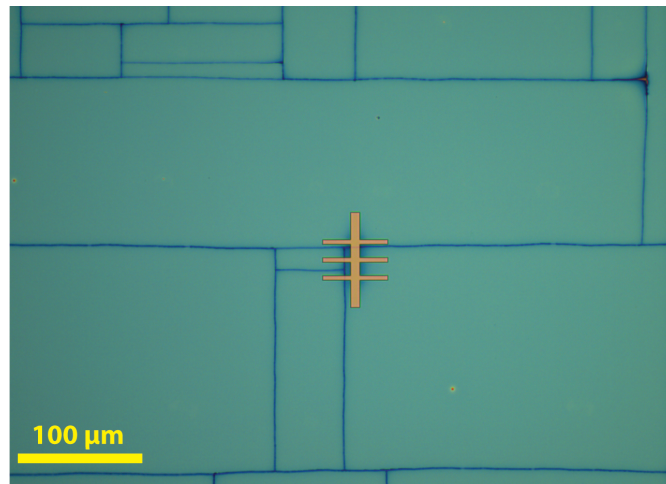


Figure 3.4: Optical image of a Hall bar structure processed on the micro-crack.

Some of the major limitations of the EBL process are cost, complexity, slower process, low throughput, and proximity effect. The EBL process is slow in comparison to some other lithography techniques, each writing step could take several hours and some samples could require multiple writing steps. When the beam operates at lower voltages the aberration is greater, thus the resolution is low and a higher working voltage is preferred. However, at higher voltages, the resist outside the targeted exposure area receives a non-zero electron dose known as the proximity effect. When the electron beam collides with the resist and the substrate underneath, forward and backscattered electrons are produced which in turn causes the exposure of the resist far from the originally targeted area. This leads to poor resolution and nonuniform exposure. Despite the limitations, EBL has proven to be beneficial for the development of applications based on submicron-sized features. The major advantages of the EBL process are high resolution, direct transfer of complex patterns, high accuracy of alignment, and flexibility.

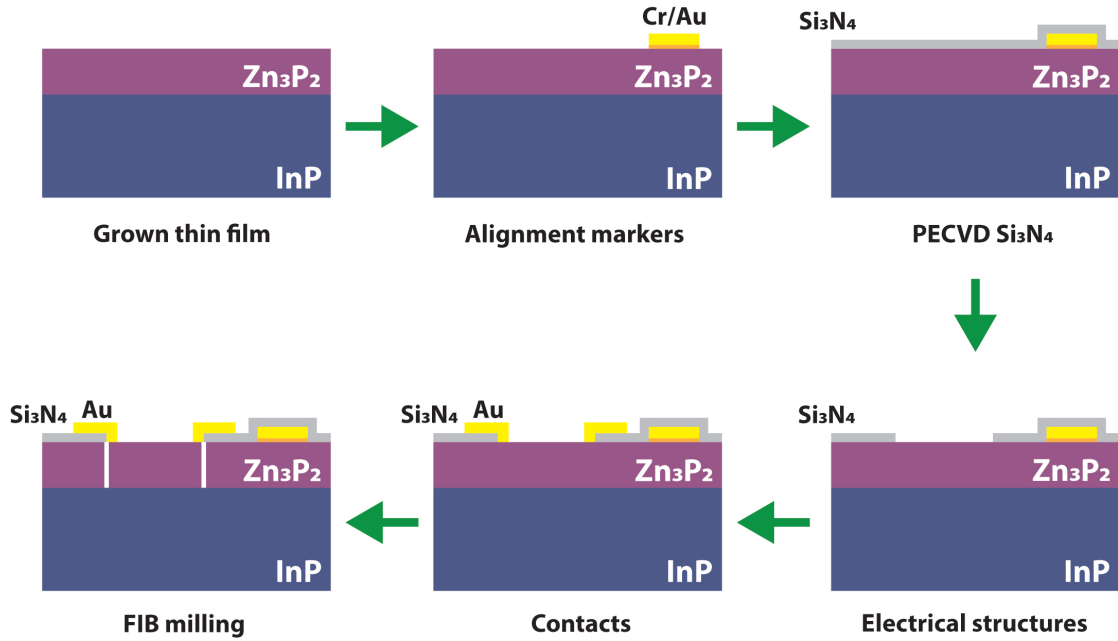


Figure 3.5: Schematic representation of the fabrication steps used for processing the electrical device structures.

The monocrystalline samples contained micro-cracks, to avoid the processing of the electrical structures on these micro-cracks EBL was used. EBL allows precise alignment of the structure with respect to the cracks. Figure 3.4 shows the optical microscope image of a hall bar processed on the micro-crack due to misalignment. The fabrication process schematic is depicted in Figure 3.5. As a first step EBL is used for defining the alignment markers on the sample. This is done by first coating the sample with ~ 440 nm of methylmethacrylate (MMA) and ~ 220 nm polymethylmethacrylate (PMMA) which are positive photoresists. Two resist are used to ensure proper lift-off of the deposited metal and the thickness of the resists is adjusted in accordance with the thickness of the metal to be deposited. The resist-coated sample is exposed selectively to the electron beam, where the dose and the current are adjusted according to the desired resolution. After the exposure, the resist is developed using MiBK:IPA (1:3) developer. The resist is removed from the exposed areas. Next, the metal used for the alignment markers is deposited using sputtering. The thickness of the metal used is ~ 100 nm comprising of 10 nm of Cr and 90 nm of Au. The metal from the rest of the sample is removed via liftoff in acetone. In the subsequent step, 30 nm of Si_3N_4 is deposited using plasma-enhanced chemical vapour deposition (PECVD). The nitride layer protects the sample and isolates the electrical structures. A second EBL step is used for creating the electrical structures on the sample. After the exposure and the development, a reactive ion etching step (~ 60 seconds) is used to selectively remove the nitride from the exposed areas. The unexposed resist (PMMA) is stripped in acetone. Finally, an EBL step is performed to make the final contacts of the electrical structures. The EBL process is followed by a metal (Au ~ 150 -180 nm) deposition using sputtering and a final liftoff in acetone. The electrical structures are isolated

using a FIB milling technique, which is discussed in the next section. Figure 3.6 shows the SEM micrograph of the final electrical structure.

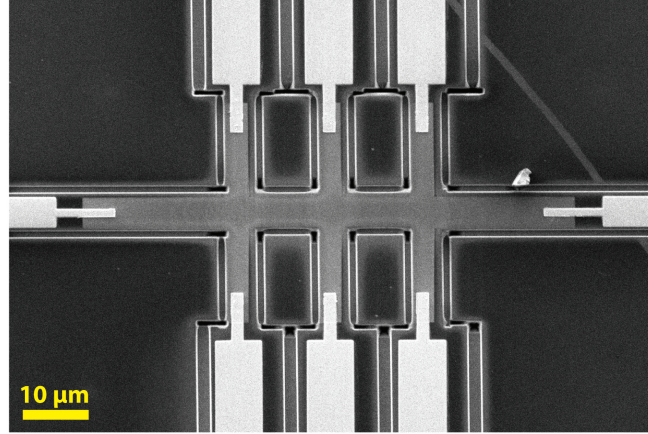


Figure 3.6: SEM image of a fabricated Hall bar structure.

The electron beam lithography system used in this thesis is Raith EBPG5000+, which is capable of writing features smaller than 10 nm. The instrument is normally set to 100 keV for operation and a thermal field emission gun is used as the source.

3.3.2 Focused Ion Beam

Focused ion beam (FIB) technique utilizes a highly-focused beam of charged ions for precise nanopatterning such as milling and material deposition. Additionally, FIB can be used for imaging, compositional analysis, and structural analysis. In this section, I describe the fundamentals of FIB in the light of device fabrication. The interaction of the focused ion beam with the material on which it impinges can be exploited for selective material removal and in presence of a gaseous precursor for material deposition. The working resolution provided by FIB ranges from hundreds of micrometres to a few nanometers, and this range largely depends on the material, ionic species, and beam configuration. FIB systems are usually combined with a scanning electron microscope (SEM) system, the main components of this instrument are an ion column, an electron column and a process chamber. The upper part of the ion column houses the ion source and the lower part encompasses a series of elements for the acceleration, focus, and steering of the beam. The ions coming from the source are accelerated and focused in the ion column. The ion column also has electromagnetic and electrostatic lenses, and apertures. The lenses present in the instrument are used for beam deflection and focus. And, the apertures are used for defining the beam size. A beam blanker is present to steer the beam away from the axis when needed. And, a Faraday cup is present to accurately measure the ion beam current. The processing occurs in the process chamber that consists of the sample stage, detectors, and processing module which includes a gas delivery system used for the injection

of precursors into the chamber for material deposition. The gas injection system (GIS) delivers the precursor material in gaseous form in close proximity to the sample using a nozzle. Some of the most common precursor materials found in FIB systems are tungsten hexacarbonyl ($\text{W}(\text{CO})_6$), methylcyclopentadienyl trimethyl platinum ($(\text{CH}_3)_3\text{Pt}(\text{CpCH}_3)$), and naphthalene (C_{10}H_8). The injected molecule should have a sufficient sticking coefficient on the sample surface to ensure deposition on decomposition upon irradiation by the beam [198].

The processing chamber is also equipped with a sample stage which can be moved in all three dimensions, rotated around its axis, and tilted to a certain angle. Most of the modules in a FIB/SEM system are calibrated to work optimally at the eucentric height. The eucentric height refers to the height of the sample at which the image does not move laterally upon tilting the sample, this height is set at the coincidence point between the two beams and the stage. The SEM column is placed at 0° tilt while the FIB column is placed at an angle ($45\text{--}55^\circ$) with respect to the SEM column.

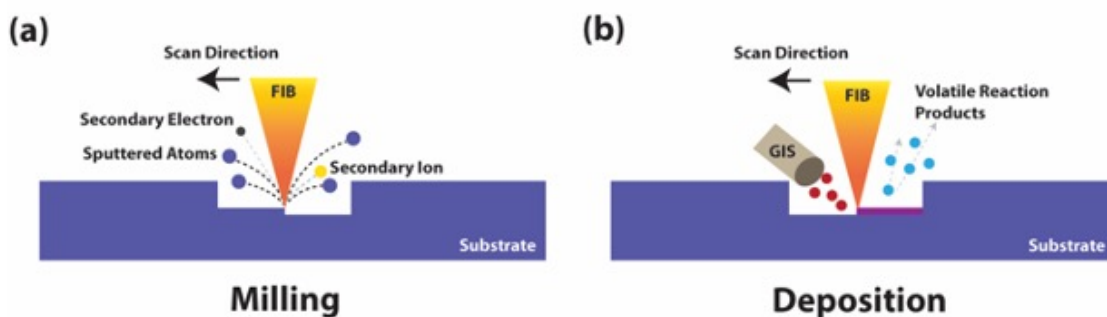


Figure 3.7: Schematic representation of FIB (a) milling, and (b) deposition, process.

When the ion beam scans over the material, a number of interactions take place. Broadly, the ion-solid interaction leads to nuclear interaction and electronic interaction. The volume of interaction is defined by the ionic species used and the sample material. Figure 3.7(a) shows the schematic representation of the ion-solid interactions that take place in FIB processing. When the incident ions elastically collide with the atoms in the sample, the atoms are displaced from their equilibrium position and a collision cascade is triggered. During a collision cascade, if the transferred momentum to the atoms close to the surface exceeds the binding energy then they are sputtered from the bulk [55]. Whereas, when the beam is used for the purpose of material deposition (as shown in Figure 3.7(b)), it is the secondary electrons emitted from the sample upon interaction with the beam that induces the decomposition reaction of the adsorbed precursor molecules. The precursor molecules are dissociated into volatile (which are pumped out) and non-volatile (which are deposited on the sample) parts. In general, the process of atomic displacement can lead to the amorphization of the material and the sputtered material can get redeposited close to the point of ejection. In order to minimize the damage caused by the FIB processing while milling the parameters used for the process should be customized according to the material. Some of the parameters that are commonly adjusted are the acceleration voltage (the potential difference used for accelerating the ions

down the column, the attainable working range is usually between 0.2 kV to 60 kV), the ion beam current (the ion charge delivered to the sample per unit time, depending on the FIB system this value can range from 0.1 pA to 2 μ A), the dose (the amount of charge received by the material per unit area in a given time interval), and the dwell time (time spent by the beam on each irradiation spot during a scan).

In this thesis the Thermofisher HeliosTM G4 PFIB UXe DualBeamTM FIB/SEM system was used, it combines the PFIB column with an SEM column. The ion source for the FIB could be a liquid metal ion source or a gas field ion source or a plasma source. A plasma source FIB (PFIB) was used in this thesis, it operates by creating a plasma of a noble gas. One major advantage of plasma source FIB is the improvement of the beam current with a relatively small spot size.

3.4 Electrical Characterization

In the following section, I will describe the electrical characterization methods used to determine the electrical properties of the as-grown Zn₃P₂ on the InP substrate. An understanding of the electrical properties is crucial for the application of the material for photovoltaics. The fabrication process required for the electrical devices has been described in detail in the previous section.

3.4.1 Transmission Line Measurement

Transmission line measurement (TLM) is used to determine a number of electrical properties of a semiconductor, such as resistivity, specific contact resistivity, transfer length, and sheet resistance. It involves current-voltage measurements between adjacent contacts of variable spacing. Figure 3.8(a) shows the schematic representation of a TLM structure, the length (L) and width (W) of the contacts are kept constant throughout the structure while the distance (d) between the contacts is varied. The total resistance between two contacts is measured and plotted as a function of the contact spacing, as shown in Figure 3.8(b). Three parameters are extracted directly from the plot, the sheet resistance R_{SH} , the contact resistance R_C , and the transfer length L_T . The sheet resistance is obtained by the slope of the plot, the contact resistance is obtained from the y-intercept, and the transfer length is obtained from the x-intercept. The total resistance (R_{TOT}) is described as:

$$R_{TOT} = 2R_M + R_S + 2R_C \quad (3.2)$$

where R_S is the resistance of the semiconductor and R_M is the resistance of the metal (this is neglected as it is very low). Alternative the total resistance can be expressed as:

$$R_{TOT} = \left(\frac{R_{SH}}{W} \right) d + 2R_C \quad (3.3)$$

The transfer length is the average distance over which the current transfer from the semiconductor into the metal and vice versa. The transfer length is described as :

$$L_T = \sqrt{\frac{\rho_c}{R_{SH}}} \quad (3.4)$$

The term ρ_c is the specific contact resistivity, on considering the path of current underneath the contact, it is evident that the distribution of the current density is dependent on the value of the specific contact resistivity [82]. For a small value of ρ_c , the current can flow quickly into the contact, as shown in Figure 3.8(c). Whereas, for a high value of ρ_c , the current path is extended as the transition resistance is high, as shown in Figure 3.8(d). In general, when $L \geq 1.5 L_T$ the contact is described as good contact with low specific contact resistivity. Whereas, when $L \leq 0.5 L_T$ the contact is described as poor contact with high specific contact resistivity, which can occur due to current crowding [316].

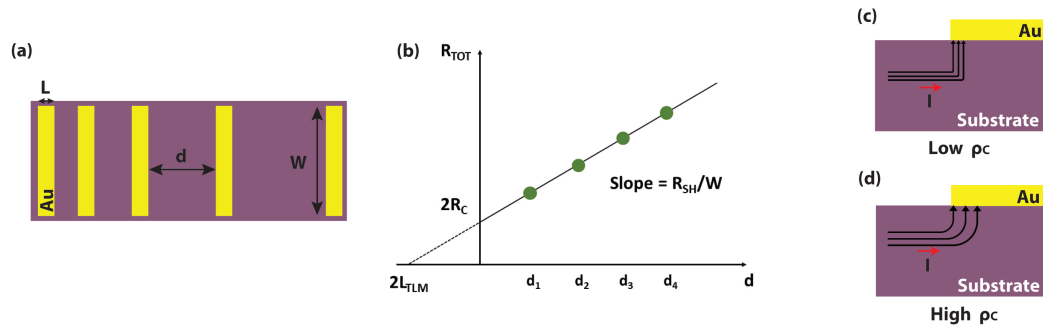


Figure 3.8: Schematic representation of (a) the top-view of a TLM structure, highlighting the dimensions, (b) a common measurement outcome, where the resistance is plotted as a function of the distance. The cross-sectional view showing the representative electric field lines (c) low ρ_c , and (d) high ρ_c .

The TLM measurements were performed in our table-top probe station at room temperature. A Keithley 6487 voltage source was used to apply the voltage and a picoammeter was used to measure the current. The measurements were carried out by placing two probes on two adjacent metal pads and applying a voltage sweep in the range ± 1 V while simultaneously measuring the current.

3.4.2 Hall Effect Measurement

When a magnetic field is applied perpendicular to the direction of current flow in a conductor an electric field is developed in the direction perpendicular to both. The underlying principle of Hall effect can be understood from the Lorentz force acting on the charge carriers due to the magnetic force and the electric force. When a charge carrier (q) moving in the x -direction with a drift velocity (v_X) experiences an external magnetic field (B_Z) in the z -direction, a force

(F) develops on the charge. This force is in the y direction and described as [164]:

$$F = -qv_X B_Z \quad (3.5)$$

As a consequence of this force, the charge carriers will be deflected to one side, which in turn creates a negative charge on one side and a positive charge on the other. This induces an electric field in the y-direction and it is proportional to the current and the magnetic field. The force on the charge carrier due to the electric field is balanced by the Lorentz force. The Hall voltage is the integral of the electrical field across the width of the sample, this can either be positive or negative. When the force from the electric field is equal and opposite to the magnetic force, the net force in the y-direction is zero, this is known as the Hall effect. And, the current flow is uniform in the x-direction and it takes only a few picoseconds to establish this steady state. Therefore the Hall voltage can be derived from:

$$-q \frac{V_{Hall}}{w} = -qv_X B_Z \quad (3.6)$$

and, v_X can be written as:

$$v_X = \frac{I}{nqw_t} \quad (3.7)$$

thus, from Equations 3.6 and 3.7 we obtain:

$$V_{Hall} = \frac{IB_Z}{nqt} \quad (3.8)$$

where n is the carrier density, t is the thickness and, the Hall coefficient is defined as $R_H = \frac{1}{nq}$. It is positive if the charge carriers are positive and negative if they are negative. The polarity of the voltage drop across the width of the hall bar determines the sign. The mobility (μ) of the carrier can be obtained by using the carrier concentration from Equation 3.8, and by using the conductivity of the material given by $\sigma = nq\mu$.

The Hall effect measurements can provide information on a number of material properties such as carrier mobility, carrier concentration, resistivity, magnetoresistance, and the type of majority carrier. The hall effect measurements are commonly done in two distinct configurations, one in the Hall bar geometry and the other in the van der Pauw geometries. Each configuration has its own advantages and disadvantages, for example, the van der Pauw method can be applied to a sample of arbitrary geometry but it is more prone to errors due to the finite size of the contacts than Hall bars. In this thesis, we will only discuss Hall bar geometry as it was most frequently used. Figure 3.9(a) shows the schematic representation of a Hall bar geometry. Placing the contacts at the ends of the contact arm reduces the contact

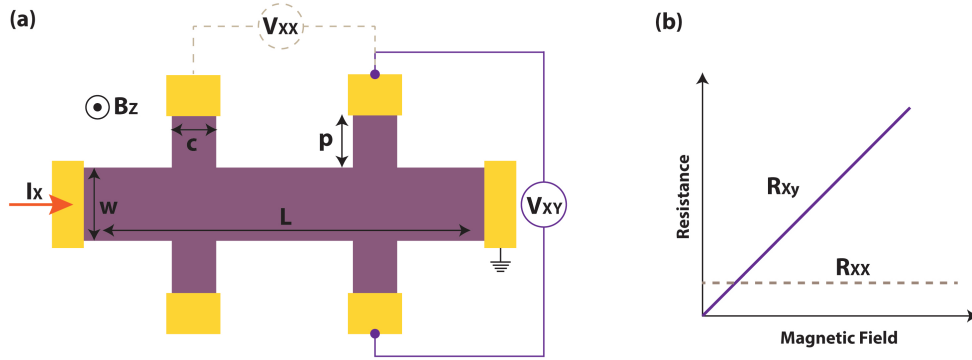


Figure 3.9: Schematic representation of (a) a Hall bar, highlighting the dimensions, the current injection, the Hall voltage, and the longitudinal voltage, and (b) a common measurement outcome, where the resistance is plotted as a function of the applied magnetic field.

size error, which is significantly high for just a rectangular bar. The length of the Hall bar should at least be three times longer than the width ($L/w \geq 3$), if the length is shorter then the end contacts could short out the Hall voltage [90, 164, 86]. The length of the contact arm should be approximately the same as the dimension of the contact ($p \approx c$). And the width of the bar should be at least 3 times larger than the arm contact ($w \geq 3c$). These are some of the geometrical considerations for the Hall bar geometry. In a typical Hall effect measurement, the longitudinal resistance (R_{xx}) and the transverse resistance (R_{xy}) are measured as a function of the applied magnetic field. Figure 3.9(b) shows the schematics of the expected measurement outcome, where the slope of the R_{xy} against the magnetic field plot gives R_H .

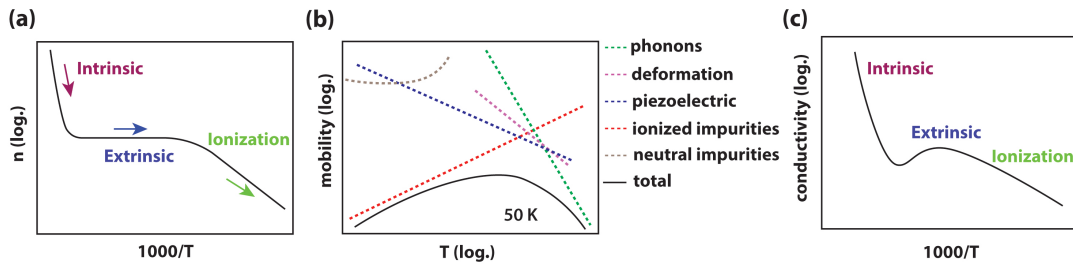


Figure 3.10: Schematic representation of the temperature dependence of (a) carrier concentration, (b) mobility and the contribution from different scattering mechanisms, and (c) conductivity, in a semiconductor adapted from [90].

Apart from room temperature Hall effect measurements, more frequently temperature dependent measurements are also done in order to understand the material better. Figure 3.10(a) shows the variation in the carrier concentration as a function of temperature, and the dependence can be expressed as $n \propto e^{-E_a/k_B T}$, where n is the carrier concentration, k_B is

the Boltzmann constant, T is the temperature, and E_a is the activation energy. The bandgap (E_g) is related to the activation energy in the case of thermally excited carriers as $E_g = 2E_a$, however, this can vary if the semiconductor has dopants, impurities, or trap states. It can be seen from Figure 3.10(a) the carrier concentration decreases with a decrease in temperature and there are three distinct temperature regimes. At high temperatures, the carrier concentration increases due to excitation across bandgap and this regime is dominated by the intrinsic carriers. At moderate temperatures, the carrier concentration is almost constant due to the fully ionized dopants and this regime is dominated by extrinsic carriers. At low temperatures, the carrier concentration decreases due to the freeze-out of the dopants. Figure 3.10(b) shows the variation in mobility as a function of temperature, all the different scattering processes make the temperature dependence of mobility quite complicated. In non-polar semiconductors like Ge and Si, the most dominant process at low temperatures is the ionized impurity scattering ($\mu \propto T^{3/2}$). And, at high temperatures, the most dominant process is deformation potential scattering ($\mu \propto T^{-3/2}$). Whereas, in polar semiconductors like GaAs, the most dominant process at high temperatures is polar optical scattering. Figure 3.10(c) shows the variation in the conductivity of the semiconductor as a function of temperature. As the carrier concentration increases with temperature and the mobility decreases, the resistivity has a minimum or conductivity has a maximum [90]. Moreover, at high temperatures, when the intrinsic conduction starts, the resistance decreases significantly due to the increase in carrier concentration.

The setup used in this thesis for Hall effect and temperature-dependent measurements is a physical property measurement system (PPMS® DynaCool™) by Quantum Design. The temperature range in which the system can be used is from 1.8 – 400 K. The magnetic field can be varied up to 14 T. It contains a built-in cryopump for high vacuum application ($<10^{-4}$ Torr).

3.4.3 Conductive Atomic Force Microscopy

When dealing with nanostructured samples it is often inconvenient to contact the sample by evaporating or sputtering metal contact pads. To directly probe the electric behaviour of the sample we use conductive atomic force microscopy (C-AFM). It is an AFM technique that utilizes a conductive cantilever and tip for measuring the current flowing between the tip/sample nanojunction while simultaneously measuring the topography [143, 173, 308]. Apart from the conductive tip, it also requires a voltage source for the application of a potential difference between the tip and the sample holder and a preamplifier for the conversion of the analogue current into digital voltage. A Faraday cage can also be present to isolate the sample from external electrical interference. The sample is placed on the sample holder using conductive tape or paste (such as silver paste). When a potential difference is applied between the sample and the tip an electrical field is created that causes a net current flow from the tip to the sample or vice versa. This allows precise measurement of the local electrical properties of the sample at high resolution. CAFM is most frequently used for current maps and current-voltage measurements. Current maps can be obtained by scanning the tip along the sample

surface. Current maps provide insight into local inhomogeneity in electrical conductivity. The difference between the current map and the topography of the surface could occur due to the reduced effective electron emission area in comparison to the physical contact area. Alternatively, current-voltage (I-V) curves can be obtained by positioning the tip at a given point on the sample and sweeping the voltage while recording the corresponding current values. It should be noted the contact between the sample and the tip should ideally be ohmic, otherwise, the tip/sample barrier should be considered.

The C-AFM setup used in this thesis is Cypher S AFM Microscope from Oxford Instruments. It has an ARC2 (Asylum Research Controller 2), which contains the power supplies and electronics required for controlling the scan and acquiring the image data. Igor pro software environment is utilized as the interface between the hardware and the user, it is capable of scientific graphing, image processing, and macro programming. A PtSi-FM tip was used for the I-V measurements, the platinum silicide coating is highly conductive and provides a good wear-out behaviour. And, a PtSi-CONT is used for the current maps. This tip has a much lower force constant (~ 0.2 N/m) and resonance frequency (~ 13 kHz).

4 van der Waals epitaxy of earth-abundant Zn_3P_2 on graphene for photovoltaics

4.1 Accompanying information

This work has been published in peer-reviewed journal *Crystal Growth & Design* 2020, 20, (6), 3816-3825. Its digital object identifier is 10.1021/acs.cgd.0c00125. The list of authors is as follows: Rajrupa Paul, Nicolas Humblot, Simon Escobar Steinvall, Elias Zsolt Stutz, Shreyas Sanjay Joglekar, Jean-Baptiste Leran, Mahdi Zamani, Cyril Cayron, Roland Logé, Andres Granados del Aguila, Qihua Xiong, and Anna Fontcuberta i Morral. My contribution includes growth of Zn_3P_2 , characterization of the material, and data analysis. I contributed significantly to the writing of the manuscript.

4.2 Abstract

Earth-abundant semiconducting materials are a potential solution for large-scale deployment of solar cells at a lower cost. Zinc phosphide (Zn_3P_2) is one such earth-abundant material with optoelectronic properties suitable for photovoltaics. Herein, we report the van der Waals epitaxy of tetragonal Zn_3P_2 ($\alpha\text{-Zn}_3\text{P}_2$) on graphene using molecular beam epitaxy. The growth on graphene progresses by the formation of Zn_3P_2 triangular flakes, which merge to form a thin film with a strong (101) crystallographic texture. Photoluminescence from the Zn_3P_2 thin films is consistent with previously reported Zn_3P_2 . This work demonstrates that the need for a lattice-matched substrate can be circumvented by the use of graphene as a substrate. Moreover, the synthesis of high-quality Zn_3P_2 flakes and films on graphene brings new material choices for low-cost photovoltaic applications.

4.3 Introduction

The global energy consumption continues to severely impact the world's climatic conditions, and this necessitates a firm shift toward clean and sustainable sources of energy. Earth-abundant semiconducting materials could be beneficial for the purpose of low-cost, large-scale deployment of photovoltaics [282, 259]. Zn_3P_2 is an Earth-abundant semiconductor with promising optoelectronic properties [177, 19, 70]. Zn_3P_2 has a high absorption coefficient ($>10^4 \text{ cm}^{-1}$) [72] in the visible part of the electromagnetic spectrum and long minority-carrier diffusion length ($>5 \mu\text{m}$) [301]. The reported band gap of Zn_3P_2 lies close to the theoretical maxima of the Shockley-Queisser limit [250], making it a suitable candidate for photovoltaics [207, 125]. The highest solar energy conversion efficiency ($\sim 6\%$) was reported by Bhushan *et al.* for $\text{Mg}-\text{Zn}_3\text{P}_2$ based solar cells [21].

Since 1981, there has been no report on the improvement of efficiency for Zn_3P_2 -based solar cells. One of the major issues associated with Zn_3P_2 is its large lattice parameter ($a = 8.089 \text{ \AA}$, $c = 11.45 \text{ \AA}$) [211], which makes high-quality epitaxial growth suitable for solar cell application challenging [25]. Furthermore, the choice of substrate is limited due to the large linear thermal expansion coefficient ($1.4 \times 10^{-5} \text{ K}^{-1}$) [162] of Zn_3P_2 [48]. Cracks were observed on Zn_3P_2 thin films grown at high temperatures ($\geq 600 \text{ }^\circ\text{C}$) on a large number of commercially available substrates [48]. Additionally, the formation energies of zinc vacancies and phosphorus interstitials are very low in Zn_3P_2 , which makes the material intrinsically p-type [305, 61]. The intrinsic p-type nature of Zn_3P_2 in principle rules out the formation of low-resistive homojunction solar cells. And most of the Zn_3P_2 solar cells are based on heterojunction or Schottky junction [21, 123]. In 1984, Atsushi Koma introduced the concept of van der Waals epitaxy (vdWE). He demonstrated the growth of an epitaxial thin film on a substrate with over 20% lattice mismatch by avoiding the formation of covalent bonds at the interface [130]. The advantage of vdWE is the use of substrates with no dangling bonds, such as two-dimensional materials (e.g., graphene) or bulk layered materials (e.g., mica) [302, 285]. Because of the absence of dangling bonds at the surface of a van der Waals substrate, the growth of the overlayer proceeds without the formation of covalent bonds at the interface. van der Waals bonds originate from the dipolar interactions between atoms. Compared to covalent bonds, the van der Waals bonds are much weaker, and this gives an unstrained epitaxial overlayer growth with a defect-free interface on a highly lattice-mismatched substrate. Hence, vdWE could be a suitable method to overcome the limitation of lattice-matched substrates for the growth of high-quality epitaxial material. Graphene is widely used for vdWE due to its two-dimensional nature as well as its high electrical and thermal conductivities [197, 14], optical transparency [188], and high mechanical strength and flexibility [145, 181, 50]. The recent advances in the synthesis technique of high-quality graphene have made it possible to fabricate large-area polycrystalline graphene substrates at a lower cost [12, 108]. Graphene can function as a low-cost, transparent, and flexible electrode, which can be exploited for the fabrication of Zn_3P_2 -graphene junction-based solar cells. Vazquez-Mena *et al.* demonstrated a field-effect solar cell using graphene that formed a tunable junction barrier with Zn_3P_2 [279].

This opens an avenue for the integration of functional material on graphene to create a new hybrid material system. Bosco *et al.* [25] demonstrated the growth of Zn₃P₂ on GaAs substrates by congruently sublimating Zn₃P₂. We believe that the use of congruent sublimation can come at the expense of controlling the stoichiometry of the material in a precise manner. As an example, Suda *et al.* reported the growth of n-type Zn₃P₂ by using elemental source MBE [262]. They attributed the n-type behavior of Zn₃P₂ on the zinc-rich growth conditions. Additionally, the use of MBE has some advantages over other growth techniques commonly used for Zn₃P₂ growth [78, 106]. MBE uses high purity source materials and an ultrahigh vacuum growth environment, which ensures low impurity incorporation. In this work, we demonstrate the growth of high-quality Zn₃P₂ on graphene with vdWE using MBE, as demonstrated by the structural and optical properties. The optimum growth parameters were established by varying the temperature, pressure, and flux ratio in our system. We present the growth mechanism, based on the observation of how the film evolves with growth time. This work shows a direct and efficient way to integrate Zn₃P₂ on graphene.

4.4 Experimental Details

4.4.1 Growth of Zn₃P₂

The Zn₃P₂ thin films were grown using Veeco GENxplor MBE on the commercially purchased graphene substrate. The graphene substrates were purchased from Graphenea, and each substrate consists of a monolayer of graphene transferred onto a 4 inch SiO₂(300 nm)/Si(100) wafer. The MBE system utilizes separate sources of zinc and phosphorus (MBE Komponenten GaP-based P₂ source). Before each growth, the graphene substrates were degassed at 500 °C for 1 h in the prep-module. The Zn₃P₂ thin films were grown in the growth-module of the MBE system, at a 150 °C manipulator temperature for 300 min using a Zn BEP of 5.20×10^{-7} Torr and a P₂ BEP of 7.50×10^{-7} Torr.

4.4.2 Characterization

The spectrometer used for PL is a LabRam HR Evolution HORIBA Raman spectrometer. A source of monochromatic light (laser) of a specific wavelength (532 or 633 nm) is used to investigate the sample. The beam is directed onto the sample using a set of mirrors allowing a controllable alignment. The use of a bandpass filter on the laser's path prevents undesirable laser lines. Neutral density (ND) filters are arranged to tune the laser intensity. After passing through a beam splitter and a dichroic mirror, the laser is focused on the sample. PL spectroscopy is implemented in back reflection geometry, consisting of a collecting signal from the same spot on which the exciting radiation is focused by the lens. The focusing lens has a large numerical aperture in order to collect as much luminescent or scattered light as possible from a large solid angle. The light is then collimated and passes through a notch filter to subtract the overwhelming laser light. It is then focused onto the entrance slit of a

spectral device. Light is dispersed into a spectrum by mean of a monochromator. For PL, the diffraction grating holds 300 grooves per millimeter (gr/mm). A charge-coupled device (CDD) detector finally collects the signal. The Raman spectroscopy measurements were done in a commercial Renishaw inVia system at room temperature. A 532 nm laser was used at 1 mW incident power. The backscattered spectrum was collected after an exposure time of 25 s, averaged over 10 accumulations. A diffraction grating of 1800 lines per millimeter (l/mm) was used. The laser spot size used in the measurement was $\sim 1 \mu\text{m}$. the spectral resolution of the setup is 1.5 cm^{-1} . The XRD measurement was done using a Panalytical Empyrean XRD setup, which uses a Cu ($\text{K-}\alpha$) X-ray source of 1.54 \AA . The EBSD maps were acquired with a Nordlys 2 EBSD camera coupled to the Aztec (Oxford Instruments) acquisition software on an XLF30 (FEI) scanning electron microscope working at 25 kV, with a step size of 40 nm, in “refined accuracy” mode to avoid pseudosymmetry miss-indexation issues. The AFM measurements were done using a commercial Bruker Dimension FastScan system. A silicon tip mounted on a silicon nitride cantilever was used for the measurements. The scan of each sample was carried out for an area ranging from 1×1 to $5 \times 5 \mu\text{m}^2$ with a frequency range of 1-1.5 Hz. The images were analyzed using Nanoscope software (version 1.7). The material was characterized using Zeiss Merlin FE-SEM and FEI Talos for conventional TEM operating at 200 kV. The TEM diffraction pattern was indexed using JEMS software, and Gatan software was used to calculate the distance between planes.

4.5 Results and Discussion

We start by reporting the influence of growth parameters on the morphology and the composition of Zn_3P_2 grown on graphene. The variation of the V/II ratio could potentially lead to the formation of different compounds, such as ZnP_2 , Zn_3P_2 , and even intermediate amorphous compounds ($\text{a-Zn}_x\text{P}_y$) [84, 25]. The reported V/II ratio in this work corresponds to the ratio between the values of Zn and P_2 beam equivalent pressure (BEP), and the temperatures correspond to the manipulator temperature. Electron microscopy characterization of the initial stages of growth provides information on the morphology of the grown material. Figure 4.1(a-f) displays the scanning electron microscopy (SEM) images of Zn_3P_2 samples obtained at different temperatures and V/II ratios. The effect of the V/II ratio at 150°C is shown in the SEM micrographs of Figure 4.1(a-c). For $\text{V/II} \geq 2.30$, the morphology of the grown material is spherical with no distinct crystal facets. When the V/II ratio is maintained between 1.30 and 1.70, we observe a change in morphology. Crystalline triangular flakes are formed on graphene. These triangular flakes are not all randomly oriented on graphene, and some of them maintain a similar orientation as can be observed from the SEM images. When the V/II ratio is decreased to a value below 0.83, the triangular flakes change to a dense columnar-like growth. The influence of temperature on morphology at a given V/II ratio is shown in the SEM images of Figure 4.1(d-f). At temperatures $\leq 100^\circ\text{C}$, we observe irregularly shaped clusters with metal-like aggregates on top, as shown in Figure 4.1(d). As the temperature is increased to 150°C , crystalline triangular flakes start to appear. By further increasing the temperature to

180 °C, there is a substantial decrease in the growth rate, and the deposition is sparse. However, the triangular morphology is preserved at 180 °C. We attribute the drastic reduction in the growth rate at higher temperatures to the increased adatom desorption.

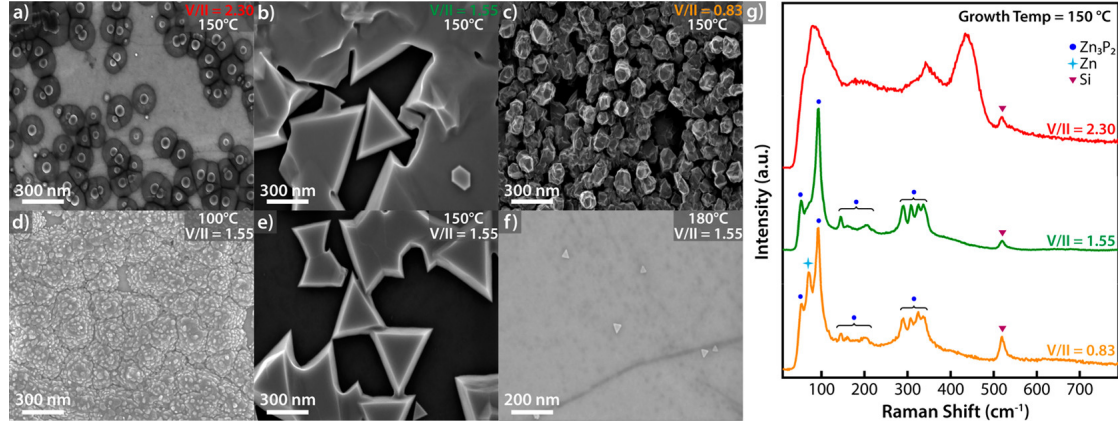


Figure 4.1: (a-f) Representative scanning electron micrographs of growths of Zn_3P_2 on graphene as a function of temperature and V/II ratio; (g) room temperature Raman spectra of samples shown in a-c, indicating that for V/II = 1.55 crystalline Zn_3P_2 is formed, while for lower V/II ratios crystalline zinc is found in addition, and for higher V/II ratios the material is amorphous.

Figure 4.1(g) presents the room temperature Raman spectra of the samples grown at 150 °C at three different V/II ratios. At a V/II ratio of 2.30, the Raman spectrum is composed of broad peaks. This is consistent with the amorphous nature of the material, which is evident from its morphology (Figure 4.1(a)). The Raman peaks become sharper for lower V/II ratios. The bands are located around the spectral zone where one would expect for $\alpha\text{-Zn}_3\text{P}_2$ [201, 176]. Both for V/II = 1.55 and 0.83, we observe a group of peaks in the range between 50 cm^{-1} and 380 cm^{-1} , with no first-order Raman active phonons present at wavenumbers higher than 380 cm^{-1} , similar to the reports from Pangilinan *et al.* for $\alpha\text{-Zn}_3\text{P}_2$ [201]. This demonstrates the formation of crystalline $\alpha\text{-Zn}_3\text{P}_2$ on graphene. For V/II = 0.83, we detect an additional peak at 71 cm^{-1} , which is related to the presence of crystalline Zn. The presence of Zn could explain the modification in the morphology of the sample, which could be due to the formation of Zn aggregates [194] (Figure 4.1(c)). The intensity of the Raman peak at 71 cm^{-1} increases when the V/II ratio is further lowered (see Supporting Information (SI) Section A, Figure A.1). The presence of Zn has been further confirmed by X-ray diffraction (XRD) measurements, as shown in Figure A.1. We find peaks corresponding to the (002) and (101) planes of Zn, along with the XRD peaks from crystalline $\alpha\text{-Zn}_3\text{P}_2$. At the given growth temperature, Zn has a low sticking coefficient on graphene [189, 98, 25]. However, the formation of Zn aggregates could imply that first a Zn_3P_2 layer is formed on graphene, which subsequently leads to the change in adsorption behavior of Zn. This explains the presence of both Zn and $\alpha\text{-Zn}_3\text{P}_2$ peaks in the Raman spectra and the XRD measurement. It is further corroborated by the SEM image shown in the inset of Figure A.2, and a clear Zn_3P_2 layer is present on top of which Zn aggregates are formed.

The growth window for crystalline $\alpha\text{-Zn}_3\text{P}_2$ on graphene is relatively narrow, unlike other semiconducting materials grown on graphene, which have robust growth conditions [2, 184]. The optimum temperature range is between 150 and 170 °C, with an optimum V/II ratio between 1.3 and 1.7. An additional dependence on the total flux was also observed (see SI, Section A, Figure A.3(a-c)). At the optimal temperature and V/II ratio, an increase in total flux leads to an expected increase in the overall growth rate; this is due to a higher surface adatom density, which causes an increase in nucleation density. Thus, the growth of Zn_3P_2 on graphene is susceptible to temperature, V/II, and total flux. All the studies reported hereafter are done on the samples grown at 150 °C with a V/II ratio of 1.55. The P_2 BEP was maintained at 7.50×10^{-7} Torr unless specified otherwise.

Figure 4.2(a) shows a representative top-view SEM image of the commercial monolayer graphene on SiO_2/Si wafer used in this work. The contrast in the image is related to the presence of grain boundaries, multilayers, wrinkles, and folds on graphene [296, 15, 148, 307]. Such features are common for graphene grown by CVD on a polycrystalline copper substrate [148, 172]. The defects on graphene play a critical role in adsorption, and nucleation of adatoms as the sticking coefficient of adatoms is significantly different at these sites [15, 95]. The nucleation probability of a new layer is higher at the defect sites than on pristine graphene due to their higher chemical reactivity [15, 315]. The growth on pristine graphene is highly suppressed due to the lack of dangling bonds [189]. Figure 4.2(b-c) elucidates the growth evolution of Zn_3P_2 on graphene substrate with time. As the growth progresses, the Zn_3P_2 flakes accumulate at the grain boundaries and other defect sites, which leads to the formation of compact islands with an irregular shape at these sites. At this stage of growth, the island formation tends to be sparse away from these defect sites, preserving the triangular shape of the flakes. The growth at the folds and grain boundaries on graphene traces their linear morphology [307]. In the case of multilayer graphene, the growth traces their patch-like morphology [318, 119, 39]. The defect sites have strikingly different growth behavior, as precursors exhibit a higher sticking coefficient at these sites [307, 289]. Overall, we find that the growth of Zn_3P_2 on commercial graphene is highly impacted by the defects, creating distinct growth regimes simultaneously on the same substrate. Figure 4.2(d) depicts our understanding of the growth mechanism of Zn_3P_2 on commercial graphene. The growth starts with the formation of small triangular flakes of Zn_3P_2 all over the substrate. With time, the nucleation density along the grain boundaries and other defect sites increases, which causes a preferential deposition of Zn_3P_2 . Eventually, the triangular flakes grow in dimension to form several micron large Zn_3P_2 islands. Finally, all Zn_3P_2 islands merge with one another, forming a compact continuous film with a coarse surface.

In order to determine the growth rate of Zn_3P_2 film, we performed a growth time series. SEM and atomic force microscopy (AFM) were used to study the vertical and lateral dimensions of the Zn_3P_2 triangular flakes as a function of time. Figure 4.2(e-g) corresponds to representative AFM images as a function of the growth time. In the early stages of growth, when the surface coverage is relatively low, the triangular flakes are well dispersed on the substrate, as illustrated in Figure 4.2(e). Some of the flakes are seen to merge mostly along the grain boundaries of

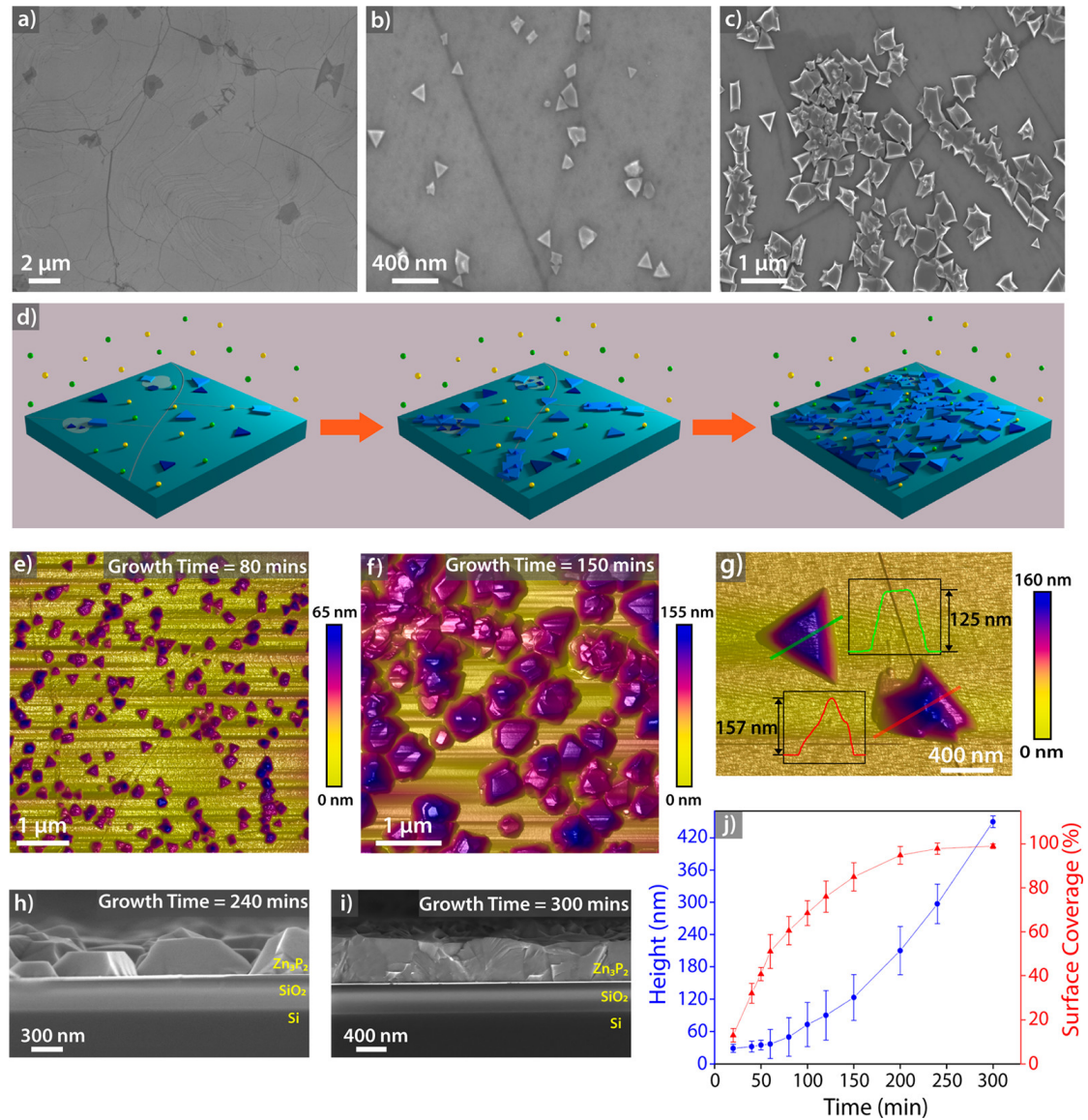


Figure 4.2: (a-c) SEM images of (a) commercial graphene, (b) Zn_3P_2 triangular flakes grown on graphene after growing for 20 min, and (c) Zn_3P_2 triangular flakes grown on graphene after growing for 90 min; (d) schematic representation of the growth evolution of Zn_3P_2 on graphene; (e-f) AFM images of Zn_3P_2 grown on graphene for (e) 80 min and (f) 150 min; (g) highlights two different morphologies of Zn_3P_2 grown on graphene; (h-i) cross-sectional SEM images of Zn_3P_2 grown on graphene for (h) 240 min and (i) 300 min; (j) plot showing the time evolution of the surface coverage (red triangular symbol) and vertical dimensions (blue circular symbol) of Zn_3P_2 flakes on graphene; the solid lines in the graph is a guide to the eye.

graphene. The average height of these flakes after 80 min of growth is 60 nm. The lateral dimension has a significant size distribution. For a longer duration of growth, the flakes start to lose its distinct triangular shape as they merge with the other neighboring flakes. The average height of the Zn_3P_2 flakes after 150 min growth is 130 nm. Figure 4.2(g) illustrates

the morphology of the top facet of the flake at two different growth sites. The Zn_3P_2 island deposited along the fold in graphene has an irregular base with a pyramid-like top facet (highlighted with a red line). The irregular base of the growing island is due to the merging of two or more triangular flakes in the initial phase of the growth. The pyramid-like facets are mainly observed on top of Zn_3P_2 islands and are denser at the folds, wrinkles, and defect sites. This type of growth behavior could be due to localized growth front pinning, which occurs at the contact point between two or more growing islands [158, 94] or could be attributed to interfacial dislocations [94, 74, 111]. In contrast, Zn_3P_2 growth away from the fold exhibits a triangular shape with a smooth top surface (highlighted with a green line). This illustrates the difference in the morphology of Zn_3P_2 islands based on their nucleation site.

For longer growth times, the height of the layers was determined by cross-section SEM, as shown in Figure 4.2(h-i). For a growth duration of 240 min, Zn_3P_2 islands were obtained with an average thickness of 300 nm (see Figure 4.2(h)). Finally, for a growth duration of 300 min and longer, the adjoining Zn_3P_2 islands merge to form a continuous film. The thickness of the film obtained for 300 min of growth time is 450 nm. The film surface is highly faceted, as seen in Figure 4.2(i).

The time evolution of surface coverage and vertical dimensions of the Zn_3P_2 flakes and islands is plotted in Figure 4.2(j). The error bars in the graph represent the broad size distribution of Zn_3P_2 flakes on graphene. We observe a dominant lateral growth at the initial stages of growth, which slows down over time, whereas the vertical growth rate increases significantly with time. For the first 20 min of growth, small triangular Zn_3P_2 flakes were observed with an average lateral dimension of 95 nm and an average height of 35 nm. After further 60 min of growth, the average lateral dimension changes to 200 nm, and the average vertical dimension changes to 60 nm. This indicates that, in the initial stages of growth when the surface coverage is low, the Zn_3P_2 flakes grow primarily laterally. This is due to the adatom kinetics: the adatom supply to the growing flakes is mainly by adsorption onto the graphene substrate followed by surface diffusion. As the migration energy barrier is low on graphene, the adatom can diffuse over a longer distance before being incorporated into an energetically favorable growing site [189, 98]. After 150 min of total growth time, the average lateral dimension is 530 nm, and the average vertical dimension is 130 nm. After an additional 60 min of growth, the average lateral dimension changes to 570 nm, and the vertical dimension changes to 235 nm. It is clear that at this stage of growth, the vertical growth rate is much higher in comparison to the lateral growth rate. Indeed, at a surface coverage of approximately 80%, a significant number of Zn_3P_2 islands merge or are closely spaced. Hence, for growth durations longer than 150 min, it is difficult to measure the lateral dimensions of individual Zn_3P_2 flakes. For longer growth durations, we compare the surface coverage with the vertical dimension of the islands. An 80% surface coverage is achieved in first 150 min; however, a further 150 min of growth is required to achieve 100% surface coverage. The significant slowdown of the lateral growth rate and the increase in vertical growth rate are primarily due to two reasons. First, at a growth stage with high surface coverage, most of the adatoms are incorporated directly onto the Zn_3P_2 islands, which have a higher absorption coefficient than graphene. And only a small fraction

of material is deposited into the trenches between these growing islands, thus increasing the vertical growth rate and slowing down the surface coverage. Second, an important factor that aids the vertical growth rate during the epitaxial growth of three-dimensional materials is the so-called Ehrlich-Schwoebel (ES) barrier [192, 214]. The ES barrier hinders the step-down diffusion of adatoms landing on a terrace [214]. The presence of ES barrier causes an accumulation of atoms on the top-facet of an island, which favors the vertical growth. One should note that there is a significant deviation in the growth rate at the grain boundaries, multilayer graphene, and other defect sites.

We believe the growth on graphene could be improved by suppressing nucleation density at the defect sites. This could be achieved by increasing the growth temperature or by decreasing the growth pressure. However, as mentioned before, the growth rate drops significantly by increasing the temperature from 150 to 180 °C. A similar effect is observed when the pressure is decreased. It is mainly because Zn and P have a very low sticking coefficient on graphene at elevated temperatures [189]. Alternatively, postgrowth annealing could be used to improve the grown film [247, 237]. However, it was reported by Bosco *et al.* that the desorption of Zn occurs at a temperature above 250 °C [25]. This limits the temperature range for annealing and hence compromises the quality of the film. In this work, we mainly focus on a one-step growth method, where a fixed temperature, V/II value, and total flux were used throughout the growth. We also attempted a two-step growth method [2]. Here, we induced first the nucleation at 150 °C and followed by a high-temperature growth step (190 °C). One should note, for the two-step growth, a negligible change in the Zn_3P_2 thin film was observed. And even after 300 min of growth, we did not obtain full coverage. Pyramidal top facets were observed for both one-step growth and two-step growth methods.

The X-ray diffraction (XRD) measurement done on the grown Zn_3P_2 film is shown in Figure 4.3(a). Four main peaks resolved at 13.54°, 27.10°, 41.09°, and 55.80° correspond to the reflections 101, 202, 303, and 404, respectively in the tetragonal phase of Zn_3P_2 . The indexing was done using the reference ICDD file no. 01-073-4212 [312]. Additionally, a low-intensity peak at 33.11° was observed, which is attributed to the substrate. The lattice parameters were calculated from profile fitting of the XRD peaks, and $a = 8.087 \text{ \AA}$ and $c = 11.43 \text{ \AA}$ were obtained, which gives a $c/a = 1.41$. This is very close to the reported bulk lattice parameter of Zn_3P_2 [312, 313]. The symmetrical θ - 2θ scan gives information on the planes that are parallel to the substrate surface. Only the peaks associated with the {101} family of planes are detected. This indicates that the Zn_3P_2 film has a preferential orientation parallel to the graphene surface. The film is thus highly textured and composed solely of the tetragonal Zn_3P_2 phase. These results were also confirmed by electron backscattered diffraction (EBSD) measurements, which showed the same preferential orientation with respect to the graphene substrate (see SI Section A, Figure A.4). EBSD measurements were performed on samples that were grown for a shorter period, with less than 60% surface coverage, whereas the XRD measurements were done on samples grown for a long period, with full surface coverage. Both samples gave the same directional dependence, indicating that the Zn_3P_2 islands maintain the same growth direction over time. Given the tetragonal crystal structure of Zn_3P_2 , the 3-fold symmetry of the

triangular flake can only be the result of a pseudosymmetry. Indeed, the Zn_3P_2 crystal structure is often defined as a pseudocubic crystal system [313], with c/a exactly equal to $\sqrt{2}$. When the tetragonal crystal system is transformed into the pseudocubic crystal system, the (101) plane is transformed to the (111) plane, which explains the morphology of the flakes. For a cubic system, the [111] 3-fold growth direction is the most common on a hexagonal (0001) substrate [185, 102, 240]. The van der Waals interaction between the grown Zn_3P_2 and graphene is confirmed by its crystallographic texture; as a (101) fiber texture is present, it indicates there is a complete degree of freedom on the rotation angle around the normal of the (101) plane of Zn_3P_2 , whereas a classical epitaxial relation would have resulted in a strict coherent orientation relationship of the grown material with the substrate. The Zn_3P_2 structure was further investigated using transmission electron microscopy (TEM), shown in Figure 4.3(b-c). For this, Zn_3P_2 flakes were transferred to a TEM grid by pressing the grid on the sample. A small force is required to remove them, due to the weak van der Waals forces attaching the flakes on the graphene. The flake exhibits a 3 nm thick native amorphous oxide at the surface. This native oxide is formed upon exposure to atmospheric conditions. Figure 4.3(d) shows a representative HRTEM micrograph. It reveals a defect-free single crystalline Zn_3P_2 triangular flake. From these measurements, we deduced the spacing between the (002) planes. We obtain 5.68 Å, which corresponds to $c = 11.36$ Å, which is in close agreement with the XRD results. The electron diffraction (Figure 4.3(e)) further confirms the single-crystalline nature of the Zn_3P_2 triangular flake. The diffraction pattern is in good agreement with the [210] zone axis of $\alpha\text{-Zn}_3\text{P}_2$.

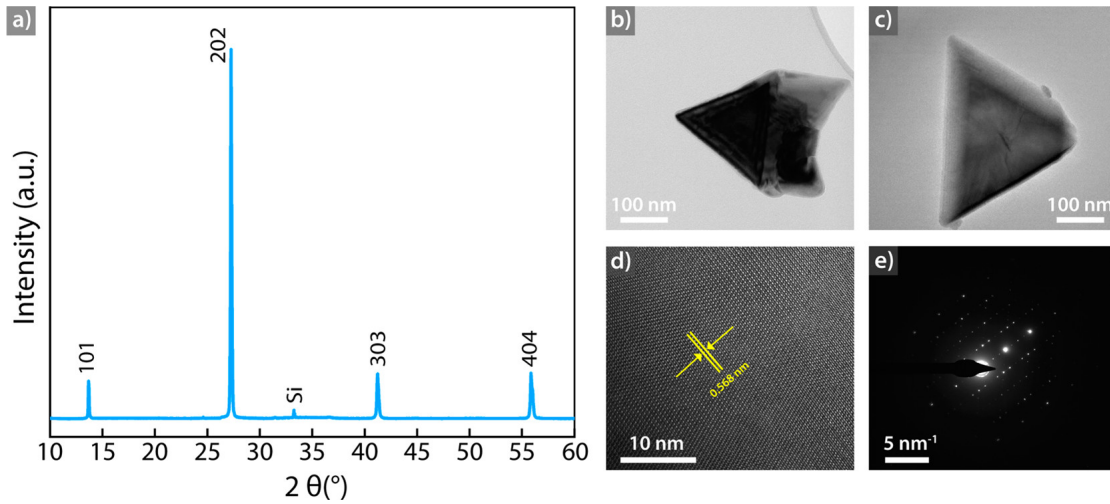


Figure 4.3: (a) XRD pattern of a Zn_3P_2 film showing the tetragonal structure and a preferential orientation. Only 101 family of planes are observed in the pattern; (b-c) Bright-field TEM images of the triangular Zn_3P_2 flake grown on graphene; (d) HRTEM image of the triangular Zn_3P_2 flake, showing a d-spacing of 0.568 nm; (e) electron diffraction pattern obtained from the Zn_3P_2 flake along the [210] zone axis.

Katsube *et al.* had previously demonstrated the fabrication of (101) oriented Zn_3P_2 film by phosphidation of Zn film [113]. They compared the electrical resistivity of the (101) oriented

Zn_3P_2 film with a differently oriented Zn_3P_2 film, and they observed the lowest resistivity for the (101) orientation. The vdWE of Zn_3P_2 on graphene is a phosphidation-free method to obtain the low resistive (101) orientated Zn_3P_2 film, which is beneficial for solar cell device fabrication.

The optical properties of Zn_3P_2 are of great interest, given the potential application in photovoltaics [21]. There has been a long-standing controversy regarding the fundamental gap of the material [207, 206]. Recently, a study done by Kimball *et al.* showed that there is a fundamental indirect bandgap at 1.38 eV and a direct bandgap at 1.50 eV [125]. The presence of both indirect and direct bandgap in close proximity is deemed beneficial in solar cell material, as the indirect bandgap could result in longer carrier lifetimes and diffusion lengths, whereas the close-lying direct bandgap could provide high photogeneration efficiencies. In order to understand the optical properties of Zn_3P_2 grown on graphene, we measured the PL response as a function of temperature and excitation power, as shown in Figure 4.4(a-h). In this study, we compared the PL response of two samples with different growth durations. Sample A was grown for 100 min (see Figure 4.4(a) inset), and sample B was grown for 250 min (see Figure 4.4(b) inset).

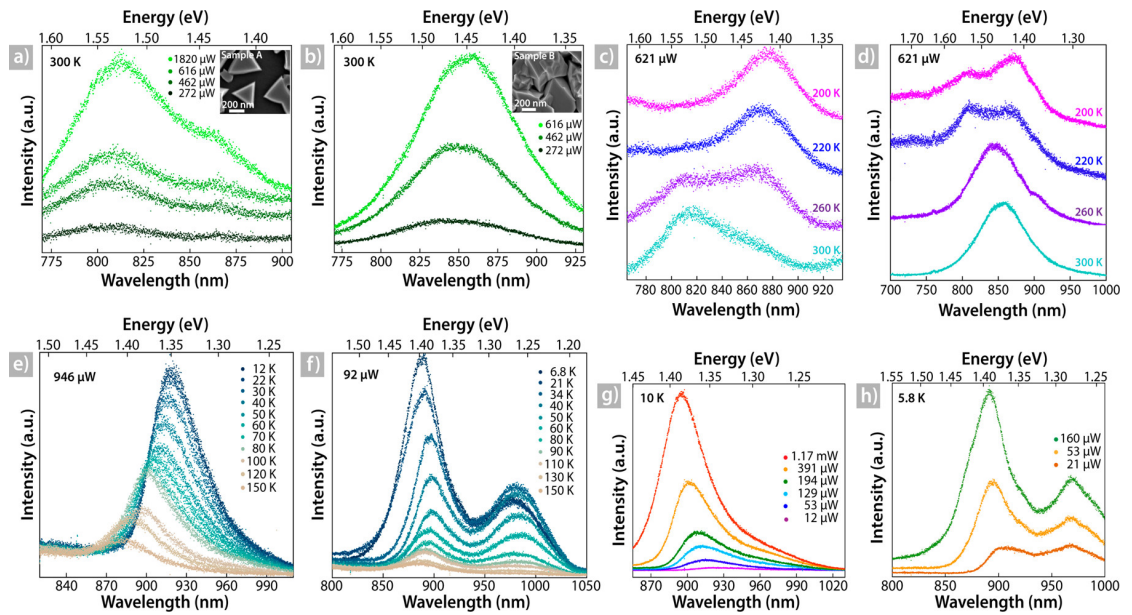


Figure 4.4: (a-b) PL spectra at room temperature excited with 633 nm illumination with different powers (a) of sample A, which is Zn_3P_2 grown on graphene for 100 min; inset shows the SEM image of sample A, (b) of sample B, which is Zn_3P_2 grown on graphene for 250 min; inset shows the SEM image of sample B; (c-d) PL spectra at temperatures from 300 to 200 K excited with 633 nm illumination at 621 μW of (c) sample A, and (d) sample B; (e-f) PL spectra done by decreasing the temperature below 200 K excited with 532 nm illumination (e) at 946 μW on sample A, and (f) at 92 μW on sample B; (g-h) PL spectra at cryogenic temperature using different powers (g) on sample A at 10 K excited with 633 nm illumination, and (h) on sample B at 5.8 K excited with 532 nm illumination.

Figure 4.4(a) demonstrates the room temperature PL response of sample A. At room temperature, we observe a broad PL peak centered at 1.52 eV and a lower energy shoulder at 1.42 eV. The peak positions does not change with the increase in laser power. The relation between the PL intensity and laser power is linear for the two peaks (see Figure A.5(a)), thus indicating a high density of states [239]. Figure 4.4(b) shows the room temperature PL response for sample B, and we observe a broad PL peak at 1.45 eV, which undergoes a slight redshift with increasing laser power. The PL emission could be a combination of peaks that behave differently upon increasing the laser power, which could potentially lead to the observed redshift.

Figure 4.4(c) depicts the PL spectra of sample A as a function of temperature. When the temperature is decreased from 300 to 200 K, the peak at 1.52 eV is quenched, whereas the shoulder peak at 1.42 eV becomes prominent. This behavior is attributed to the fact that at room temperature the thermal energy allows high-energy transitions. At lower temperatures, the high-energy transition is quenched, and the low-energy transition is favored [266]. The PL response is consistent with the study done by Kimball *et al.*, where they observed quenching of the peak at 1.5 eV around 200 K [125]. We additionally measured the power dependence PL of sample A at 200 K (see Figure A.5(b)); the peak position does not change with increasing laser power, and the peak has a tail in the high-energy side. Such power dependence and line shape of PL peak are indicative of band-to-band recombinations [80]. Figure 4.4(d) represents the PL spectra of sample B as a function of temperature. When the temperature is decreased from 300 to 260 K, the peak at 1.45 eV is blueshifted to 1.46 eV. However, an additional peak at 1.53 eV is observed when the temperature is decreased to 200 K, and the main peak is red-shifted to 1.42 eV. This behavior is strikingly different from PL emission observed by Kimball *et al.*, where they observed two distinct peaks only at temperatures above 250 K, and the peak at 1.5 eV was more prominent at higher temperatures [125].

Figure 4.4(e-f) shows the PL response as a function of temperature (below 200 K) for samples A and B, respectively. We observe a clear redshift when the temperature is decreased from 150 to 12.1 K for sample A, as shown in Figure 4.4(e). At 150 K, the peak is measured at 1.40 eV, which redshifts to 1.35 eV at 12.1 K. The redshift of the peak at lower temperatures has been previously reported by different groups [125, 28, 138]. The positive temperature coefficient of this peak has been previously speculated to be associated with an indirect transition to higher-lying energy states [138]. For sample B, we observed a similar redshift of the peak when the temperature is decreased from 200 to 50 K, as shown in Figure 4.4(f). The peak at 1.42 eV at 200 K redshifts to 1.38 eV at 50 K, whereas the peak at 1.52 eV undergoes a rapid quenching at low temperatures. Additionally, a second smaller peak at 1.26 eV becomes prominent at below 150 K (see Figure 4.4(f)). On further decreasing the temperature from 50 to 6.3 K, there is an observable blueshift of the main peak at 1.38-1.40 eV, which is similar to the work done by Briones *et al.*, where below 40 K, major emission bands with negative temperature coefficients emerge and are responsible for the intense PL signal [28]. The sample grown for shorter growth duration (sample A) lacks the low-temperature blue shift behavior reported by Briones *et al.* [28], but rather has a similar low-temperature response reported by Kimball *et al.* [125].

Figure 4.4(g-h) shows the cryogenic PL response as a function of laser power for the samples A and B, respectively. For both the samples at cryogenic temperatures, the PL signal exhibited a significant blueshift as the laser excitation intensity was increased, and this behavior has been previously reported by Briones *et al.* [28]. The peak at 1.26 eV present in sample B remains constant, and the intensity of the peaks saturates at a higher laser power (see Figure A.5(c)); the nonshifting behavior of the peak at 1.26 eV and its eventual saturation indicate it is a defect related transition [239].

Given the similarity between the PL study reported in the literature and sample A, we assign the room temperature PL peaks at 1.52 and 1.42 eV to direct and indirect transitions, respectively. Even though the low-temperature behavior of sample B is similar to the one reported by Briones *et al.* [28], the room temperature PL response is significantly different. The dissimilarity between the room temperature PL response of sample A and B is attributed to the presence of defects in sample B, which is evident by the presence of the defect peak at lower temperatures in sample B. Indeed, for a higher growth time and surface coverage, the probability of defect formation is higher in sample B.

4.6 Conclusions

In summary, we demonstrated the growth of high-quality crystalline Zn_3P_2 on graphene via vdWE using MBE. The growth on graphene is highly sensitive to the growth conditions, and the defects on graphene play an integral role in nucleation and growth. The growth mechanism was outlined by studying the temporal evolution of the Zn_3P_2 flakes. In the initial phase of the growth, lateral growth is more pronounced. In the later stages of growth, with the increase in areal coverage, there is a switch to dominant vertical growth. We attribute this change to the difference in adsorption and diffusion characteristics of the adatoms on graphene and on well-formed Zn_3P_2 layer (at higher areal coverage). XRD and EBSD revealed a preferential growth direction of Zn_3P_2 on graphene. The {101} family of planes were oriented parallel to the surface of graphene, and the preferential orientation was maintained irrespective of growth duration. The PL response of Zn_3P_2 on graphene as a function of temperature and power is consistent with the optical behavior reported in the literature for Zn_3P_2 grown using different techniques. We compared the PL response of two samples grown for different durations. The difference in the PL behavior between the two samples is attributed to the presence of defects in the sample grown for longer duration. This work demonstrates an efficient integration of an earth-abundant material on graphene, which could be used to fabricate earth-abundant semiconductors and graphene-based solar cells. Future work will be in the direction to improve the growth on van der Waals substrate by reducing the dependence of the growth behavior on the presence of defects on the substrate and to materialize earth-abundant semiconductor-based

4.7 Acknowledgments

Authors acknowledge funding from the SNF Consolidator Grant (BSCGI0-157705). Q.X. gratefully acknowledges the support from Ministry of Education by AcRF Tier1 grants (RG194/117). A.G.d.A. gratefully acknowledges the financial support of the Presidential Postdoctoral Fellowship program of the Nanyang Technological University.

5 Zn/P ratio and microstructure defines carrier density and electrical transport mechanism in earth-abundant $\text{Zn}_{3-x}\text{P}_{2+y}$ thin films

5.1 Accompanying information

This work is a collaborative effort that is under preparation for submission to a peer-reviewed journal. The list of authors is as follows: Rajrupa Paul, Vanessa Conti, Mahdi Zamani, Simon Escobar-Steinvall, Héctor Sánchez-Martín, Carlotta Gastaldi, Mihai Adrian Ionescu, Ignacio Iñiquez-de-la-Torre, Mirjana Dimitrievska, Valerio Piazza, Anna Fontcuberta i Morral. My contributions to this work include device fabrication, data acquisition, data analysis, and writing the manuscript.

5.2 Abstract

Scalable and sustainable photovoltaic technology requires low-cost and earth-abundant semiconducting materials. Zinc phosphide is purported to be an absorber material with optimal photovoltaic properties. Herein we report the electrical properties of Zn_3P_2 thin films with different crystallinity grown on InP substrates. The room temperature electrical resistivity of the as-grown single crystal thin films was in the range of 42–1050 Ωcm . We correlate the crystalline quality and composition to the electrical properties. The capacitance-voltage measurements and the secondary ion mass spectroscopy demonstrate the direct correlation between the carrier concentration and the Zn/P ratio. The highest hole mobility value (125 cm^2/Vs) was obtained from high-quality single crystalline Zn_3P_2 thin films. The electrical characteristics of the heterojunction between the thin film and the substrate were also illustrated. This work sheds light on the electrical properties and conduction mechanism, thus providing a better understanding of the limitations and potentials of the electrical devices related to the material.

5.3 Introduction

A sustainable approach to large-scale deployment of photovoltaic technology must involve the utilization of earth-abundant solar cell materials. These materials can further reduce the cost associated with the terrestrial installation of solar cells, thus encouraging wide-scale deployment. Zinc phosphide (Zn_3P_2) is an earth-abundant photovoltaic absorber material with promising photovoltaic properties [261, 70, 72, 177]. It exhibits a direct bandgap around 1.50 eV and a high absorption coefficient (10^4 - 10^5 cm^{-1}) in the visible light range near the band edge [63, 269, 210, 209, 176, 125, 203]. Additionally, it has a long minority carrier diffusion length (5-10 μm) and electrically passive grain boundaries. All these characteristics are beneficial for its use in photovoltaic devices [300, 25, 20, 265]. The highest reported efficiency for Zn_3P_2 -based solar cells is just about 6%, demonstrated for Mg/ Zn_3P_2 Schottky junction solar cells by Catalano *et al.* in 1979 [36]. A major limitation of Zn_3P_2 -based solar cells is the lack of controllability on the doping in the material.

Zn_3P_2 is intrinsically p-type in nature due to the low formation energies of the Zn vacancies and P interstitials, which act as p-type dopants [61, 251, 256, 160, 264]. Previous studies have shown growth conditions play an integral role in the electrical properties of the samples [25, 35, 109]. The reported hole mobility values lie in the range of 10-300 cm^2/Vs at 300 K for Zn_3P_2 thin films [25, 264, 35, 109, 140, 122, 287]. Suda *et al.* reported a hole mobility value of 310 cm^2/Vs for epitaxial Zn_3P_2 thin films grown on GaAs (001) substrates [264]. In contrast, epitaxial thin films synthesized by Bosco *et al.* exhibited hole mobility values of 10-45 cm^2/Vs . For similar hole concentrations ($\sim 4 \times 10^{16} \text{ cm}^{-3}$) [25], the discrepancy in the hole mobility arises due to the difference in resistivity of the samples, which could be caused by the difference in the local microstructure and defect density of the samples. These are largely dependent on the growth technique, growth condition, and thermal history. A large variation has been observed in the room temperature resistivity of Zn_3P_2 thin films, resistivity values ranging from 0.1- $10^6 \Omega\text{cm}$ has been measured [265, 35, 124]. A systematic study on the effect of vapour composition during annealing showed the resistivity of the sample monotonically decreases with an increase in phosphorous partial pressure [35]. The corresponding Hall measurements showed an increase in the carrier concentrations (from 10^{12} to 10^{16} cm^{-3}) with no significant variation in mobility [35]. Thus, by regulating the composition of the vapour during growth or annealing, the p-type carrier concentration in Zn_3P_2 can be modified.

Doping the material n-type is challenging due to self-compensation by intrinsic acceptors. Studies indicate the introduction of the donor impurity is compensated by the formation of the intrinsic p-type defect in the crystal lattice [262, 114]. Only a few instances of n-type doping of Zn_3P_2 have been reported, Suda *et al.* demonstrated the n-type doping of Zn_3P_2 thin films epitaxially grown on GaAs substrates [262]. Their results indicate that the presence of excess Zn during growth can lead to n-type doping of the material. The reported room-temperature electron mobility values were in the range 3000-7000 cm^2/Vs and the carrier concentration values were in the range $3\text{-}9 \times 10^{10} \text{ cm}^{-3}$. Furthermore, the measured carrier concentration did not increase above a certain point instead Zn segregation occurred. Additionally, the

resistivity for the Zn_3P_2 epitaxial thin films was $\sim 10^3\text{-}10^4 \Omega\text{cm}$, the low carrier concentration and high resistivity are attributed to the self-compensation effect of Zn_3P_2 . Whereas, the electron mobility values reported by Katsube *et al.* for n-type doping of bulk Zn_3P_2 were $< 10 \text{ cm}^2/\text{Vs}$ [114]. Low carrier concentration values were measured even though the bulk dopant concentration was about 10^{20} cm^{-3} .

Despite the previous attempts, Zn_3P_2 still lacks a reliable n-type doping route. Additionally, the literature is sparse for extrinsic p-type doping of Zn_3P_2 . Even though there is a consensus about the intrinsic p-type nature of Zn_3P_2 , there is a wide variation in mobility and resistivity values for similar types of materials. We believe that the limited efficiency of Zn_3P_2 -based solar cells is largely due to the limited control of the electrical properties of the material, such as the minority carrier mobility and the carrier diffusion lengths. For a p-type absorber, the electrical behaviour of the minority carrier to a large extent determines the electrical performance of the solar cell. Furthermore, recently Stutz *et al.* have highlighted the compositional tolerance of the Zn_3P_2 tetragonal unit cell. Compound compositions largely off-stoichiometric do not imply significant changes in the material phase or crystalline quality [310]. Still, variations in composition would impact the transport properties of the material and should be investigated. In this work, we investigate the electrical properties of polycrystalline and monocrystalline Zn_3P_2 thin films grown on InP(100) substrates and correlate it to their chemical composition and microstructure. We demonstrate a device fabrication technique that circumvents challenges arising from micro-cracks present in monocrystalline thin films. We measure and compare the resistivity, carrier concentration, and mobility between polycrystalline and monocrystalline Zn_3P_2 thin films. Temperature-dependent measurements elucidated the defect states and their contribution to the transport in Zn_3P_2 thin films. We thus show that the growth conditions play a vital role in determining the electrical properties of the given thin films. Finally, we describe the junction behaviour between Zn_3P_2 and InP (n-, p-, and i-type), which gives an understanding of $\text{Zn}_3\text{P}_2/\text{InP}$ -based devices. Our study provides an insight into the influence of composition on the electrical behaviour of Zn_3P_2 thin films, which in turn can help bridge the gap between the structural quality and functionality of Zn_3P_2 and provide the base to improve Zn_3P_2 -based solar cell devices.

5.4 Experimental Details

5.4.1 Materials and devices

Zn_3P_2 thin films were grown on InP(100) substrates using molecular beam epitaxy (Veeco GENxplor MBE) system equipped with separate zinc and phosphorous sources. Prior to the growth, the substrate was degassed in the MBE in three steps. In the first two steps, the substrate was degassed at 150°C and 300°C for 2 hours. Followed by a third degassing step at 580°C under phosphorous beam equivalent pressure (BEP) $> 1 \times 10^{-6}$ Torr for 10 minutes (in the case of polycrystalline Zn_3P_2) and 30 minutes or higher (in the case of monocrystalline Zn_3P_2). During the growth, the substrate temperature was set in the range of $240\text{-}270^\circ\text{C}$.

Additionally, the BEP of zinc and phosphorous fluxes were set to control the Zn/P ratio between 1.5 and 0.72. The detailed growth method is explained in our previous paper [311]. To study the electrical properties of the as-grown monocrystalline Zn_3P_2 (mono- Zn_3P_2) and polycrystalline Zn_3P_2 (poly- Zn_3P_2) thin films, different electrical devices were fabricated on the samples. These devices include structures for Hall Effect measurements, transmission line measurements (TLM), and capacitance-voltage (C-V) circuits. Thin films grown on the undoped InP substrates were used for the investigation of charge transport in Zn_3P_2 . Whereas doped InP (both n-, p-type) and undoped (i-type) InP substrates were used to examine the current-voltage characteristic of Zn_3P_2 /InP heterojunction.

Figure 5.1(a) shows the schematic representation of the fabrication steps. First, a 30 nm of Si_3N_4 is deposited on the Zn_3P_2 thin film using a plasma-enhanced chemical vapour deposition (PECVD) system. A first electron beam lithography (EBL) step defines the alignment markers, which are settled by metal (Cr/Au) sputtering. In the second EBL step, the device structures were defined and a subsequent reactive ion etching (RIE) step was performed to remove the Si_3N_4 from the defined structures. The hall bars were fabricated with varying dimensions (the lengths of the hall bars were in the range of 50-100 μm while keeping the geometrical proportions constant) to accommodate the micro-cracks that are present in some of the mono- Zn_3P_2 samples (as shown in SI Section B, Figure B.1). A final EBL step was performed to pattern the micro-contacts and subsequently, the contacts were deposited using sputtering. For fabricating the Ohmic contacts, Au, Ag, or Pt was used, as these metals showed linear behaviour with Zn_3P_2 (as shown in SI Section B, Figure B.2). Prior to any metal deposition, 30-45 seconds of Ar milling was done to remove the native oxide of the Zn_3P_2 to ensure good contact quality. Finally, for the hall bars, the devices were electrically isolated from the surrounding thin film using focused ion beam (FIB) milling. This approach allows to probe the charge transport via parallel and perpendicular paths in samples containing micro-cracks without the need for correction factors required in the Van der Pauw approach for non-uniform continuous films [222]. For the sake of comparison, the same approach has been used for the poly- Zn_3P_2 sample although no micro-cracks were observed. Figure 5.1(b) shows the SEM micrograph of the final device fabricated on the mono- Zn_3P_2 thin film. The processing of the structures for TLM and C-V measurements remains the same, except for the FIB milling. The C-V measurements were done in a planar configuration utilizing Schottky and Ohmic contacts. Sputtered Al was used as the Schottky contact. The distance between the Schottky and the Ohmic pads was varied from 1-1000 μm , to identify the parasitic effects arising from this configuration.

5.4.2 Characterization

The morphology of the thin films was characterized using a scanning electron microscope (Zeiss Merlin FE-SEM). The crystallinity and orientation were measured using out-of-plane diffraction on a Bruker D8 Discover Plus equipped with a Cu ($\text{K}\alpha$) rotating anode X-ray source (1.54 \AA). Out-of-plane scans were performed using Dectris Eiger2 500 K detector in 2D scan-

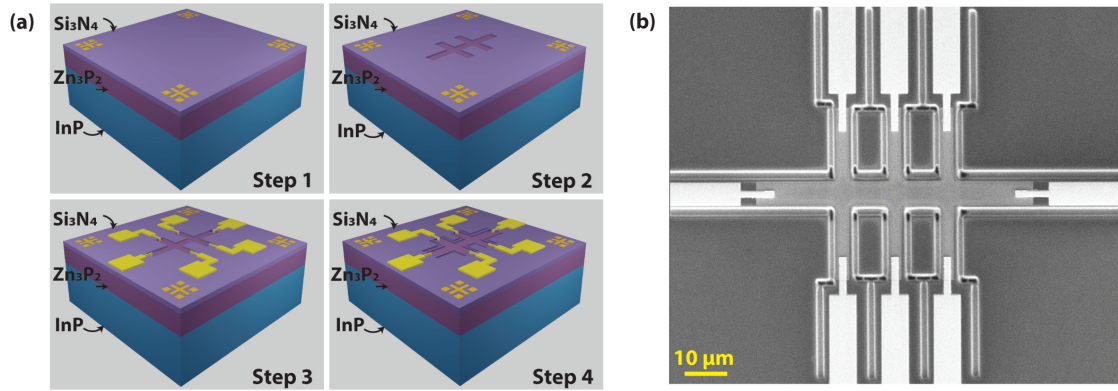


Figure 5.1: Fabrication process of the electrical device on Zn_3P_2 thin films: (a) schematic representation of the device fabrication steps, (step 1) alignment marker definition, (step 2) hall bar definition after the second EBL and RIE process, (step 3) contact deposition using sputtering after the third EBL process, (step 4) isolation of the device using FIB milling. (b) SEM image of the final device.

ning mode (gamma coverage of approximately 30 °), and conditioning the primary beam with a focusing mirror and collimating optics of 0.5 mm. The Secondary Ion Mass Spectroscopy (SIMS) was carried out by Eurofins EAG laboratories. PHI Model 6600 Quadrupole Secondary Ion Mass Spectrometer was utilized to determine the concentration distribution of Zn_3P_2 and InP layers qualitatively, using ion implant standards with known concentrations for approximation. In quadrupole SIMS, Cs^+ is used as the primary beam and the molecular ions (CsE^+) of Cs and the ions of interest are counted in the quadrupole SIMS mass analyzer. The TLM and the current-voltage (I-V) measurements were done using a Keithley 6487 voltage source and picoammeter to apply voltage and measure the current. The voltage sweep range was between ± 2 V. For 4-point measurements, a Keithley 6517A nanovoltmeter was used to measure the voltage. Temperature-dependent I-V measurements were done using LakeShore CRX-VF cryogenic probe station, connected to a Keithley SCS 4200 used as amperemeter and voltmeter. Four continuously variable temperature (ZN50R-CVT) probes allow the measurement of temperature sweeps without the need to lift and re-position the probes, the 336 controller adjusts the temperature. Hall effect and temperature-dependent measurements were done using a physical property measurement system (PPMS ®DynaCoolTM by Quantum Design). The measurements can be carried out in a cryogenic temperature range and the built-in cryopump ensures high vacuum applications ($< 10^{-4}$ Torr). The excitation current was varied in the range of 0.1 μA to 1 μA and the magnetic field was swept in the range ± 5 T. All the C-V measurements have been performed at room temperature under ambient conditions, a conventional semiconductor parameter analyzers and electrical probes were used (Keithley 4200A-SCS). The DC voltage was set in the range of ± 2 V and the AC signal had a frequency of 1-2 MHz with a 30-50 mV amplitude.

5.5 Results and Discussion

5.5.1 Structural properties of Zn_3P_2 thin films

We start by elucidating the structural differences between mono- Zn_3P_2 and poly- Zn_3P_2 thin films. Figure 5.2(a-b) show the representative SEM cross-section micrographs of the mono- Zn_3P_2 and poly- Zn_3P_2 thin film, respectively. The thickness of both thin films is $\sim 1\ \mu\text{m}$. The cross-sectional morphology of the poly- Zn_3P_2 thin film is granulated and it has a columnar-like growth perpendicular to the substrate. The top surface of the poly- Zn_3P_2 thin film is distinctly rough. Whereas, the mono- Zn_3P_2 thin film has a smooth cross-sectional morphology and relatively flat top surface. To identify the crystallographic growth direction and the relation with the substrate, out-of-plane scans were performed with an area detector using X-ray scattering. Figure 5.2(c) show the resulting image of bare InP(100) substrate, where only the reflections associated with the (200) and (400) planes are observed. Additionally, the intensity is concentrated in the spots, which is indicative of its highly ordered crystalline nature [168]. Figure 5.2(d-e) show the out-of-plane scans of mono- Zn_3P_2 and poly- Zn_3P_2 thin films, respectively. The reflections associated with the (002), (004), and (006) planes are observed for the mono- Zn_3P_2 thin film. Thus indicating the growth proceeds along the [001] direction and the epitaxial relation with the InP(100) substrate. Whereas the poly- Zn_3P_2 thin film has textured growth, we observe a few different families of planes perpendicular to the growth direction. More prominent growth planes observed in X-ray scattering are (101), (201), and (200). Finally, we also investigate the compositional variation between the different crystalline thin films. SIMS measurements demonstrate a clear distinction in the composition between mono- Zn_3P_2 and poly- Zn_3P_2 . The Zn/P ratio for the mono- Zn_3P_2 sample is ~ 1.47 , which indicates the sample is slightly off-stoichiometric (as shown in Figure 5.2(f)). Whereas the Zn/P ratio for the poly- Zn_3P_2 sample is ~ 1.64 , indicating the sample is Zn rich (as shown in Figure 5.2(g)). Additionally, the interface between the thin film and the substrate is sharp and well-defined for both samples. It is important to note that we do observe a compositional variation among different samples. This variation is attributed to the growth conditions (such as temperature and flux), while the difference in crystallinity is mainly due to the degassing process [311]. In general, most of the poly- Zn_3P_2 thin films have a Zn/P ratio > 1.5 . Whereas, the mono- Zn_3P_2 thin films have a Zn/P ratio ≤ 1.5 . Table 5.1 contains an overview of the samples used in this study along with the characterization results obtained in this study; hereon the sample name will be used to refer to a specific sample.

5.5.2 Electrical Measurements

The understanding of the material's fundamental properties establishes the first step toward the achievement of functional devices. TLM measurements were performed to gain insight into the resistivity of the mono- Zn_3P_2 and poly- Zn_3P_2 thin films. Representative results of these measurements of different samples are outlined in Figure 5.3, and resistivity values are reported in Table 5.1. Figure 5.3(a) shows an optical microscope image of a typical device.

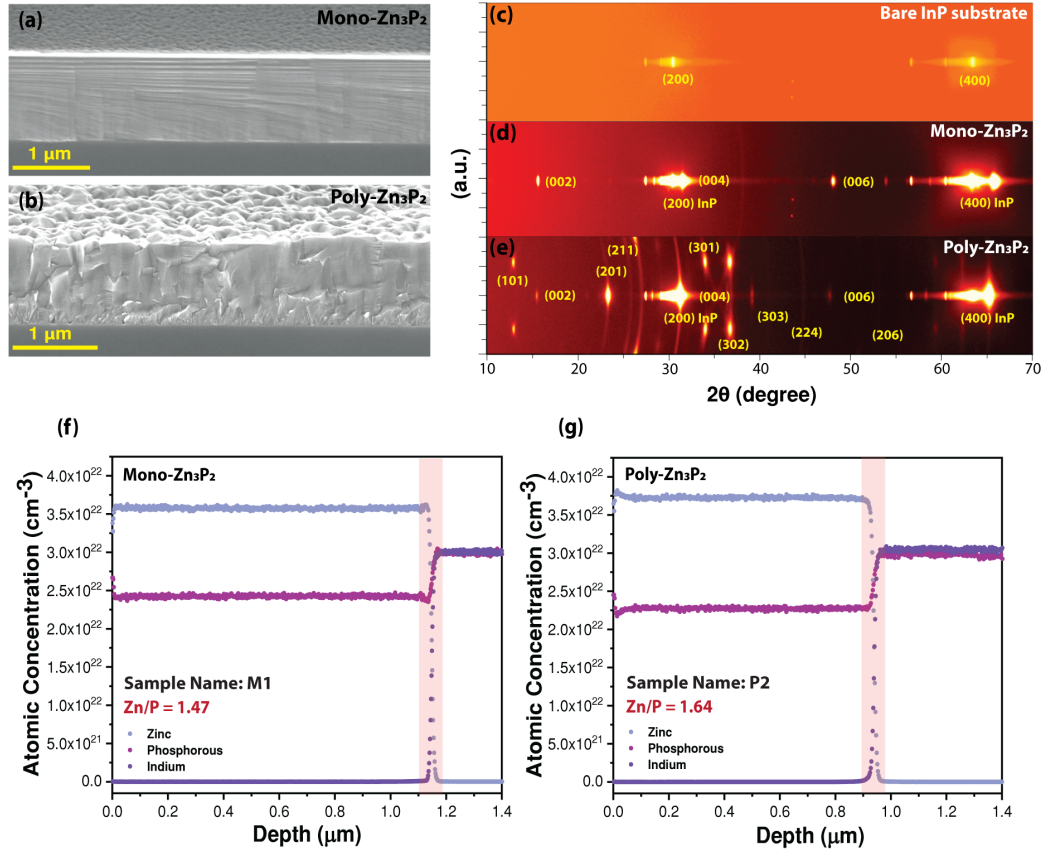


Figure 5.2: Cross-sectional SEM micrographs of the (a) monocrystalline Zn_3P_2 thin film (b) polycrystalline Zn_3P_2 thin film. Out-of-plane diffraction from (c) InP (100) substrate (d) monocrystalline Zn_3P_2 thin film showing only the 00h family of planes (e) polycrystalline Zn_3P_2 thin film showing a textured growth. SIMS measurements from (f) monocrystalline Zn_3P_2 thin film (M1) with Zn/P ratio ~ 1.47 (g) polycrystalline Zn_3P_2 thin film (P2) with Zn/P ratio ~ 1.64 .

It is constituted by a series of multiple electrical contacts with increasing distances. The smallest spacing between two adjacent contact pads is 30 μm . The total resistance (R_{TOT}) between two metal contact pads is measured as a function of the distance between two contact pads. It is given by $R_{TOT} = 2R_M + 2R_C + R_S$, where R_M is the resistance of the metal, R_C is the contact resistance, and R_S is the resistance of the material between the electrical pads. As the R_M value is relatively smaller than the other terms, it can be neglected. Figure 5.3(b-c) show the TLM plots obtained from thin film samples M1 and P2 grown on i-InP substrates, respectively. The resistance increases linearly as a function of length, as expected. The contact resistance ($2R_C$) is obtained from the y-intercept of the plot of the linear fit. The estimated contact resistivity from the TLM plots is $0.95 \pm 0.4 \Omega\text{cm}^2$ for M1 and $0.63 \pm 0.05 \text{ k}\Omega\text{cm}^2$ for P2. The contact resistivity value obtained from M1 is in the same range as previously reported

Table 5.1: Measured sample names with corresponding substrate type, crystallinity, Zn/P ratio, resistivity, and carrier concentration.

Sample Name	Substrate Type	Crystallinity	Zn/P	Resistivity (Ωcm)	Carrier Concentration (cm^{-3})
M0	n-InP	Monocrystalline	1.164	51.6 ± 5.0	$(1.22 \pm 0.19) \times 10^{19}$
M1	i-InP	Monocrystalline	1.469	154.6 ± 10.7	$(4.03 \pm 0.31) \times 10^{15}$
M2	n-InP	Monocrystalline	1.474	42.6 ± 9.8	$(4.00 \pm 0.23) \times 10^{15}$
M3	n-InP	Monocrystalline	1.502	44.9 ± 3.7	$(1.09 \pm 0.11) \times 10^{15}$
M4	i-InP	Monocrystalline	1.578	1050 ± 263	$(1.17 \pm 0.95) \times 10^{14}$
P1	i-InP	Polycrystalline	1.610	8794 ± 350	$(1.06 \pm 0.15) \times 10^{13}$
P2	i-InP	Polycrystalline	1.642	6632 ± 421	$(3.84 \pm 0.33) \times 10^{13}$

values of as-deposited Au contacts on Zn_3P_2 [287]. It should be noted that we did not observe any significant reduction of the contact resistance when using other metals such as Ag, Pt, and Zn/Au. Thermal treatments are often used for reducing contact resistance. We did not apply any thermal treatment in this study as post-growth annealing could affect the thin film composition by desorption of Zn [203, 25]. The resistivities obtained from the poly- Zn_3P_2 (P1 and P2) thin films were in the range of 6500-9000 Ωcm . Whereas the resistivities obtained from the mono- Zn_3P_2 (M1 and M4) thin films were in the range of 150-1050 Ωcm . The vast difference in resistivity value is attributed to the presence of grain boundaries in the poly- Zn_3P_2 thin films, which could contribute to increased scattering of the charge carriers. Figure 5.3(d) shows the TLM data obtained from M3, which is a mono- Zn_3P_2 thin film grown on n-type InP substrates. The TLM characteristics of the mono- Zn_3P_2 thin film grown on n-InP are distinctly different from the mono- Zn_3P_2 grown on i-InP. Two distinct slopes can be observed from the plot, the first slope (depicted by the red dashed line) can be assigned to the Zn_3P_2 thin film. Whereas the second slope (depicted by the blue dashed line) is attributed to the flow of current into the substrate. The change in the TLM slope is accompanied by a change from linear to non-linear I-V curves (as shown in SI Section B, Figure B.3). The change occurs when the distance between two contact pads increases over 100 μm . We attribute the non-linearity of the I-V curves to the current crossing the heterojunction. In contrast, the I-V curves obtained from the (poly-and mono-) Zn_3P_2 on i-InP are linear irrespective of the distance between the two contact pads (as shown in SI Section B, Figure B.2). The junction behaviour between the Zn_3P_2 and n-InP plays an integral role in the leakage current, over a critical distance of 100 μm leakage current dominates. We will highlight this behaviour in the later section when we describe the junction properties between Zn_3P_2 thin film and differently doped InP substrate. A resistivity value of $\sim 45 \Omega\text{cm}$ was obtained on fitting the first slope of the TLM and the contact resistivity value of $0.6 \pm 0.17 \Omega\text{cm}^2$ was obtained. These values are in good agreement with the values obtained from the mono- Zn_3P_2 thin films grown on the i-InP substrate. Thus, indicating the first slope of the TLM plot provides information regarding the thin film. From here on, we discuss the electric properties of the thin films grown on i-InP, unless specified otherwise.

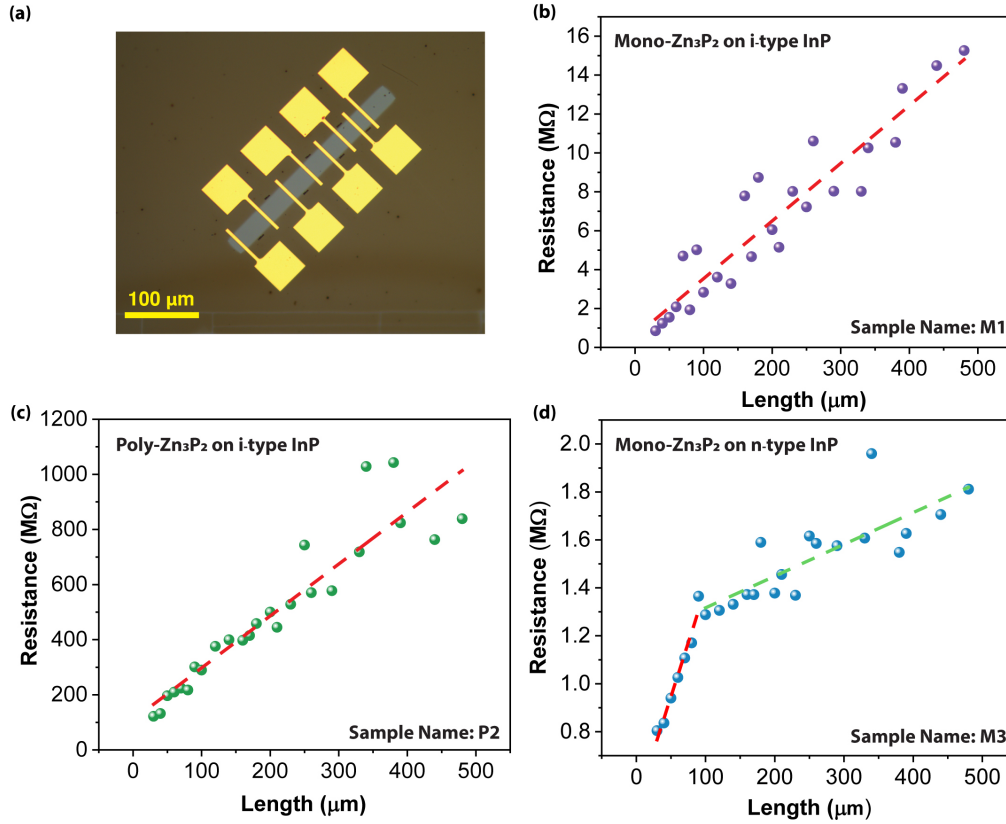


Figure 5.3: (a) Optical image of the TLM structure used for the measurements. TLM plots showing resistance as a function of the length, obtained from (a) monocrystalline Zn_3P_2 thin film (M1) (b) polycrystalline Zn_3P_2 thin film (P2), on i-InP (100) substrates (c) monocrystalline Zn_3P_2 thin film on n-InP (100) substrate (M3).

We now turn to the temperature dependence of the conductivity for different samples, in view of further understanding of the electrical transport properties of Zn_3P_2 . Figure 5.4(a-b) depict the dependence of resistivity with temperature for M1 and P2, respectively, over a range of 100 to 300 K. The resistivity of the thin films increases as the temperature decreases, in agreement with the semiconducting nature of the material. The increase in resistivity for P2 over a 200 K decrease in temperature is significantly steeper than the M1. The temperature dependence of resistivity gives insight into the conduction mechanism in a material. Thermally activated band conduction in semiconductors is described by an Arrhenius temperature dependence, given by [7, 136]:

$$\sigma(T) = \sigma_0 e^{\frac{-E_a}{k_B T}} \quad (5.1)$$

where σ_0 is a constant, E_a is the activation energy, and k_B is the Boltzmann constant. Given the exponential relation between thermally activated conduction and temperature, a linear

line can be obtained by plotting $\ln \sigma$ vs $1/T$ or $\ln \rho$ vs $1/T$. The insets in Figure 5.4(a-b) show the plot of $\ln \rho$ vs $1/T$, on fitting Eq. 5.1 to the experimental data we obtain a good fit for higher temperature values. For the temperature range of 150 to 300 K, the activation energy obtained for M1 is 22.53 meV. This value is consistent with the energy levels expected for phosphorus interstitial levels in bulk Zn_3P_2 . Both phosphorous interstitials and zinc vacancies act as acceptors in Zn_3P_2 , typically zinc vacancies have energy levels ranging from 190 meV to 290 meV and phosphorous interstitials have energy levels ranging from 14 meV to 90 meV [251, 160, 310, 174]. For temperature values less than 150 K we observe a gradual decrease in resistivity, this is due to the interplay of temperature variations of the carrier density and mobility. The carrier density diminishes with a decrease in temperature while the mobility increases, thus the resistivity has a minimum typically around 70 K [90]. The activation energy obtained from P2 was 317.69 meV for the temperature range of 200 to 300 K. This activation energy is slightly higher than the expected energy level for zinc vacancy levels [160]. The activation energy value could be due to the presence of crystalline disorder in the polycrystalline thin film. Still, one should note that the activation energy in the thermally activated conduction regime depends on the carrier concentration and the impurity energy levels [136]. A decrease in carrier concentration due to a lower amount of acceptors would lead to an increase in the activation energy due to the change in the Fermi level. At temperatures below 200 K, a distinct change in the slope of the $\ln \rho$ vs $1/T$ plot is observed, indicating a change in the conduction mechanism. A hypothesis is that at lower temperatures, holes are recaptured by the acceptors and hopping starts to be the dominating mechanism. There are two types of hopping mechanisms that dominate the conduction process in semiconductors at lower temperature ranges, which are Nearest-Neighbor Hopping (NNH) and Variable Range Hopping (VRH) [7, 136, 227, 171, 17]. NNH and VRH can coexist in a material, however, NNH usually tends to dominate at higher temperatures. In NNH, the holes hop to the nearest-neighbour vacant site and this requires a thermal activation. The activation energy for NNH is much lower than the activation energy for thermally activated band conduction. For the NNH conduction, temperature and conductivity have a similar exponential dependence [7]. We fitted the temperature dependence of the resistivity in the range between 100 to 200 K and an activation energy value of 14.72 meV was obtained. On further decreasing the temperature, the VRH conduction mechanism often comes into play. Here charge carriers hop between levels close to the Fermi level irrespective of their spatial distribution [170]. The plotted data ($\ln \rho$ vs $1/T$) does not show any deviation from linearity in the measured range (200-100 K). Therefore we conclude, that for the measured temperature range, we do not observe the VRH (for which conductivity can be expressed as $\sigma = \sigma_0 e^{-[\frac{T_0}{T}]^{\frac{1}{4}}}$, where T_0 is the characteristic temperature, and σ_0 is a constant parameter) conduction mechanism as this would lead to a non-linear behaviour [38]. It is evident that the thermally activated conduction mechanism dominates at higher temperatures (above 200 K for P2 and above 150 K for M1) for both thin films. Now we turn toward a specific sample (M4) that showed atypical I-V characteristics. Figure 5.4(c) shows the semi-logarithmic I-V plots measured at different temperatures for M4 (that has a high Zn/P ratio ~1.58). The typical I-V characteristic of mono- Zn_3P_2 and poly- Zn_3P_2 thin films are linear (as shown in SI Section B, Figure B.2). The I-V plots obtained from sample M4 show

a non-linear asymmetric behaviour and demonstrate a deviation from the ohmic or Schottky behaviour [90]. Furthermore, on decreasing the temperature, the overall current decreases and the deviation becomes more pronounced. To understand the electrical properties of the sample, the I-V characteristic in the forward bias is plotted in a log-log scale, as shown in Figure 5.4(d). The slope of the log-log plot gives the power dependence of current and voltage [57, 317]. At low voltages (below 0.2 V) an ohmic relation is observed between the current and voltage ($I \propto V$) over all the measured temperature ranges. Between the voltage ranges of 0.2 to 0.7 V, the slope changes to 8 for 300 K and 15 for 150 K ($I \propto V^m$, where m is the slope in the log-log plot). Whereas above 0.7 V the slope is 2 ($I \propto V^2$) for all the temperature ranges. We observe three distinct regimes in the log-log I-V plot: first, a low-voltage ohmic regime with a slope of 1, followed by a trap filling regime with a large slope (>2), and a high voltage space-charge-limited current (SCLC) regime with a slope of 2. The SCLC conduction mechanism has been widely reported for organic semiconductors and insulators [144, 233, 67, 271]. There are also some instances of SCLC conduction in inorganic semiconductors such as III-nitrides and semi-insulating II-V materials [253, 245]. The presence of trapping states caused by impurities and defects can capture and immobilize a fraction of the injected carriers, thereby influencing the current transport process. Zn_3P_2 is known to form band tails due to the presence of impurity levels [310] and deep-level traps at ~ 0.7 eV [251, 263]. Depending on the trap density and distribution, it might be feasible to observe SCLC conduction in Zn_3P_2 . The trap density can be calculated from the trap-filled-limit voltage, given by [144]:

$$V_{\text{TFL}} = \frac{qn_t L^2}{2\epsilon} \quad (5.2)$$

Where q is the elementary charge, n_t is the trap density, L is the thickness, and ϵ is the dielectric constant. The crossing point between the tangent of the SCLC regime and the trap-filled-limited regime is used as the V_{TFL} [144]. We estimated the trap density using Eq. 5.2, the obtained values were $3.62 \times 10^{13} \text{ cm}^{-3}$ and $4.28 \times 10^{13} \text{ cm}^{-3}$ for 300 and 150 K, respectively. SCLC measurements are often used to extract the mobility of the carrier, where the mobility value is extracted from the quadratic regime. However, the estimation of mobility is prone to misinterpretation [144, 141]. Given the asymmetric nature of the I-V plot, we decided not to use this method to extract the mobility values.

Hall effect measurements can be used to measure the carrier density. However, our measurements showed a non-linear transverse resistance behaviour (refer to SI Section B, Figure B.4 for more information). Therefore, the carrier concentrations in different thin films were analyzed using C-V measurements. Figure 5.5(a) shows the schematic representation of the planar configuration used for the measurements. The set-up consists of two adjacent dissimilar contacts, separated by a distance (L_t). The Au contact was ohmic, while the Al was Schottky. Figure 5.5(b-c) show $1/C^2$ against voltage, also known as the Mott-Schottky plot, for M1 and P2, respectively. The data display a negative Mott-Schottky slope, indicating a p-type conductivity for all the measured Zn_3P_2 thin films [92]. For a Schottky-diode under bias, the C-V relation

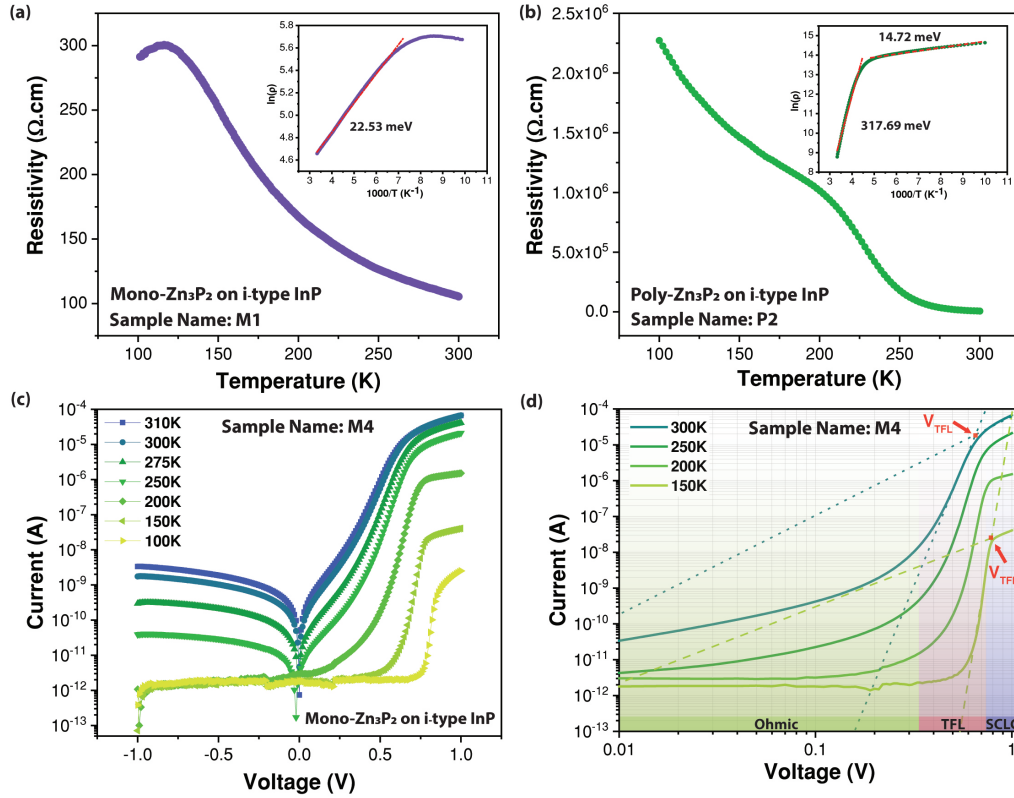


Figure 5.4: Temperature-dependent resistance plot showcasing the semiconducting behaviour of (a) monocrystalline Zn_3P_2 thin film (M1), and the corresponding fitting for thermally activated conduction (inset) (b) polycrystalline Zn_3P_2 thin film (P2), and the corresponding fitting for thermally activated conduction between 300-200 K and NNR between 200-100 K (inset). (c) Temperature-dependent I-V characteristics obtained from monocrystalline Zn_3P_2 thin film with a Zn/P ratio ~ 1.58 (M4) plotted on a semi-logarithmic scale (d) the corresponding temperature-dependent I-V characteristics plotted on a log-log scale, three distinct transport regions are visible : ($I \propto V$) ohmic region, ($I \propto V^m$, $m > 2$) TFL region, and ($I \propto V^2$) SCLC region, the dashed lines represent the tangents with slopes 2 and 8 used for determining V_{TFL} at 300 K and slopes 2 and 15 for determining V_{TFL} at 150 K

can be expressed as [246]:

$$\frac{A^2}{C^2} = \frac{2(V_{bi} - V - \frac{kT}{q})}{q\epsilon_s N} \quad (5.3)$$

where C is the capacitance, V_{bi} is the built-in potential of the diode, ϵ_s is the relative permittivity of Zn_3P_2 , A is the area of the anode, and N is the carrier concentration. The slope of the Mott-Schottky plot gives the carrier concentration and the x-axis intercept gives the V_{bi} . The carrier concentration for M1 was found to be $\sim 4.03 \times 10^{15} \text{ cm}^{-3}$, whereas the carrier

concentration of P2 was $\sim 3.84 \times 10^{13} \text{ cm}^{-3}$. We did not observe any significant variation in the carrier concentration arising from distance (L_t) variation between the contact pads (at least for the measured distances). While the carrier density difference between the monocrystalline and polycrystalline samples could eventually be attributed to the microstructure, one should consider chemical composition. Zn_3P_2 is an unusual compound semiconductor as the Zn/P ratio can deviate strongly from 3/2 without loss of the semiconductor functionality [70]. The temperature dependence of the samples has also hinted at a relation between the composition and the carrier density, as given by the different activation energy for the relatively zinc richer or poorer nature of samples M1 and P2. These activation energies could be related to zinc vacancies and phosphorous interstitials, which act as dopants in the material.

The compositional analysis performed using SIMS was correlated with the carrier density obtained from the capacitance method (see Table 5.1). The results are presented in Figure 5.5(d). The carrier concentration ($\sim 1.22 \times 10^{19} \text{ cm}^{-3}$) is highest for M0 that has a Zn/P = 1.16. The carrier concentration strongly decreases for Zn/P ratios approaching 1.5. The sample M3 that is almost at stoichiometry (Zn/P = 1.502) has a carrier concentration of $\sim 1.09 \times 10^{15} \text{ cm}^{-3}$. For Zn/P > 1.5 carrier densities are extremely low, below $\sim 1.5 \times 10^{14} \text{ cm}^{-3}$. The measured carrier concentrations as a function of the Zn/P ratio for different samples follow an exponential behaviour. To further confirm this, Figure 5.5(d) inset depicts the data in a semi-logarithmic scale, which displays the linear behaviour and shows the sample with the highest carrier concentration in the same plot. The role of chemical composition in carrier density can be found in the nature of interstitials in Zn_3P_2 . Phosphorus interstitials act as a p-type dopant with low formation energy in Zn_3P_2 [61, 306], thus explaining the increased carrier concentration in the samples with Zn/P less than 1.5. Instead, Zn inclusion in the lattice should act as an n-type dopant in Zn_3P_2 [306]. However, we do not observe n-type nature in any of the samples with a high Zn/P ratio. This is attributed to the prevalent self-compensation effect in Zn_3P_2 [114, 10]. Given the low formation energy of P interstitials, excess Zn in the material is compensated by the formation of P interstitials. This results in a decrease in the carrier concentration with an increase in the Zn/P ratio. Additionally, this also leads to higher resistivity in the sample [35]. The monocrystalline Zn_3P_2 thin film with a higher Zn/P ratio (M4) exhibits higher resistivity ($\sim 1050 \Omega \text{ cm}$) in comparison to the stoichiometric monocrystalline Zn_3P_2 thin film (M3) that has resistivity of $\sim 45 \Omega \text{ cm}$. We extract the mobility values using $\sigma = nq\mu$, where σ is the conductivity obtained from TLM, while n is the carrier concentration obtained from C-V profiling. For monocrystalline samples, the mobility values are in the range of 15-125 cm^2/Vs . Whereas for polycrystalline samples, the mobility values are in the range of 19-60 cm^2/Vs . The higher values of mobility obtained from the monocrystalline Zn_3P_2 thin films are among the upper bound of values reported in the literature for Zn_3P_2 [264, 286], thus indicating the high-quality crystalline Zn_3P_2 thin films.

Finally, we probe the junction behaviour between the Zn_3P_2 thin film and the InP substrate. Figure 5.6(a) inset shows the configuration used for the I-V measurements. Figure 5.6(a) shows the comparison of the I-V characteristics of mono- Zn_3P_2 and poly- Zn_3P_2 thin films grown on i-InP substrate. Both thin films have a rectifying behaviour. The current values obtained

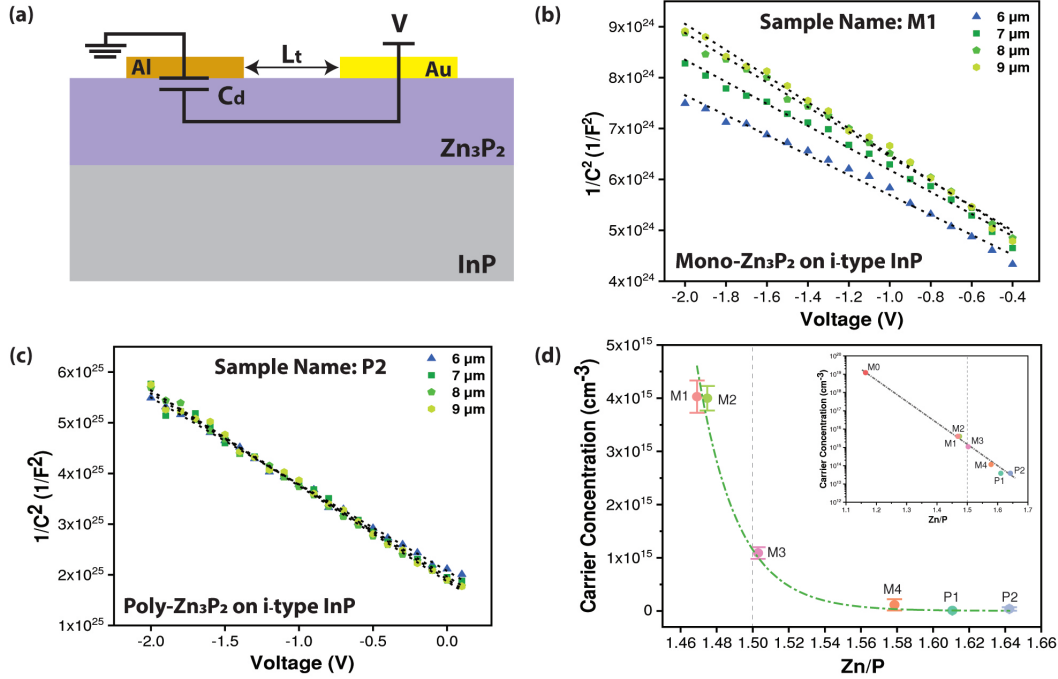


Figure 5.5: (a) Schematic representation of the planar configuration used for the C-V measurements, L_t is the distance between the Schottky and the ohmic contacts. The C-V plot obtained by varying L_t from (b) monocrystalline Zn₃P₂ thin film (M1) (c) polycrystalline Zn₃P₂ thin film (P2). (d) Plot showing the measured carrier concentration as a function of the Zn/P ratio (the error bars represent standard deviation due to L_t variation for each sample), the corresponding semi-logarithmic plot (inset) highlights the sample with the highest carrier concentration ($1.22 \times 10^{19} \text{ cm}^{-3}$) and lowest Zn/P (1.16) ratio. The stoichiometric Zn/P ratio is 1.5, represented by the dashed line. The details of the plotted sample are listed in Table 5.1

at higher voltages from mono-Zn₃P₂ are much higher in comparison to the poly-Zn₃P₂. We attribute the lower current value of the polycrystalline thin film to the high resistivity in the material. To better understand the influence of the doping in the InP on the junction behaviour we measure the I-V characteristic of Zn₃P₂ thin films grown on differently doped InP substrates. Figure 5.6(b) shows the semi-logarithmic plot of the I-V characteristic obtained from monocrystalline Zn₃P₂ thin films grown on (p-, n-, i-) InP and polycrystalline Zn₃P₂ grown on i-InP. The Zn₃P₂ thin film grown on p-InP illustrates a linear and symmetric behaviour, which is indicative of a poor diodic behaviour between the two p-type materials (theoretical band alignment between p-type Zn₃P₂ and p-type InP is shown in SI Section B, Figure B.5). When comparing the I-V characteristic of monocrystalline Zn₃P₂ on i-InP and n-InP we observe in the case of n-InP there is a large leakage current in the reverse bias. Additionally, the thin film grown on i-InP has a much greater threshold voltage value (0.68 V) in comparison to the thin film grown on n-InP (0.47 V). Moreover, the ideality factor obtained on fitting the linear part of the I-V plot was 2.03 ± 0.14 for thin film grown on i-InP and 3.46 ± 0.2 for thin

film grown on n-InP. These differences demonstrate the monocrystalline Zn_3P_2 thin film grown in i-InP has relatively better diode parameters than the ones on n-InP. Thus, the junction behaviour between monocrystalline Zn_3P_2 and n-InP corroborates the flow of current into the substrate during TLM measurements.

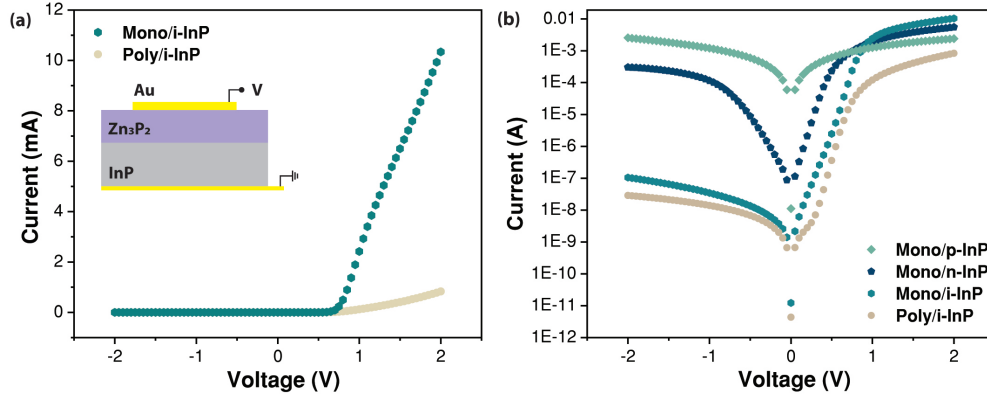


Figure 5.6: (a) I-V characteristic of the monocrystalline and polycrystalline Zn_3P_2 thin film grown on i-InP (100) substrate measured in a top-down configuration (inset). (b) Semi-logarithmic I-V curve obtained from monocrystalline Zn_3P_2 thin film grown on (p-, n-, i-) InP substrates and polycrystalline Zn_3P_2 thin film grown on i-InP.

5.6 Conclusion

In conclusion, we compared and contrasted the difference in the structural, compositional, and electrical behaviour between polycrystalline Zn_3P_2 and monocrystalline Zn_3P_2 thin films. We identified the conduction mechanism involved in different crystalline Zn_3P_2 thin films. Thermally activated conduction mechanism dominates at higher temperatures, whereas nearest-neighbour hopping mechanism was observed for polycrystalline thin films at lower temperatures. The corresponding activation energies obtained from our measurements are primarily associated with the phosphorous interstitials in the monocrystalline sample. Temperature-dependent I-V characteristic of Zn_3P_2 thin film with low carrier concentration revealed the occurrence of SCLC transport. High-quality monocrystalline Zn_3P_2 thin films with moderate carrier concentration demonstrated a high hole mobility ($125 \text{ cm}^2/\text{Vs}$) at room temperature, indicating the growth conditions and composition of the material play an integral role in tuning the material functionality. We unveiled the impact of unintentional doping caused due to changes in the Zn/P ratio on the electrical properties of the material. Carrier concentrations were directly correlated to the Zn/P ratio. They were attributed to a variation in Zn vacancies and P interstitials, in agreement with the activation energies deduced for conductivity. Finally, the effect of substrate doping on the electrical behaviour of the heterojunction has been highlighted. Hence, the present study provides insight into the electrical properties of Zn_3P_2 thin films and allows for a better understanding of the limitations and prospects of

Zn_3P_2 thin film-based solar cells.

5.7 Acknowledgements

The authors EPFL acknowledge the funding from SNF Consolidator Grant (BSCGI0-157705). V.P. gratefully acknowledges the funding from Piaget. Authors also thank funding from Horizon Europe Pathfinder project SOLARUP. This work was supported by the Swiss State Secretariat for Education, Research and Innovation (SERI) under contract number 22.00153. M.D. thanks funding from H2020 through SMARTCELL project (project number: 101022257). The authors also thank CIME and CMI facilities of EPFL for their technical support. H.S.M acknowledges his contract to Junta de Castilla y León.

6 Carrier generation and collection in $\text{Zn}_3\text{P}_2/\text{InP}$ heterojunction solar cells

6.1 Accompanying information

This work is a part of a collaborative effort that is under preparation for submission to a peer-reviewed journal. The list of authors is as follows: Rajrupa Paul, Stefan W. Tabernig, Joel Reñé Sopera, Julien Hurni, Anja Tiede, Xinyun Liu, Djamshid A. Damry, Vanessa Conti, Mahdi Zamani, Simon Escobar Steinvall, Mirjana Dimitrievska, Valerio Piazza, Jessica L. Boland, Franz-Josef Haug, Albert Polman, and Anna Fontcuberta i Morral. My contributions to this work include writing the manuscript and analysis of the current-voltage characteristics (in dark and under illumination) and the external quantum efficiency data.

6.2 Abstract

Zinc phosphide (Zn_3P_2) has been lauded as a promising solar absorber material due to its functional properties and the abundance of zinc and phosphorous. In the last 4 decades, there has not been any significant improvement in the efficiencies of Zn_3P_2 -based solar cells. This is vastly due to the limited understanding of how to tune its optoelectronic properties. Recently, significant progress has been made in the growth and characterization of the material, which has shed light on its potential. In this study, we report an energy conversion efficiency as high as 4.4% for a solar cell based on a polycrystalline Zn_3P_2 thin film on an InP substrate. We investigated the dominant recombination mechanisms in the device using different techniques and identified the key factors that limit the device efficiency. Additionally, we provide a perspective on the next-generation Zn_3P_2 -based solar cells.

6.3 Introduction

Zinc phosphide (Zn_3P_2) is a highly suitable candidate for the large-scale deployment of photovoltaic technology [281]. It has a direct bandgap at 1.5 eV [125, 261], which places it close to the optimum following the Shockley-Queisser detailed balance efficiency calculation [250]. In addition, it has been demonstrated that Zn_3P_2 exhibits a high absorption coefficient ($>10^4\text{-}10^5\text{ cm}^{-1}$) [72, 269] and a long minority carrier diffusion length (5-10 μm) [125]. Additionally, zinc and phosphorous are earth-abundant elements with a low cost and high extraction volume. However, despite of these promising material characteristics, there has not been any significant improvement in the efficiency values related to Zn_3P_2 -based solar cells. The record for highest efficiency was reported in 1981 and has remained for the past few decades at 5.96% for $\text{Mg}/\text{Zn}_3\text{P}_2$ Schottky junction solar cells [36].

One of the shortcomings of Zn_3P_2 is the lack of understanding of how to engineer its carrier density by doping. Zinc vacancies and phosphorous interstitials exhibit relatively low formation energies (which are between 14 meV and 90 meV for phosphorous interstitials and 190 meV to 290 meV for zinc vacancies) [160, 35, 174], and they act as acceptors in Zn_3P_2 . Consequently, Zn_3P_2 is naturally, p-type. Doping the material n-type has proven to be challenging due to the self-compensation effect [114]. This has hindered the fabrication of p-n homojunction solar cells. Instead, the majority of the Zn_3P_2 -based solar cells are either heterojunction or Schottky junction solar cells. The Schottky junction solar cells with high efficiencies were fabricated on multi-crystalline large grain Zn_3P_2 wafers with Mg as the Schottky contact [20]. While similar Schottky junction solar cells fabricated on polycrystalline Zn_3P_2 thin films have efficiency values close to 4.3% [19]. The reduced efficiency associated with polycrystalline Zn_3P_2 thin films is due to the reduced fill factor arising from higher series resistance. Alternatively, heterojunction device architecture has been proposed to overcome the inherent limitations of the Schottky junction solar cells. Some commonly used n-type emitters for Zn_3P_2 heterojunction solar cells are ZnO, ZnSe, ZnS, and CdS [191, 205, 24, 109, 22]. Even though Zn_3P_2 p-n heterojunction solar cells have not shown efficiencies greater than the Schottky junction solar cells, they did demonstrate higher open-circuit voltage values. For instance, p- Zn_3P_2 /n-ZnSe solar cells showed an efficiency of 0.8% but demonstrated record high open-circuit voltage of 810 mV [22]. Similarly, an efficiency of 1.1% was obtained with p- Zn_3P_2 /n-ITO heterojunction solar cell with a short-circuit current value of 18.4 mA/cm² [265]. Prior studies on Zn_3P_2 heterojunction solar cells indicate the possibility of efficiency enhancement by utilizing high-quality single-crystalline Zn_3P_2 and an optimal heterojunction device design. However, improvement in the crystallinity has not translated into enhancement in the efficiency of Zn_3P_2 -based solar cells [24, 279]. Epitaxial Zn_3P_2 thin film grown on GaAs (001) substrate by Bosco *et al.* showed low short-circuit current ($<0.1\text{ mA/cm}^2$ under 1 Sun simulated illumination) [24]. This hints toward the need for an efficient device architecture capable of harnessing the full potential of Zn_3P_2 as a solar absorber material.

In this work, we demonstrate a minimally processed Zn_3P_2 -based solar cell, by employing an ITO top contact on a polycrystalline Zn_3P_2 thin film, we were able to achieve 4.4% efficiency.

We analyze the illumination-dependent electronic behaviour, as well as the external quantum efficiency to determine the dominant limiting factors of the device. Additionally, we propose a working principle for the device, highlight the role of ITO, and investigate the contribution of Zn_3P_2 to the overall working of the device. Finally, we provide an overview of the prospects associated with the next generation of Zn_3P_2 -based solar cells.

6.4 Experimental Details

6.4.1 Materials and device fabrication

Molecular beam epitaxy (MBE) was used for the growth of micron-thick Zn_3P_2 films on undoped InP(100) substrates. The growth method is described in detail in reference [311]. Under optimal growth conditions, we are able to tune the crystallinity of the Zn_3P_2 thin films by controlling the degassing time of the substrate. Short degassing times of 10-20 minutes resulted in polycrystalline growth, whereas degassing times of 30-60 minutes ensured monocrystalline growth. The presence of oxide at the interface determines the crystalline quality of the Zn_3P_2 thin film. The schematic representation of the process flow used for fabricating Zn_3P_2 -based solar cells is shown in Figure 6.1(a). A polycrystalline Zn_3P_2 thin film was grown on an InP substrate at 265 °C for 240 minutes. Prior to the device fabrication, the sample surface was cleaned using argon milling in the sputtering chamber for 30-45 seconds (at an Ar flow of 50 sccm and 100 W power) to remove the native oxide. Subsequently, a transparent conductive oxide (ITO = $\text{In}_2\text{O}_3:\text{SnO} = 90\%:10\%$) electrode was sputtered on top. The nominal thickness of sputtered ITO was ~ 100 nm, however, depending on the reactor conditions this value could fluctuate between $\pm 10\%$. Before the deposition of the top grid, 100 nm of Au was sputtered on the backside of the InP substrate to act as the back contact. Finally, the top Ag finger grid was deposited by sputtering using a shadow mask. Figure 6.1(b) shows the schematic representation of the fabricated device and Figure 6.1(c) shows the photograph of a completely fabricated device.

6.4.2 Characterization

To first characterize the composition of the Zn_3P_2 thin films. Rutherford backscattering spectrometry measurements were performed by EAG Laboratories. A nearly-normal-incident beam of 2.275 MeV alpha particles was used for the measurements, where the normal detector angle collected particles scattered by 160 ° and the grazing detector was set at 104 °. The atomic concentration uncertainty is $\pm 1\%$, and an assumption of 6.61×10^{22} atoms/ cm^{-3} in the Zn_3P_2 layer and 5.26×10^{22} atoms/ cm^{-3} in the InP substrate was used. Following this, optical-pump terahertz-probe spectroscopy measurements were performed using a spectrometer with an ultrafast Ti:Sapphire amplifier (Newport Spectra Physics Spitfire Ace, 13mJ, 1kHz, 40 fs), which described in detail in another study [182]. An optical pulse centered at 750 nm ($E = 1.65$ eV) was used to photoexcite the sample with a pulse duration of 40 fs at fluences between 12 and

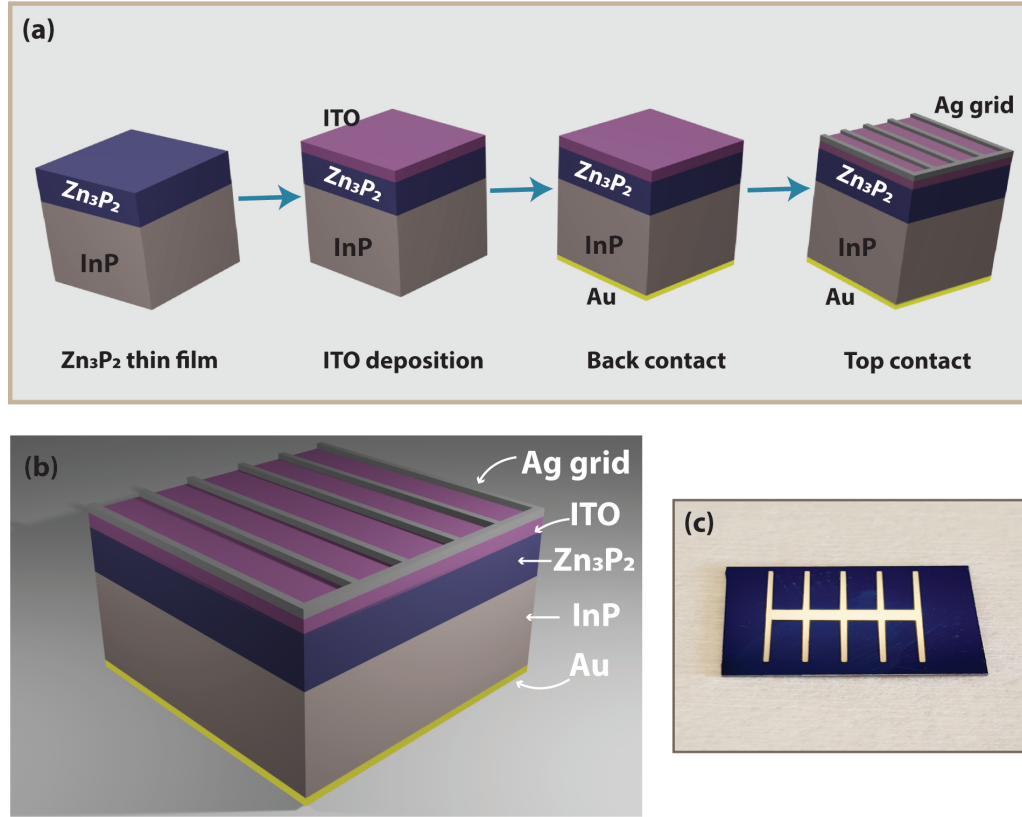


Figure 6.1: (a) Schematic representation of the process employed for the fabrication of Zn_3P_2 solar cell, ITO is deposited on the surface of the as-grown Zn_3P_2 thin film with sputtering, followed by the deposition of Au as the back contact, and Ag is sputtered using a mask to form the top contact. (b) Schematic representation of the final device containing the Au back contact, InP substrate, Zn_3P_2 thin film, sputtered ITO layer, and the Ag top contact. (c) Photograph of a fully fabricated cell.

$128 \mu\text{J cm}^{-2}$. The terahertz probe was generated by optical rectification in GaP crystal and was directed to the sample at an angle of incidence $< 15^\circ$ by a silver-coated prism, which was positioned near the focus of the optical-pump terahertz-probe spectrometer at the sample position. The terahertz beam reflected from the sample was then collected via the same prism and detected by electro-optic sampling in a ZnTe crystal.

Finally, the dark current-voltage (I-V) measurements were performed to assess the device performance using a Keithley 6487 voltage source and picoammeter to apply voltage and measure the current. The measurements were performed in the voltage range of $\pm 1\text{V}$. The light measurements were done using a solar simulator with continuous illumination, composed of a Halogen lamp (IR+VIS) and Xenon lamp (VIS+UV) with a temperature-controlled chuck. Measurements were performed according to the standard testing procedure (1-sun (1000

Wm^2), AM 1.5 Global, 25°C). For all the I-V measurements, one of the probes was placed on the Ag grid and the other on the back contact. The external quantum efficiency measurements were done using a Newport Oriel QuantX 300 tool. The basic gain was set to "1M", the wavelength spacing to 5 nm; the measurement range to 330-1000 nm; and the voltage bias was 0 V. The system calibration was checked using the reference Si solar cell of the system. The I-V curves were measured using a Newport Oriel Sol2A tool. The I-V curve was measured with a measurement delay of 0.009 s, voltage steps of 2 mV, and measured going from -1V to 1V and from 1V to -1V. The intensity was checked with the system's power calibration solar cell.

6.5 Results and Discussion

We start by outlining the functional properties of the as-grown polycrystalline Zn_3P_2 thin film. Figure 6.2(a) shows the scanning electron microscopy (SEM) image of the thin film. The 20° -tilted SEM micrograph shows the cross-section and the top surface of the sample. The growth is granulated and columnar in nature with a coarse top surface. The thickness of the thin film was estimated to be $\sim 0.7 \mu\text{m}$. Previous studies have shown that grain boundaries in polycrystalline Zn_3P_2 thin films are electrically passive with no detrimental effect on the photocurrent collection and the open-circuit voltage [25, 178]. The composition of the thin film across the depth was analyzed using Rutherford backscattering spectrometry (RBS), as shown in Figure 6.2(b). The lattice of Zn_3P_2 has demonstrated a high tolerance for compositional variations [310]. Zn_3P_2 can maintain its crystalline structure even at large off-stoichiometric compositions; the RBS measurements show a uniform composition of $\sim 57\%$ zinc and $\sim 43\%$ phosphorous. The thin film is slightly phosphorous rich, with a Zn:P ratio of 1.32 in comparison to 1.5 at stoichiometry (Zn:P = 60:40). Previous studies have shown that changes in the Zn:P ratio have no significant impact on the crystalline structure of the material, however, it can impact the optical and electrical properties of the material [261, 35]. More importantly, the carrier concentration in the material can significantly vary as excess phosphorous in the lattice acts as an acceptor-type impurity making the thin film p-type. To understand the temporal dynamics of the photoexcited carriers in the as-grown polycrystalline Zn_3P_2 thin film, we used optical pump-terahertz probe (OPTP) spectroscopy. It is a versatile noncontact technique that is capable of measuring the photoconductivity and thereby the carrier mobilities, surface recombination velocities, carrier lifetimes, and doping levels of the material [107, 159]. The measurements were conducted in reflection mode at room temperature and the sample was photoexcited with an optical pump with an FWHM of 1.2 mm, a centre wavelength of 750 nm wavelength with incident fluence values of 12, 28, 57, and $128 \mu\text{J cm}^{-2}$. The higher photon energy of the optical pump ($E = 1.65 \text{ eV}$) compared to the bandgap of Zn_3P_2 ($E_g = 1.50 \text{ eV}$) provides above-bandgap photoexcitation, generating free electron-hole pairs in Zn_3P_2 thin film. While the photon energy of the pump is also above-bandgap for the InP substrate, the thickness of the Zn_3P_2 film is greater than the absorption depth of photons with 750 nm wavelength. The majority of the optical pump photons are consequently absorbed within the Zn_3P_2 film, so the InP substrate can be considered to be in equilibrium (i.e. not

excited by the optical pump) with a negligible response on the measured THz response (see SI, Figure. C.1). The above-bandgap photoexcitation, therefore, generates free electron-hole pairs predominately in Zn_3P_2 film inducing a change in its dielectric function. This photoinduced change is measured by monitoring the change, ΔE , of the reflected electric field of the terahertz probe, E . The ratio of the differential change in the reflected THz field compared to the response in equilibrium, $\Delta E/E$, is directly related to free carrier concentration and photoconductivity in the sample. Monitoring the change $\Delta E/E$, as a function of time after photoexcitation, therefore, provides information about the carrier recombination rates and carrier lifetimes of the thin film. Figure 6.2(c) shows the variation in photoconductivity as a function of time after photoexcitation for different photoexcitation fluences. As the photoexcitation fluence was increased from 12 to $128 \mu\text{J cm}^{-2}$ the extracted photoinduced carrier densities also increased from $0.47 \times 10^{18} \text{ cm}^{-3}$ to $5.01 \times 10^{18} \text{ cm}^{-3}$. For all fluences, a sharp increase in the photoconductivity was observed within 10 ps after photoexcitation followed by a monoexponential decay. The characteristic decay times of the monoexponential fits of the carrier decay data are shown in the inset of Figure 6.2(c). A carrier lifetime of 4.6 ns was observed for $12 \mu\text{J cm}^{-2}$, whereas an increase in the carrier lifetime is observed with an increase in the laser fluence. The monoexponential decay indicates that monomolecular recombination (or trap-assisted recombination) is dominant recombination mechanism affecting the carrier lifetime.

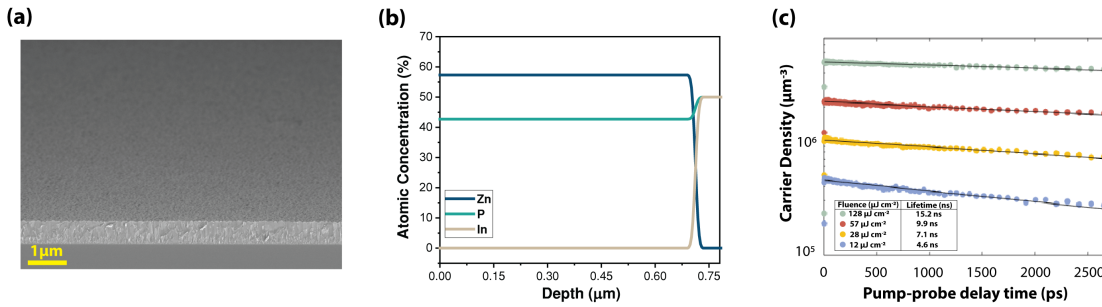


Figure 6.2: (a) SEM image of the as-grown Zn_3P_2 thin film on InP substrate. (b) RBS measurements from Zn_3P_2 thin film depicts a Zn/P ratio ≈ 1.32 . (c) The decay of photoinduced charge carrier density plotted as a function of pump-probe delay time measured by OPTP spectroscopy at different pump fluence.

Having investigated the material properties of the as-grown polycrystalline Zn_3P_2 thin film we now turn toward the demonstration of the photovoltaic device. The current density-voltage (J-V) curves of the device measured in dark and under simulated AM 1.5G 1-sun solar illumination are shown in Figure 6.3(a). The inset in Figure 6.3(a) shows the photograph of the measured device, the device has an active area of 0.467 cm^2 . Under simulated solar radiance the open-circuit voltage (V_{oc}) and short-circuit current (J_{sc}) obtained from the device were 528.8 V and 13.7 mA/cm^2 , respectively. A fill-factor (FF) of 60.7% was measured, resulting in a power-conversion efficiency (PCE) of 4.4%. In contrast to the previous study on the bulk $\text{Zn}_3\text{P}_2/\text{ITO}$ solar cells, the V_{oc} , FF, and PCE show a significant improvement, whereas the J_{sc} is

found to be in the same range [265]. The series resistance was found to be $\sim 18.35 \text{ k}\Omega\text{cm}^2$ and the shunt resistance was found to be $\sim 1.03 \text{ k}\Omega\text{cm}^2$. When comparing the J-V curves under illumination and dark we observe a crossover behaviour at a voltage around 537 mV. This behaviour leads to a failure of the dark/light superposition of the J-V curve [270]. To achieve the same current density at the forward bias, the dark curve needs more voltage compared to the light curve. Crossover is often associated with the presence of an electric barrier at the interface [49, 216, 272, 217, 238] as an illumination-dependent barrier height variation can lead to a crossover of dark and light J-V curves. Under illumination, this barrier height is reduced due to photodoping, thus resulting in a higher diode current [216, 238]. The presence of a conduction band “spike” between ZnS and Zn₃P₂ has shown similar crossover behaviour and it is known to hinder electron transport across the heterojunction interface in ZnS/Zn₃P₂-solar cells [24]. Another common reason for crossover behaviour is attributed to the high density of acceptors-like deep-level defects in the absorber near the interface region, which lead to a modification of the electric barrier. A strong potential drop associated with the large negative charge in the acceptor states leads to an electric barrier in the dark. Upon illumination, the acceptor states are filled with holes, resulting in a reduction in the acceptor charge and thereby decreasing the electric barrier [49, 272, 193, 32]. Additionally, the illumination-dependent series resistance in solar cells is ascribed to photogating, which implies the excited carriers are captured in long-lived trap states, thereby increasing the conductivity [81, 165]. This coincides with our OPTP measurements, which demonstrated that trap-assisted recombination was the dominant mechanism governing carrier transport in the Zn₃P₂ thin films. However, it should be noted that the distortion in the J-V curve could be a combination of these effects [49, 32].

To identify the dominant form of recombination one can look at the ideality factor of the solar cell, which is typically obtained from the Shockley diode equation. The Shockley diode equation is derived from drift-diffusion theory [249], and it is expressed as:

$$J_{dark} = J_0 \left[e^{\frac{V}{V_T n_{id}}} - 1 \right] \quad (6.1)$$

where J_{dark} is the dark current density, J_0 is the saturation current, n_{id} is the ideality factor, and $V_T = k_B T/q$ is the thermal voltage. The above equation does not take into account parasitic resistances. The ideality factor is described as a fitting parameter that determines how closely a diode behaviour matches the theory, ideally, $n_{id} = 1$ for direct radiative recombination. However, when other types of bulk recombination dominate the ideality factor is given by $n_{id} = 2/\gamma$ where γ is reaction order. When $\gamma = 1$, it indicates first-order recombination (typically $n_{id} = 2$ is associated with trap-assisted Shockley-Read-Hall (SRH) recombination) [231]. A γ value of 2 signifies bimolecular band-to-band recombination, whereas a γ value of 3 suggests trimolecular Auger recombination [128, 234, 52]. In addition, there are other interpretations of the γ values [33]. Figure 6.3(b) depicts the dark J-V characteristic in a semi-logarithmic scale. The dark J-V curve shows a rectifying behaviour and the curve can be divided into three distinct regions (as shown in Figure 6.3(b)). At low voltages ($< 0.25 \text{ V}$, region I), the selected device layout shows a low parasitical leakage current. In this low voltage region, the shunt

resistance dominates the J-V characteristics. The presence of pinholes and micro-cracks in a device can serve as a shunt pathway [137]. A high shunt resistance is preferred to ensure a low leakage current. A sharp increase in the current is observed at the intermediate voltage ($0.25 < V < 0.53$, region II) region. The sharp transition arises due to a diffusion-dominated current [30]. At high voltages (> 0.53 , region III), above the built-in potential, the dark J-V curve shows an expected shift to a less sharp current-voltage behaviour as a result of drift-dominated current. The drift-dominated current is limited by either the charge injection or the formation of space charge [293]. Additionally, the series resistance determines the J-V characteristics at the high voltage region, a steep slope in this region typically indicates low series resistance [243]. It should be noted here that the ideality factor is determined from the regime below the built-in voltage, as solar cells operate below the built-in voltage. The ideality factor was obtained from the slope of the semi-logarithmic dark J-V plot using Equation (6.1), which is valid only in the exponential region. The ideality factor obtained on fitting the plot was 2.07. We also plot the ideality factor as a function of the applied bias (as shown SI in Figure C.2), where the ideality factor is obtained from the plateau value [290]. This method prevents erroneous fitting, as the exponential region is clearly distinguishable. The ideality factor values obtained from both methods are significantly larger than unity, indicating trap-assisted recombination plays a dominant role in the recombination process. This corroborates the monomolecular recombination behaviour obtained from the OPTP spectroscopy. Even though the device consists of ITO and additional processes, the predominant recombination mechanism remains the same.

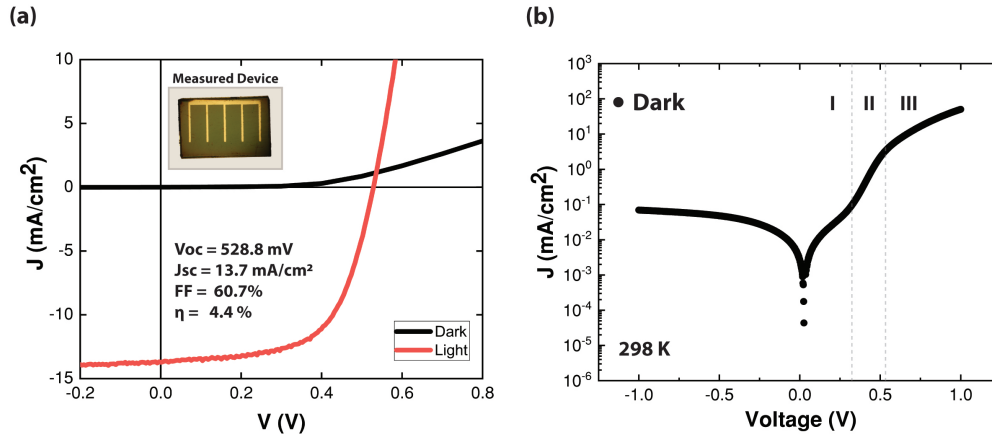


Figure 6.3: (a) Representative J-V curves obtained in dark (denoted by black line) and under 1-sun illumination (denoted by red line), the inset shows the actual device measure that had an active area of 0.467 cm^2 . (b) Dark J-V curve plotted in semi-logarithmic scale depicting the three distinct regions, region I corresponds to the voltage range $< 0.25 \text{ V}$, region II corresponds to the voltage range between 0.25 V and 0.53 V , region III corresponds to the voltage range $> 0.53 \text{ V}$.

Nonetheless, the interpretation of the ideality factor obtained from the dark J-V can be prone to error. As the series and shunt resistance can influence the current dependence on voltage,

it is difficult to attribute the variations in the estimated ideality factor as an influence of resistance (series and shunt) or recombination. Alternatively, we analyzed the V_{oc} as a function of illumination intensity. This method is also known as the Suns- V_{oc} method and it is deemed more reliable as the measurement is performed at open-circuit, which eliminates the dependence on the parasitic series resistance [273, 229, 127]. Figure 6.4(a) shows the systematic variation of the J-V curve of the thin film solar cell with respect to the illumination intensity of the solar simulator, where the incident nominal power is varied between 0 and 1125 W/m² (0-1.125 suns). The V_{oc} obtained at 1.125 suns was ~0.5 V for an aged device. The variation in the J_{sc} , V_{oc} , and FF leads to a combined light-intensity dependence of the PCE. A sharp increase in the J_{sc} is observed, while the V_{oc} shows a gradual increase with the increase in light intensity. Moreover, there is a slight variation in the FF as a function of the light intensity. The solar cell parameters are extracted from the J-V curve and plotted individually as a function of the illumination intensity in Figure 6.4(b-d). The J_{sc} shows a monotonic increase with the increase in the illumination intensity and shows no sign of saturation over the measured range of optical power, as shown in Figure 6.4(b). The FF obtained from $P_{max}/(J_{sc}V_{oc})$ is plotted in Figure 6.4(c), where P_{max} denotes the output at the maximum power point. We observe a small variation in FF as a function of illumination intensity and the maximum FF (~66 %) is reached at 1.125 suns. Additionally, the PCE is expressed as P_{max}/P_{in} , where P_{in} is the input power. Figure 6.4(d) shows the variation in the PCE against the illumination intensity. We observe a PCE value of $4 \pm 0.1\%$ throughout the range. It should be noted here that the J-V curve showing an efficiency of 4.4% (as shown in Figure 6.3(a)) was obtained using a different setup, so a differences in the illumination input (power, spectrum, homogeneity) could lead to a slight discrepancy in the measured efficiencies. Additionally, the illumination power-dependent studies were done after several weeks after fabrication, which could have resulted in the degradation of the device. Finally, the V_{oc} is plotted as a function of the light intensity, as shown in Figure 6.4(e). The V_{oc} increases steadily with the increase in the light intensity until 0.8 suns, with a slight fluctuation at the higher illumination intensities. The slope of the semi-logarithmic plot of V_{oc} against the illumination intensity can be used for estimating the ideality factor, where the slope has the unit of k_T/q . A change in the slope is observed at higher illumination intensities, previous studies have shown that the change in the slope can arise due to the discrepancy in recombination mechanisms [229, 134, 54, 29, 258, 280]. As mentioned previously that the ideality factor can be determined more reliably from the illumination intensity and the V_{oc} than the dark J-V curve. At the open circuit and steady-state conditions, to ensure net zero current flow, the integrated generation and recombination rates must be the same [127]. As the photogeneration is proportional to the illumination intensity, under light the ideality factor can be expressed as:

$$n_{id,l} = \left(\frac{q}{k_B T} \frac{dV_{oc}}{d \ln(P_{opt})} \right) \quad (6.2)$$

where $n_{id,l}$ is the ideality factor under illumination, and P_{opt} is the illumination intensity. At open circuit conditions, the ideality factor is affected by the shunt resistance, however, the

voltage drop over the series resistance is zero, which allows a more accurate description of the recombination mechanism. The ideality factor obtained on fitting the plot was found to be 1.03, it should be noted that as the slope changes over higher illumination intensities, the last two points are neglected (in case we include the last two points we obtain an ideality factor of 0.92). The results show a clear dominance of bimolecular recombination in presence of light. The shift from trap-assisted in the dark ($n_{id} > 1$) to band-to-band recombination under illumination ($n_{id,l} \approx 1$) has been previously reported [134, 53, 292, 291]. Cowan *et al.* hypothesized that a higher density of charge carriers under illumination could lead to the shift from monomolecular to bimolecular recombination [54], as these recombination mechanisms have different density dependencies [290, 135]. Alternatively, the difference in the ideality factor obtained from two methods could arise due to poor conductivities, which could give rise to large gradient in quasi-Fermi levels at V_{oc} [273].

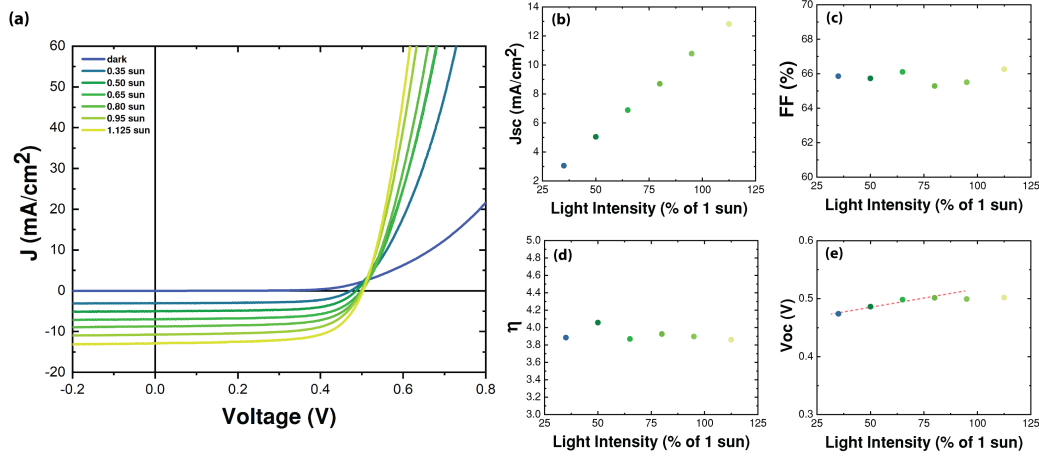


Figure 6.4: (a) Light intensity dependence of J-V characteristics of the device, the measurements were performed at different illumination intensities ranging from 0 sun (dark) to 1.125 suns (which corresponds to 1125 W/m²). The different solar cell parameters are extracted from the light intensity dependent J-V curve and plotted as a function of the light intensity (b) short-circuit current density J_{sc} , (c) fill factor FF , (d) power conversion efficiency η , (e) open-circuit voltage V_{oc} , the red dashed line denotes the part of the plot used for extracting the ideality factor from the semi-logarithmic plot of light intensity against the V_{oc} .

Having assessed the recombination mechanism, we now turn to the contribution of Zn_3P_2 and InP to the working device. Figure 6.5(a-d) show the simulated band alignment between the Zn_3P_2 , the ITO (on the front side) and an intrinsic InP substrate. We present the band alignment under an applied bias ranging between 0 to 1 V. The simulated band alignment indicates that the electrons drift in the direction from the Zn_3P_2 to the InP and the holes in the opposite direction. This is in agreement with the polarity of the I-V curve given the direction of the applied bias. The collection of holes at the front of the device could be counterintuitive as ITO is traditionally used as an n-type contact and Zn_3P_2 is a p-type semiconductor [265]. This would suggest that electron collection is facilitated at the Zn_3P_2 -ITO interface. However, the junction with i-InP dominates the behaviour of the device and electrons are actually collected

at the rear side of the device.

Figure 6.5(e) shows the external quantum efficiency (EQE) of the device as a function of wavelength. The EQE of solar cells corresponds to the conversion efficiency of the incident photons to collected electron [220, 4], which provides understanding of the charge collection behaviour as a function of the energy of an incident photon. We observe a maximum EQE of 85% at 847 nm wavelength. A sharp rise in the EQE is observed at a wavelength of 940 nm, which corresponds to 1.32 eV. This value coincides with the absorption onset of InP (which has a bandgap of 1.34 eV), although there might be a slight contribution from the Zn₃P₂ band tails [278, 248, 284]. The band gap of Zn₃P₂ is widely reported to be 1.5 eV [125, 261, 187], and thus cannot account for the EQE contribution at energies below its bandgap. Still, a recent study by Stutz *et al.* demonstrated the presence of band tails that lead to band gap narrowing in Zn₃P₂ [261]. This observation gives room to an alternative explanation, in which the Zn₃P₂ already absorbs around the energy of the observed high-intensity PL peak. However, this would mean that the Zn₃P₂ has an effective bandgap around 1.32 eV instead, but at the same time does not explain why the EQE is 0% for wavelengths of 550 nm and lower, as Zn₃P₂ demonstrates a high optical absorption coefficient in the visible spectral range [269]. To clarify the contribution of Zn₃P₂ and InP to the measured EQE, we simulated the absorption of InP (10 μ m thick) and Zn₃P₂ (700 nm thick), as shown in Figure 6.5(f). It can be seen that a significant part of the incident light is absorbed by the InP substrate. Additionally, the measured EQE and the simulated InP absorption show a large spectral overlap, while the simulated Zn₃P₂ absorption spectrum cannot be recognized from the shape of the measured EQE curve. This suggests that the Zn₃P₂ layer contributes significantly less to the measured EQE than the InP. To simulate the contribution of InP and Zn₃P₂ to the overall current density, we selectively switched the charge carrier generation in the individual layers on and off, to obtain I-V curves for the different contributions, as shown in Figure 6.5(g). The orange line depicts the contribution from Zn₃P₂; the green line depicts the contribution from InP; and the purple line indicates their combined contribution. The simulation predicts that combining the two materials gives a higher current density, where the 700 nm of Zn₃P₂ contributes only 3.3 mA/cm² to the overall current density. It is interesting to note that the simulated absorption predicts there could be a contribution of up to 18.2 mA/cm² from the 700 nm thick Zn₃P₂. In comparison, the InP contributes 12.4 mA/cm² and almost the same amount (13.0 mA/cm²) is predicted from the simulated absorption. This indicates the internal quantum efficiency of InP is around 95%, whereas it is solely 18% for Zn₃P₂. The insufficient charge carrier extraction in the Zn₃P₂ can be explained in the following way: we note that there is a slight downward bending in the CB of Zn₃P₂ towards the ITO interface (as shown in Fig. 5(a-d)). This means that electrons that are generated within the first few hundreds of nanometers of the Zn₃P₂ layer can get stuck and recombine instead of being collected at the back. The photo-generated carriers further away from the surface and in the vicinity of the InP and Zn₃P₂ interface can be separated more efficiently. Thus, the reduced carrier collection from Zn₃P₂ in comparison to InP is due to unfavorable energy alignment at the Zn₃P₂-ITO interface, which should be addressed in the future.

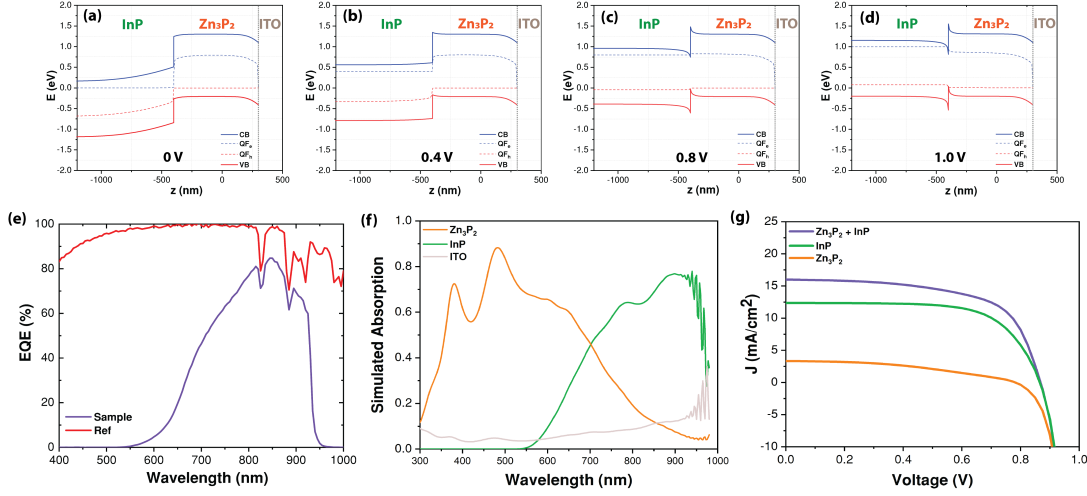


Figure 6.5: Simulated band alignment between the Zn_3P_2 layer and ITO at the front side, and the Zn_3P_2 layer and InP at the back side, the blue solid line represents the conduction band (CB), the red solid line represents the valence band (VB), the blue dashed line depicts the quasi-fermi level for electrons (QF_e), and the red line depicts the quasi-fermi level for holes (QF_h), the simulation is done under different bias voltages (a) 0 V, (b) 0.4 V, (c) 0.8 V, and (d) 1 V. (e) The EQE obtained from the measured device (denoted with purple line) and the reference Si (denoted with red line). (f) Simulated absorption obtained from Zn_3P_2 (denoted by the solid orange line), InP (denoted by the green solid line), and ITO (denoted by grey line) for the wavelength range of 300 nm to 1000 nm. (g) Simulated I-V diagram obtained from Zn_3P_2 generation (denoted by the solid orange line), from InP generation (denoted by the green solid line), and from the combined (Zn_3P_2 and InP) generation (denoted by the solid purple line).

High energy photons are absorbed much closer to the surface, and hence are affected more strongly by the low extraction efficiency in the Zn_3P_2 . This explains the EQE loss at shorter wavelengths. If the small Zn_3P_2 contribution predicted by the simulations indeed also occurs experimentally, then it is spectrally overlapping with the InP contribution. Note that the comparison between experiment and simulation relies mainly on band alignment arguments, as the simulations assume fairly ideal bulk recombination parameters and no interface/surface recombination. Similar loss behaviour has been reported for $\text{Zn}_3\text{P}_2/\text{ZnSe}$ heterojunction solar cells [22].

An alternative device design should be considered to enhance the EQE and the overall efficiency of the device. Instead of ITO, a front contact with a larger work function could reduce the band bending at the front interface. Alternatively, to still utilize the transparency of the ITO, one could insert a dedicated hole-selective layer between the Zn_3P_2 and ITO which would have an equivalent function. Passivation of the Zn_3P_2 thin films has been shown to reduce the surface recombination velocity and could also be implemented [122] to reduce surface recombination effects. Additionally, reflection losses can be prevented by using an anti-reflective coating on the device surface and/or by texturing. To ensure efficient absorption in the Zn_3P_2

layer, the thickness of the film can also be increased (from 700 nm to several micrometres). In the long term, a different substrate material has to be used along with the Zn_3P_2 absorber layer, to make sure that light is solely absorbed in the dedicated Zn_3P_2 layer.

6.6 Conclusion

We demonstrated an efficiency of 4.4% for a solar cell consisting of polycrystalline Zn_3P_2 thin film on an intrinsic InP substrate. The fabrication of the device entails a straightforward method of depositing transparent conductive oxide and metal contacts on the as-grown thin film. The optimization of power conversion efficiency is related to improving the solar cell parameters; therefore, it is important to identify the limiting parameters and their causes. We observed a crossover behaviour between the light and the dark IV curves; even though the exact origin of this behaviour is unknown. We highlight some of the main factors that could lead to crossover, as the crossover behaviour could lead to a reduction in the V_{oc} and FF. Additionally, losses in the FF could arise from the high series resistance. The high series resistance could be attributed to the polycrystalline nature of the thin film and to the interface between the ITO and Zn_3P_2 . The OPTP spectroscopy measurements elucidate a monomolecular recombination behaviour in the Zn_3P_2 thin film. This is in good agreement with the recombination mechanism obtained from the ideality factor of the device, which shows trap-assisted recombination mechanism is dominant in our system. Whereas the switch from the high ideality factor ($n > 1$) in dark to the low ideality factor in light ($n \approx 1$) could arise from the fitting. As the light ideality factor is determined by the slope of the V_{oc} against illumination intensity, this could average out over different recombination mechanisms. The recombination mechanism is dependent on the light intensity, charge density, and density of traps. Any variation in these factors can cause a switch from one recombination mechanism to the other, in particular the strength of the bimolecular recombination coefficient, the carrier density, the occupation and capture cross-section of the traps, and the thermal velocity of charge carriers. The presence of non-radiative recombination centers, such as crystallographic defects and impurities, leads to losses in the PCE. Additionally, band tails can significantly impede the V_{oc} values obtained from the device; they constitute a density of state that extend into the band gap, which can give rise to radiative and non-radiative recombination channels. In prior studies, a linear trend between V_{oc} -loss and the Urbach energy has been demonstrated. Finally, the loss in EQE is mainly ascribed to the poor spatial collection efficiency of charges generated in the Zn_3P_2 layer, arising due to unfavorable energy level alignment. The carrier lifetime (≈ 4.6 ns) obtained from OPTP spectroscopy measurements is significantly lower than carrier lifetimes previously reported for Zn_3P_2 . Having identified some of the key limitations of the fabricated solar cell and the contribution of InP to the working device, we believe the path toward high-efficiency Zn_3P_2 solar cells entails a strategic device design. To minimize the dependence on the InP substrate for epitaxial growth one can utilize a InP buffer layer or use Zn_3P_2 nanostructures. Alternatively, the InP substrate can be replaced by earth-abundant material like Si (for the nanostructure growth) or van der Waals substrates. Stoichiometric

(Zn:P = 60:40) Zn_3P_2 growth is imperative to avoid the formation of band tails, which in turn can lead to bandgap narrowing. Deviation from stoichiometry has proven to incorporate defect states, which causes poor carrier lifetime and recombination losses. The thickness of the Zn_3P_2 layer can be further increased and the optical device architecture improved to ensure the majority of the incident light is absorbed in the Zn_3P_2 layer. Additionally, a different device design can be implemented, which does not rely on heterojunction or Schottky junction, but utilizes selective contacts instead, which could potentially lead to highly efficient Zn_3P_2 -solar cells.

6.7 Acknowledgments

The authors EPFL acknowledge the funding from SNF Consolidator Grant (BSCGI0-157705). Authors also thank funding from Horizon Europe Pathfinder project SOLARUP. This work was supported by the Swiss State Secretariat for Education, Research and Innovation (SERI) under contract number 22.00153. V.P. gratefully acknowledges the funding from Piaget. M.D. thanks funding from H2020 through SMARTCELL project (project number: 101022257). The authors also acknowledge the CMI facilities of EPFL for their technical support. FJH and JH acknowledge support within the project ZIPPO of EPFL's interdisciplinary funding action eSeed. The authors from Manchester gratefully acknowledge support from EPSRC via project EP/S037438/1, UKRI via JLB's Future Leader Fellowship, MR/T022140/1 and from the Leverhulme Trust via JLB's Philip Leverhulme Prize. They would also like to thank the University of Warwick for providing access to the Warwick Centre for Ultrafast Spectroscopy (WCUS) facility and Dr Michael Staniforth for conducting the initial THz spectroscopy measurements using the facility. J. L. B. also thanks Dr Christopher Beckerleg for fruitful discussions. The contributions of S.W. Tabernig and A. Polman are part of the research program of the Dutch Research Council (NWO).

7 Conclusion and Outlook

In this thesis, we investigated the growth and properties of Zn_3P_2 . We focused on its crystal structure, optical, and electrical properties. The gained understanding was used to determine the factors that hinder the performance of Zn_3P_2 -based devices. We observe a correlation between the composition and the material properties. Our results contribute to the understanding of the growth of Zn_3P_2 on alternative substrates and they provide insights into the limitations and potential of the material.

In this first part, we demonstrated the growth of Zn_3P_2 on an alternative substrate that circumvents the requirement of a lattice-matched substrate. The large unit cell of Zn_3P_2 makes the growth on conventional substrate challenging. In this study, we demonstrated the growth of Zn_3P_2 on graphene via van der Waals epitaxy. We provided a detailed account of the growth condition and proposed a suitable growth mechanism. We found the growth window is relatively narrow on graphene and the growth temperatures are significantly lower than on traditional substrates like GaAs and InP. The lower temperatures prevent the formation of microcracks, which are commonly observed in Zn_3P_2 growth due to its large coefficient of thermal expansion. A preferential orientation of the grown Zn_3P_2 with respect to the substrate has been observed, which is highlighted by the triangular flake-like growth. For a longer duration of growth, we observe an increase in growth rate that is predominantly influenced by the defects present on the graphene surface. The PL measurements showed similar behaviour as conventionally grown Zn_3P_2 with a bandgap of ~ 1.5 eV. Thus, van der Waals epitaxy has proven to be an efficient growth technique to overcome the limitation of lattice-matched substrate. As a follow up of this work, it will be interesting to understand the growth of Zn_3P_2 on graphene with lower defect densities, such as by utilizing high-quality graphene on silicon carbide. One could hope to obtain larger grains in this way. Moreover, the role of defects on growth can be investigated by locally tuning the defects using focused ion beam. One can also think about new pathways for device fabrication using the Zn_3P_2 grown with van der Waals epitaxy, one can easily transfer the grown layer to any other suitable substrate. For example, the grown Zn_3P_2 could be transferred on a glass substrate coated with transparent conductive oxide and an electron collecting layer. Whereas on the top surface a hole collecting layer and a

metal contact can be used. Additionally, it would be interesting to explore the selective area growth of Zn_3P_2 using graphene as a mask.

In the second part, we investigated the electrical transport properties of Zn_3P_2 thin films grown on InP substrates. We demonstrated an efficient process for fabricating electrical devices on thin films exhibiting microcracks, which involves electron beam lithography and focused ion beam processing. The difference in the electrical properties of monocrystalline and polycrystalline Zn_3P_2 as well as Zn/P composition has been highlighted. We identified the dominant conduction mechanism in the different crystalline thin films as a function of temperature. It was shown that the thermally activated conduction mechanism is prevalent in all the measured thin films. The estimation of the activation energies shows the presence of a trapping level consistent with that of phosphorous interstitials. Only p-type transport behaviour was observed for different compositions of Zn_3P_2 , with the Zn/P ratio ranging from 1.16 to 1.64. Furthermore, we demonstrated a relatively high hole mobility of $125 \text{ cm}^2/\text{Vs}$ for high-quality single crystalline Zn_3P_2 thin films. We correlated the composition obtained from SIMS measurements to the carrier concentration. We found an exponential relation between the two for the measured range of data. Finally, we highlighted the role of the substrate on the transport behaviour, we probed the junction between Zn_3P_2 and InP to demonstrate the influence of the substrate. Monocrystalline Zn_3P_2 grown on n-InP shows considerable leakage in the reverse bias condition in comparison to monocrystalline Zn_3P_2 on i-InP. This work demonstrates the influence of composition and microstructure on the electrical properties. Further work would entail the understanding of how to tune reproducibly the Zn/P ratio in the film.

In the final part, we demonstrated a photovoltaic device utilizing the as-grown Zn_3P_2 with minimal post-growth processing. This study provided insight into the prevalent recombination mechanisms in the device. The terahertz spectroscopy measurements show the dominant recombination mechanism in Zn_3P_2 thin film is monomolecular in nature. Furthermore, the ideality factor obtained from the dark I-V characteristics was compared to the ideality factor obtained from illumination-dependent measurements. We observe a difference in the recombination mechanism estimated from the two methods, we attribute this difference to different density dependencies of the two recombination mechanisms. However, this requires further investigation. We accounted for the various loss mechanisms in the device and recommend ways to further improve the efficiency of Zn_3P_2 -based solar cells. Indeed, one cannot ignore the contribution of InP to the working device, given the similar bandgap of the two materials. Among the different devices we tested, we found significant variations mostly arising from the difference in composition in Zn_3P_2 . Additionally, our prior study done on the absorption properties of Zn_3P_2 shows that the majority of the absorption occurs in Zn_3P_2 for the given thickness of the film. Thus, the loss in the EQE of the device is attributed to the unfavourable band alignment between Zn_3P_2 and ITO. The decoupling of the contribution of Zn_3P_2 and InP needs further investigation. This study largely indicates that the growth of Zn_3P_2 for its application in photovoltaics requires an alternative substrate, which is earth-abundant and eliminates uncertainty from measurements.

A continuation of this work would entail the growth of Zn_3P_2 thin films on a buffered InP layer to avoid the use of the whole substrate. This would ensure the epitaxial relation required for the growth but would significantly reduce the contribution of InP to the fabricated device. Alternatively, we could explore the selective area growth of Zn_3P_2 on silicon substrates. These two materials have a relatively large lattice-mismatch; however, starting the growth with a nanostructure can significantly relax the requirement for a lattice-matched substrate. These two growth techniques could provide a path to reduce (if not eliminate) the use of rare-earth material in the fabrication of earth-abundant material for photovoltaics. To conclude, the present work contributes significantly to the understanding of zinc phosphide. Through in-depth characterization, we have demonstrated the impact of microstructure and composition on the electrical and optical properties. We also opened new avenues for Zn_3P_2 growth, which reduces the dependency on the substrate. Furthermore, we believe this work will serve as a foundation for the growth and fabrication of next-generation Zn_3P_2 -based devices. This work leaves off with a plethora of possible follow-up studies, with the prospect of optimization of Zn_3P_2 -based photovoltaics.

A Supplementary information for “van der Waals epitaxy of earth-abundant Zn_3P_2 on graphene for photovoltaics”

A.1 Raman spectra

Figure A.1 represents the room temperature Raman spectroscopy measurements for samples grown at 150 °C at three different V/II ratios. These V/II ratios are lower than the optimum V/II range for Zn_3P_2 growth on graphene at 150 °C. It is observed that an additional peak at 71 cm^{-1} is present along with the room temperature Raman peaks of Zn_3P_2 . The intensity of the peak at 71 cm^{-1} increases with decreasing V/II ratio. Whereas the intensity of the Raman peaks assigned to Zn_3P_2 does not change, this indicates that the Zn content in the sample increases with lower V/II ratio. The presence of excess Zn in the sample leads to a change in morphology of the grown sample, as shown in Figure 4.1(c).

A.2 XRD measurements

Figure A.2 depicts the SEM and XRD measurements for Zn_3P_2 samples grown at 150 °C at a V/II = 0.83. Figure A.2(a) represents the SEM image and XRD peaks for the sample grown for 240 minutes. Dense aggregates are observed in the SEM image, and the presence of Zn is confirmed by the corresponding XRD measurements. The XRD peaks consist of (101), (202), (303), and (404) planes of Zn_3P_2 along with (002) and (101) planes of Zn. The Zn peaks are matched using the ICDD file no 00-004-0831 [268]. Figure A.2(b) represents the SEM image and XRD measurements for the sample grown for 150 minutes under the same growth conditions as above. It is seen from the SEM image that for lower growth time, fewer aggregates are present on top of a well-formed Zn_3P_2 layer. The XRD peaks consist of (101), (202), (004), (203), (303) and (404) planes from Zn_3P_2 and plane (002) from Zn. The intensity of (002) and (101) planes of Zn is much stronger for the sample grown for a longer duration (240 minutes, Figure A.2(a)), this indicates that aggregates formed on top of Zn_3P_2 layer are of Zn at the given conditions and the Zn aggregates become denser with time. The aggregation of Zn occurs due to higher absorption behaviour on Zn_3P_2 than on graphene at the given growth

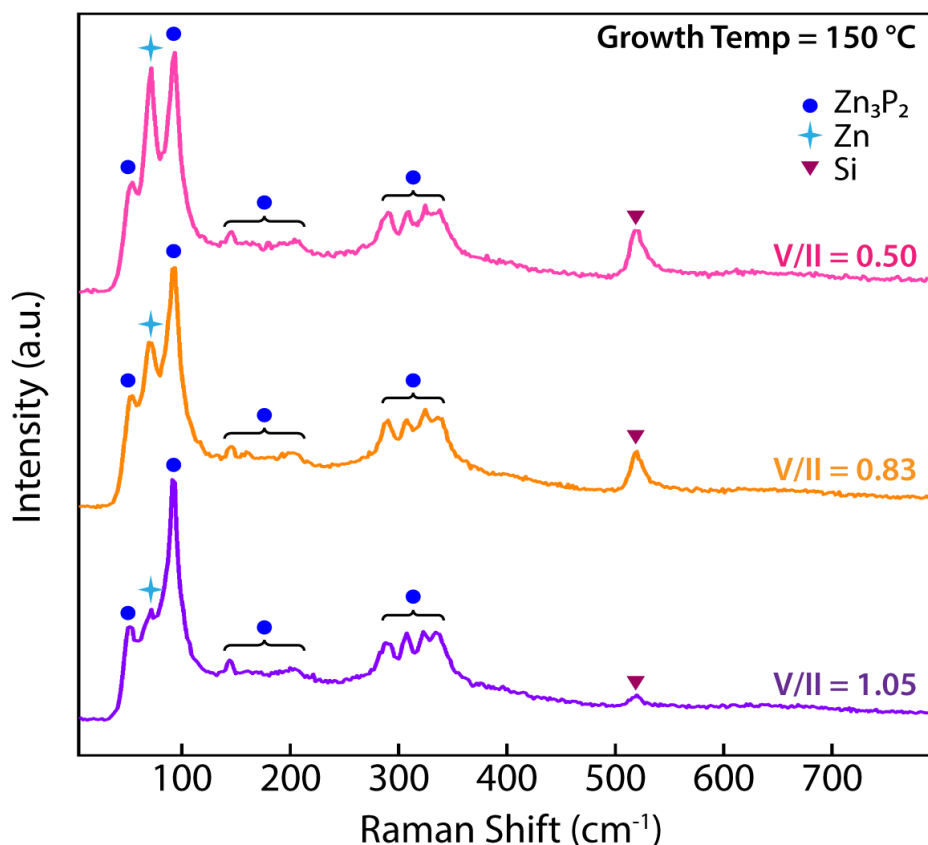


Figure A.1: Raman spectra of Zn_3P_2 grown on graphene at 150 °C with varying V/II ratio

conditions. The growth starts with the formation of Zn_3P_2 on graphene, when a layer of Zn_3P_2 is formed the absorption of Zn increases and leads to the formation of Zn aggregates. The presence of (004) and (203) planes of Zn_3P_2 in the XRD measurement indicates that the growth of Zn_3P_2 on graphene in the normal growth conditions is more random than under optimal growth conditions, which causes the loss of preferential orientation of Zn_3P_2 on graphene. Indeed, such drastic change in adsorption behaviour is not observed under the optimum growth conditions.

A.3 Effect of Total Flux

Figures A.3(a-c) illustrate the SEM images for Zn_3P_2 grown on graphene by varying the total flux conditions for 30 minutes. The growth temperature and V/II ratio were maintained at the optimal growth conditions. The Zn and P_2 fluxes were adjusted to maintain the V/II ratio at different overall flux ranges. The growth rate increases with the increase in total flux. Figure A.3(c) shows the SEM image of the sample grown at P_2 BEP of 9.18×10^{-7} Torr, as expected the surface coverage of the sample is higher than the samples grown at lower pressure conditions. This demonstrates that the growth parameters significantly influence the growth rate.

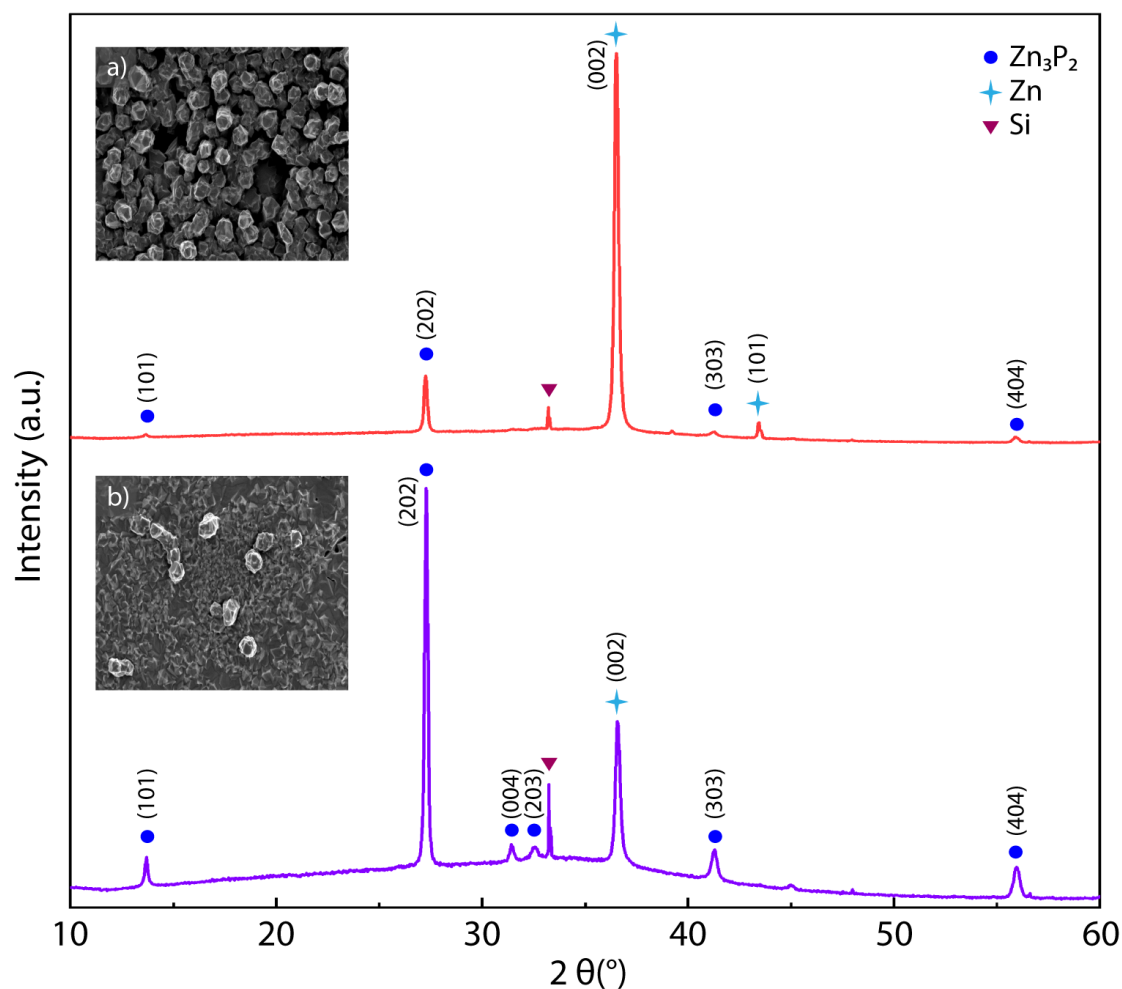


Figure A.2: (a) XRD of Zn_3P_2 samples grown on graphene at 150 °C at a $V/II = 0.83$ for 240 minutes, inset represents the corresponding SEM image for the sample: (b) XRD of Zn_3P_2 samples grown on graphene at 150 °C at a $V/II = 0.83$ for 150 minutes

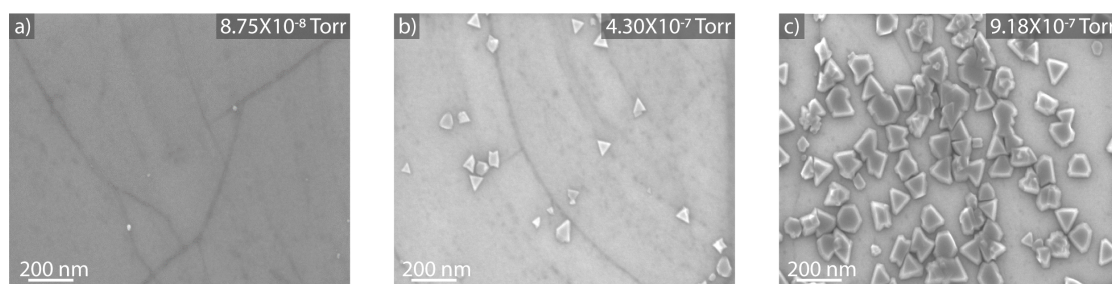


Figure A.3: (a-c) SEM images of Zn_3P_2 grown on graphene for 30 minutes at 150 °C and at a $V/II = 1.55$ with (a) P_2 BEP of 8.75×10^{-8} Torr, (b) P_2 BEP of 4.30×10^{-7} Torr, (c) P_2 BEP of 9.18×10^{-7} Torr.

A.4 EBSD

The EBSD measurement was done by placing the sample on the SEM stage with a 70°C tilt. Kikuchi band obtained at the surface of the Zn_3P_2 flakes were indexed with the expected

α -Zn₃P₂. Figure A.4(a) represents the EBSD map of Zn₃P₂ grown on graphene under optimal growth conditions. The EBSD map was acquired for 4 hours on aXLF30 SEM equipped with EBSD system (Nordlys 2 camera, Aztec software, Oxford Instruments). Since 95% the Zn₃P₂ flakes in the map coloured in IPFz (inverse pole figure in the z-direction) mode have the same green/yellow colour, it is clear that the crystallographic plane parallel to the graphene surface is the same. The pole figure plot was used to determine that the (101) plane of α -Zn₃P₂ have a strong texturization parallel to the surface. These results are corroborated by the XRD measurements shown in Figure 4.3(a). This indicates the Zn₃P₂ grown on graphene has a preferential (101) orientation under optimal growth conditions. Figure A.4(b) shows the schematic representation of the tetragonal unit cell of Zn₃P₂. Each phosphorous atom (green spheres) is 6 surrounded by eight tetrahedral cavities, six are occupied by Zn atoms (yellow spheres) and the other two is vacant [202, 208]. Each Zn atom is tetrahedrally bonded to four P atoms. The unit cell of tetragonal Zn₃P₂ can be constructed by stacking slightly distorted cubic cells of fluorite (grey) and zinc-blende (blue). The a and b lattice parameters of the tetragonal unit cell of Zn₃P₂ are oriented along the diagonal faces of the cubic cells, and the c lattice parameter is equivalent to twice the lattice parameter of a single cubic unit cell. The total volume of the tetragonal unit cell is equal to 4 cubic cells³. Given the lattice, parameter c is equivalent to for the tetragonal unita cell, one can expect an orientation relationship between the tetragonal phase and pseudo-cubic phase. The phase transformation of the Zn₃P₂ tetragonal unit cell to a pseudo-cubic phase can be done the following way:

The orientation relationship matrix X is built using the equivalent directions of the tetragonal unit cell in pseudo-cubic form, as shown in the table of Figure A.4(b).

$$X = \begin{pmatrix} 1 & -1 & 0 \\ 1 & 1 & 0 \\ 0 & 0 & 2 \end{pmatrix}$$

the transpose of the matrix X is:

$$X^T = \begin{pmatrix} 1 & 1 & 0 \\ -1 & 1 & 0 \\ 0 & 0 & 2 \end{pmatrix}$$

The inverse of the X^T is :

$$X^{-T} = \frac{1}{2} \begin{pmatrix} 1 & -1 & 0 \\ 1 & 1 & 0 \\ 0 & 0 & 1 \end{pmatrix}$$

The matrix X^{-T} is the orientation relationship matrix for the planes. It multiplied by a plane in

the tetragonal crystal system (t) to obtain its equivalent pseudo-cubic form (c).

$$\begin{pmatrix} 1 & -1 & 0 \\ 1 & 1 & 0 \\ 0 & 0 & 1 \end{pmatrix} \begin{pmatrix} 1 \\ 0 \\ 1 \end{pmatrix}_T = \begin{pmatrix} 1 \\ 1 \\ 1 \end{pmatrix}_C$$

This proves that the (101) tetragonal plane is equivalent to the (111) pseudo-cubic plane. The quasi-hexagonal shape of the Zn_3P_2 comes from the quasi three-fold symmetry of the [111] axis.

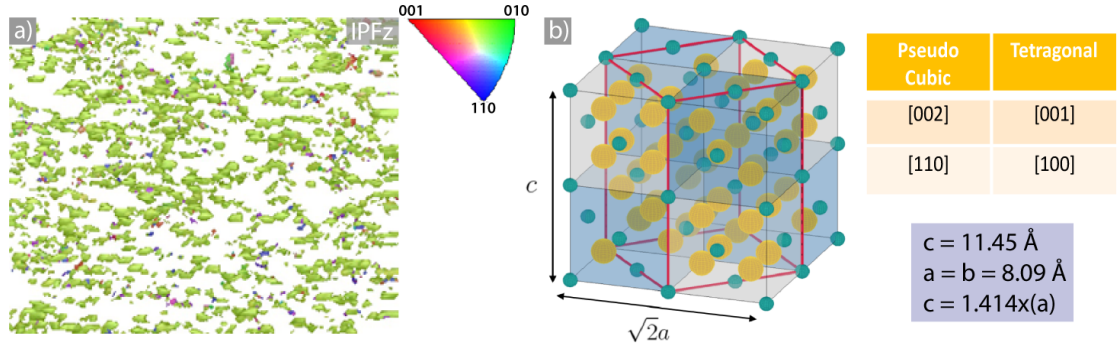


Figure A.4: (a) EBSD map of Zn_3P_2 grown on graphene under optimal growth conditions showing the preferential orientation, (b) corresponding EBSD pole figure, (c) Schematic representation of the tetragonal unit cell of Zn_3P_2 in pseudo-cubic form.

A.5 Photoluminescence

In sample A, we observed two room-temperature PL peaks at 1.52 eV and 1.42 eV. The intensities were derived for the two peaks and the corresponding power dependence is shown in Figure A.5(a). It is seen that the PL intensity for both the peaks increases linearly with the laser power. No saturation of these two peaks was observed for the power range used. The slopes for peaks 1.52 eV and 1.42 eV, $k = \log(\text{PL intensity})/\log(\text{laser intensity})$ 1.6 and $1.7 \approx$ respectively, which suggests exciton line [239]. Figure A.5(b) shows the PL peak as a function of power at 200 K for sample A. The peak position does not change with the increase in laser power, and the slope of the peak is ~ 1.28 , which suggests an exciton line [239]. The PL peak has a tail in its high energy side, which is common in many crystal systems (example: GaAs) [80]. Figure A.5(c) shows the plot of intensities of the peak at 1.26 eV in sample B as a function of laser power at 5.8 K. The peak position does not change with increase in laser power. However the intensity of the peak starts to saturate at higher laser powers, which suggests a defect-related peak [239].

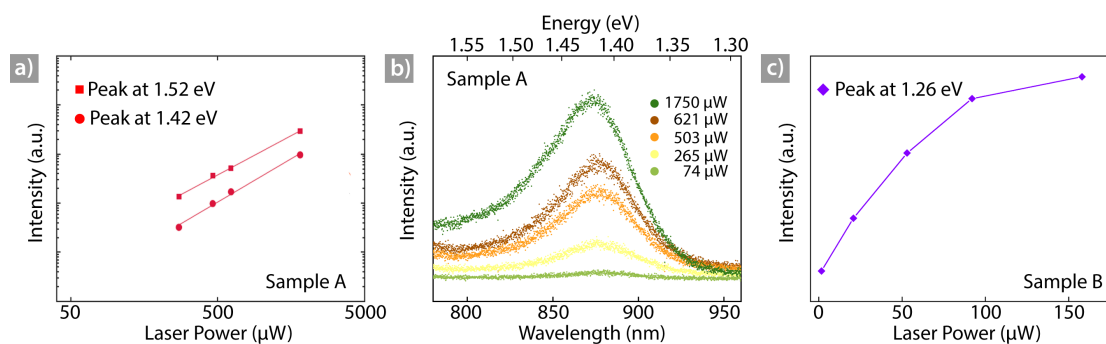


Figure A.5: (a) Plot of room temperature PL intensities for peaks at 1.52 eV and 1.42 eV as a function of laser power done on sample A with 633 nm illumination, (b) PL spectra of sample A at 200 K as a function of laser power excited with 633 illumination; (c) Plot of PL intensities for peak at 1.26 eV as a function of laser power done on sample B at 5.8 K excited with 532 nm illumination.

B Supplementary information for “Zn/P ratio and microstructure defines carrier density and electrical transport mechanism in earth-abundant $\text{Zn}_{3-x}\text{P}_{2+y}$ thin films ”

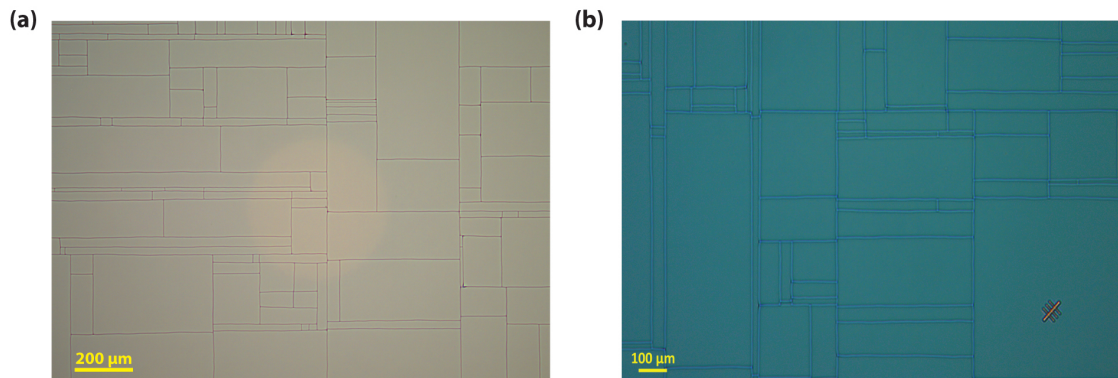


Figure B.1: Optical microscope image of the monocrystalline Zn_3P_2 thin film demonstrating micro-cracks formed due to large thermal coefficient mismatch between the Zn_3P_2 thin film ($14 \times 10^{-6} \text{K}^{-1}$) [163] and the substrate ($4.35 \times 10^{-6} \text{K}^{-1}$) [85] (a) bare thin film (b) thin film after the second EBL step, the surface is coated with PMMA except for the exposed area, which contains the hall bar. The hall bar is positioned away from the existing micro-cracks on the sample.

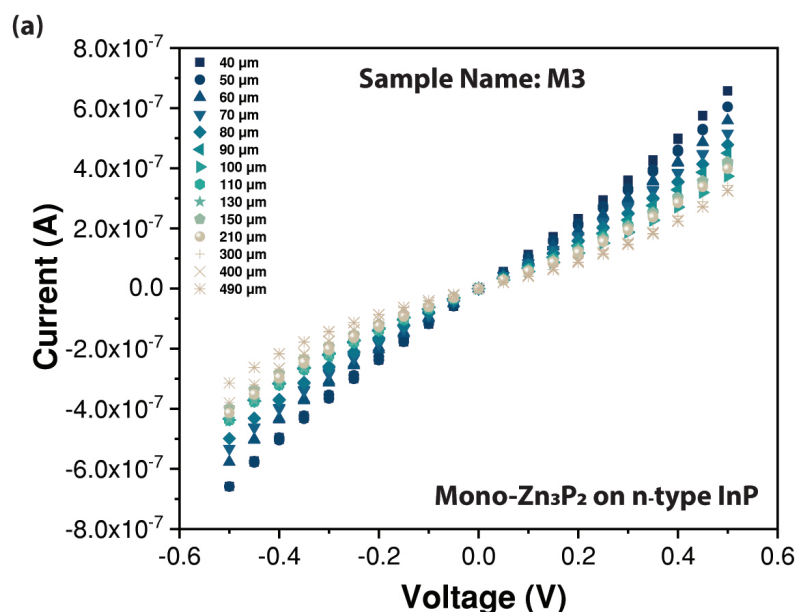


Figure B.2: I-V characteristic obtained as a function of distance between two contacts from (a) monocrystalline Zn_3P_2 thin film (M1) (b) polycrystalline Zn_3P_2 thin film (P2), on i-InP (100) substrate

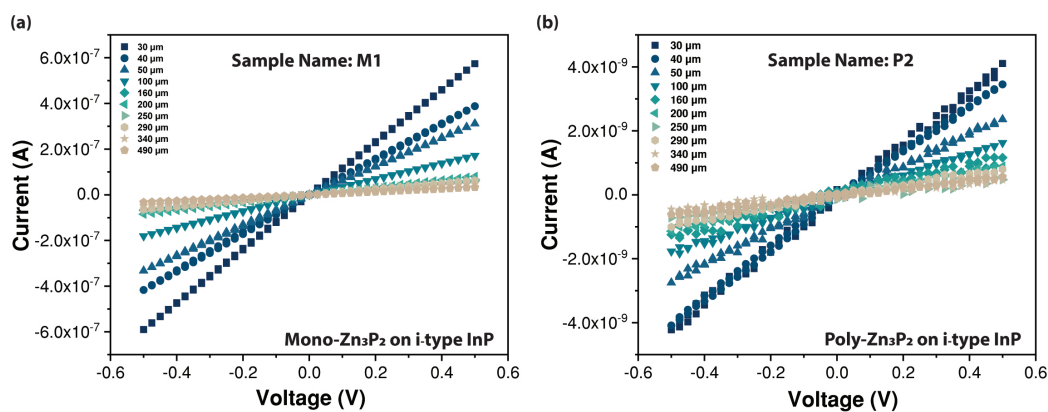


Figure B.3: I-V characteristic obtained as a function of distance between two contacts from (a) monocrystalline Zn_3P_2 thin film on n-InP (100) substrate (M3), a switch from linear I-V curve to non-linear I-V curve is observed at $\sim 100 \mu\text{m}$.

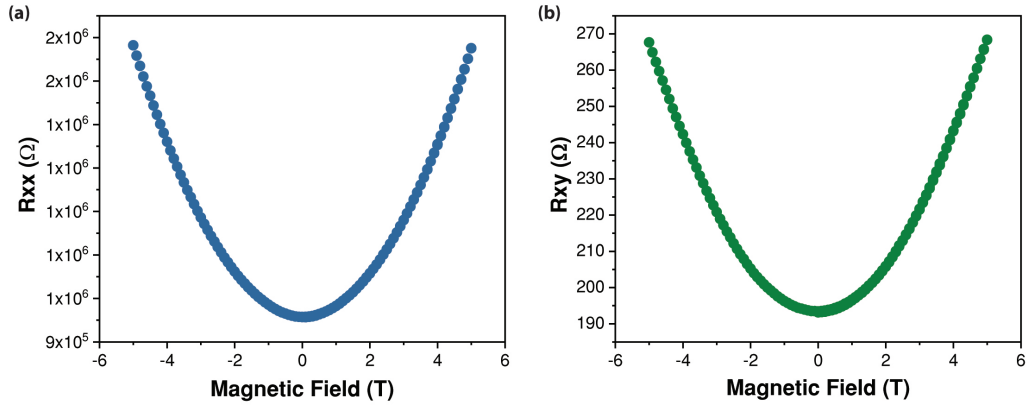


Figure B.4: Hall effect measurement done at 300 K using an injection current 0.1 μA (a) longitudinal resistance (R_{xx}) (b) transverse resistance (R_{xy}), plotted as a function of magnetic field.

Figure B.4(a) and b show the longitudinal resistance (R_{xx}) and transverse resistance (R_{xy}), respectively, as a function of the magnetic field. The measured R_{xx} increases with increase in the magnetic field and follows a parabolic dependence, as seen in Figure B.4(a). However, a parabolic dependence is also observed for the measurement of R_{xy} as a function of the magnetic field. Qualitatively, a non-linear behaviour with a clear offset from the origin indicates the R_{xy} measurements are largely influenced by the R_{xx} component, which could occur due to misalignment in hall probes [11].

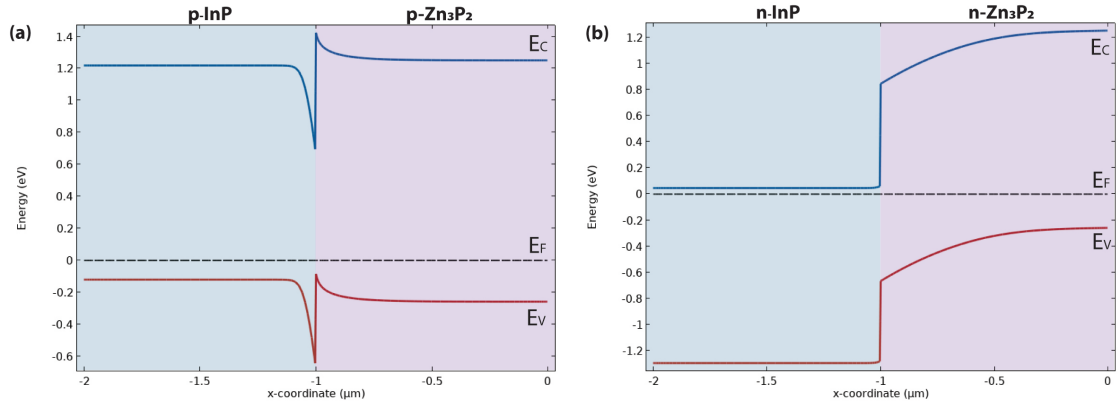


Figure B.5: COMSOL simulation of the band alignment between (a) p-InP and p- Zn_3P_2 (b) n-InP and p- Zn_3P_2 , a nominal carrier concentration of 10^{15}cm^{-3} is assumed for Zn_3P_2 and 10^{18}cm^{-3} for InP

C Supplementary information for “Carrier generation and collection in Zn₃P₂/InP heterojunction solar cells”

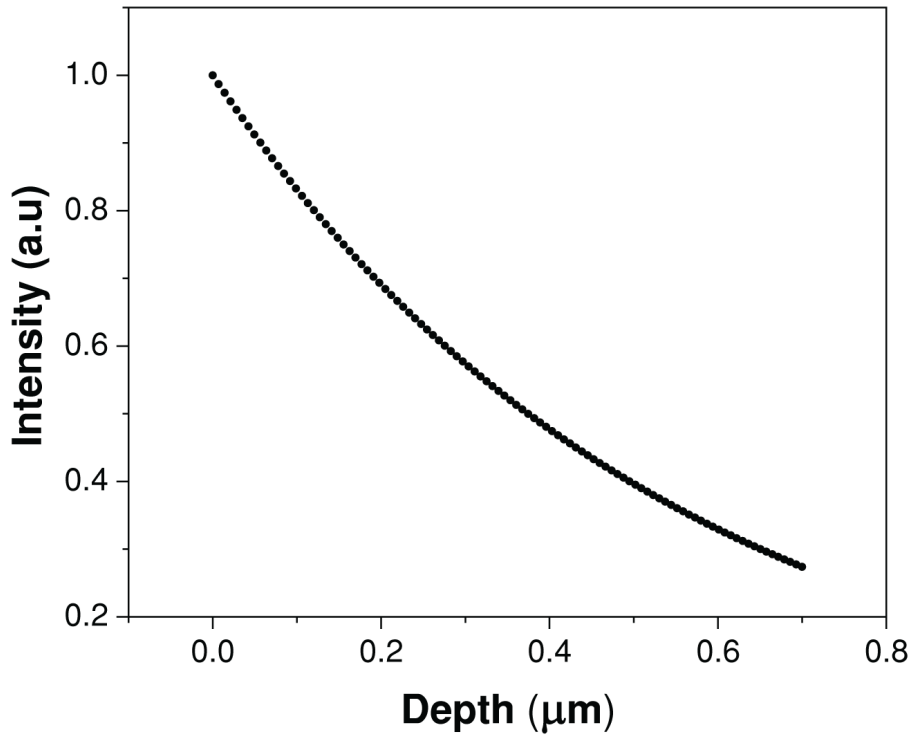


Figure C.1: The decay of pump intensity in the Zn₃P₂ thin film.

The decay of pump intensity in the Zn₃P₂ layer is calculated using the Beer-Lambert law

$$I = I_0 e^{-\alpha d} \quad (\text{C.1})$$

Where I and I_0 are pump intensity reaching thickness d and pump intensity at the front surface.

α is the absorption coefficient at the pump wavelength. Based on 700 nm thickness, almost ~75% of pump energy is absorbed in the Zn₃P₂ layer, leaving only ~25% reaching the InP substrate. Moreover, the OPTP measurements were taken in reflection mode, which is more sensitive to the surface layer. Thus, the overall response from THz measurements can be considered from the Zn₃P₂ layer itself.

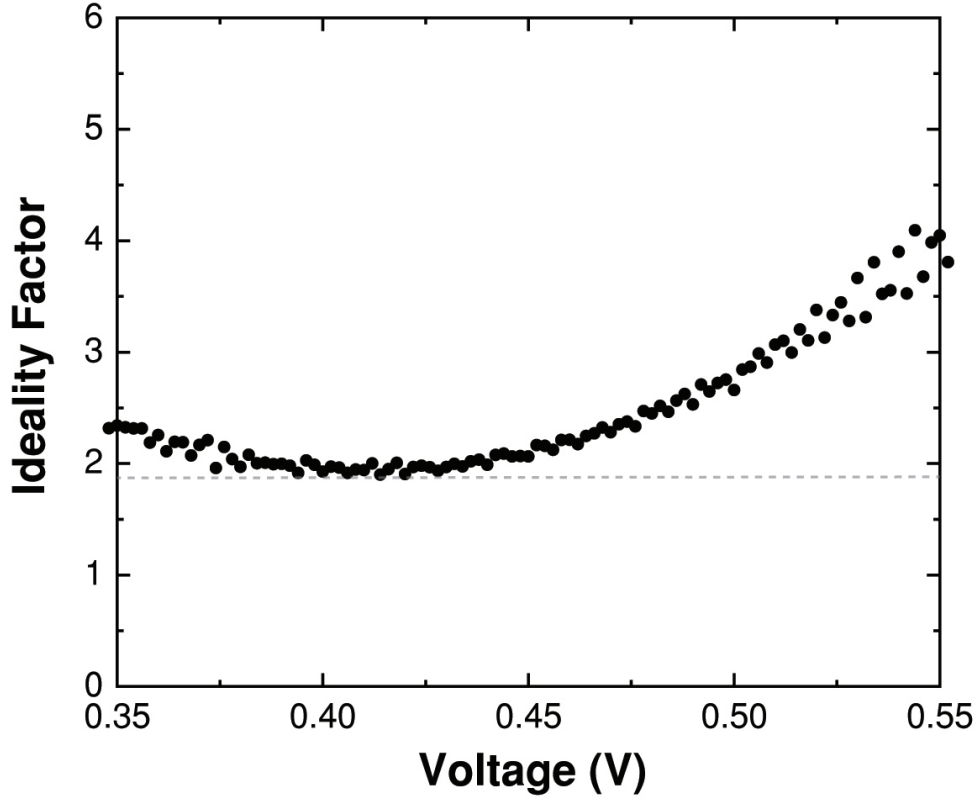


Figure C.2: The dark ideality factor is plotted as a function of the voltage, where the ideality factor-voltage characteristic is calculated by numerical differentiation according to Equation. C.2, and the ideality factor is obtained from the plateau.

The J-V curve is dominated by parasitic effects arising due to shunt and series resistance [273]. Therefore, the ideality factor can be plotted as a function of the voltage, where the ideality factor is derived from:

$$n_{id,l} = \left(\frac{k_B T}{q} \frac{d \ln J}{dV} \right)^{-1} \quad (C.2)$$

Figure C.2 shows the plot of the voltage-dependent ideality factor, the dashed line corresponds

to the minimum in the exponential region of the diode curve. The increase in the ideality factor towards the lower and higher voltage values is due to shunt and series resistance, respectively. The ideality factor obtained from the plateau in the n_{id} -V plot was 1.85. This is slightly lower than the value obtained by the other method (which is ~ 2).

C.1 Optical simulations

We use a finite-difference time-domain (FDTD) solver (Ansys Lumerical FDTD) for optical simulations. The following device stack was simulated (top to bottom): ITO (85 nm), Zn₃P₂ (700 nm), InP (10 μ m), Au (500 nm); The mesh accuracy was set to 10 nm normal to the layer stack, and 100 nm parallel to the stack for a “uniform” mesh type. The mesh refinement was set to “conformal variant 1”. The simulations were done in 3D, with periodic boundary conditions along the plane of the cell (500 nm range in x-/y-direction), and perfectly matched layers (PMLs) at both ends of the simulation region in z-direction. A plane-wave source at a distance of 2.4 μ m from the front of the solar cell was used as input, and dedicated “Transmission box” and “Solar generation rate” analysis groups were used to obtain absorption spectra and generation profiles, respectively.

C.2 Electronic simulations

A finite-element method-based drift-diffusion equation solver (Ansys Lumerical CHARGE) is used to calculate the electronic device performance. The device stack is the same as for the optical simulations. The mesh edge lengths are limited to a range between 10 nm and 1 μ m via “Global Mesh Constraints”. The device is simulated in the steady-state solver mode, and in 2D, with a “norm length” of 1 cm for the 3rd dimension. To simulate the device within an electric circuit, the front and back contacts are identified as electronic connection points. The front contact (ITO, $\varphi = 4.7$) is set to “force ohmic = false”, while the back contact (Au, $\varphi = 5.1$) is set to “force ohmic = true”. Surface/interface recombination is neglected, and the generation profiles from the optical simulations are imported via the designated import function. Band diagrams are recorded with the dedicated “Band Structure Monitor”, and IV curves are directly extracted from the “CHARGE”-solver window. A detailed listing of the parameter values used for the semiconductors (Zn₃P₂, InP) can be found in Table C.1.

Supplementary information for “Carrier generation and collection in Zn₃P₂/InP heterojunction solar cells”

Appendix

Table C.1: List of parameters used for the semiconductors in the drift-diffusion simulations.

Property	Units				
material name		Zn ₃ P ₂	InP	ITO	Au
material type		semiconductor	semiconductor	metal	metal
dc permittivity		11	12.4		
work function	eV	4.355	5.0105	4.7	5.1
E _c valley		Gamma	Gamma		
effective mass electrons	1/me	0.268	0.073		
effective mass holes	1/me	1.069	0.59		
E _g	eV	1.51	1.35		
n _i	1/cm ³	2.04E+06	1.08E+07		
mobility electrons	cm ² /(Vs)	1000	5300		
mobility holes	cm ² /(Vs)	20	200		
lifetime electrons	s	2.70E-08	1.00E-08		
lifetime holes	s	2.70E-08	3.00E-06		
Capture Coefficient Auger e.	cm ⁶ /s	n.a.	1.70E-33		
Capture Coefficient Auger h.	cm ⁶ /s	n.a.	9.00E-31		
radiative recombination coefficient	cm ³ /s	n.a.	2.00E-10		
n-type doping	cm ⁻³	0.00E+00	1.00E+16		
p-type doping	cm ⁻³	1.00E+15	0.00E+00		

Bibliography

- [1] Zakaria Y. Al Balushi et al. “The impact of graphene properties on GaN and AlN nucleation”. In: *Surface Science* 634 (2015). Graphene and Graphene Related Materials Growth on Surfaces, pp. 81–88. ISSN: 0039-6028. DOI: <https://doi.org/10.1016/j.susc.2014.11.020>. URL: <https://www.sciencedirect.com/science/article/pii/S0039602814003665>.
- [2] Yazeed Alaskar et al. “Towards van der Waals Epitaxial Growth of GaAs on Si using a Graphene Buffer Layer”. In: *Advanced Functional Materials* 24.42 (2014), pp. 6629–6638. DOI: <https://doi.org/10.1002/adfm.201400960>. eprint: <https://onlinelibrary.wiley.com/doi/pdf/10.1002/adfm.201400960>. URL: <https://onlinelibrary.wiley.com/doi/abs/10.1002/adfm.201400960>.
- [3] Matthew J. Allen, Vincent C. Tung, and Richard B. Kaner. “Honeycomb Carbon: A Review of Graphene”. In: *Chemical Reviews* 110.1 (2010). PMID: 19610631, pp. 132–145. DOI: 10.1021/cr900070d. eprint: <https://doi.org/10.1021/cr900070d>. URL: <https://doi.org/10.1021/cr900070d>.
- [4] Osbel Almora et al. “Quantifying the Absorption Onset in the Quantum Efficiency of Emerging Photovoltaic Devices”. In: *Advanced Energy Materials* 11.16 (2021). _eprint: <https://onlinelibrary.wiley.com/doi/pdf/10.1002/aenm.202100022>, p. 2100022. ISSN: 1614-6840. DOI: 10.1002/aenm.202100022. URL: <https://onlinelibrary.wiley.com/doi/abs/10.1002/aenm.202100022> (visited on 09/15/2022).
- [5] Pietro P. Altermatt et al. “Specifying targets of future research in photovoltaic devices containing pyrite (FeS₂) by numerical modelling”. In: *Solar Energy Materials and Solar Cells* 71.2 (Feb. 2002), pp. 181–195. ISSN: 0927-0248. DOI: 10.1016/S0927-0248(01)00053-8. URL: <https://www.sciencedirect.com/science/article/pii/S0927024801000538> (visited on 09/13/2022).
- [6] M H Ani et al. “A critical review on the contributions of chemical and physical factors toward the nucleation and growth of large-area graphene”. In: *Journal of Materials Science* 53.10 (2018), pp. 7095–7111. ISSN: 1573-4803. DOI: 10.1007/s10853-018-1994-0. URL: <https://doi.org/10.1007/s10853-018-1994-0>.

- [7] Mohd zubair Ansari and Neeraj Khare. "Thermally activated band conduction and variable range hopping conduction in Cu₂ZnSnS₄ thin films". In: *Journal of Applied Physics* 117 (2015), p. 025706. DOI: 10.1063/1.4905673.
- [8] Ezekiel Anyebe Anyebe and Manoj Kesaria. "Recent advances in the Van der Waals epitaxy growth of III-V semiconductor nanowires on graphene". In: *Nano Select* 2.4 (2021), pp. 688–711. DOI: <https://doi.org/10.1002/nano.202000142>. eprint: <https://onlinelibrary.wiley.com/doi/pdf/10.1002/nano.202000142>. URL: <https://onlinelibrary.wiley.com/doi/abs/10.1002/nano.202000142>.
- [9] T.V. Arjunan and T.S. Senthil. "Review: Dye sensitised solar cells". In: *Materials Technology* 28.1-2 (2013), pp. 9–14. ISSN: 1753-5557. DOI: 10.1179/1753555712Y.0000000040.
- [10] V Suresh Babu, P R Vaya, and J Sobhanadri. "Doping of Zn₃P₂ thin films during growth using the hot wall deposition technique and some properties of the grown films". In: *Semicond. Sci. Technol.* 4.7 (July 1989), pp. 521–525. ISSN: 0268-1242, 1361-6641. DOI: 10.1088/0268-1242/4/7/004. URL: <https://iopscience.iop.org/article/10.1088/0268-1242/4/7/004> (visited on 08/31/2022).
- [11] D. Backes et al. "Disentangling surface and bulk transport in topological insulator p-n junctions". In: *Physical Review B* 96 (May 2016). DOI: 10.1103/PhysRevB.96.125125.
- [12] S. Bae et al. "Roll-to-Roll Production of 30-Inch Graphene Films for Transparent Electrodes". In: *Nat. Nanotechnol.* 5 (2010), p. 574.
- [13] Muhammad Iqbal Bakti Utama et al. "Recent developments and future directions in the growth of nanostructures by van der Waals epitaxy". In: *Nanoscale* 5 (9 2013), pp. 3570–3588. DOI: 10.1039/C3NR34011B. URL: <http://dx.doi.org/10.1039/C3NR34011B>.
- [14] Alexander A. Balandin et al. "Superior Thermal Conductivity of Single-Layer Graphene". In: *Nano Letters* 8.3 (2008). PMID: 18284217, pp. 902–907. DOI: 10.1021/nl0731872. eprint: <https://doi.org/10.1021/nl0731872>. URL: <https://doi.org/10.1021/nl0731872>.
- [15] E. Banhart, J. Kotakoski, and A. V. Krasheninnikov. "Structural Defects in Graphene". In: *ACS Nano* 5 (2011), p. 26.
- [16] J. C. Bean et al. "Pseudomorphic growth of Ge_xSi_{1-x} on silicon by molecular beam epitaxy". In: *Applied Physics Letters* 44.1 (1984), pp. 102–104. DOI: 10.1063/1.94571. eprint: <https://doi.org/10.1063/1.94571>. URL: <https://doi.org/10.1063/1.94571>.
- [17] Biplab Bhattacharyya et al. "Evidence of robust 2D transport and Efros-Shklovskii variable range hopping in disordered topological insulator (Bi₂Se₃) nanowires". In: *Scientific Reports* 7 (2017). DOI: 10.1038/s41598-017-08018-6.
- [18] M. Bhushan. "Mg diffused zinc phosphide n/p junctions". In: *Journal of Applied Physics* 53.1 (1982), pp. 514–519. DOI: 10.1063/1.329956. eprint: <https://doi.org/10.1063/1.329956>. URL: <https://doi.org/10.1063/1.329956>.
- [19] M. Bhushan. "Schottky solar cells on thin polycrystalline Zn₃P₂ films". In: *Applied Physics Letters* 40.1 (1982), pp. 51–53. DOI: 10.1063/1.92921. eprint: <https://doi.org/10.1063/1.92921>. URL: <https://doi.org/10.1063/1.92921>.

Bibliography

- [20] M. Bhushan and A. Catalano. “Polycrystalline Zn_3P_2 Schottky barrier solar cells”. In: *Appl. Phys. Lett.* 38.1 (1981). Publisher: American Institute of Physics, pp. 39–41. ISSN: 0003-6951. DOI: 10.1063/1.92124. URL: <https://aip.scitation.org/doi/abs/10.1063/1.92124> (visited on 09/13/2022).
- [21] M. Bhushan and A. Catalano. “Polycrystalline Zn_3P_2 Schottky barrier solar cells”. In: *Applied Physics Letters* 38.1 (1981), pp. 39–41. DOI: 10.1063/1.92124. eprint: <https://doi.org/10.1063/1.92124>. URL: <https://doi.org/10.1063/1.92124>.
- [22] M. Bhushan and J. D. Meakin. *Zn_3P_2 as an improved semiconductor for photovoltaic solar cells*. Tech. rep. Publication Title: Final Report ADS Bibcode: 1985dela.reptQ....B. Mar. 1985. URL: <https://ui.adsabs.harvard.edu/abs/1985dela.reptQ....B> (visited on 09/13/2022).
- [23] P. Bonazzi et al. “A model for the mechanism of incorporation of Cu, Fe and Zn in the stannite - Kesterite series, $\text{Cu}_2\text{FeSnS}_4$ - $\text{Cu}_2\text{ZnSnS}_4$ ”. In: *Canadian Mineralogist* 41.3 (2003), pp. 639–647. ISSN: 0008-4476. DOI: 10.2113/gscanmin.41.3.639.
- [24] J.P. Bosco et al. “Band alignment of epitaxial $\text{ZnS}/\text{Zn}_3\text{P}_2$ heterojunctions”. In: *Journal of Applied Physics* 112.9 (2012). ISSN: 0021-8979. DOI: 10.1063/1.4759280.
- [25] Jeffrey P. Bosco et al. “Pseudomorphic growth and strain relaxation of α - Zn_3P_2 on GaAs(001) by molecular beam epitaxy”. In: *Journal of Crystal Growth* 363 (2013), pp. 205–210. ISSN: 0022-0248. DOI: <https://doi.org/10.1016/j.jcrysgro.2012.10.054>. URL: <https://www.sciencedirect.com/science/article/pii/S0022024812007695>.
- [26] Stéphane Bourdais et al. “Is the Cu/Zn Disorder the Main Culprit for the Voltage Deficit in Kesterite Solar Cells?” In: *Advanced Energy Materials* 6.12 (2016). _eprint: <https://onlinelibrary.wiley.com/doi/pdf/10.1002/aenm.201502276>, p. 1502276. ISSN: 1614-6840. DOI: 10.1002/aenm.201502276. URL: <https://onlinelibrary.wiley.com/doi/abs/10.1002/aenm.201502276> (visited on 09/13/2022).
- [27] J.A. Bragagnolo et al. “The design and fabrication of thin-film $\text{CdS}/\text{Cu}_2\text{S}$ cells of 9.15-percent conversion efficiency”. In: *IEEE Transactions on Electron Devices* 27.4 (Apr. 1980). Conference Name: IEEE Transactions on Electron Devices, pp. 645–651. ISSN: 1557-9646. DOI: 10.1109/T-ED.1980.19917.
- [28] Fernando Briones, Faa-Ching Wang, and Richard H. Bube. “Pair transitions in Zn_3P_2 ”. In: *Appl. Phys. Lett.* 39.10 (1981). Publisher: American Institute of Physics, pp. 805–807. ISSN: 0003-6951. DOI: 10.1063/1.92564. URL: <https://aip.scitation.org/doi/10.1063/1.92564> (visited on 09/13/2022).
- [29] V. V. Brus. “Light dependent open-circuit voltage of organic bulk heterojunction solar cells in the presence of surface recombination”. In: *Organic Electronics* 29 (Feb. 2016), pp. 1–6. ISSN: 1566-1199. DOI: 10.1016/j.orgel.2015.11.025. URL: <https://www.sciencedirect.com/science/article/pii/S1566119915302068> (visited on 09/14/2022).

-
- [30] P. de Bruyn et al. "Diffusion-Limited Current in Organic Metal-Insulator-Metal Diodes". In: *Physical Review Letters* 111.18 (Oct. 2013). Publisher: American Physical Society, p. 186801. DOI: 10.1103/PhysRevLett.111.186801. URL: <https://link.aps.org/doi/10.1103/PhysRevLett.111.186801> (visited on 09/14/2022).
 - [31] Richard H. Bube. *Photoelectronic Properties of Semiconductors*. Google-Books-ID: rVnCVGE6G34C. Cambridge University Press, May 1992. ISBN: 978-0-521-40681-9.
 - [32] M. Burgelman et al. "Defects in Cu(In, Ga) Se₂ semiconductors and their role in the device performance of thin-film solar cells". In: *Progress in Photovoltaics: Research and Applications* 5.2 (1997), pp. 121–130. ISSN: 1099-159X. DOI: 10.1002/(SICI)1099-159X(199703/04)5:2<121::AID-PIP159>3.0.CO;2-4. (Visited on 09/14/2022).
 - [33] Phil Calado et al. "Identifying Dominant Recombination Mechanisms in Perovskite Solar Cells by Measuring the Transient Ideality Factor". In: *Physical Review Applied* 11.4 (Apr. 2019). Publisher: American Physical Society, p. 044005. DOI: 10.1103/PhysRevApplied.11.044005. URL: <https://link.aps.org/doi/10.1103/PhysRevApplied.11.044005> (visited on 09/14/2022).
 - [34] A. Catalano and M. Bhushan. "Evidence of p/n homojunction formation in Zn₃P₂". In: *Applied Physics Letters* 37.6 (1980), pp. 567–569. DOI: 10.1063/1.91786. eprint: <https://doi.org/10.1063/1.91786>. URL: <https://doi.org/10.1063/1.91786>.
 - [35] A. Catalano and R. B. Hall. "Defect dominated conductivity in Zn₃P₂". In: *Journal of Physics and Chemistry of Solids* 41.6 (1980), pp. 635–640. ISSN: 0022-3697. DOI: 10.1016/0022-3697(80)90015-3. URL: <https://www.sciencedirect.com/science/article/pii/0022369780900153> (visited on 08/26/2022).
 - [36] Anthony Catalano, James Masi, and N. Wyeth. "Schottky Barrier Grid Devices on Zn₃P₂". In: *Journal of Applied Metalworking* (Jan. 1979). DOI: 10.1007/978-94-009-9487-4_50.
 - [37] Lin Chai et al. "A new strategy for the efficient exfoliation of graphite into graphene". In: *New Carbon Materials* 36.6 (2021), pp. 1179–1186. ISSN: 1872-5805. DOI: [https://doi.org/10.1016/S1872-5805\(21\)60100-2](https://doi.org/10.1016/S1872-5805(21)60100-2). URL: <https://www.sciencedirect.com/science/article/pii/S1872580521601002>.
 - [38] L. L. Chang and K. Ploog. *Molecular Beam Epitaxy and Heterostructures*. Google-Books-ID: GID1CAAQBAJ. Springer Science & Business Media, 2012. ISBN: 978-94-009-5073-3.
 - [39] C. Chen, J. Avila, and M. C. Asensio. "Chemical and Electronic Structure Imaging of Graphene on Cu: A NanoARPES Study". In: *J. Phys.: Condens. Matter* 29 (2017), p. 183001.
 - [40] Jian-Hao Chen et al. "Defect Scattering in Graphene". In: *Phys. Rev. Lett.* 102.23 (June 2009). Publisher: American Physical Society, p. 236805. DOI: 10.1103/PhysRevLett.102.236805. URL: <https://link.aps.org/doi/10.1103/PhysRevLett.102.236805> (visited on 09/12/2022).

- [41] Shiyu Chen et al. "Classification of Lattice Defects in the Kesterite Cu₂ZnSnS₄ and Cu₂ZnSnSe₄ Earth-Abundant Solar Cell Absorbers". In: *Advanced Materials* 25.11 (2013), pp. 1522–1539. ISSN: 1521-4095. DOI: 10.1002/adma.201203146. URL: <https://onlinelibrary.wiley.com/doi/abs/10.1002/adma.201203146> (visited on 09/13/2022).
- [42] Xiangping Chen, Lili Zhang, and Shanshan Chen. "Large area CVD growth of graphene". In: *Synthetic Metals* 210 (2015). Reviews of Current Advances in Graphene Science and Technology, pp. 95–108. ISSN: 0379-6779. DOI: <https://doi.org/10.1016/j.synthmet.2015.07.005>. URL: <https://www.sciencedirect.com/science/article/pii/S0379677915300138>.
- [43] Yang Chen et al. "Improved nucleation of AlN on in situ nitrogen doped graphene for GaN quasi-van der Waals epitaxy". In: *Applied Physics Letters* 117.5 (2020), p. 051601. DOI: 10.1063/5.0016054. eprint: <https://doi.org/10.1063/5.0016054>. URL: <https://doi.org/10.1063/5.0016054>.
- [44] Daniel A. Chenet et al. "In-Plane Anisotropy in Mono- and Few-Layer ReS₂ Probed by Raman Spectroscopy and Scanning Transmission Electron Microscopy". In: *Nano Lett.* 15.9 (Sept. 2015). Publisher: American Chemical Society, pp. 5667–5672. ISSN: 1530-6984. DOI: 10.1021/acs.nanolett.5b00910. URL: <https://doi.org/10.1021/acs.nanolett.5b00910> (visited on 09/12/2022).
- [45] A. Y. Cho. "Morphology of Epitaxial Growth of GaAs by a Molecular Beam Method: The Observation of Surface Structure". en. In: *Journal of Applied Physics* 41.7 (1970), pp. 2780–2786. ISSN: 0021-8979, 1089-7550. DOI: 10.1063/1.1659315. URL: <http://aip.scitation.org/doi/10.1063/1.1659315> (visited on 09/12/2022).
- [46] A. Y. Cho and J. R. Arthur. "Molecular beam epitaxy". In: *Progress in Solid State Chemistry* 10 (Jan. 1975), pp. 157–191. ISSN: 0079-6786. DOI: 10.1016/0079-6786(75)90005-9. URL: <https://www.sciencedirect.com/science/article/pii/0079678675900059> (visited on 09/12/2022).
- [47] S. Chu and A. Majumdar. "Opportunities and challenges for a sustainable energy future". In: *Nature* 488.7411 (2012), pp. 294–303. ISSN: 1476-4687. DOI: 10.1038/nature11475.
- [48] T. L. Chu et al. "Deposition and Properties of Zinc Phosphide Films". In: *J. Appl. Phys.* 54 (1983), p. 2063.
- [49] Choong-Heui Chung et al. "Current–voltage characteristics of fully solution processed high performance CuIn(S,Se)₂ solar cells: Crossover and red kink". In: *Solar Energy Materials and Solar Cells* 120 (Jan. 2014), pp. 642–646. ISSN: 0927-0248. DOI: 10.1016/j.solmat.2013.10.013. URL: <https://www.sciencedirect.com/science/article/pii/S0927024813005345>.
- [50] Kunook Chung et al. "Flexible GaN Light-Emitting Diodes Using GaN Microdisks Epitaxial Laterally Overgrown on Graphene Dots". In: *Advanced Materials* 28.35 (2016), pp. 7688–7694. DOI: <https://doi.org/10.1002/adma.201601894>. eprint: <https://onlinelibrary.wiley.com/doi/pdf/10.1002/adma.201601894>. URL: <https://onlinelibrary.wiley.com/doi/abs/10.1002/adma.201601894>.

- [51] Kunook Chung et al. "High-quality GaN films grown on chemical vapor-deposited graphene films". In: *NPG Asia Materials* 4.9 (2012), e24–e24. ISSN: 1884-4057. DOI: 10.1038/am.2012.45. URL: <https://doi.org/10.1038/am.2012.45>.
- [52] N.E. Courtier. "Interpreting Ideality Factors for Planar Perovskite Solar Cells: Ectypal Diode Theory for Steady-State Operation". In: *Physical Review Applied* 14.2 (Aug. 2020). Publisher: American Physical Society, p. 024031. DOI: 10.1103/PhysRevApplied.14.024031. URL: <https://link.aps.org/doi/10.1103/PhysRevApplied.14.024031> (visited on 09/14/2022).
- [53] Sarah R. Cowan, Anshuman Roy, and Alan J. Heeger. "Recombination in polymer-fullerene bulk heterojunction solar cells". In: *Physical Review B* 82.24 (Dec. 2010). Publisher: American Physical Society, p. 245207. DOI: 10.1103/PhysRevB.82.245207. URL: <https://link.aps.org/doi/10.1103/PhysRevB.82.245207> (visited on 09/14/2022).
- [54] Sarah R. Cowan et al. "Identifying a Threshold Impurity Level for Organic Solar Cells: Enhanced First-Order Recombination Via Well-Defined PC84BM Traps in Organic Bulk Heterojunction Solar Cells". In: *Advanced Functional Materials* 21.16 (2011). eprint: <https://onlinelibrary.wiley.com/doi/pdf/10.1002/adfm.201100514>, pp. 3083–3092. ISSN: 1616-3028. DOI: 10.1002/adfm.201100514. URL: <https://onlinelibrary.wiley.com/doi/abs/10.1002/adfm.201100514> (visited on 09/14/2022).
- [55] David C. Cox. *Introduction to Focused Ion Beam Nanometrology*. en. Morgan & Claypool Publishers, Oct. 2015. ISBN: 978-1-68174-084-3. URL: <https://iopscience.iop.org/book/mono/978-1-6817-4084-3> (visited on 09/12/2022).
- [56] M.T. Craig et al. "Overcoming the disconnect between energy system and climate modeling". In: *Joule* 6.7 (2022), pp. 1405–1417. ISSN: 2542-4351. DOI: 10.1016/j.joule.2022.05.010.
- [57] Giuseppe Cucinotta et al. "Space Charge-Limited Current Transport Mechanism in Crossbar Junction Embedding Molecular Spin Crossovers". In: *ACS Appl. Mater. Interfaces* 12.28 (July 2020). Publisher: American Chemical Society, pp. 31696–31705. ISSN: 1944-8244. DOI: 10.1021/acsami.0c07445. URL: <https://doi.org/10.1021/acsami.0c07445> (visited on 08/31/2022).
- [58] Ruchita S. Das and Y. K. Agrawal. "Raman spectroscopy: Recent advancements, techniques and applications". In: *Vibrational Spectroscopy* 57.2 (Nov. 2011), pp. 163–176. ISSN: 0924-2031. DOI: 10.1016/j.vibspec.2011.08.003. URL: <https://www.sciencedirect.com/science/article/pii/S0924203111001111> (visited on 09/12/2022).
- [59] P. Data et al. "Kesterite Inorganic-Organic Heterojunction for Solution Processable Solar Cells". In: *Electrochimica Acta* 201 (2016), pp. 78–85. ISSN: 0013-4686. DOI: 10.1016/j.electacta.2016.03.132.
- [60] John E. Davey and Titus Pankey. "Epitaxial GaAs Films Deposited by Vacuum Evaporation". In: *Journal of Applied Physics* 39.4 (1968), pp. 1941–1948. DOI: 10.1063/1.1656467. eprint: <https://doi.org/10.1063/1.1656467>. URL: <https://doi.org/10.1063/1.1656467>.

- [61] Steven Demers and Axel van de Walle. “Intrinsic defects and dopability of zinc phosphide”. In: *Phys. Rev. B* 85 (19 2012), p. 195208. DOI: 10.1103/PhysRevB.85.195208. URL: <https://link.aps.org/doi/10.1103/PhysRevB.85.195208>.
- [62] Mirjana Dimitrievska et al. “Influence of compositionally induced defects on the vibrational properties of device grade $\text{Cu}_2\text{ZnSnSe}_4$ absorbers for kesterite based solar cells”. In: *Appl. Phys. Lett.* 106.7 (Feb. 2015). Publisher: American Institute of Physics, p. 073903. ISSN: 0003-6951. DOI: 10.1063/1.4913262. URL: <https://aip.scitation.org/doi/10.1063/1.4913262> (visited on 09/12/2022).
- [63] Mirjana Dimitrievska et al. “The Advantage of Nanowire Configuration in Band Structure Determination (Adv. Funct. Mater. 41/2021)”. In: *Advanced Functional Materials* 31.41 (2021), p. 2170305. ISSN: 1616-3028. DOI: 10.1002/adfm.202170305. URL: <https://onlinelibrary.wiley.com/doi/abs/10.1002/adfm.202170305> (visited on 08/31/2022).
- [64] Alexander Dorodnyy et al. “Efficient Multiterminal Spectrum Splitting via a Nanowire Array Solar Cell”. In: *ACS Photonics* 2.9 (Sept. 2015). Publisher: American Chemical Society, pp. 1284–1288. DOI: 10.1021/acsp Photonics.5b00222. URL: <https://doi.org/10.1021/acsp Photonics.5b00222> (visited on 09/12/2022).
- [65] P. K. Dubey and V. V. Paranjape. “Open-circuit voltage of a Schottky-barrier solar cell”. In: *Journal of Applied Physics* 48.1 (1977), pp. 324–328. DOI: 10.1063/1.323381. eprint: <https://doi.org/10.1063/1.323381>. URL: <https://doi.org/10.1063/1.323381>.
- [66] Vladimir G. Dubrovskii et al. “Modeling the Shape Evolution of Selective Area Grown Zn_3P_2 Nanoislands”. In: *Crystal Growth & Design* 21.8 (2021), pp. 4732–4737. DOI: 10.1021/acs.cgd.1c00569. eprint: <https://doi.org/10.1021/acs.cgd.1c00569>. URL: <https://doi.org/10.1021/acs.cgd.1c00569>.
- [67] Elisabeth A. Duijnsteet et al. “Toward Understanding Space-Charge Limited Current Measurements on Metal Halide Perovskites”. In: *ACS Energy Lett.* 5.2 (Feb. 2020). Publisher: American Chemical Society, pp. 376–384. DOI: 10.1021/acsenerylett.9b02720. URL: <https://doi.org/10.1021/acsenerylett.9b02720> (visited on 08/31/2022).
- [68] Bruno Ehrler et al. “Photovoltaics Reaching for the Shockley–Queisser Limit”. In: *ACS Energy Lett.* 5.9 (Sept. 2020). Publisher: American Chemical Society, pp. 3029–3033. DOI: 10.1021/acsenerylett.0c01790. URL: <https://doi.org/10.1021/acsenerylett.0c01790> (visited on 09/13/2022).
- [69] A. Ennaoui and H. Tributsch. “Iron sulphide solar cells”. English. In: *Solar Cells* 13.2 (1984), pp. 197–200. ISSN: 0379-6787. DOI: 10.1016/0379-6787(84)90009-7.
- [70] Simon Escobar Steinvall et al. “Multiple morphologies and functionality of nanowires made from earth-abundant zinc phosphide”. In: *Nanoscale Horiz.* 5 (2 2020), pp. 274–282. DOI: 10.1039/C9NH00398C. URL: <http://dx.doi.org/10.1039/C9NH00398C>.
- [71] Saul Estandía et al. “Domain-Matching Epitaxy of Ferroelectric $\text{Hf}_{0.5}\text{Zr}_{0.5}\text{O}_2(111)$ on $\text{La}_{2/3}\text{Sr}_{1/3}\text{MnO}_3(001)$ ”. In: *Crystal Growth & Design* 20.6 (2020), pp. 3801–3806. DOI: 10.1021/acs.cgd.0c00095. eprint: <https://doi.org/10.1021/acs.cgd.0c00095>. URL: <https://doi.org/10.1021/acs.cgd.0c00095>.

- [72] E. A. Fagen. "Optical properties of Zn_3P_2 ". In: *Journal of Applied Physics* 50.10 (1979), pp. 6505–6515. DOI: 10.1063/1.325746. eprint: <https://doi.org/10.1063/1.325746>. URL: <https://doi.org/10.1063/1.325746>.
- [73] Robin F. C. Farrow. *Molecular Beam Epitaxy: Applications to Key Materials*. Google-Books-ID: wToPhW5TZosC. Elsevier, 1995. ISBN: 978-0-8155-1840-2.
- [74] M. Ferhat, J. C. Tedenac, and J. Nagao. "Mechanisms of Spiral Growth in Bi_2Te_3 Thin Films Grown by the Hot-Wall-Epitaxy Technique". In: *J. Cryst. Growth* 218 (2000), p. 250.
- [75] A. C. Ferrari et al. "Raman Spectrum of Graphene and Graphene Layers". In: *Phys. Rev. Lett.* 97.18 (Oct. 2006). Publisher: American Physical Society, p. 187401. DOI: 10.1103/PhysRevLett.97.187401. URL: <https://link.aps.org/doi/10.1103/PhysRevLett.97.187401> (visited on 09/12/2022).
- [76] Mischa Flór et al. "Raman tensor of zinc-phosphide (Zn_3P_2): from polarization measurements to simulation of Raman spectra". In: *Phys. Chem. Chem. Phys.* 24.1 (Dec. 2021). Publisher: The Royal Society of Chemistry, pp. 63–72. ISSN: 1463-9084. DOI: 10.1039/D1CP04322F. URL: <https://pubs.rsc.org/en/content/articlelanding/2022/cp/d1cp04322f> (visited on 09/12/2022).
- [77] Bryan D. Foster and R.E. Tressler. "SILICON PROCESSING WITH SILICON CARBIDE FURNACE COMPONENTS." In: *Solid State Technology* 27.10 (1984), pp. 143–146. ISSN: 0038-111X.
- [78] C.T. Foxon. "Three decades of molecular beam epitaxy". In: *Journal of Crystal Growth* 251.1 (2003). Proceedings of the Twelfth International Conference on Molecular Beam Epitaxy, pp. 1–8. ISSN: 0022-0248. DOI: [https://doi.org/10.1016/S0022-0248\(02\)02396-5](https://doi.org/10.1016/S0022-0248(02)02396-5). URL: <https://www.sciencedirect.com/science/article/pii/S0022024802023965>.
- [79] S. Franchi et al. "Quantum dot nanostructures and molecular beam epitaxy". In: *Progress in Crystal Growth and Characterization of Materials* 47.2 (2003). Vapour Growth of Bulk Crystals and Epitaxy: Part I, pp. 166–195. ISSN: 0960-8974. DOI: <https://doi.org/10.1016/j.pcrysgrow.2005.01.002>. URL: <https://www.sciencedirect.com/science/article/pii/S0960897405000021>.
- [80] Y. Fu et al. "Photoluminescence Spectra of Doped GaAs Films". In: *Appl. Phys. A: Mater. Sci. Process.* 79 (2004), p. 619.
- [81] Marco M. Furchi et al. "Photovoltaic Effect in an Electrically Tunable van der Waals Heterojunction". In: *Nano Letters* 14.8 (Aug. 2014). Publisher: American Chemical Society, pp. 4785–4791. ISSN: 1530-6984. DOI: 10.1021/nl501962c. URL: <https://doi.org/10.1021/nl501962c> (visited on 09/14/2022).
- [82] K. Gallacher et al. "Ohmic contacts to n-type germanium with low specific contact resistivity". In: *Appl. Phys. Lett.* 100.2 (Jan. 2012). Publisher: American Institute of Physics, p. 022113. ISSN: 0003-6951. DOI: 10.1063/1.3676667. URL: <https://aip.scitation.org/doi/abs/10.1063/1.3676667> (visited on 09/13/2022).

- [83] L.K. Ganta et al. "Synthesis of FeS₂ nano crystals for ink-based solar cells". In: *MRS Advances* 1447 (2012). ISBN: 9781510880320, pp. 108–113. ISSN: 2059-8521. DOI: 10.1557/opl.2012.1064.
- [84] Masoomeh Ghasemi et al. "Thermodynamic re-assessment of the Zn–P binary system". In: *Materialia* 6 (2019), p. 100301. ISSN: 2589-1529. DOI: <https://doi.org/10.1016/j.mtla.2019.100301>. URL: <https://www.sciencedirect.com/science/article/pii/S2589152919300973>.
- [85] V. M. Glazov, A. S. Pashinkin, and L. M. Pavlova. "Thermal Expansion of Gallium and Indium Phosphides: Thermodynamic Evaluation". In: *Inorganic Materials* 37.12 (Dec. 2001), pp. 1207–1215. ISSN: 1608-3172. DOI: 10.1023/A:1012928104121. URL: <https://doi.org/10.1023/A:1012928104121> (visited on 09/01/2022).
- [86] Jan G. Gluschke et al. "Impact of invasive metal probes on Hall measurements in semiconductor nanostructures". en. In: *Nanoscale* 12.39 (Oct. 2020). Publisher: The Royal Society of Chemistry, pp. 20317–20325. ISSN: 2040-3372. DOI: 10.1039/D0NR04402D. URL: <https://pubs.rsc.org/en/content/articlelanding/2020/nr/d0nr04402d> (visited on 09/13/2022).
- [87] Tayfun Gokmen et al. "Band tailing and efficiency limitation in kesterite solar cells". In: *Appl. Phys. Lett.* 103.10 (Sept. 2013). Publisher: American Institute of Physics, p. 103506. ISSN: 0003-6951. DOI: 10.1063/1.4820250. URL: <https://aip.scitation.org/doi/full/10.1063/1.4820250> (visited on 09/13/2022).
- [88] Yuancai Gong, Hao Xin, and Liming Ding. "Voc deficit in kesterite solar cells". In: *Journal of Semiconductors* 42.10 (June 2021), p. 100201. ISSN: 1674-4926. DOI: 10.1088/1674-4926/42/10/100201.
- [89] Yuancai Gong et al. "Identifying the origin of the Voc deficit of kesterite solar cells from the two grain growth mechanisms induced by Sn²⁺ and Sn⁴⁺ precursors in DMSO solution". In: *Energy Environ. Sci.* 14.4 (Apr. 2021). Publisher: The Royal Society of Chemistry, pp. 2369–2380. ISSN: 1754-5706. DOI: 10.1039/D0EE03702H. URL: <https://pubs.rsc.org/en/content/articlelanding/2021/ee/d0ee03702h> (visited on 09/13/2022).
- [90] Marius Grundmann. *The Physics of Semiconductors: An Introduction Including Nanophysics and Applications*. en. Graduate Texts in Physics. Springer International Publishing, 2016. DOI: 10.1007/978-3-319-23880-7. URL: <http://link.springer.com/10.1007/978-3-319-23880-7> (visited on 08/31/2022).
- [91] A. Gupta et al. "Raman Scattering from High-Frequency Phonons in Supported n-Graphene Layer Films". In: *Nano Lett.* 6.12 (Dec. 2006). Publisher: American Chemical Society, pp. 2667–2673. ISSN: 1530-6984. DOI: 10.1021/nl061420a. URL: <https://doi.org/10.1021/nl061420a> (visited on 09/12/2022).
- [92] Goutam Kumar Gupta, V. R. Reddy, and Ambesh Dixit. "Impact of excess and disordered Sn sites on Cu₂ZnSnS₄ absorber material and device performance: A ¹¹⁹Sn Mössbauer study". In: *Materials Chemistry and Physics* 225 (Mar. 2019), pp. 410–416. ISSN: 0254-

0584. DOI: 10.1016/j.matchemphys.2018.12.078. URL: <https://www.sciencedirect.com/science/article/pii/S0254058418311222> (visited on 08/31/2022).
- [93] M.S.G. Hamed and G.T. Mola. "Copper sulphide as a mechanism to improve energy harvesting in thin film solar cells". In: *Journal of Alloys and Compounds* 802 (2019), pp. 252–258. ISSN: 0925-8388. DOI: 10.1016/j.jallcom.2019.06.108.
- [94] S. E. Harrison et al. "Two-Step Growth of High Quality Bi₂Te₃ Thin Films on Al₂O₃ (0001) by Molecular Beam Epitaxy". In: *Appl. Phys. Lett.* 102 (2013), p. 171906.
- [95] M. Heilmann et al. "Vertically Oriented Growth of GaN Nanorods on Si Using Graphene as an Atomically Thin Buffer Layer". In: *Nano Lett.* 16 (2016), p. 3524.
- [96] Mohamed Henini. *Molecular Beam Epitaxy: From Research to Mass Production*. Google-Books-ID: OPZ5YGXpdC0C. Newnes, 2012. ISBN: 978-0-12-391859-8.
- [97] Young Joon Hong et al. "van der Waals Epitaxy of InAs Nanowires Vertically Aligned on Single-Layer Graphene". In: *Nano Letters* 12.3 (2012). PMID: 22324301, pp. 1431–1436. DOI: 10.1021/nl204109t. eprint: <https://doi.org/10.1021/nl204109t>. URL: <https://doi.org/10.1021/nl204109t>.
- [98] A Ishii et al. "DFT calculation for adatom adsorption on graphene sheet as a prototype of carbon nanotube functionalization". In: *Journal of Physics: Conference Series* 100.5 (2008), p. 052087. DOI: 10.1088/1742-6596/100/5/052087. URL: <https://doi.org/10.1088/1742-6596/100/5/052087>.
- [99] W Jaegermann et al. "Perspectives of the concept of van der Waals epitaxy: growth of lattice mismatched GaSe(0001) films on Si(111), Si(110) and Si(100)". In: *Thin Solid Films* 380.1 (2000), pp. 276–281. ISSN: 0040-6090. DOI: [https://doi.org/10.1016/S0040-6090\(00\)01523-6](https://doi.org/10.1016/S0040-6090(00)01523-6). URL: <https://www.sciencedirect.com/science/article/pii/S0040609000015236>.
- [100] Dongsoo Jang et al. *Thru-Hole Epitaxy: Is Remote Epitaxy Really Remote?* 2021. DOI: 10.48550/ARXIV.2110.01429. URL: <https://arxiv.org/abs/2110.01429>.
- [101] X. Ji, D. Yang, and J. Da. "Researches of preparation technologies, defects and properties of silicon based single-junction solar cells". In: *Cailiao Daobao/Materials Review* 30.2 (2016), 15–18 and 28. ISSN: 1005-023X. DOI: 10.11896/j.issn.1005-023X.2016.03.003.
- [102] J. Johansson et al. "Structural Properties of <111>B -oriented III-V Nanowires". In: *Nat. Mater.* 5 (2006), p. 574.
- [103] M. D. Johnson et al. "Stable and unstable growth in molecular beam epitaxy". In: *Phys. Rev. Lett.* 72.1 (1994). Publisher: American Physical Society, pp. 116–119. DOI: 10.1103/PhysRevLett.72.116. URL: <https://link.aps.org/doi/10.1103/PhysRevLett.72.116> (visited on 09/12/2022).
- [104] Robin R. Jones et al. "Raman Techniques: Fundamentals and Frontiers". In: *Nanoscale Res Lett* 14.1 (Dec. 2019), p. 231. ISSN: 1931-7573, 1556-276X. DOI: 10.1186/s11671-019-3039-2. URL: <https://nanoscalereslett.springeropen.com/articles/10.1186/s11671-019-3039-2> (visited on 09/12/2022).

Bibliography

- [105] T Journot et al. “Remote epitaxy using graphene enables growth of stress-free GaN”. In: *Nanotechnology* 30.50 (2019), p. 505603. DOI: 10.1088/1361-6528/ab4501. URL: <https://doi.org/10.1088/1361-6528/ab4501>.
- [106] Bruce A Joyce and Tim B Joyce. “Basic studies of molecular beam epitaxy—past, present and some future directions”. In: *Journal of Crystal Growth* 264.4 (2004). Proceedings of the Symposium - Progress in Crystal Growth, pp. 605–619. ISSN: 0022-0248. DOI: <https://doi.org/10.1016/j.jcrysgro.2003.12.045>. URL: <https://www.sciencedirect.com/science/article/pii/S0022024803022498>.
- [107] Hannah J. Joyce et al. “A review of the electrical properties of semiconductor nanowires: insights gained from terahertz conductivity spectroscopy”. In: *Semiconductor Science and Technology* 31.10 (Sept. 2016). Publisher: IOP Publishing, p. 103003. ISSN: 0268-1242. DOI: 10.1088/0268-1242/31/10/103003. URL: <https://doi.org/10.1088/0268-1242/31/10/103003> (visited on 09/15/2022).
- [108] Zhen-Yu Juang et al. “Graphene synthesis by chemical vapor deposition and transfer by a roll-to-roll process”. In: *Carbon* 48.11 (2010), pp. 3169–3174. ISSN: 0008-6223. DOI: <https://doi.org/10.1016/j.carbon.2010.05.001>. URL: <https://www.sciencedirect.com/science/article/pii/S0008622310003222>.
- [109] Kazuhiko Kakishita, Toshio Baba, and Toshikazu Suda. “Zn₃P₂ thin films grown on glass substrates by MOCVD”. In: *Thin Solid Films* 334.1 (1998), pp. 25–29. ISSN: 0040-6090. DOI: 10.1016/S0040-6090(98)01110-9. URL: <https://www.sciencedirect.com/science/article/pii/S0040609098011109> (visited on 08/31/2022).
- [110] E.O. Kane. “Band tails in semiconductors”. In: *Solid State Electronics* 28.1-2 (1985), pp. 3–10. ISSN: 0038-1101. DOI: 10.1016/0038-1101(85)90203-5.
- [111] A. Karma and M. Plapp. “Spiral Surface Growth without Desorption”. In: *Phys. Rev. Lett.* 81 (1998), p. 4444.
- [112] Hironori Katagiri et al. “Preparation and evaluation of Cu₂ZnSnS₄ thin films by sulfurization of E-B evaporated precursors”. In: *Solar Energy Materials and Solar Cells* 49.1 (Dec. 1997), pp. 407–414. ISSN: 0927-0248. DOI: 10.1016/S0927-0248(97)00119-0. URL: <https://www.sciencedirect.com/science/article/pii/S0927024897001190> (visited on 09/13/2022).
- [113] R. Katsube and Y. Nose. “Orientation of Zn₃P₂ Films via Phosphidation of Zn Precursors”. In: *J. Cryst. Growth* 459 (2017), p. 95.
- [114] Ryoji Katsube et al. “Growth and characterization of indium-doped Zn₃P₂ bulk crystals”. In: *Japanese Journal of Applied Physics* 55 (2016). DOI: 10.7567/JJAP.55.041201.
- [115] Ryoji Katsube et al. “Reactive Epitaxial Formation of a Mg–P–Zn Ternary Semiconductor in Mg/Zn₃P₂ Solar Cells”. In: *ACS Applied Materials & Interfaces* 10.42 (2018), pp. 36102–36107. DOI: 10.1021/acsami.8b11423. eprint: <https://doi.org/10.1021/acsami.8b11423>. URL: <https://doi.org/10.1021/acsami.8b11423>.

- [116] Piran R. Kidambi et al. "Observing Graphene Grow: Catalyst–Graphene Interactions during Scalable Graphene Growth on Polycrystalline Copper". In: *Nano Letters* 13.10 (2013). PMID: 24041311, pp. 4769–4778. DOI: 10.1021/nl4023572. eprint: <https://doi.org/10.1021/nl4023572>. URL: <https://doi.org/10.1021/nl4023572>.
- [117] N. Kilinc-Ata. "The evaluation of renewable energy policies across EU countries and US states: An econometric approach". In: *Energy for Sustainable Development* 31 (2016), pp. 83–90. ISSN: 0973-0826. DOI: 10.1016/j.esd.2015.12.006.
- [118] Jeehwan Kim et al. "Principle of direct van der Waals epitaxy of single-crystalline films on epitaxial graphene". In: *Nature Communications* 5.1 (2014), p. 4836. ISSN: 2041-1723. DOI: 10.1038/ncomms5836. URL: <https://doi.org/10.1038/ncomms5836>.
- [119] Y. Kim et al. "Synthesis of High Quality Graphene on Capped (111) Cu Thin Films Obtained by High Temperature Secondary Grain Growth on c-Plane Sapphire Substrates". In: *2D Mater.* 5 (2018), p. 035008.
- [120] Yong-Jin Kim, Jae-Hyun Lee, and Gyu-Chul Yi. "Vertically aligned ZnO nanostructures grown on graphene layers". In: *Applied Physics Letters* 95.21 (2009), p. 213101. DOI: 10.1063/1.3266836. eprint: <https://doi.org/10.1063/1.3266836>. URL: <https://doi.org/10.1063/1.3266836>.
- [121] G.M. Kimball, N.S. Lewis, and H.A. Atwater. "Mg doping and alloying in Zn_3P_2 heterojunction solar cells". In: ISSN: 0160-8371. 2010, pp. 1039–1043. ISBN: 978-1-4244-5891-2. DOI: 10.1109/PVSC.2010.5614641.
- [122] G.M. Kimball et al. "Passivation of Zn_3P_2 substrates by aqueous chemical etching and air oxidation". In: *Journal of Applied Physics* 112.10 (2012). ISSN: 0021-8979. DOI: 10.1063/1.4765030.
- [123] Gregory M. Kimball, Nathan S. Lewis, and Harry A. Atwater. "Direct evidence of Mg-Zn-P alloy formation in Mg/ Zn_3P_2 solar cells". In: (2011), pp. 003381–003381. DOI: 10.1109/PVSC.2011.6186672.
- [124] Gregory M. Kimball, Nathan S. Lewis, and Harry A. Atwater. "Synthesis and surface chemistry of Zn_3P_2 ". In: *2008 33rd IEEE Photovoltaic Specialists Conference*. ISSN: 0160-8371. 2008, pp. 1–6. DOI: 10.1109/PVSC.2008.4922747.
- [125] Gregory M. Kimball et al. "Photoluminescence-based measurements of the energy gap and diffusion length of Zn_3P_2 ". In: *Applied Physics Letters* 95.11 (2009), p. 112103. DOI: 10.1063/1.3225151. eprint: <https://doi.org/10.1063/1.3225151>. URL: <https://doi.org/10.1063/1.3225151>.
- [126] L.C. Kimerling. "Defect control in silicon processing". In: vol. 90. ISSN: 0161-6374 Issue: 7. 1990, pp. 117–130.
- [127] Thomas Kirchartz et al. "On the Differences between Dark and Light Ideality Factor in Polymer:Fullerene Solar Cells". In: *The Journal of Physical Chemistry Letters* 4.14 (July 2013). Publisher: American Chemical Society, pp. 2371–2376. DOI: 10.1021/jz4012146. URL: <https://doi.org/10.1021/jz4012146> (visited on 09/14/2022).

- [128] Thomas Kirchartz et al. “Recombination via tail states in polythiophene:fullerene solar cells”. In: *Physical Review B* 83.11 (Mar. 2011). Publisher: American Physical Society, p. 115209. DOI: 10.1103/PhysRevB.83.115209. URL: <https://link.aps.org/doi/10.1103/PhysRevB.83.115209> (visited on 09/14/2022).
- [129] Diane S. Knight and William B. White. “Characterization of diamond films by Raman spectroscopy”. In: *Journal of Materials Research* 4.2 (Mar. 1989), pp. 385–393. ISSN: 2044-5326. DOI: 10.1557/JMR.1989.0385. URL: <https://doi.org/10.1557/JMR.1989.0385> (visited on 09/12/2022).
- [130] A. Koma, K. Sunouchi, and T. Miyajima. “Fabrication and Characterization of Heterostructures with Subnanometer Thickness”. In: *Microelectron. Eng.* 2 (1984), p. 129.
- [131] Atsushi Koma. “Van der Waals epitaxy—a new epitaxial growth method for a highly lattice-mismatched system”. In: *Thin Solid Films* 216.1 (1992). Papers presented at the International Workshop on Science and Technology of Thin Films for the 21st Century, Evanston, IL, USA, July 28–August 2, 1991, pp. 72–76. ISSN: 0040-6090. DOI: [https://doi.org/10.1016/0040-6090\(92\)90872-9](https://doi.org/10.1016/0040-6090(92)90872-9). URL: <https://www.sciencedirect.com/science/article/pii/0040609092908729>.
- [132] M. Kondo. “Future prospects for Silicon solar cells”. In: *Nihon Enerugi Gakkaishi/Journal of the Japan Institute of Energy* 87.3 (2008), pp. 163–168. ISSN: 0916-8753.
- [133] Wei Kong et al. “Polarity governs atomic interaction through two-dimensional materials”. In: *Nature Materials* 17.11 (2018), pp. 999–1004. ISSN: 1476-4660. DOI: 10.1038/s41563-018-0176-4. URL: <https://doi.org/10.1038/s41563-018-0176-4>.
- [134] L. J. A. Koster et al. “Light intensity dependence of open-circuit voltage of polymer:fullerene solar cells”. In: *Applied Physics Letters* 86.12 (Mar. 2005). Publisher: American Institute of Physics, p. 123509. ISSN: 0003-6951. DOI: 10.1063/1.1889240.
- [135] Martijn Kuik et al. “Determination of the trap-assisted recombination strength in polymer light emitting diodes”. In: *Applied Physics Letters* 98.9 (Feb. 2011). Publisher: American Institute of Physics, p. 093301. ISSN: 0003-6951. DOI: 10.1063/1.3559911. URL: <https://aip.scitation.org/doi/10.1063/1.3559911> (visited on 09/14/2022).
- [136] Rajesh Kumar and Neeraj Khare. “Temperature dependence of conduction mechanism of ZnO and Co-doped ZnO thin films”. In: *Thin Solid Films* 516.6 (2008), pp. 1302–1307. ISSN: 0040-6090. DOI: 10.1016/j.tsf.2007.06.121. URL: <https://www.sciencedirect.com/science/article/pii/S0040609007010656> (visited on 08/31/2022).
- [137] O. Kunz et al. “Shunting problems due to sub-micron pinholes in evaporated solid-phase crystallised poly-Si thin-film solar cells on glass”. In: *Progress in Photovoltaics: Research and Applications* 17.1 (2009), pp. 35–46. ISSN: 1099-159X. DOI: 10.1002/pip.866. URL: <https://onlinelibrary.wiley.com/doi/abs/10.1002/pip.866> (visited on 09/15/2022).
- [138] L. N. Kurbatov et al. “Luminescence of Cadmium and Zinc Phosphides”. In: *Sov. J. Quantum Electron.* 6 (1976), p. 166.

- [139] Akio Kuroyanagi and Toshikazu Suda. "Photovoltaic Properties in CdS/Zn₃P₂ Heterojunctions Prepared by Ionized Evaporation of CdS". In: *Ieej Transactions on Electronics, Information and Systems* 108 (1988), pp. 891–895.
- [140] Akio Kuroyanagi and Tosikazu Suda. "Single crystal growth and characterization of zinc phosphide". In: *Journal of Crystal Growth* 100.1 (1990), pp. 1–4. ISSN: 0022-0248. DOI: 10.1016/0022-0248(90)90601-G. URL: <https://www.sciencedirect.com/science/article/pii/002202489090601G> (visited on 08/31/2022).
- [141] Murray A. Lampert. "Simplified Theory of Space-Charge-Limited Currents in an Insulator with Traps". en. In: *Phys. Rev.* 103.6 (Sept. 1956), pp. 1648–1656. ISSN: 0031-899X. DOI: 10.1103/PhysRev.103.1648. URL: <https://link.aps.org/doi/10.1103/PhysRev.103.1648> (visited on 09/01/2022).
- [142] Sandra M. Lang et al. "Thermal stability of iron–sulfur clusters". In: *Phys. Chem. Chem. Phys.* 20.11 (Mar. 2018). Publisher: The Royal Society of Chemistry, pp. 7781–7790. ISSN: 1463-9084. DOI: 10.1039/C8CP00515J. URL: <https://pubs.rsc.org/en/content/articlelanding/2018/cp/c8cp00515j> (visited on 09/13/2022).
- [143] Mario Lanza. *Conductive Atomic Force Microscopy: Applications in Nanomaterials*. en. Google-Books-ID: _EozDwAAQBAJ. John Wiley & Sons, Dec. 2017. ISBN: 978-3-527-34091-0.
- [144] Vincent M. Le Corre et al. "Revealing Charge Carrier Mobility and Defect Densities in Metal Halide Perovskites via Space-Charge-Limited Current Measurements". In: *ACS Energy Lett.* 6.3 (Mar. 2021). Publisher: American Chemical Society, pp. 1087–1094. DOI: 10.1021/acsenerylett.0c02599. URL: <https://doi.org/10.1021/acsenerylett.0c02599> (visited on 08/31/2022).
- [145] C. Lee et al. "Measurement of the Elastic Properties and Intrinsic Strength of Monolayer Graphene". In: *Science* 321 (2008), p. 385.
- [146] C.W. Lee and J. Zhong. "Top down strategy for renewable energy investment: Conceptual framework and implementation". In: *Renewable Energy* 68 (2014), pp. 761–773. ISSN: 0960-1481. DOI: 10.1016/j.renene.2014.03.015.
- [147] H. Cheun Lee et al. "Synthesis of Single-layer Graphene: A Review of Recent Development". In: *Procedia Chemistry* 19 (2016). 5th International Conference on Recent Advances in Materials, Minerals and Environment (RAMM) & 2nd International Postgraduate Conference on Materials, Mineral and Polymer (MAMIP), pp. 916–921. ISSN: 1876-6196. DOI: <https://doi.org/10.1016/j.proche.2016.03.135>. URL: <https://www.sciencedirect.com/science/article/pii/S1876619616001819>.
- [148] S.-M. Lee, J.-H. Kim, and J.-H. Ahn. "Graphene as a Flexible Electronic Material: Mechanical Limitations by Defect Formation and Efforts to Overcome". In: *Mater. Today* 18 (2015), p. 336.
- [149] G. Lei et al. "Influence factor analysis of solar absorptivity of crystalline silicon solar cell". In: *Taiyangneng Xuebao/Acta Energiæ Solaris Sinica* 36.10 (2015), pp. 2329–2334. ISSN: 0254-0096.

Bibliography

- [150] J. Li et al. "Cation Substitution in Earth-Abundant Kesterite Photovoltaic Materials". In: *Advanced Science* 5.4 (2018). ISSN: 2198-3844. DOI: 10.1002/adv.201700744.
- [151] Tianbao Li et al. "Understanding the Growth Mechanism of GaN Epitaxial Layers on Mechanically Exfoliated Graphite". In: *Nanoscale Research Letters* 13.1 (2018), p. 130. ISSN: 1556-276X. DOI: 10.1186/s11671-018-2546-x. URL: <https://doi.org/10.1186/s11671-018-2546-x>.
- [152] Dongdong Liang et al. "Quasi van der Waals epitaxy nitride materials and devices on two dimension materials". In: *Nano Energy* 69 (2020), p. 104463. ISSN: 2211-2855. DOI: <https://doi.org/10.1016/j.nanoen.2020.104463>. URL: <https://www.sciencedirect.com/science/article/pii/S2211285520300197>.
- [153] G. Lindwall et al. "Thermodynamics of the S-Sn system: Implication for synthesis of earth abundant photovoltaic absorber materials". In: *Solar Energy* 125 (2016), pp. 314–323. ISSN: 0038-092X. DOI: 10.1016/j.solener.2015.12.013.
- [154] A. J. Littlejohn et al. "van der Waals epitaxy of Ge films on mica". In: *Journal of Applied Physics* 122.18 (2017), p. 185305. DOI: 10.1063/1.5000502. eprint: <https://doi.org/10.1063/1.5000502>. URL: <https://doi.org/10.1063/1.5000502>.
- [155] Maixian Liu et al. "Recent advances in copper sulphide-based nanoheterostructures". In: *Chem. Soc. Rev.* 48.19 (Sept. 2019). Publisher: The Royal Society of Chemistry, pp. 4950–4965. ISSN: 1460-4744. DOI: 10.1039/C8CS00832A. URL: <https://pubs.rsc.org/en/content/articlelanding/2019/cs/c8cs00832a> (visited on 09/13/2022).
- [156] Nan Liu et al. "Universal Segregation Growth Approach to Wafer-Size Graphene from Non-Noble Metals". In: *Nano Letters* 11.1 (2011). PMID: 21128676, pp. 297–303. DOI: 10.1021/nl103962a. eprint: <https://doi.org/10.1021/nl103962a>. URL: <https://doi.org/10.1021/nl103962a>.
- [157] X. Liu et al. "The current status and future prospects of kesterite solar cells: A brief review". In: *Progress in Photovoltaics: Research and Applications* 24.6 (2016), pp. 879–898. ISSN: 1062-7995. DOI: 10.1002/pip.2741.
- [158] Y. Liu, M. Weinert, and L. Li. "Spiral Growth without Dislocations: Molecular Beam Epitaxy of the Topological Insulator Bi₂Se₃ on Epitaxial Graphene/SiC(0001)". In: *Phys. Rev. Lett.* 108 (2012), p. 115501.
- [159] James Lloyd-Hughes and Tae-In Jeon. "A Review of the Terahertz Conductivity of Bulk and Nano-Materials". In: *Journal of Infrared, Millimeter, and Terahertz Waves* 33.9 (Sept. 2012), pp. 871–925. ISSN: 1866-6906. DOI: 10.1007/s10762-012-9905-y. URL: <https://doi.org/10.1007/s10762-012-9905-y> (visited on 09/15/2022).
- [160] G. Lombardi et al. "Investigation of trapping levels in p-type Zn₃P₂ nanowires using transport and optical properties". In: *Applied Physics Letters* 112 (2018), p. 193103. DOI: 10.1063/1.5026548.

- [161] Derek Long. "The Raman Effect: A Unified Treatment of the Theory of Raman Scattering by Molecules". In: May 2002, pp. 49–84. ISBN: 978-0-470-84576-9. DOI: 10.1002/0470845767.ch4.
- [162] J. Long. "The Growth of Zn_3P_2 by Metalorganic Chemical Vapor Deposition". In: *J. Electrochem. Soc.* 130 (1983), p. 725.
- [163] Judith Long. "The Growth of Zn_3P_2 by Metalorganic Chemical Vapor Deposition". In: *J. Electrochem. Soc.* 130.3 (Mar. 1983). Publisher: IOP Publishing, p. 725. ISSN: 1945-7111. DOI: 10.1149/1.2119791. URL: <https://iopscience.iop.org/article/10.1149/1.2119791/meta> (visited on 09/01/2022).
- [164] David Look. "Electrical Characterization of GaAs Materials and Devices". In: *Books Authored by Wright State Faculty/Staff* (Jan. 1989). URL: <https://corescholar.libraries.wright.edu/books/32>.
- [165] Oriol Lopez-Sanchez et al. "Ultrasensitive photodetectors based on monolayer MoS_2 ". In: *Nature Nanotechnology* 8.7 (July 2013). Number: 7 Publisher: Nature Publishing Group, pp. 497–501. ISSN: 1748-3395. DOI: 10.1038/nnano.2013.100. URL: <https://www.nature.com/articles/nnano.2013.100> (visited on 09/14/2022).
- [166] D. L. Mafra et al. "Determination of LA and TO phonon dispersion relations of graphene near the Dirac point by double resonance Raman scattering". In: *Phys. Rev. B* 76.23 (Dec. 2007). Publisher: American Physical Society, p. 233407. DOI: 10.1103/PhysRevB.76.233407. URL: <https://link.aps.org/doi/10.1103/PhysRevB.76.233407> (visited on 09/12/2022).
- [167] S. Mahajan. "Defects in semiconductors and their effects on devices". In: *Acta Materialia* 48.1 (2000), pp. 137–149. ISSN: 1359-6454. DOI: [https://doi.org/10.1016/S1359-6454\(99\)00292-X](https://doi.org/10.1016/S1359-6454(99)00292-X). URL: <https://www.sciencedirect.com/science/article/pii/S135964549900292X>.
- [168] Asif Mahmood and Jin-Liang Wang. "A Review of Grazing Incidence Small- and Wide-Angle X-Ray Scattering Techniques for Exploring the Film Morphology of Organic Solar Cells". In: *Solar RRL* 4.10 (2020), p. 2000337. ISSN: 2367-198X. DOI: 10.1002/solr.202000337. URL: <https://onlinelibrary.wiley.com/doi/abs/10.1002/solr.202000337> (visited on 08/31/2022).
- [169] L.M. Malard et al. "Raman spectroscopy in graphene". In: *Physics Reports* 473.5 (2009), pp. 51–87. ISSN: 0370-1573. DOI: <https://doi.org/10.1016/j.physrep.2009.02.003>. URL: <https://www.sciencedirect.com/science/article/pii/S0370157309000520>.
- [170] Anha Masarrat et al. "Enhancement of the Thermoelectric Properties and Transition of Conduction Mechanism from Nearest Neighbor to Variable Range Hopping of Ni-Doped CoSb_3 ". In: *J. Electron. Mater.* 51.6 (2022), pp. 3350–3358. ISSN: 1543-186X. DOI: 10.1007/s11664-022-09547-1. URL: <https://doi.org/10.1007/s11664-022-09547-1> (visited on 08/31/2022).

Bibliography

- [171] Hideharu Matsuura et al. “Transition of conduction mechanism from band to variable-range hopping conduction due to Al doping in heavily Al-doped 4H-SiC epilayers”. In: *Jpn. J. Appl. Phys.* 58.9 (2019), p. 098004. ISSN: 0021-4922, 1347-4065. DOI: 10.7567/1347-4065/ab3c2c. URL: <https://iopscience.iop.org/article/10.7567/1347-4065/ab3c2c> (visited on 08/26/2022).
- [172] J. C. Meyer et al. “Direct Imaging of Lattice Atoms and Topological Defects in Graphene Membranes”. In: *Nano Lett.* 8 (2008), p. 3582.
- [173] Dmitry Mikulik et al. “Conductive-probe atomic force microscopy as a characterization tool for nanowire-based solar cells”. In: *Nano Energy* 41 (Nov. 2017), pp. 566–572. ISSN: 2211-2855. DOI: 10.1016/j.nanoen.2017.10.016. URL: <https://www.sciencedirect.com/science/article/pii/S2211285517306201> (visited on 09/13/2022).
- [174] N Mirowska and J Misiewicz. “Defect-related transitions in Zn_3P_2 studied by means of photovoltaic effect spectroscopy”. In: *Semiconductor Science and Technology* 7.11 (1992), pp. 1332–1336. DOI: 10.1088/0268-1242/7/11/007. URL: <https://doi.org/10.1088/0268-1242/7/11/007>.
- [175] J Misiewicz. “Optical vibrations in the Zn_3P_2 lattice”. en. In: *J. Phys.: Condens. Matter* 1.47 (Nov. 1989), pp. 9283–9299. ISSN: 0953-8984, 1361-648X. DOI: 10.1088/0953-8984/1/47/002. URL: <https://iopscience.iop.org/article/10.1088/0953-8984/1/47/002> (visited on 09/12/2022).
- [176] J. Misiewicz. “Inter-band transitions in Zn_3P_2 ”. en. In: *J. Phys.: Condens. Matter* 2.8 (1990). Publisher: IOP Publishing, p. 2053. ISSN: 0953-8984. DOI: 10.1088/0953-8984/2/8/012. URL: <https://iopscience.iop.org/article/10.1088/0953-8984/2/8/012/meta> (visited on 09/13/2022).
- [177] J. Misiewicz et al. “ Zn_3P_2 —a new material for optoelectronic devices”. In: *Microelectronics Journal* 25.5 (1994), pp. xxiii–xxviii. ISSN: 0026-2692. DOI: [https://doi.org/10.1016/0026-2692\(94\)90078-7](https://doi.org/10.1016/0026-2692(94)90078-7). URL: <https://www.sciencedirect.com/science/article/pii/0026269294900787>.
- [178] K W Mitchell. “Status of New Thin-Film Photovoltaic Technologies”. In: *Annual Review of Materials Science* 12.1 (1982), pp. 401–413. DOI: 10.1146/annurev.ms.12.080182.002153. URL: <https://doi.org/10.1146/annurev.ms.12.080182.002153>.
- [179] P Moch, A. T. Abdalian, and B. Briat. “Raman Scattering Studies of Optical Magnons and of High-Energy Magnetic Excitons”. In: *Magnetic Excitations and Fluctuations II*. Ed. by Umberto Balucani et al. Springer Proceedings in Physics. Berlin, Heidelberg: Springer, 1987, pp. 191–195. ISBN: 978-3-642-73107-5. DOI: 10.1007/978-3-642-73107-5_37.
- [180] Dibyajyoti Mohanty et al. “van der Waals epitaxy of CdTe thin film on graphene”. In: *Applied Physics Letters* 109.14 (2016), p. 143109. DOI: 10.1063/1.4964127. eprint: <https://doi.org/10.1063/1.4964127>. URL: <https://doi.org/10.1063/1.4964127>.

-
- [181] Parsian K. Mohseni et al. "Monolithic III-V Nanowire Solar Cells on Graphene via Direct van der Waals Epitaxy". In: *Advanced Materials* 26.22 (2014), pp. 3755–3760. DOI: <https://doi.org/10.1002/adma.201305909>. eprint: <https://onlinelibrary.wiley.com/doi/pdf/10.1002/adma.201305909>. URL: <https://onlinelibrary.wiley.com/doi/abs/10.1002/adma.201305909>.
 - [182] M. Monti et al. "Efficient Intraband Hot Carrier Relaxation in the Perovskite Semiconductor $\text{Cs}_{1-x}\text{Rb}_x\text{SnI}_3$ Mediated by Strong Electron–Phonon Coupling". In: *The Journal of Physical Chemistry C* 122.36 (Sept. 2018). Publisher: American Chemical Society, pp. 20669–20675. ISSN: 1932-7447. DOI: 10.1021/acs.jpcc.8b07792. URL: <https://doi.org/10.1021/acs.jpcc.8b07792> (visited on 09/15/2022).
 - [183] M.M.A. Moon et al. "Design and Simulation of FeSi_2 -Based Novel Heterojunction Solar Cells for Harnessing Visible and Near-Infrared Light". In: *Physica Status Solidi (A) Applications and Materials Science* 217.6 (2020). ISSN: 1862-6300. DOI: 10.1002/pssa.201900921.
 - [184] S. Mukherjee et al. "Growth and Luminescence of Polytypic InP on Epitaxial Graphene". In: *Adv. Funct. Mater.* 28 (2018), p. 1705592.
 - [185] A. M. Munshi et al. "Vertically Aligned GaAs Nanowires on Graphite and Few-Layer Graphene: Generic Model and Epitaxial Growth". In: *Nano Lett.* 12 (2012), p. 4570.
 - [186] A. Mazid Munshi et al. "Selective area growth of AlGaN nanopyramid arrays on graphene by metal-organic vapor phase epitaxy". In: *Applied Physics Letters* 113.26 (2018), p. 263102. DOI: 10.1063/1.5052054. eprint: <https://doi.org/10.1063/1.5052054>. URL: <https://doi.org/10.1063/1.5052054>.
 - [187] K. R. Murali and D. R. Rao. "Optical band gap of $\alpha\text{-Zn}_3\text{P}_2$ ". In: *Thin Solid Films* 86.4 (Dec. 1981), pp. 283–286. ISSN: 0040-6090. DOI: 10.1016/0040-6090(81)90335-7. URL: <https://www.sciencedirect.com/science/article/pii/0040609081903357> (visited on 09/15/2022).
 - [188] R. R. Nair et al. "Fine Structure Constant Defines Visual Transparency of Graphene". In: *Science* 320 (2008), p. 1308.
 - [189] K. Nakada and A. Ishii. "Migration of adatom adsorption on graphene using DFT calculation". In: *Solid State Communications* 151.1 (2011), pp. 13–16. ISSN: 0038-1098. DOI: <https://doi.org/10.1016/j.ssc.2010.10.036>. URL: <https://www.sciencedirect.com/science/article/pii/S0038109810006423>.
 - [190] S. Narayanan. "Fifty years of crystalline silicon solar cells". English. In: 1991, pp. 678–683. DOI: 10.1109/ELECTR.1991.718297.
 - [191] P.S. Nayar and A. Catalano. "Zinc phosphide-zinc oxide heterojunction solar cells". In: *Applied Physics Letters* 39.1 (1981), pp. 105–107. ISSN: 0003-6951. DOI: 10.1063/1.92537.
 - [192] Y. Nie et al. "A Kinetic Monte Carlo Simulation Method of van Der Waals Epitaxy for Atomistic Nucleation-Growth Processes of Transition Metal Dichalcogenides". In: *Sci. Rep.* 7 (2017), p. 1.

Bibliography

- [193] A. Niemegeers et al. "Model for electronic transport in Cu(In,Ga)Se₂ solar cells". In: *Progress in Photovoltaics: Research and Applications* 6.6 (1998), pp. 407–421. ISSN: 1099-159X. DOI: 10.1002/(SICI)1099-159X(199811/12)6:6<407::AID-PIP230>3.0.CO;2-U. (Visited on 09/14/2022).
- [194] D. Niraula et al. "Electric field stimulated growth of Zn whiskers". In: *AIP Advances* 6.7 (2016), p. 075201. DOI: 10.1063/1.4955764. eprint: <https://doi.org/10.1063/1.4955764>. URL: <https://doi.org/10.1063/1.4955764>.
- [195] K S Novoselov et al. "Two-dimensional gas of massless Dirac fermions in graphene". In: *Nature* 438.7065 (2005), pp. 197–200. ISSN: 1476-4687. DOI: 10.1038/nature04233. URL: <https://doi.org/10.1038/nature04233>.
- [196] Mitsuhiro Okada et al. "Direct Chemical Vapor Deposition Growth of WS₂ Atomic Layers on Hexagonal Boron Nitride". In: *ACS Nano* 8.8 (2014). PMID: 25093606, pp. 8273–8277. DOI: 10.1021/nn503093k. eprint: <https://doi.org/10.1021/nn503093k>. URL: <https://doi.org/10.1021/nn503093k>.
- [197] M. Orlita et al. "Approaching the Dirac Point in High-Mobility Multilayer Epitaxial Graphene". In: *Phys. Rev. Lett.* 101 (26 2008), p. 267601. DOI: 10.1103/PhysRevLett.101.267601. URL: <https://link.aps.org/doi/10.1103/PhysRevLett.101.267601>.
- [198] Pablo Orús, Rosa Córdoba, and José María De Teresa. "Focused ion beam induced processing". en. In: *Nanofabrication: Nanolithography techniques and their applications* (Dec. 2020). Publisher: IOP Publishing. DOI: 10.1088/978-0-7503-2608-7ch5. URL: <https://iopscience.iop.org/book/edit/978-0-7503-2608-7/chapter/bk978-0-7503-2608-7ch5> (visited on 09/12/2022).
- [199] G. C. Osbourn. "Strained-layer superlattices from lattice mismatched materials". In: *Journal of Applied Physics* 53.3 (1982), pp. 1586–1589. DOI: 10.1063/1.330615. eprint: <https://doi.org/10.1063/1.330615>. URL: <https://doi.org/10.1063/1.330615>.
- [200] M. Page et al. "Copper sulfide as a light absorber in wet-chemical synthesized extremely thin absorber (ETA) solar cells". In: *Energy and Environmental Science* 2.2 (2009), pp. 220–223. ISSN: 1754-5706. DOI: 10.1039/b813740d.
- [201] G. Pangilinan, R. Sooryakumar, and J. Misiewicz. "Raman Activity of Zn₃P₂". In: *Phys. Rev. B: Condens. Matter Mater. Phys.* 44 (1991), p. 2582.
- [202] G. Pangilinan et al. "New Long-Range Atomic Order and Heteroepitaxy of Single-Crystal Zn₃As₂". In: *Phys. Rev. Lett.* 62 (5 1989), pp. 551–554. DOI: 10.1103/PhysRevLett.62.551. URL: <https://link.aps.org/doi/10.1103/PhysRevLett.62.551>.
- [203] Rajrupa Paul et al. "van der Waals Epitaxy of Earth-Abundant Zn₃P₂ on Graphene for Photovoltaics". In: *Crystal Growth & Design* 20.6 (2020). Publisher: American Chemical Society, pp. 3816–3825. ISSN: 1528-7483. DOI: 10.1021/acs.cgd.0c00125. URL: <https://doi.org/10.1021/acs.cgd.0c00125> (visited on 08/31/2022).

- [204] S. Paul et al. "Review on the development scenario of renewable energy in different country". English. In: 2021. ISBN: 978-1-66541-259-9. DOI: 10.1109/IEMRE52042.2021.9386748.
- [205] J. M. Pawlikowski. "Preparation and characterization of close-spaced vapour transport thin films of ZnSe for heterojunction solar cells". In: *Thin Solid Films* 127.1 (May 1985), pp. 9–28. ISSN: 0040-6090. DOI: 10.1016/0040-6090(85)90209-3. URL: <https://www.sciencedirect.com/science/article/pii/0040609085902093> (visited on 09/15/2022).
- [206] J. M. Pawlikowski, J. Misiewicz, and N. Mirowska. "Direct and Indirect Optical Transitions in Zn_3P_2 ". In: *J. Phys. Chem. Solids* 40 (1979), p. 1027.
- [207] J. M. Pawlikowski et al. "Absorption Edge of Zn_3P_2 at 5, 80, and 300 K". In: *physica status solidi (b)* 88.2 (1978), K153–K156. DOI: <https://doi.org/10.1002/pssb.2220880263>. eprint: <https://onlinelibrary.wiley.com/doi/pdf/10.1002/pssb.2220880263>. URL: <https://onlinelibrary.wiley.com/doi/abs/10.1002/pssb.2220880263>.
- [208] J.M. Pawlikowski. " Zn_3P_2 as infrared-to-ultraviolet photoconverter". In: *Infrared Physics* 28.3 (1988), pp. 177–182. ISSN: 0020-0891. DOI: [https://doi.org/10.1016/0020-0891\(88\)90007-3](https://doi.org/10.1016/0020-0891(88)90007-3). URL: <https://www.sciencedirect.com/science/article/pii/0020089188900073>.
- [209] Janusz M. Pawlikowski. "Absorption edge of Zn_3P_2 ". In: *Phys. Rev. B* 26.8 (1982). Publisher: American Physical Society, pp. 4711–4713. DOI: 10.1103/PhysRevB.26.4711. URL: <https://link.aps.org/doi/10.1103/PhysRevB.26.4711> (visited on 08/31/2022).
- [210] Janusz M. Pawlikowski. "Band structure and properties of Zn_3P_2 - promising new infrared material". en. In: *Infrared Physics* 21.3 (1981), pp. 181–187. ISSN: 0020-0891. DOI: 10.1016/0020-0891(81)90027-0. URL: <https://www.sciencedirect.com/science/article/pii/0020089181900270> (visited on 08/31/2022).
- [211] C. W. F. T. Pistorius et al. "High-Pressure Phase Relations And Crystal Structure Determination For Zinc Phosphide, Zn_3P_2 , And Cadmium Phosphide, Cd_3P_2 ". In: *High Temp. - High Press.* 9 (1977), p. 471.
- [212] H.A.S. Platt et al. "Wide-gap iron sulfides for polycrystalline thin-film solar cells". In: ISSN: 0065-7727. 2008. ISBN: 978-0-8412-6985-9.
- [213] S. Podsiadlo et al. "Synthesis of bulk kesterite - A prospective photovoltaic material". In: *European Journal of Inorganic Chemistry* 2014.28 (2014), pp. 4730–4733. ISSN: 1434-1948. DOI: 10.1002/ejic.201402392.
- [214] P. Politi and J. Villain. "Ehrlich-Schwoebel Instability in Molecular-Beam Epitaxy: A Minimal Model". In: *Phys. Rev. B: Condens. Matter Mater. Phys.* 54 (1996), p. 5114.
- [215] A. Polizzotti et al. "The state and future prospects of kesterite photovoltaics". In: *Energy and Environmental Science* 6.11 (2013), pp. 3171–3182. ISSN: 1754-5706. DOI: 10.1039/c3ee41781f.

Bibliography

- [216] A. O. Pudov et al. "CIGS J-V distortion in the absence of blue photons". In: *Thin Solid Films*. EMRS 2004 480-481 (June 2005), pp. 273–278. ISSN: 0040-6090. DOI: 10.1016/j.tsf.2004.11.099. URL: <https://www.sciencedirect.com/science/article/pii/S0040609004016281> (visited on 09/14/2022).
- [217] A. O. Pudov et al. "Secondary barriers in CdS–CuIn_{1-x}Ga_xSe₂ solar cells". In: *Journal of Applied Physics* 97.6 (Mar. 2005). Publisher: American Institute of Physics, p. 064901. ISSN: 0021-8979. DOI: 10.1063/1.1850604. URL: <https://aip.scitation.org/doi/full/10.1063/1.1850604> (visited on 09/14/2022).
- [218] Z.L. Qian. "Improved engineering simplification model of silicon solar cells". English. In: 2020, pp. 2015–2018. ISBN: 978-1-72815-281-3. DOI: 10.1109/ACPEE48638.2020.9136364.
- [219] C. V. Raman and K. S. Krishnan. "A New Type of Secondary Radiation". en. In: *Nature* 121.3048 (Mar. 1928). Number: 3048 Publisher: Nature Publishing Group, pp. 501–502. ISSN: 1476-4687. DOI: 10.1038/121501c0. URL: <https://www.nature.com/articles/121501c0> (visited on 09/12/2022).
- [220] Sandheep Ravishankar et al. "Effects of Frequency Dependence of the External Quantum Efficiency of Perovskite Solar Cells". In: *The Journal of Physical Chemistry Letters* 9.11 (June 2018). Publisher: American Chemical Society, pp. 3099–3104. DOI: 10.1021/acs.jpcclett.8b01245. URL: <https://doi.org/10.1021/acs.jpcclett.8b01245> (visited on 09/15/2022).
- [221] Kate Reidy et al. "Mechanisms of Quasi van der Waals Epitaxy of Three-Dimensional Metallic Nanoislands on Suspended Two-Dimensional Materials". In: *Nano Letters* 22.14 (2022), pp. 5849–5858. DOI: 10.1021/acs.nanolett.2c01682. eprint: <https://doi.org/10.1021/acs.nanolett.2c01682>. URL: <https://doi.org/10.1021/acs.nanolett.2c01682>.
- [222] Mardochee Reveil et al. "Finite element and analytical solutions for van der Pauw and four-point probe correction factors when multiple non-ideal measurement conditions coexist". In: *Review of Scientific Instruments* 88.9 (2017). Publisher: American Institute of Physics, p. 094704. ISSN: 0034-6748. DOI: 10.1063/1.5001830. URL: <https://aip.scitation.org/doi/10.1063/1.5001830> (visited on 08/31/2022).
- [223] G. Rey et al. "On the origin of band-tails in kesterite". In: *Solar Energy Materials and Solar Cells* 179 (2018), pp. 142–151. ISSN: 0927-0248. DOI: 10.1016/j.solmat.2017.11.005.
- [224] B. Rezig, H. Dahman, and M. Kenzari. "Iron pyrite FeS₂ for flexible solar cells". In: *Renewable Energy* 2.2 (Apr. 1992), pp. 125–128. ISSN: 0960-1481. DOI: 10.1016/0960-1481(92)90098-N. URL: <https://www.sciencedirect.com/science/article/pii/096014819290098N> (visited on 09/13/2022).
- [225] C. Rice et al. "Raman-scattering measurements and first-principles calculations of strain-induced phonon shifts in monolayer MoS₂". In: *Phys. Rev. B* 87.8 (Feb. 2013). Publisher: American Physical Society, p. 081307. DOI: 10.1103/PhysRevB.87.081307. URL: <https://link.aps.org/doi/10.1103/PhysRevB.87.081307> (visited on 09/12/2022).

- [226] D. Rickard and G.W. Luther III. "Chemistry of iron sulfides". In: *Chemical Reviews* 107.2 (2007), pp. 514–562. ISSN: 0009-2665. DOI: 10.1021/cr0503658.
- [227] Moumin Rudra et al. "Existence of nearest-neighbor and variable range hopping in Pr₂ZnMnO₆ oxygen-intercalated pseudocapacitor electrode". In: *Materials Chemistry and Physics* 258 (2021), p. 123907. ISSN: 0254-0584. DOI: 10.1016/j.matchemphys.2020.123907. URL: <https://www.sciencedirect.com/science/article/pii/S0254058420312670> (visited on 09/08/2022).
- [228] Huije Ryu et al. "Two-dimensional material templates for van der Waals epitaxy, remote epitaxy, and intercalation growth". In: *Applied Physics Reviews* 9.3 (2022), p. 031305. DOI: 10.1063/5.0090373. eprint: <https://doi.org/10.1063/5.0090373>. URL: <https://doi.org/10.1063/5.0090373>.
- [229] Shinyoung Ryu et al. "Light intensity dependence of organic solar cell operation and dominance switching between Shockley–Read–Hall and bimolecular recombination losses". In: *Scientific Reports* 11.1 (Aug. 2021). Number: 1 Publisher: Nature Publishing Group, p. 16781. ISSN: 2045-2322. DOI: 10.1038/s41598-021-96222-w. URL: <https://www.nature.com/articles/s41598-021-96222-w> (visited on 09/14/2022).
- [230] Sadanand et al. "Comparative study of the CZTS, CuSbS₂ and CuSbSe₂ solar photovoltaic cell with an earth-abundant non-toxic buffer layer". In: *Solar Energy* 222 (2021), pp. 175–185. ISSN: 0038-092X. DOI: 10.1016/j.solener.2021.05.013.
- [231] Chih-tang Sah, Robert N. Noyce, and William Shockley. "Carrier Generation and Recombination in P-N Junctions and P-N Junction Characteristics". In: *Proceedings of the IRE* 45.9 (Sept. 1957). Conference Name: Proceedings of the IRE, pp. 1228–1243. ISSN: 2162-6634. DOI: 10.1109/JRPROC.1957.278528.
- [232] H. Sai, T. Matsui, and K. Matsubara. "Key Points in the Latest Developments of High-Efficiency Thin-Film Silicon Solar Cells". In: *Physica Status Solidi (A) Applications and Materials Science* 214.12 (2017). ISSN: 1862-6300. DOI: 10.1002/pssa.201700544.
- [233] Mohammad Sajedi Alvar, Paul W. M. Blom, and Gert-Jan A. H. Wetzelaer. "Space-charge-limited electron and hole currents in hybrid organic-inorganic perovskites". In: *Nat Commun* 11.1 (Aug. 2020). Number: 1 Publisher: Nature Publishing Group, pp. 1–9. ISSN: 2041-1723. DOI: 10.1038/s41467-020-17868-0. URL: <https://www.nature.com/articles/s41467-020-17868-0> (visited on 08/31/2022).
- [234] Oskar J. Sandberg et al. "Relating Charge Transport, Contact Properties, and Recombination to Open-Circuit Voltage in Sandwich-Type Thin-Film Solar Cells". In: *Physical Review Applied* 5 (Apr. 2016). ADS Bibcode: 2016PhRvP...5d4005S, p. 044005. DOI: 10.1103/PhysRevApplied.5.044005. URL: <https://ui.adsabs.harvard.edu/abs/2016PhRvP...5d4005S> (visited on 09/14/2022).
- [235] T. Sander et al. "Correlation of intrinsic point defects and the Raman modes of cuprous oxide". In: *Phys. Rev. B* 90.4 (July 2014). Publisher: American Physical Society, p. 045203. DOI: 10.1103/PhysRevB.90.045203. URL: <https://link.aps.org/doi/10.1103/PhysRevB.90.045203> (visited on 09/12/2022).

Bibliography

- [236] Prasad Sarangapani et al. “Band-tail Formation and Band-gap Narrowing Driven by Polar Optical Phonons and Charged Impurities in Atomically Resolved III-V Semiconductors and Nanodevices”. In: *Phys. Rev. Applied* 12 (4 2019), p. 044045. DOI: 10.1103/PhysRevApplied.12.044045. URL: <https://link.aps.org/doi/10.1103/PhysRevApplied.12.044045>.
- [237] R. Sathyamoorthy et al. “Influence of Annealing on Structural and Optical Properties of Zn₃P₂ Thin Films”. In: *Mater. Charact.* 58 (2007), p. 745.
- [238] Roland Scheer and Hans-Werner Schock. “Thin Film Heterostructures”. In: *Chalcogenide Photovoltaics*. John Wiley & Sons, Ltd, 2011. Chap. 2, pp. 9–127. ISBN: 9783527633708. DOI: <https://doi.org/10.1002/9783527633708.ch2>. URL: <https://onlinelibrary.wiley.com/doi/abs/10.1002/9783527633708.ch2>.
- [239] T. Schmidt, K. Lischka, and W. Zulehner. “Excitation-Power Dependence of the near-Band-Edge Photoluminescence of Semiconductors”. In: *Phys. Rev. B: Condens. Matter Mater. Phys.* 45 (1992), p. 8989.
- [240] V. Schmidt et al. “Silicon Nanowires: A Review on Aspects of Their Growth and Their Electrical Properties”. In: *Adv. Mater.* 21 (2009), p. 2681.
- [241] Jonathan J. S. Scragg et al. “A low-temperature order-disorder transition in Cu₂ZnSnS₄ thin films”. In: *Appl. Phys. Lett.* 104.4 (Jan. 2014). Publisher: American Institute of Physics, p. 041911. ISSN: 0003-6951. DOI: 10.1063/1.4863685. URL: <https://aip.scitation.org/doi/10.1063/1.4863685> (visited on 09/13/2022).
- [242] M.O. Semenenko et al. “RF Electromagnetic Field Treatment of Tetragonal Kesterite CZTSSe Light Absorbers”. In: *Nanoscale Research Letters* 12 (2017). ISSN: 1931-7573. DOI: 10.1186/s11671-017-2183-9.
- [243] Jonathan D. Servaites, Mark A. Ratner, and Tobin J. Marks. “Organic solar cells: A new look at traditional models”. In: *Energy & Environmental Science* 4.11 (Oct. 2011). Publisher: The Royal Society of Chemistry, pp. 4410–4422. ISSN: 1754-5706. DOI: 10.1039/C1EE01663F. URL: <https://pubs.rsc.org/en/content/articlelanding/2011/ee/c1ee01663f> (visited on 09/14/2022).
- [244] M. Shahbaz et al. “The effect of renewable energy consumption on economic growth: Evidence from the renewable energy country attractive index”. In: *Energy* 207 (2020). ISSN: 0360-5442. DOI: 10.1016/j.energy.2020.118162.
- [245] X. M. Shen et al. “Space-charge-limited currents in GaN Schottky diodes”. In: *Solid-State Electronics*. 5th International Workshop on the Ultimate Intergration of Silicon, ULIS 2004 49.5 (May 2005), pp. 847–852. ISSN: 0038-1101. DOI: 10.1016/j.sse.2005.02.003. URL: <https://www.sciencedirect.com/science/article/pii/S0038110105000651> (visited on 08/31/2022).

- [246] Hardhyan Sheoran, Vikram Kumar, and Rajendra Singh. "A Comprehensive Review on Recent Developments in Ohmic and Schottky Contacts on Ga₂O₃ for Device Applications". In: *ACS Appl. Electron. Mater.* 4.6 (June 2022). Publisher: American Chemical Society, pp. 2589–2628. DOI: 10.1021/acsaelm.2c00101. URL: <https://doi.org/10.1021/acsaelm.2c00101> (visited on 08/31/2022).
- [247] L. Shi et al. "Annealing Temperature Effects on Photoelectrochemical Performance of Bismuth Vanadate Thin Film Photoelectrodes". In: *RSC Adv.* 8 (2018), p. 29179.
- [248] D. Shin, B. Saparov, and D.B. Mitzi. "Defect Engineering in Multinary Earth-Abundant Chalcogenide Photovoltaic Materials". In: *Advanced Energy Materials* 7.11 (2017). ISSN: 1614-6832. DOI: 10.1002/aenm.201602366.
- [249] W. Shockley. "The theory of p-n junctions in semiconductors and p-n junction transistors". In: *Bell System Technical Journal* 28.3 (1949), pp. 435–489. ISSN: 1538-7305. DOI: 10.1002/j.1538-7305.1949.tb03645.x. URL: <https://onlinelibrary.wiley.com/doi/abs/10.1002/j.1538-7305.1949.tb03645.x> (visited on 09/14/2022).
- [250] William Shockley and Hans J. Queisser. "Detailed Balance Limit of Efficiency of p-n Junction Solar Cells". In: *Journal of Applied Physics* 32.3 (1961), pp. 510–519. DOI: 10.1063/1.1736034. eprint: <https://doi.org/10.1063/1.1736034>. URL: <https://doi.org/10.1063/1.1736034>.
- [251] K. Sierański, J. Szatkowski, and A. Hajdusianek. "Deep levels in low resistive Zn₃P₂". In: *physica status solidi (a)* 214.5 (2017), p. 1600553. ISSN: 1862-6319. DOI: 10.1002/pssa.201600553. URL: <https://onlinelibrary.wiley.com/doi/abs/10.1002/pssa.201600553> (visited on 08/31/2022).
- [252] Oliver Skibitzki et al. "Lattice-engineered Si_{1-x}Gex-buffer on Si(001) for GaP integration". In: *Journal of Applied Physics* 115.10 (2014), p. 103501. DOI: 10.1063/1.4864777. eprint: <https://doi.org/10.1063/1.4864777>. URL: <https://doi.org/10.1063/1.4864777>.
- [253] M. Soyulu and B. Abay. "Analysing space charge-limited conduction in Au/n-InP Schottky diodes". In: *Physica E: Low-dimensional Systems and Nanostructures* 43.1 (Nov. 2010), pp. 534–538. ISSN: 1386-9477. DOI: 10.1016/j.physe.2010.09.012. URL: <https://www.sciencedirect.com/science/article/pii/S1386947710005734> (visited on 08/31/2022).
- [254] Maria Chiara Spadaro et al. "Rotated domains in selective area epitaxy grown Zn₃P₂: formation mechanism and functionality". In: *Nanoscale* 13.44 (Nov. 2021). Publisher: The Royal Society of Chemistry, pp. 18441–18450. ISSN: 2040-3372. DOI: 10.1039/D1NR06190A. URL: <https://pubs.rsc.org/en/content/articlelanding/2021/nr/d1nr06190a> (visited on 09/13/2022).
- [255] Simon Escobar Steinvall et al. "Towards defect-free thin films of the earth-abundant absorber zinc phosphide by nanopatterning". In: *Nanoscale Adv.* 3.2 (Jan. 2021). Publisher: RSC, pp. 326–332. ISSN: 2516-0230. DOI: 10.1039/D0NA00841A. URL: <https://pubs.rsc.org/en/content/articlelanding/2021/na/d0na00841a> (visited on 09/13/2022).

- [256] Dmitry Stepanchikov and Gennady Chuiko. “Excitons into one-axis crystals of zinc phosphide (Zn_3P_2)”. In: *Condensed Matter Physics* 12 (2009). DOI: 10.5488/CMP.12.2.239.
- [257] A. M. Stoneham. “Non-radiative transitions in semiconductors”. In: *Rep. Prog. Phys.* 44.12 (Dec. 1981). Publisher: IOP Publishing, pp. 1251–1295. ISSN: 0034-4885. DOI: 10.1088/0034-4885/44/12/001. URL: <https://doi.org/10.1088/0034-4885/44/12/001> (visited on 09/13/2022).
- [258] Robert A. Street, Alexa Krakaris, and Sarah R. Cowan. “Recombination Through Different Types of Localized States in Organic Solar Cells”. In: *Advanced Functional Materials* 22.21 (2012). _eprint: <https://onlinelibrary.wiley.com/doi/pdf/10.1002/adfm.201200031>, pp. 4608–4619. ISSN: 1616-3028. DOI: 10.1002/adfm.201200031. URL: <https://onlinelibrary.wiley.com/doi/abs/10.1002/adfm.201200031> (visited on 09/14/2022).
- [259] Elias Z. Stutz et al. “Nanosails Showcasing Zn_3As_2 as an Optoelectronic-Grade Earth Abundant Semiconductor”. In: *physica status solidi (RRL) – Rapid Research Letters* 13.7 (2019), p. 1900084. DOI: <https://doi.org/10.1002/pssr.201900084>. eprint: <https://onlinelibrary.wiley.com/doi/pdf/10.1002/pssr.201900084>. URL: <https://onlinelibrary.wiley.com/doi/abs/10.1002/pssr.201900084>.
- [260] Elias Z. Stutz et al. “Raman spectroscopy and lattice dynamics calculations of tetragonally-structured single crystal zinc phosphide (Zn_3P_2) nanowires”. In: *Nanotechnology* 32.8 (Dec. 2020). Publisher: IOP Publishing, p. 085704. ISSN: 0957-4484. DOI: 10.1088/1361-6528/abc91b. URL: <https://doi.org/10.1088/1361-6528/abc91b> (visited on 09/12/2022).
- [261] Elias Z. Stutz et al. “Showcasing the optical properties of monocrystalline zinc phosphide thin films as an earth-abundant photovoltaic absorber”. In: *Mater. Adv.* 3 (2 2022), pp. 1295–1303. DOI: 10.1039/D1MA00922B. URL: <http://dx.doi.org/10.1039/D1MA00922B>.
- [262] T. Suda et al. “N-type Zinc Phosphide Grown by Molecular Beam Epitaxy”. In: *Appl. Phys. Lett.* 69 (1996), p. 2426. DOI: 10.1063/1.117659.
- [263] Toshikazu Suda and Richard H. Bube. “Deep levels in zinc phosphide”. In: *Appl. Phys. Lett.* 45.7 (Oct. 1984). Publisher: American Institute of Physics, pp. 775–777. ISSN: 0003-6951. DOI: 10.1063/1.95400. URL: <https://aip.scitation.org/doi/abs/10.1063/1.95400> (visited on 08/31/2022).
- [264] Toshikazu Suda and Kazuhiko Kakishita. “Epitaxial growth of zinc phosphide”. In: *Journal of Applied Physics* 71.6 (1992). Publisher: American Institute of Physics, pp. 3039–3041. ISSN: 0021-8979. DOI: 10.1063/1.350989. URL: <https://aip.scitation.org/doi/abs/10.1063/1.350989> (visited on 08/31/2022).
- [265] Toshikazu Suda et al. “ Zn_3P_2 /ITO Heterojunction Solar Cells”. en. In: *Jpn. J. Appl. Phys.* 21.S2 (1982). Publisher: IOP Publishing, p. 63. ISSN: 1347-4065. DOI: 10.7567/JJAPS.21S2.63. URL: <https://iopscience.iop.org/article/10.7567/JJAPS.21S2.63/meta> (visited on 09/13/2022).

- [266] X. Sun et al. "Direct Gap Photoluminescence of N-Type Tensile-Strained Ge-on-Si". In: *Appl. Phys. Lett.* 95 (2009), p. 011911.
- [267] Xin Sun et al. "van der Waals epitaxy of CdS thin films on single-crystalline graphene". In: *Applied Physics Letters* 110.15 (2017), p. 153104. DOI: 10.1063/1.4980088. eprint: <https://doi.org/10.1063/1.4980088>. URL: <https://doi.org/10.1063/1.4980088>.
- [268] H.E. Swanson and United States. National Bureau of Standards. *Standard X-ray Diffraction Powder Patterns: Data for 81 substances*. NBS monograph. National Bureau of Standards, 1969. URL: <https://books.google.ch/books?id=PbDcqoBRBl0C>.
- [269] Milo Yaro Swinkels et al. "Measuring the Optical Absorption of Single Nanowires". In: *Phys. Rev. Applied* 14.2 (2020). Publisher: American Physical Society, p. 024045. DOI: 10.1103/PhysRevApplied.14.024045. URL: <https://link.aps.org/doi/10.1103/PhysRevApplied.14.024045> (visited on 08/31/2022).
- [270] N. G. Tarr and D. L. Pulfrey. "An investigation of dark current and photocurrent superposition in photovoltaic devices". In: *Solid-State Electronics* 22.3 (Mar. 1979), pp. 265–270. ISSN: 0038-1101. DOI: 10.1016/0038-1101(79)90032-7. URL: <https://www.sciencedirect.com/science/article/pii/0038110179900327> (visited on 09/14/2022).
- [271] Mohd Taukeer Khan et al. "Electrical Methods to Elucidate Charge Transport in Hybrid Perovskites Thin Films and Devices". In: *The Chemical Record* 20.5 (2020). _eprint: <https://onlinelibrary.wiley.com/doi/pdf/10.1002/tcr.201900055>, pp. 452–465. ISSN: 1528-0691. DOI: 10.1002/tcr.201900055. URL: <https://onlinelibrary.wiley.com/doi/abs/10.1002/tcr.201900055> (visited on 08/31/2022).
- [272] M. Topič, F. Smole, and J. Furlan. "Examination of blocking current-voltage behaviour through defect chalcopyrite layer in ZnO/CdS/Cu(In,Ga)Se₂/Mo solar cell". In: *Solar Energy Materials and Solar Cells* 49.1 (Dec. 1997), pp. 311–317. ISSN: 0927-0248. DOI: 10.1016/S0927-0248(97)00058-5. URL: <https://www.sciencedirect.com/science/article/pii/S0927024897000585> (visited on 09/14/2022).
- [273] Wolfgang Tress et al. "Interpretation and evolution of open-circuit voltage, recombination, ideality factor and subgap defect states during reversible light-soaking and irreversible degradation of perovskite solar cells". In: *Energy & Environmental Science* 11.1 (Jan. 2018). Publisher: The Royal Society of Chemistry, pp. 151–165. ISSN: 1754-5706. DOI: 10.1039/C7EE02415K. URL: <https://pubs.rsc.org/en/content/articlelanding/2018/ee/c7ee02415k> (visited on 09/14/2022).
- [274] Jeffrey Y. Tsao. *Materials Fundamentals of Molecular Beam Epitaxy*. Google-Books-ID: 1kgfS1JKhi4C. Academic Press, 2012. ISBN: 978-0-08-057135-5.
- [275] Muhammad Iqbal Bakti Utama et al. "Incommensurate van der Waals Epitaxy of Nanowire Arrays: A Case Study with ZnO on Muscovite Mica Substrates". In: *Nano Letters* 12.4 (2012). PMID: 22432695, pp. 2146–2152. DOI: 10.1021/nl300554t. eprint: <https://doi.org/10.1021/nl300554t>. URL: <https://doi.org/10.1021/nl300554t>.

Bibliography

- [276] F. Vaillant, D. Jousse, and J.-C. Bruyere. “Recombination at dangling bonds and band tails: Temperature dependence of photoconductivity in hydrogenated amorphous silicon”. In: *Philosophical Magazine B: Physics of Condensed Matter; Statistical Mechanics, Electronic, Optical and Magnetic Properties* 57.5 (1988), pp. 649–661. ISSN: 1364-2812. DOI: 10.1080/13642818808211235.
- [277] J. M. Van Hove, P. R. Pukite, and P. I. Cohen. “The dependence of RHEED oscillations on MBE growth parameters”. In: *Journal of Vacuum Science & Technology B: Microelectronics Processing and Phenomena* 3.2 (Mar. 1985). Publisher: American Institute of Physics, pp. 563–567. ISSN: 0734-211X. DOI: 10.1116/1.583180. URL: <https://avs.scitation.org/doi/abs/10.1116/1.583180> (visited on 09/12/2022).
- [278] Piet Van Mieghem. “Theory of band tails in heavily doped semiconductors”. In: *Rev. Mod. Phys.* 64.3 (July 1992). Publisher: American Physical Society, pp. 755–793. DOI: 10.1103/RevModPhys.64.755. URL: <https://link.aps.org/doi/10.1103/RevModPhys.64.755> (visited on 09/13/2022).
- [279] Oscar Vazquez-Mena et al. “Performance Enhancement of a Graphene-Zinc Phosphide Solar Cell Using the Electric Field-Effect”. In: *Nano Letters* 14.8 (2014). PMID: 25058004, pp. 4280–4285. DOI: 10.1021/nl500925n. eprint: <https://doi.org/10.1021/nl500925n>. URL: <https://doi.org/10.1021/nl500925n>.
- [280] Joachim Vollbrecht and Viktor V. Brus. “On the recombination order of surface recombination under open circuit conditions”. In: *Organic Electronics* 86 (Nov. 2020), p. 105905. ISSN: 1566-1199. DOI: 10.1016/j.orgel.2020.105905. URL: <https://www.sciencedirect.com/science/article/pii/S1566119920302901> (visited on 09/14/2022).
- [281] Cyrus Wadia, A. Paul Alivisatos, and Daniel M. Kammen. “Materials Availability Expands the Opportunity for Large-Scale Photovoltaics Deployment”. In: *Environ. Sci. Technol.* 43.6 (Mar. 2009), pp. 2072–2077. ISSN: 0013-936X. DOI: 10.1021/es8019534. URL: <https://doi.org/10.1021/es8019534> (visited on 10/24/2019).
- [282] Cyrus Wadia, A. Paul Alivisatos, and Daniel M. Kammen. “Materials Availability Expands the Opportunity for Large-Scale Photovoltaics Deployment”. In: *Environmental Science & Technology* 43.6 (2009). PMID: 19368216, pp. 2072–2077. DOI: 10.1021/es8019534. eprint: <https://doi.org/10.1021/es8019534>. URL: <https://doi.org/10.1021/es8019534>.
- [283] A. Wagner et al. “Oxides for sustainable photovoltaics with earth-abundant materials”. In: vol. 8987. ISSN: 0277-786X. 2014. ISBN: 978-0-8194-9900-4. DOI: 10.1117/12.2044734.
- [284] Suzanne K. Wallace, David B. Mitzi, and Aron Walsh. “The Steady Rise of Kesterite Solar Cells”. In: *ACS Energy Lett.* 2.4 (Apr. 2017). Publisher: American Chemical Society, pp. 776–779. DOI: 10.1021/acsenerylett.7b00131. URL: <https://doi.org/10.1021/acsenerylett.7b00131> (visited on 09/13/2022).

- [285] Lee A. Walsh and Christopher L. Hinkle. “van der Waals epitaxy: 2D materials and topological insulators”. In: *Applied Materials Today* 9 (2017), pp. 504–515. ISSN: 2352-9407. DOI: <https://doi.org/10.1016/j.apmt.2017.09.010>. URL: <https://www.sciencedirect.com/science/article/pii/S2352940717302822>.
- [286] E.-C. Wang, A. L. Fahrenbruch, and R. H. Bube. *Single crystal growth and electrical properties of Zn₃P₂*. Jan. 1981. URL: <https://ui.adsabs.harvard.edu/abs/1981pvsp.conf.1265W> (visited on 08/31/2022).
- [287] Faa-Ching Wang, Alan Fahrenbruch, and Richard Bube. “Electrical properties of Zn₃P₂ single crystals”. In: *Journal of Electronic Materials* 11 (1982), pp. 75–88. DOI: 10.1007/BF02654610.
- [288] Wei Wang et al. “Device Characteristics of CZTSSe Thin-Film Solar Cells with 12.6% Efficiency”. In: *Advanced Energy Materials* 4.7 (2014), p. 1301465. ISSN: 1614-6840. DOI: 10.1002/aenm.201301465. URL: <https://onlinelibrary.wiley.com/doi/abs/10.1002/aenm.201301465> (visited on 09/13/2022).
- [289] X. Wang, S. M. Tabakman, and H. Dai. “Atomic Layer Deposition of Metal Oxides on Pristine and Functionalized Graphene”. In: *J. Am. Chem. Soc.* 130 (2008), p. 8152.
- [290] G. A. H. Wetzelaer et al. “Trap-assisted and Langevin-type recombination in organic light-emitting diodes”. In: *Physical Review B* 83.16 (Apr. 2011). Publisher: American Physical Society, p. 165204. DOI: 10.1103/PhysRevB.83.165204. URL: <https://link.aps.org/doi/10.1103/PhysRevB.83.165204> (visited on 09/14/2022).
- [291] G. a. H. Wetzelaer et al. “Origin of the dark-current ideality factor in polymer:fullerene bulk heterojunction solar cells”. In: *Applied Physics Letters* 99.15 (Oct. 2011). Publisher: American Institute of Physics, p. 153506. ISSN: 0003-6951. DOI: 10.1063/1.3651752. URL: <https://aip.scitation.org/doi/full/10.1063/1.3651752> (visited on 09/14/2022).
- [292] Gert-Jan A. H. Wetzelaer, Martijn Kuik, and Paul W. M. Blom. “Identifying the Nature of Charge Recombination in Organic Solar Cells from Charge-Transfer State Electroluminescence”. In: *Advanced Energy Materials* 2.10 (2012), pp. 1232–1237. ISSN: 1614-6840. DOI: 10.1002/aenm.201200009. URL: <https://onlinelibrary.wiley.com/doi/abs/10.1002/aenm.201200009> (visited on 09/14/2022).
- [293] Gert-Jan A. H. Wetzelaer et al. “Trap-Assisted Non-Radiative Recombination in Organic-Inorganic Perovskite Solar Cells”. In: *Advanced Materials* 27.11 (2015). _eprint: <https://onlinelibrary.wiley.com/doi/pdf/10.1002/adma.201405372>, pp. 1837–1841. ISSN: 1521-4095. DOI: 10.1002/adma.201405372. URL: <https://onlinelibrary.wiley.com/doi/abs/10.1002/adma.201405372> (visited on 09/14/2022).
- [294] J. P. Wilcoxon, P. P. Newcomer, and G. A. Samara. “Strong quantum confinement effects in semiconductors: FeS₂ nanoclusters”. In: *Solid State Communications* 98.6 (May 1996), pp. 581–585. ISSN: 0038-1098. DOI: 10.1016/0038-1098(95)00822-5. URL: <https://www.sciencedirect.com/science/article/pii/0038109895008225> (visited on 09/13/2022).

Bibliography

- [295] E Wisotzki, A Klein, and W Jaegermann. “Quasi van der Waals epitaxy of ZnSe on the layered chalcogenides InSe and GaSe”. In: *Thin Solid Films* 380.1 (2000), pp. 263–265. ISSN: 0040-6090. DOI: [https://doi.org/10.1016/S0040-6090\(00\)01520-0](https://doi.org/10.1016/S0040-6090(00)01520-0). URL: <https://www.sciencedirect.com/science/article/pii/S0040609000015200>.
- [296] J. M. Wofford et al. “Graphene Islands on Cu Foils: The Interplay between Shape, Orientation, and Defects”. In: *Nano Lett.* 10 (2010), p. 4890.
- [297] M.H. Wolter et al. “How band tail recombination influences the open-circuit voltage of solar cells”. In: *Progress in Photovoltaics: Research and Applications* 30.7 (2022), pp. 702–712. ISSN: 1062-7995. DOI: 10.1002/pip.3449.
- [298] J. Wong, S.T. Omelchenko, and H.A. Atwater. “Impact of Semiconductor Band Tails and Band Filling on Photovoltaic Efficiency Limits”. In: ISSN: 0160-8371. 2021, pp. 1315–1317. ISBN: 978-1-66541-922-2. DOI: 10.1109/PVSC43889.2021.9518548.
- [299] N. Convers Wyeth and A. Catalano. “Barrier heights of evaporated metal contacts on Zn_3P_2 ”. In: *Journal of Applied Physics* 51.4 (1980), pp. 2286–2288. DOI: 10.1063/1.327862. eprint: <https://aip.scitation.org/doi/pdf/10.1063/1.327862>. URL: <https://aip.scitation.org/doi/abs/10.1063/1.327862>.
- [300] N. Convers Wyeth and A. Catalano. “Spectral response measurements of minority-carrier diffusion length in Zn_3P_2 ”. In: *Journal of Applied Physics* 50.3 (1979). Publisher: American Institute of Physics, pp. 1403–1407. ISSN: 0021-8979. DOI: 10.1063/1.326122. URL: <https://aip.scitation.org/doi/10.1063/1.326122> (visited on 09/13/2022).
- [301] N. Convers Wyeth and A. Catalano. “Spectral response measurements of minority-carrier diffusion length in Zn_3P_2 ”. In: *Journal of Applied Physics* 50.3 (1979), pp. 1403–1407. DOI: 10.1063/1.326122. eprint: <https://doi.org/10.1063/1.326122>. URL: <https://doi.org/10.1063/1.326122>.
- [302] Wanshun Xia et al. “Recent progress in van der Waals heterojunctions”. In: *Nanoscale* 9 (13 2017), pp. 4324–4365. DOI: 10.1039/C7NR00844A. URL: <http://dx.doi.org/10.1039/C7NR00844A>.
- [303] C. Xiao et al. “Impact of solar irradiance intensity and temperature on the performance of compensated crystalline silicon solar cells”. In: *Solar Energy Materials and Solar Cells* 128 (2014), pp. 427–434. ISSN: 0927-0248. DOI: 10.1016/j.solmat.2014.06.018.
- [304] Gao Yang et al. “Structure of graphene and its disorders: a review”. In: *Science and Technology of Advanced Materials* 19.1 (2018). PMID: 30181789, pp. 613–648. DOI: 10.1080/14686996.2018.1494493. eprint: <https://doi.org/10.1080/14686996.2018.1494493>. URL: <https://doi.org/10.1080/14686996.2018.1494493>.
- [305] Wan-Jian Yin and Yanfa Yan. “The electronic properties of point defects in earth-abundant photovoltaic material Zn_3P_2 : A hybrid functional method study”. In: *Journal of Applied Physics* 113.1 (2013), p. 013708. DOI: 10.1063/1.4772708. eprint: <https://doi.org/10.1063/1.4772708>. URL: <https://doi.org/10.1063/1.4772708>.

- [306] Wan-Jian Yin and Yanfa Yan. "The electronic properties of point defects in earth-abundant photovoltaic material Zn_3P_2 : A hybrid functional method study". In: *Journal of Applied Physics* 113.1 (Jan. 2013), p. 013708. ISSN: 0021-8979. DOI: 10.1063/1.4772708. URL: <https://aip.scitation.org/doi/10.1063/1.4772708> (visited on 10/25/2019).
- [307] S. U. Yu et al. "Simultaneous Visualization of Graphene Grain Boundaries and Wrinkles with Structural Information by Gold Deposition". In: *ACS Nano* 8 (2014), p. 8662.
- [308] Weilai Yu et al. "Atomic force microscopy: Emerging illuminated and operando techniques for solar fuel research". In: *J. Chem. Phys.* 153.2 (July 2020). Publisher: American Institute of Physics, p. 020902. ISSN: 0021-9606. DOI: 10.1063/5.0009858. URL: <https://aip.scitation.org/doi/10.1063/5.0009858> (visited on 09/13/2022).
- [309] Z.-K. Yuan et al. "Engineering Solar Cell Absorbers by Exploring the Band Alignment and Defect Disparity: The Case of Cu- and Ag-Based Kesterite Compounds". In: *Advanced Functional Materials* 25.43 (2015), pp. 6733–6743. ISSN: 1616-301X. DOI: 10.1002/adfm.201502272.
- [310] Elias Z. Stutz et al. "Stoichiometry modulates the optoelectronic functionality of zinc phosphide ($\text{Zn}_{3-x}\text{P}_{2+x}$)". en. In: *Faraday Discussions* (2022). Publisher: Royal Society of Chemistry. DOI: 10.1039/D2FD00055E. URL: <https://pubs.rsc.org/en/content/articlelanding/2022/fd/d2fd00055e> (visited on 08/31/2022).
- [311] Mahdi Zamani et al. "The path towards 1 μm monocrystalline Zn_3P_2 films on InP: substrate preparation, growth conditions and luminescence properties". In: *Journal of Physics: Energy* 3.3 (2021), p. 034011. DOI: 10.1088/2515-7655/abf723. URL: <https://doi.org/10.1088/2515-7655/abf723>.
- [312] I. E. Zanin et al. "Analysis of Chemical Bonding in Zn_3P_2 Crystals from X-Ray Diffraction Data". In: *Crystallogr. Rep.* 49 (2004), p. 579.
- [313] I. E. Zanin et al. "Structure of Zn_3P_2 ". In: *J. Struct. Chem.* 45 (2004), p. 844.
- [314] M. Zeman and D. Zhang. "Heterojunction Silicon Based Solar Cells". In: *Engineering Materials* (2012), pp. 13–43. ISSN: 1612-1317. DOI: 10.1007/978-3-642-22275-7_2.
- [315] Q. Zeng et al. "Graphene-Assisted Growth of High-Quality AlN by Metalorganic Chemical Vapor Deposition". In: *Jpn. J. Appl. Phys.* 55 (2016), p. 085501.
- [316] Peng Zhang and Y. Y. Lau. "An exact field solution of contact resistance and comparison with the transmission line model". In: *Appl. Phys. Lett.* 104.20 (May 2014). Publisher: American Institute of Physics, p. 204102. ISSN: 0003-6951. DOI: 10.1063/1.4878841. URL: <https://aip.scitation.org/doi/full/10.1063/1.4878841> (visited on 09/13/2022).
- [317] X.-G. Zhang and Sokrates T. Pantelides. "Theory of Space Charge Limited Currents". In: *Phys. Rev. Lett.* 108.26 (June 2012). Publisher: American Physical Society, p. 266602. DOI: 10.1103/PhysRevLett.108.266602. URL: <https://link.aps.org/doi/10.1103/PhysRevLett.108.266602> (visited on 08/31/2022).
- [318] H. Zhou et al. "Thickness-Dependent Morphologies of Gold on N-Layer Graphenes". In: *J. Am. Chem. Soc.* 132 (2010), p. 944.

Rajrupa Paul

Address: Avenue de Tivoli 6, Lausanne, Switzerland

Cell phone: +41 76 517 57 74

✉ rajrupa.paulo1@gmail.com

Education

- 2010-2014 **Bachelor of Technology in Nanotechnology**, SRM University, India
Thesis: "Synthesis of electrocatalyst for enzymatic fuel cells." Advisor: Prof. Prakash Ghosh
- 2015-2017 **Master of Nanoscience and Nanotechnology**, Katholieke Universiteit Leuven (KU Leuven), Belgium and Grenoble Alpes, France
Thesis: "In situ mapping of catalytic activity in nano-electrode using Raman spectroscopy". **Magna cum Laude**, CEA Grenoble. Advisors: Dr. Pascale Chenevier and Prof. Philippe M. Vereecken.
- Nov 2017 - Oct 2022 **Doctoral program in Material Science and Engineering**, École Polytechnique Fédérale de Lausanne (EPFL), Switzerland
Thesis: "Zn₃P₂ as an earth-abundant photovoltaic material: from growth to device fabrication", Advisor: Prof. Anna Fontcuberta i Morral.
- 2021 - 2022 *Online Courses Certification in Python for data science, Probability and Statistics in Data Science using Python, and Machine Learning Fundamentals*, UC San Diego (UCSanDiegoX).
- March 2022 *Princez Foundation Certification Agile PM Foundation*.

Awards and Honors

- 2015-2017 *Erasmus Mundus Master of Nanoscience and Nanotechnology Full Consortium Scholarship*
2017 *Magna cum laude Master of Science in Nanoscience and Nanotechnology, KU Leuven*

Research Experience

- 2017-present **École Polytechnique Fédérale de Lausanne**, Laboratory of Semiconducting Materials (LMSC), *Doctoral assistant in Material Science and Engineering*,
Activities: (1) Growth of epitaxial earth-abundant photovoltaic material using molecular beam epitaxy system, (2) Structural, optical, and electrical characterization, (3) Fabrication of electrical devices and photovoltaic device, (4) Innovation of thin-film transfer using van der Waals epitaxy. Advisor: Prof. Anna Fontcuberta i Morral.
- Feb 2016 - Sep 2016 **IMEC (Leuven, Belgium)**,
Activities: (1) Determination of carrier-lifetime in germanium using TRPL. Advisor: Dr. Marianna Pantouvaki.
- Oct 2014 - Jun 2015 **ARCI (India)**,
Activities: (1) Electrochemical reduction of CO₂, (2) Building experimental set-up for artificial photosynthesis. Advisor: Dr. Ibram Ganesh.

Teaching Experience

- 2018 - Present *EPFL* Supervision of Bachelor's and Master's thesis,
Professor: Anna Fontcuberta i Morral.
- 2018 - Present *EPFL* Teaching Assistant (undergraduate courses), Fall semesters.

Papers – Peer-Reviewed Journals

Google Scholar. [Rajrupa Paul](#).

Patents

[Layer transfer of epitaxial layers and thin films obtained by van der waals growth initiation](#)

Skills

SEMICONDUCTING DEVICE FABRICATION

Electron Beam Lithography, Photolithography, Nanoimprinting, Focused Ion Beam, Reactive Ion Etching, Chemical Etching.

MATERIAL SYNTHESIS

Molecular Beam Epitaxy, Chemical Vapor Deposition, Plasma Enhanced Physical Vapor Deposition, Sputtering, Atomic Layer Deposition, Evaporation, Wet Chemical Synthesis.

CHARACTERIZATION TECHNIQUES

Hall Effect Measurement, Four-Point Probe Measurement, Conductive Atomic Force Microscopy, Raman Spectroscopy, Photoluminescence, Time-Resolved Photoluminescence, X-ray Diffraction, Scanning Electron Microscopy, Transmission Electron Microscopy, Energy Dispersive X-Ray Spectroscopy, Atomic Force Microscopy, UV-Vis Spectroscopy, Fourier-Transform Infrared Spectroscopy, Cyclic Voltammetry, High-Performance Liquid Chromatography.

PROJECT AND DATA MANAGEMENT

Agile Project Management, Kanban Board, Laboratory Information Management Systems (SLIMS), Collaboration and Coordination of Projects.

SOFTWARE AND DATA ANALYSIS

Python, Pandas, NumPy, Seaborn, COMSOL, CAD Autodesk Inventor, Blender, ImageJ, Vesta, Gwyddion, Adobe Illustrator.

LANGUAGES

Bengali (Bilingual Proficiency)
German (Beginner A2)

English (Bilingual Proficiency)
Hindi (Fluent)

Last updated: September 19, 2022 •